INTERACTIONS OF ISOTROPIC AND HOMOGENEOUS TURBULENCE WITH SHOCK WAVES

by

George K. Briassulis

A dissertation submitted to the Graduate Faculty in Engineering
in partial fulfillment of the requirements for the degree of
Doctor of Philosophy, The City University of New York

1996

This manuscript has been read and accepted for the Graduate Faculty in Engineering in satisfaction of the dissertation requirement for the degree of Doctor of Philosophy.

1-29-96
Date

Professor Yiannis Andreopoulos
Chair of Examining Committee

1/29/96
Date

Dean Gerald Lowen
Executive Officer

Professor Yiannis Andreopoulos
Dept. of Mech. Eng., CCNY

Professor Joel Koplik
Dept. of Physics, CCNY

Professor George Triantafyllou
Dept. of Mech. Eng., CCNY

Dean Charles B. Watkins
Dept. of Mech. Eng., CCNY

Professor Stavros Tavoularis
Dept. of Mech. Eng., Univ. of Ottawa

Supervisory Committee

THE CITY UNIVERSITY OF NEW YORK

Abstract

INTERACTIONS OF ISOTROPIC AND HOMOGENEOUS TURBULENCE WITH SHOCK WAVES

by

George K. Briassulis

Adviser: Professor Yiannis Andreopoulos

An experimental study of the interaction of a normal shock wave with decaying grid generated turbulence has been performed using time resolved pressure, velocity, temperature and Mach number measurements in a shock tube. Spatial resolution of the order of 7-26 Kolmogorov viscous length scales was achieved in the measurements of turbulence. A variety of turbulence generating grids provide a wide range of turbulence scales with flow Mach numbers ranging from 0.3 to 0.7 and shock Mach numbers from 1.2 to 1.6.

Analysis of the acquired data revealed that the amplification of the pressure fluctuations after the interaction of the normal shock wave with the flowfield depend on the grid's mesh size (initial turbulence level) and shock strength. Furthermore, spectral analysis confirmed that there exists amplification in the wavenumbers after the interaction and this amplification is not constant for the whole range of wavenumbers resolved.

The present results verified a proposed power law decay of the turbulent Mach number M_t in the range of 0.01 to 0.1. Mach number fluctuations were increased with increasing mean flow Mach number and decrease with coarser grid.

The dissipation rate of kinetic energy was found to decrease after the interaction while the dissipative, Taylor's microscale and Kolmogorov's length scale were found to increase.

Integral length scales were found to substantially decrease through the interaction with the shock wave in all investigated cases. It appears that at the weakest of the present interactions the eddies are compressed in the longitudinal direction drastically while their extent in the normal direction remains relatively the same. As the shock strength increases the lateral length scale increases while the longitudinal decreases. At the strongest interaction of the present cases the eddies are compressed in both directions. The outcome of the interaction strongly depends on the initial conditions.

The present results clearly show that most of the changes, either attenuation or amplification occur at large x/M distances where the length scales of the incoming flows are large and turbulence intensities low. Thus large in size eddies with low velocity fluctuations are affected the most by the interaction with the shock.

ACKNOWLEDGEMENTS

I would like to thank my mentor Professor Yiannis Andreopoulos for his constant and unrestricted guidance throughout the years of my research. His patience, vast knowledge of fluid mechanics and his willingness to listen and understand my problems (of scientific nature or not) helped me in clarifying my research goals. His office was never closed for discussions and explanations. Most importantly, I am grateful to him for allowing me the time and freedom to experiment and familiarize myself with sophisticated and expensive equipment.

I am thankful to all the members of the supervisory committee for their time and their thoughtful comments on how to improve this thesis.

The discussions and help of my friend and colleague, Juan Agui are gratefully appreciated; always helpful either assisting in experiments or providing the numerical simulations results or any other type of discussion. It was a pleasure to share the laboratory with such a nice person.

A special recognition to my friend Apostolis Kostazos, PhD candidate in Chemical Engineering, for his time and help in the hot wire experiments. Also it would be an oversight not thank the technicians of the Mechanical Engineering machine shop, Jin Rui Chen and Luis Hernandez, for their valuable assistance.

Finally, there are no words to express my gratitude to my wife Teresa and my parents and sister whose emotional support made the difference between melancholy and hope. It is meaningless to say that without them I could not have finished my work. That is why this work is affectionately dedicated to my wife and my family.

TABLE OF CONTENTS

Chapter 3

Chapter 4

Chapter 5

Chapter 6

Chapter 7

Chapter 8

Chapter 9

APPENDICES

Appendix A

Appendix B

Calibration Techniques

Appendix C

Probe Construction

Appendix D

Rayleigh Scattering

Appendix E

Data Reduction

Appendix F

Sensitivity Analysis and Error Estimates

Appendix G

Calculation of the Skewness of the Velocity Derivative

References

LIST OF TABLES

LIST OF FIGURES

1. INTRODUCTION

The interaction of shock waves with turbulent flows modifies considerably the flowfield by vorticity and entropy production and transport. Thus, the interaction immensely complicates the flowfield. The development of future aircrafts and rotorcrafts as well as the design of inlets and combustion processes demands a better physical understanding of shock wave interactions with turbulent flows.

Such interactions can be found in the entrance flows in supersonic inlets as well as supersonic combustor or exhaust turbine nozzles. Rotorcrafts with angular tip velocities higher than Mach 1 produce a standing shock in front of the blade that in turn interacts with the incoming flow. As a result of the interaction of the turbulent flow with the shock wave, sound is produced. Therefore, an understanding of the phenomenon can propose possible ways of controlling it.

Codes based on numerical solution of the Navier-Stokes equation have achieved some success in treating idealized shocked flows. However problems have surfaced, and such methods failed when modelling of separated flows or turbulent flows were attempted. In general the rapid distortion of the flow field, which characterizes such interactions, was attributed with such failures. Several other simpler and more flexible to execute closed form theoretical studies exist other than the direct solution of the Navier-Stokes. However, their results offer only an indication of the anticipated mean flow field and not that of the fluctuating flow field.

Most of the experimental work is concerned with the interaction of the shock wave

with a boundary layer or a shear layer. When a shock wave interacts with a turbulent flow, the turbulent intensity which is measured after the interaction with the shock, is amplified with respect to its value before interaction. Amplification of the Reynold's stresses and turbulence intensity, observed in most of the experiments, leads us to further investigate this phenomenon. Strong evidence suggests that compressibility effects are responsible for such behavior. In a compressible flowfield three fluctuating modes, that are non linearly coupled, exist. The three modes as proposed by Kovasznay (1950) are:

1. Acoustic (pressure and irrotational velocity fluctuations)
2. Turbulent (vorticity fluctuations)
3. Entropy (temperature, density fluctuations)

When any one of the above modes is transferred through the shock, the other two modes can be generated, and they may also be amplified considerably.

Since all of the added effects of the shocked region are not quite known, experiments must be performed to reveal the new physics involved with the flowfield. The questions of greater importance remaining to be explored by experiments are:

A. Which is the mechanism that modifies the turbulent quantities due to compression by the incoming shock wave?

B. By what amount the turbulent quantities are altered due to compression by the incoming shock wave?

C. What is the behavior of the length scales subjected to compression by the shock wave or to high dilatational fluctuations?

Experiments on grid generated turbulence - shock wave interactions and isotropic decaying

turbulence free of any shock wave interaction at high subsonic Mach number flowfields are scarce, as it will be evident in the literature review. The present work is concentrating on investigating and understanding the compressibility effects on the decay of turbulence as well as the unsteady interaction of a grid generated nearly homogeneous, nearly isotropic turbulence with a normal shock wave. The research work will provide reliable data to validate the numerical codes describing such flows, as well as explaining the physics of such interactions.

2. PREVIOUS WORK

Shock wave interactions with turbulent flows are of great interest due to the fact that the properties of the fluid are significantly altered. The experiments that are performed to investigate and analyze such interactions can be classified into three main categories:

A. Shock wave - boundary layer interaction shown in figure 2.1a.

B. Shock wave - free shear layer interaction shown in figure 2.1b.

C. Traveling normal shock - compressible pipe flow interaction shown in figure 2.1c.

In the first two cases, the flow interacts with an oblique shock wave generated by a compression corner. The presence of the compression corner in the flowfield also produces large gradients in static pressure and skin friction downstream of the flow. The additional gradients present in the flow further complicate the flowfield. In many cases, because of high ramp angles, the flow becomes separated and the shock wave oscillates resulting in an unsteady flow.

In the experiments where there is an oblique shock wave interaction, some additional phenomena were introduced into the flow which complicated it significantly. Such phenomena include:

A. Oscillation of the shock wave in the longitudinal direction and wrinkles in the spanwise direction.

B. Separation of the flow at high ramp angles which leads to unsteady flow.

C. Compression of the flow downstream of the shock depending on the ramp angle.

D. Wall effects (high turbulence intensity) tend to make the flow highly anisotropic.

E. Streamline curvature

All of the above phenomena influence the turbulence amplification phenomena and claims of turbulence amplification due to Rankine-Hygoniot jump alone, are not clearly supported.

The third mentioned category refers to flows inside a shock tube where a traveling normal shock is reflected off the end wall and then it interacts with the induced flow. The interaction of the flow with the shock wave in a shock tube, is nearly free of the above mentioned added effects that are disturbing and complicating the flow. Such an experiment will produce a flowfield where its interaction with the shock wave is much simpler than the flowfield produced in the other two categories that were mentioned before.

The level of turbulence intensity and length scales in the shock tube flow can be controlled by using various grids. The different grid sizes essentially act as a control parameter of turbulence i.e. its velocity fluctuations and mean length scales present. Since it is very difficult to set up an experiment where decaying grid generated turbulence will interact with the shock, previous work on that is very limited. When a grid is placed in a supersonic tunnel, a standing shock wave will be produced upstream of it. If the grid is placed in a settling chamber, the nearly isotropic flow becomes non-isotropic. It should be obvious that the best way to investigate the interaction of the shock wave with the turbulent flow is with the use of a shock tube.

Few investigators have carried out experiments using a shock tube and grid generated with successful results. This work is a continuation of previous experiments that were carried out at CCNY. The present work uses another, larger in diameter and longer, shock tube so

that the spatial resolution of the turbulence measurements has dramatically improved and optical accessibility of the shock wave can be accomplished. In addition to these improvements the duration of the flow has increased due to the larger length of the facility.

A detailed and up to date literature review follows which is divided in five sections. The first section reviews the experimental works of shock wave interaction with boundary layers. Analysis of the shock wave interaction with a shear layer experiments follow in the second section, while section three reviews the shock tube experiments. Finally, the last two sections review experiments performed with grid generated turbulence and in the last section some of the most interesting and significant computational works available.

2.1 Experiments of shock wave-boundary layer interaction

Most of the recent experimental work involving the interaction of a shock wave with a boundary layer using a compression corner is analyzed in this section.

Debieve and Lacharme (1985) experimented with a compression corner which generated a shock wave / free turbulence interaction. Data was acquired using the Hot Wire Anemometry (HWA) technique. They reported a 10-fold increase in the velocity rms value in the region of interaction, an increase in the spectra slope based on velocity data and an increase of the low frequencies (n<20 kHz) of the velocity flowfield due to the interaction. The latter suggests an increase in the integral time scales due to the interaction. Although the flowfield upstream of the shock is practically homogeneous and isotropic, the air injector

introduces turbulence in flow before its interaction with the shock wave. Thus, the flowfield becomes anisotropic and therefore, the interaction with the shock can also be assumed anisotropic.

Ardonceau (1983) investigated the turbulent flowfield in a supersonic shock wave/boundary layer interaction at M=2.25 using a two dimensional compression corner. He used Hot Wire Anemometry (HWA) and Laser Doppler Anemometry (LDA) techniques to show that the turbulent kinetic energy is contained in the large scale structures which are still present downstream of the shock wave. Furthermore, turbulent kinetic energy and the shear component of the Reynold's stress tensor increases rapidly in the first part of the interaction with the shock wave and decrease further downstream. He also shows the limitation of this technique at M_1 close to 1. That is, the technique is not valid where a weak shock wave is involved during the interaction.

Kuntz, Amatucci and Addy (1987) studied the interaction of the shock wave/boundary layer at M=2.94 for various ramp angles, so that the effect of the increasing shock strength on the turbulent properties of the boundary layer to be acquired and analyzed using the 2-D Laser Doppler Velocimetry (LDV) technique. They extensively discuss the uncertainty associated with the above mentioned technique. In their experiment, turbulence intensities as well as the Reynold's stresses were significantly increased by the interaction with the shock and the amount of increase was shown to be related to the shock strength. Large scale turbulent structures were found to be responsible for the increases in the above quantities.

Brown, Kussoy and Coakley (1985) in a I.U.T.A.M. conference note that when the flow becomes separated several factors complicate dramatically the interpretation of the data,

such as shock unsteadiness and large turning angles of the streamlines. The above unsteadiness of the shock wave produced additional turbulence as well as a rise in the normal and shear stresses. In regard to numerical analysis used in the same work, they mentioned that Navier-Stokes solutions with a two eddy viscosity turbulence model could predict the experimental mean flow field but not the fluctuating flow fields.

Kussoy, Brown, Brown, Lockman and Horstman (1987) analyzed the interaction of the shock wave with the boundary layer using two compression corners at $M_\infty = 2.85$. Flow measurements were obtained by the LDV technique. The unsteady motion of the shock wave associated with this type of experiments dealt with two different positions of the shock. They reported that the computed intensity of the turbulent kinetic energy did not resemble the experimental data. Furthermore, they concluded that due to shock unsteadiness "pseudo-turbulence", seemed to dominate the turbulent field for highly separated flows. For lesser turning angles, the turbulent field is affected in the near vicinity of the shock.

The boundary layer behind a moving shock wave produced in a rectangular duct was studied by Decker and Weeks (1976) using a Schlieren system and the HWA technique. The shock strengths that were studied were varying from 1.28 to 2.24. They pointed out that stronger waves (stronger than $P_2/P_1=1.28$) not only effect the boundary layer by the longitudinal disturbances, but also by lateral disturbances which became significant. They concluded that boundary layer closure can be characterized by the Reynolds number based on flow length, and for sufficiently strong waves, the boundary layer closure is affected by lateral disturbances and interaction between the wave front and the contact surface.

Andreopoulos and Muck (1987) presented results of their experiments using a two-

dimensional compression corner in M_∞=2.9 flow. Pressure measurements of the shock wave interaction with the incoming flow confirmed the unsteadiness of the shock wave. The authors showed that the frequency of the oscillation is of the same order as the bursting frequency of the upstream boundary layer. Their results strongly suggest that turbulence is significantly amplified by the incoming shock.

Shock wave / boundary layer interaction experiments were performed by Smits and Muck (1987) using three different compression corners in a M_∞=2.9 flow. Measurements were acquired using the HWA technique. The turbulent stresses and mass flux were dramatically amplified and the above amplification was shown to increase with increasing ramp angles. The authors state that the shock unsteadiness significantly contributed to the amplification of the normal stresses.

Spina et al. (1994) offers the most recent review of works concerning compressible shear flows or boundary layers.

2.2 Experiments of shock wave / shear layer interactions

The results of the interaction of a shear layer with a shock wave was reported by Settles, Fitzpatrick and Bogdonoff (1979). The interaction was generated using several two-dimensional compression corners. The mean quantities of the flowfield were acquired using pitot probes. Results from the above experiment show that separation of the flow exists at high ramp angles. Their results were compared with a numerical simulation of the time

averaged compressible Navier-Stokes equations using three different turbulence models. When flow separation occurred, the results that were generated from the numerical simulation were incompatible with the results of the experiments. The authors extensively discussed the evolution of the flowfield properties from the non-separated case to the separated case.

Settles, Williams, Baca and Bogdonoff (1982) studied the two dimensional free shear layer interaction with a shock wave using the HWA technique and mean pressure probes. Their results showed a small tremble of the wave system which corresponded to the unsteadiness of the flowfield. Yet, the mean mass flux of the shear layer before and after interaction with the shock wave shows a significant amplification (order of 3).

Hayakawa, Smits and Bogdonoff (1984) presented measurements of mass flow fluctuations in a shear layer/shock wave interaction experiment. Data was acquired using the HWA technique. Substantial increase in turbulence intensity and mass flow rate was found in the compression region. Based on their analyses, such as pdf of velocity, shadowgrams and the turbulent kinetic energy transport equation, the authors concluded that the length scale was considerably increased through the interaction.

The LDV technique was used to study the shock wave/shear layer interaction by Samimy, Petrie and Addy (1986). They showed that turbulence intensities, shear stresses and turbulent triple products were substantially increased during interaction of the shear layer with the shock wave. Finally, the authors suggested that calculation of the triple turbulent products are required when the physical understanding and modelling of such interactions are needed.

The most recent review of compressible turbulence investigated through compressible

shear layers is offered by Gutmark et al.(1994).

2.3 Experiments of normal shock wave interaction with turbulent flows in shock tubes.

Jacquin, Blin and Geffroy (1991) conducted an experiment where grid generated turbulence would interact with a normal shock in a rectangular duct. They reported that no amplification of the turbulent kinetic energy was observed due to the interaction of the turbulent flowfield with the shock wave. The measurements were collected using an LDV system where the signal to noise ratio was low and, thus, the measured amplification / attenuation is expected to be low.

To analyze the shocked flow, Keller and Merzkirch (1990) experimented with a rectangular shock tube using a speckle photographic method. They analyzed the interaction of a shock wave with grid generated turbulence for three different driver pressure ratios P_4/P_1=3.0, 3.5, 4.0. Velocity fluctuations were measured at a non-dimensionalized downstream location x/M=19. According to Corrsin (1951), for comparable Reynolds number based on the mesh size, isotropic turbulence can be assumed at a downstream location of x/M>40. Despite the questionable claim of isotropic turbulence, they concluded that amplification was observed at the lower wave numbers (large scale structures) and was not observed for high wave numbers. The estimation of error was about 10% due to the small cross section of the tube as well as the error associated with the assumptions made for the calculation of mean induced velocities and mean speed of sound.

Correlation measurements in air flow of isotropic turbulence with density and temperature fluctuations have been performed by Erbeck and Merzkirch (1988) using the speckle photography technique. Isotropy was assumed, again as in the previous work, at a location downstream from the grid, x/M=18. One dimensional energy spectrum of temperature fluctuations did not verify the -5/3 law. Nevertheless, the technique although non intrusive, required the assumption of isotropy as well as repeated measurements at various downstream locations.

Trolier and Duffy (1985) experimented with a shock tube 4" inches in diameter and 62 feet long at various diaphragm rupture pressure ranges up to 100 psi, equivalent of $M_s \approx 1.7$. Turbulence generating grids were not used in their work, yet they found that mass flux fluctuations were between 0.6 and 1.6% in the incident region and about 2 and 6% in the reflected region. They also concluded that turbulence quantities were amplified across the reflected shock (about 6 times max.) and in general they decreased with increasing Re # based on the wire diameter. In their analysis, they considered a zero - pressure fluctuation (no grid turbulence). Nevertheless, amplification of all turbulence quantities of mass flux, velocity, density and temperature (except pressure) was evident, except at Re # = 160×10^{-3} where no amplification was evident.

The interaction of a shock wave with a vortex was analyzed in the work of Weeks and Dosanjh (1967). They reported that for the far field, experiments and theory were closely matched. They also claim that compressibility effects were not an important factor of the interaction. Such conclusions come in contrast with today's experiments were compressibility effects are shown to substantially influence the flowfield. A possible explanation is that the

far field that was investigated in the above work was free of compressibility effects, i.e. turbulence was decayed at levels where it could not be recorded.

Honkan and Andreopoulos (1992) carried out experiments on grid generated turbulence interacting with a normal shock wave in a 1¾" in diameter shock tube using the hot wire technique and pressure transducers. The major conclusions of their work was that turbulent intensities and the length scales of the flow are increased after the shock interaction since the eddies coalesce and amalgamate to form larger eddies. Amplification of the length scales is not the same for the whole range of wavenumbers of the flow. In particular, the authors mentioned that the small size eddies are amplified more than the large size eddies.

Similar experiments were performed by Honkan, Watkins and Andreopoulos (1994) using the previous mentioned shock tube. A Cold Wire technique was used in addition and complementary to the Hot Wire Anemometry technique. The length scales, velocity and temperature fluctuations had been found to be amplified. Anisotropy of the flow after the interaction was found to be caused by the different amplifications of the velocity fluctuations. The authors identify a new controlling parameter ($r=Ls/q$) of the interaction which relates the time scale of the mean strain across the shock wave, s, to the time scale of turbulence, L/q. When (r) reaches small values, inviscid rapid distortion theory and its compressible version can describe the bulk characteristics of the interaction.

2.4 Numerical Simulations

Work that revolves around numerical studies attempting to simulate the shock wave turbulent flow interaction are in abundance in the literature. Many different techniques are applied with equally many different results. Some of the most interesting and recent ones are analyzed now.

The linearized analysis of McKenzie and Westphal (1968) showed that incident entropy-vorticity waves can generate sound waves behind the shock. The transmission coefficient $\delta P_2/\delta P_1$ was found to be proportional to the third power of the Mach number. They showed that the energy flux carried by the reflected sound and entropy waves is greater than the energy flux carried by the sound wave incident to the shock. Amplification of energy is shown for various Mach numbers to be increasing with increasing Mach numbers.

Anyiwo and Bushnell (1982), using a linearized analysis for the interaction of an oblique shock with a boundary layer and comparing the results of the analysis with experimental data, concluded that turbulence amplification is influenced by some critical parameters such as M_s (incident Mach #), shock angle θ_s, γ. Since the actual physical problem is nonlinear, their analysis is only a crude rule of thumb for expected amplifications.

Horstman, Settles, Williams and Bogdonoff (1982) presented a numerical simulation of the time dependent N-S equations for the data obtained by Settles et al. (1982). The authors reported that the length scale was inadequately predicted before and after the interaction of the shear layer with the shock wave. Nevertheless, they found that the mass flux fluctuations as well as the surface pressure and skin friction were significantly amplified after the reattachment of the shear layer and, thus, its interaction with the shock wave.

Lacey and Long (1990) worked on a numerical simulation of the processes involved in a shock tube using a finite difference approach. Several conditions of the pressure ratio were tested as well as different lengths of the driver. Results are not matching the existing experimental data. The authors explain the above difference by viscous losses and on planar distortions of the shock wave interface in an experiment.

Rotman (1991) used a second order Godunov's method to solve the time dependent Euler equation in order to study the effects of a passing shock wave to a turbulent flow. He pointed out that amplification in the turbulent kinetic energy due to shock passage was of the order of two. The more turbulent the flow was, the less it was amplified. The density and pressure fields were found to agree very well with those obtained from experiments after the passage of the shock wave. The disagreement with some experiments surfaced when the length scales, before and after the shock, were compared. This difference may be attributed to the method that was used. This study is a large eddy simulation and the transfer of energy from the shock wave to the flow from the small scales is not incorporated in this work.

Buckingham (1990) applied a minimally diffusive, high resolution, Godunov method on shock wave interactions with turbulence. Results from the analysis showed that there exists energy in three fluctuating components, velocity, entropy and acoustical. The acoustical mode contains the least amount. Amplification was verified for all cases, although the amplification rates increased less and less with increasing Mach number. This researcher also points out that the dynamical interaction range of the shock with the flow becomes significantly compressed with increasing Mach number.

The direct numerical simulation (DNS) work of Coleman and Mansour (1991) under

isotropic mean compression turbulence shows that the high Mach number flows depend strongly on acoustic (pressure) initial conditions. The author implies that models which are used to analyze the interactions of velocity and/or pressure fluctuations modes with a shock wave should include both modes in the analysis.

Viecelli (1989) used a second order numerical method to integrate the hydrodynamic equations so that the interaction of shock waves with turbulent flows can be investigated. Amplification of turbulent kinetic energy was found to be decreasing with increasing viscous effects. Although amplification of the turbulent kinetic energy is decreasing with increasing kinetic energy, the fraction of the total energy in rotation continues to increase after compression. Small scale structures according to the above analysis tend to retain their identity and amplification of kinetic energy of these structures can be very large.

Ribner (1986), extending the NACA works of 1950's, points out that the amplification exists in both the longitudinal and lateral components of turbulence in the velocity mode. One dimensional spectral analysis revealed that the acoustic field just after interaction is mainly composed of low frequencies and decays asymptotically like $k^{-5/3}$, while the far field is not carrying any low frequencies. Nevertheless, the far field is also decaying like $k^{-5/3}$ (Kolmogorov's law). Postshock/ preshock spectral ratio shows that increasing the Mach number favors the low frequencies of longitudinal turbulence component in the velocity mode. Similar results are presented for temperature and pressure fluctuations where low frequencies are enhanced in the temperature mode and are deficient in the pressure mode. Both of them present a fold over of the curves with increasing Mach number.

Lee, Lele and Moin (1991) simulated the interaction of a shock wave with turbulence

using three different computational methods with turbulent Mach numbers of the order of 0.6 which is much larrger that those obtained in experiments. One was the incompressible rapid distortion theory and the others were the compression linear interaction analysis and the direct numerical simulation of a 2-D isotropic turbulence interaction with a normal shock. Although the acoustic (pressure) mode was not taken into account, amplification of vorticity as well as turbulent kinetic energy components was found. The authors claimed that their analysis shows that shock front curvature and shock front oscillation would not effect the enhancement of turbulent kinetic energy, even though the effects of "pseudo-turbulence" experimentally are well established to influence the amplification of the turbulent quantities. Spectral analysis comparing the upstream and downstream energy spectra showed that there exists more amplification at smaller scales than at large scales. The above will result in a decrease in the overall length scale. Enstrophy, 1/2 the mean square vorticity, is shown to be amplified through the shock wave and then to decay with downstream distance. The same authors, in a more recent work (1994), using a similar numerical simulation confirmed, as in the previous work, that the turbulent kinetic energy was amplified across the shock wave. They found that most energy spectra were amplified more at large wavenumbers rather than at small wavenumbers. They concluded that most of the length scales decrease across the shock wave, except some length scales which increase only for weak shock waves.

2.5 Grid Generated Turbulence

Although the induced flow in the shock tube is the best candidate for testing calculation methods and turbulence modeling, previous work on homogeneous and isotropic compressible turbulence is very limited. A substantial amount of experimental work dealing with the incompressible grid generated turbulence already exists. The effects of grids and perforated plates as flow straighteners on the free stream turbulence was studied by Tan-Atichat et al.(1982) for Reynolds number based on mesh size Re_M up to 735. They found that the performance of the grid is dependent on the characteristics of the incoming flow. For a larger range of mesh Reynolds number Re_M ranging from 12800 to 81000 Frenkiel et al. (1979) observed that the data exhibited a high degree of similarity. Analysis of the higher order correlations and moments of the turbulent velocity components revealed that the turbulent fluctuations is of a non-Gaussian character. Grid turbulence at large mesh Reynolds number ($1.2x10^5$ to $2.4x10^6$) was studied by Kistler and Vrebalovich (1966). To avoid compressibility effects the mean flow was kept below 60 m/sec. The flowfield under investigation was anisotropic and they concluded that if the -5/3 slope is to be used for the spectral curve then a minimum turbulence Reynolds number (Re_λ) of 300 is required. The velocity derivative skewness in a nearly isotropic turbulence was extensively discussed by Tavoularis et al (1978). Experimental measurements show that the skewness of the streamwise velocity derivative depends on the turbulent Reynolds number, Re_λ. It appears that for $Re_\lambda \approx 4$ the skewness factor has its maximum. It is evident that in all of the above studies on grid generated turbulence compressibility effects were absent or undesirable. One

of the first attempts to generate compressible isotropic turbulence is described by Honkan and Andreopoulos (1992) who set up a flow with $Re_\lambda \approx 1000$. Recently Budwig et al (1995) and Zwart et al. (1996) worked with compressible streams in three different Mach numbers. The decay coefficient for the lowest Mach number of 0.16 was found to be -1.24 and for the highest Mach number of 1.6 was -0.49. Inhomogeneity across the test section prevented them from measuring decaying turbulence. The present experimental work is a fundamental study of compressibility effects focusing in grid generated turbulence for flows with Mach numbers ranging from 0.3 to 0.6.

2.6 Literature review summary

It is evident from the literature review that there are different flow configurations that are used to study the interactions of turbulent flows with shock waves and many more numerical simulations trying to perform the analysis of the above interaction. It is clear that numerical simulations offer a quantitative approach to the problem. Most of them fail to capture the main essence of the shock wave interaction with a turbulent flow, which is to describe qualitatively and quantitatively the change of the different length scales.

All the different flow configurations, except the ones utilizing the capabilities of the shock tubes, complicate the flowfield immensely and therefore qualitative analysis of the interaction phenomenon cannot be isolated.

The shock tube experiments are the ones which produce a 'clean' flowfield after the

interaction with the shock wave without the presence of any other added disturbances.

The physics involved with the interaction of the shock wave with the turbulent flows as well as the compressibility effects on isotropic decaying turbulence are still vaguely understood and thus more fundamental work is needed to explain and describe the interaction phenomena accurately.

The fundamental questions that remain unanswered are how the turbulent quantities and their associated turbulent scales are altered due to the compression by the shock wave and the associated compressibility effects for a wide range of mean flow Mach numbers, mean length scales and shock strengths. Namely how, how much, and for how long the fluctuating pressure, velocity, temperature and density fields are altered. Also it is known that all associated turbulent length, velocity and time scales, yet the exact degrees and the exact locations of these changes are unknown . Furthermore a detailed and reliable data set, vital for the development of the numerical simulations, of the shocked flow or a compressible decaying turbulent flowfield has not yet been gathered.

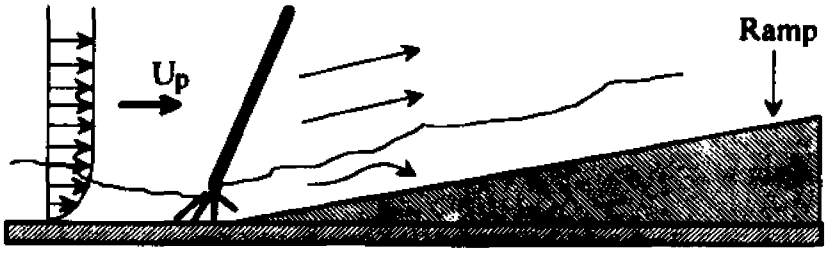

BOUNDARY LAYER INTERACTION

(a)

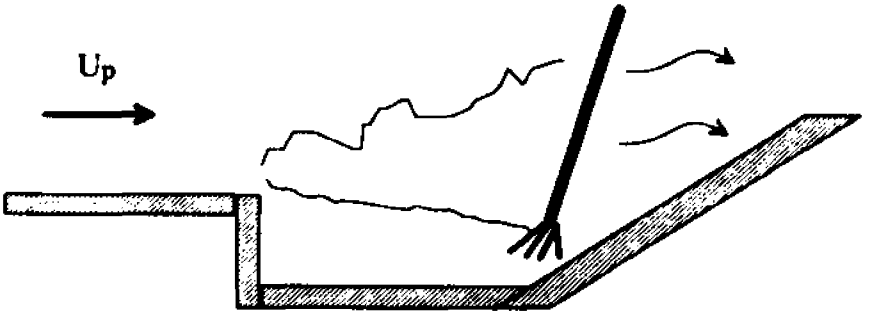

SHEAR LAYER INTERACTION

(b)

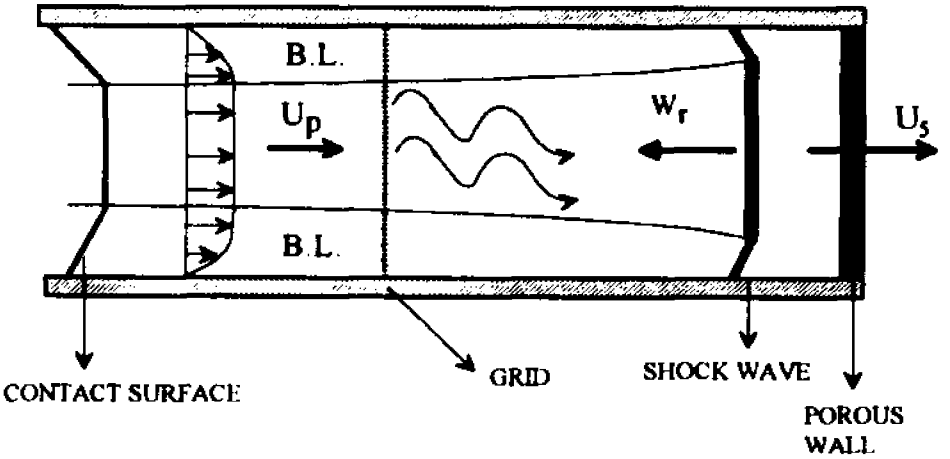

TURBULENT FLOW INTERACTION

(c)

Figure 2.1: Sketch of different types of shock wave interactions

3. OBJECTIVES

The shock tube is probably the most suitable and efficient apparatus used to simulate the interaction of homogeneous and isotropic turbulence with a shock wave. In reviewing the existing work on the subject, it became clear that knowledge of the mechanics and physics of the shock wave interaction with the turbulence as well as compressibility effects due to high dilatational term on the turbulent flowfield are of great importance to the scientific and engineering community. It is also true that there is only scarce and incomplete work available on the subject.

The present work focuses on studying the unsteady interaction of decaying grid generated nearly isotropic turbulence with a shock wave in a shock tube and producing reliable data to validate the numerical codes capable of describing such flows. This work is a continuation of previous experiments that were carried out at CCNY. The present work uses a larger in diameter and longer shock tube and therefore the spatial and temporal resolutions of the measurements are dramatically improved.

This experimental work investigates the flowfield modification due to its interaction with the traveling shock wave as well as compressibility effects on decaying grid generated nearly isotropic turbulence. This work aims at providing a thorough understanding of the physics and the mechanics involved in such interactions. It also produced valuable information on the status of the fluctuating quantities of the flowfield, i.e. pressure, velocity and temperature fields, before and after interaction. The present work investigated the effects on turbulence of the following variables:

A. Shock wave Mach numbers (incident and reflected).

B. Reynold's number based on the mesh size.

C. Turbulence Reynold's number.

D. Magnitude of the dominant length scales.

Furthermore, the performed experiments shed light on the different turbulent scales and wavenumbers associated with the interaction of nearly isotropic and nearly homogeneous turbulence with a normal shock wave. That is the integral, Taylor, Kolmogorov's and dissipative length scales as well as the integral, micro and Kolmogorov's velocity and time scales of the flow associated with the interaction were calculated to show the degree of change after the above mentioned compression of the flowfield from the shock wave. Moreover, it is important to show which quantities are minimally affected and if there are any turbulent quantities which are preserved during and after the interaction. Turbulence levels were controlled with the usage of different mesh sizes. Analysis of compressibility effects produced from high dilatational fluctuations present in high speed flows, on the previously mentioned scales is also a scope of this work. Dissipation rates and associated dissipative length scales of decaying isotropic turbulence were also calculated for different initial turbulence levels, as well as for different downstream locations.

A detailed description and analysis of the techniques and methods that were applied in the experiments is given in the following chapters. This experimental work is of great importance since for the first time data of the interaction were acquired at multiple downstream locations simultaneously. The size of the facility allows the investigation of the above interaction at downstream locations that were never before been attempted. Complete

results can assist us to understand the physics that are involved with the interaction as well as to identify the influence of the compressibility effects associated with high speed flows. The knowledge obtained by the results can be further used in other similar experiments dealing with noise reduction, mixing, supersonic inlet flows, etc., as well as to predict the behavior of different processes and applications undergoing through similar operating conditions. Examples of the above mentioned processes and applications can be found in the combustion chamber of a reciprocating engine, in a supersonic combustor, in the inlet of a supersonic jet engine and numerous other applications involving high speed flows.

3.1 Thesis Organization

In the next chapters the following will be covered:

A. In chapter 4 1-D theory and relations of the mean flow in the shock tube is offered as well as viscous corrections to account for the coefficient of friction in the shock tube.

B. Following the theory (chapter 4), the physical description of the shock tube as well as pioneering work in shock tubes is presented (chapter 5).

C. Description of the experiments and the associated techniques can be found in chapter 6. Data acquisition and electronic equipment used in the different experiments are described at the end of this chapter.

D. The different types of time dependent traces and the extent of useful data obtained from the performed experiments are explained in chapter 7.

E. Results and discussion of the performed experiments are offered in chapter 8. This chapter is subdivided in four sets of experiments. Each set of experiments is

autonomous and results from one set of experiments do not directly influence the other sets.

F. Conclusions are presented in the last chapter in this work.

Several appendices are also offered. The operation of the shock tube is presented in the first appendix. Appendix B presents all calibration techniques used to calibrate the instruments used. The third appendix presents sketches and photographs of the instruments that were used in the different set of experiments. Rayleigh scattering calculation and some theory is offered in appendix D. The relations that were relevant to this work are offered in appendix E. Finally sensitivity analysis and error estimates are offered in the last appendix, F.

4. THEORY

For shock tube flows, the normal shock relations obtained by the 1-D inviscid and adiabatic compressible continuity, momentum and energy equations were used to provide all the theoretical relations of the mean flowfield before and after the reflection of the shock wave off a porous or solid end wall. The end wall is a solid or a porous boundary where the shock wave can be reflected totally or partially back into the shock tube. The porous end wall can be seen in figure 2.1c.

4.1 Introduction

There are not many different types of apparatus to study unsteady wave motion. A shock tube is usually the choice of experimental apparatus for such research. This apparatus is a tube closed at both ends, in the case where a solid end wall is used, or with one end closed and the other end partially open in the case where a porous end wall is used. A diaphragm is separating a region of high pressure gas from a region of low pressure gas. When the diaphragm breaks, a shock wave propagates into the low pressure region with a velocity W_s. This propagation of the shock wave induces a mass flow with velocity U_p and it also increases the pressure behind it as shown in figure 4.1a. The ratio of the pressures behind and in front of the shock wave is an important parameter that controls the physical changes taking place across the shock wave. This ratio is called the incident shock strength or simply shock strength.

4.2 Nomenclature

The variables that are listed below are used repeatedly in this section.

A: Shock tube cross sectional area

a: Speed of sound

C_f: Piecewise average coefficient of friction

C_p: Specific heat

D: Diameter of the shock tube

L: Length of segment in the shock tube

M: Mach number

U: Flow velocity

P: Pressure

Q: Heat

R: Universal gas constant

Re_D: Reynolds number based on the diameter of the shock tube

St: Stanton number

T: Temperature

W_I: Incident wave velocity

W_R: Reflected wave velocity

x: Porosity of the end wall

γ: Specific heat ratio

ρ: Density

χ: Velocity ratio (exit to incident)

4.3 Incident shock relations

For one dimensional adiabatic inviscid compressible flow the equations of continuity, momentum and energy between regions 2 and 1 are given by Anderson (1982) and Saad (1985) as:

$$\rho_1 W_s = \rho_2 (W_s - U_p) \qquad (1)$$

$$P_1 + \rho_1 W_s^2 = P_2 + \rho_2 (W_s - U_p)^2 \qquad (2)$$

$$C_{p_1} T_1 + \frac{W_s^2}{2} = C_{p_2} T_2 + \frac{(W_s - U_p)^2}{2} \qquad (3)$$

Furthermore, for a perfect gas the equation of state for region 2 and 1 are given as:

$$P_1 = \rho_1 R_1 T_1, \quad P_2 = \rho_2 R_2 T_2 \qquad (4)$$

When the incident shock strength, P_2/P_1, is known as well as the parameters in region 1 then the above equations can provide solutions for T_2, ρ_2, U_p and W_s.

$$T_2 = T_1 \frac{P_2}{P_1} \left[\frac{\frac{\gamma_1 + 1}{\gamma_1 - 1} + \frac{P_2}{P_1}}{1 + \frac{\gamma_1 + 1}{\gamma_1 - 1} \frac{P_2}{P_1}} \right] \qquad (5)$$

$$\frac{\rho_2}{\rho_1} = \frac{1 + \frac{\gamma_1+1}{\gamma_1-1}\frac{P_2}{P_1}}{\frac{\gamma_1+1}{\gamma_1-1} + \frac{P_2}{P_1}} \qquad (6)$$

and

$$M_s = \left[\frac{\gamma_1+1}{2\gamma_1}\left(\frac{P_2}{P_1}-1\right)+1\right]^{\frac{1}{2}} \qquad (7)$$

$$W_s = M_s \cdot a_1 \qquad (8)$$

where $a_1 = (\gamma_1 R_1 T_1)^{1/2}$ and for air $R_1 = 287$ J/Kg/°K.

Solving the continuity equation one can calculate the flow velocity behind the wave.

$$U_p = W_s\left(1 - \frac{\rho_1}{\rho_2}\right) \qquad (9)$$

Substituting equations (6), (7) and (8) into (9) one can get the flow velocity behind the shock as a function of the incident shock strength (P_2/P_1).

$$U_p = \frac{a_1}{\gamma_1}\left(\frac{P_2}{P_1}-1\right)\left[\frac{\frac{2\gamma_1}{\gamma_1+1}}{\frac{P_2}{P_1}+\frac{\gamma_1-1}{\gamma_1+1}}\right]^{\frac{1}{2}} \qquad (10)$$

For an infinitely strong shock ($P_2/P_1 \rightarrow \infty$) U_p is approaching:

$$\lim_{P_2/P_1 \rightarrow} U_p = a_2\sqrt{\frac{2}{\gamma_4(\gamma_4-1)}}$$

For air max $U_p/a_2 \rightarrow 1.89$ and for helium max $U_p/a_2 \rightarrow 1.34$.

4.4 Shock wave reflections off a porous wall

When the shock wave impinges on the end-wall, it is reflected back and propagates with speed W_R which is lower than W_s. When the end-wall is solid, then there is no mass motion behind the reflected shock wave (region 5). In the above case $U_5 = 0$. However, most of the present experiments were conducted using a porous end-wall and so U_5 is no longer zero (see fig. 4.1b). The maximum value of U_5 can be considered to be equal to U_p (open end, no reflected wave) and the minimum value of U_5 is zero when the incident shock is totally reflected from a solid (non-porous) end-wall. The reflected shock further compresses the flow to a pressure P_5 higher than P_2. The flow velocity (U_5) behind the shock is a function of the porosity of the end wall and, therefore, it can be considered to be known. Continuity, momentum and energy equation for a non-stationary control volume become (Honkan and Andreopoulos (1990)):

$$\rho_2(W_R+U_p)=\rho_5(W_R+U_5) \qquad (11)$$

$$P_2+\rho_2(W_R+U_p)^2=P_5+\rho_5(W_R+U_5)^2 \qquad (12)$$

$$C_pT_2+\frac{(W_R+U_p)^2}{2}=C_pT_5+\frac{(W_R+U_5)^2}{2} \qquad (13)$$

From the incident shock relations (1), (2), (3) and the above reflected shock equations a relation between M_R and M_s can be obtained:

$$\frac{M_R}{M_R^2-1}=\frac{M_s}{M_s^2-1}\left[1+\frac{2(\gamma_1-1)}{(\gamma_1+1)^2}(M_s^2-1)\left(\gamma_1+\frac{1}{M_s^2}\right)\right]^{\frac{1}{2}} \qquad (14)$$

The above equation has two solutions. One of them (the imaginary one) is rejected. Furthermore, the reflected shock propagates into the gas ahead of it with a Mach number:

$$M_R = \left(\frac{W_R + U_p}{a_2} \right) \quad \rightarrow \quad W_R = M_R a_2 - U_p \qquad (15a)$$

The above equation (14) assumes that the incident shock is totally reflected at the solid boundary. A new equation is now introduced, replacing equation 14, to include the effects of a porous end wall on the mean flowfield. If there is a porous medium, then the mean flow velocity behind the reflected shock (U_5) is a fraction (χ) of the incoming mean flow velocity U_p. In a compressible flow through a porous medium, the mass flux that exits the shock tube is needed to be calculated. Since the mass flux is dependent on the density of the flow and, thus, its temperature, it is cumbersome to calculate the mass flux exiting the tube. Thus, it is advantageous to use the fraction χ of the incoming velocity as the exiting velocity. Then the percentage of mass flux exiting the shock tube can be easily obtained by $x = \frac{\rho_5 U_5}{\rho_2 U_2} = \frac{\rho_5}{\rho_2}\chi$.

When the temperature and, therefore, the density of the exiting fluid are calculated, then by substituting $U_5 = \chi U_p$ into equations (11), (12), (13) one can obtain an expression relating the Mach number of the reflected shock with the flow velocity and the porosity of the wall. Furthermore, since $M_2 = f(P_2/P_1) = f(M_s)$ then $M_R = f(M_s, x)$. The resulting equation is:

$$M_R^2 - \left(\frac{\gamma_1 + 1}{2} \right) M_R (1 - x) M_2 - 1 = 0 \qquad (15b)$$

The discriminant of equation 15b is always positive and therefore two real solutions are obtained. One of the solutions will always give a negative value for M_R and thus it can be discarded.

Solving equations (11), (12), (13) and using the equation of state for region 5, one can obtain

the pressure and temperature relations at this region as a function of U_s, U_p, P_2 and ρ_2.

$$P_5 = P_2 + \rho_2 (W_R + U_p)[(W_R + U_p) - (W_R + U_5)] \qquad (16)$$

$$T_5 = \frac{P_5}{R\rho_2}\frac{W_R + U_5}{W_R + U_p} \qquad (17)$$

4.4.1 Conical Diffuser

The interface between the driver (high pressure region) and the driven gases is called the contact surface, which is also moving with velocity U_p. This contact surface is portrayed as the slip line across which entropy changes discontinuously. Yet, the pressure and velocity are preserved. Therefore $P_3 = P_2$, and $U_3 = U_2 = U_p$ if both driver and driven gases are the same. In many experiments the driver gas is usually different than the driven gas (most cases air) then $M_3 = U_p/a_3$ and $M_2 = U_p/a_2$. One needs T_3 in order to calculate M_3. Because of the existence of the conical reducer additional unknowns are introduced and T_3 has to be calculated with the use of a numerical scheme. An initial estimate of T_3 is obtained by the isentropic relation for a shock tube without a cone. The new calculated driver temperature T_{4c} is compared with the known driver temperature T_4. The numerical scheme after some iterations can produce T_3 so the numerical driver temperature T_{4c} matches the known driver temperature T_4. See fig. 4.1a and 4.1b for the different flow regimes associated with the shock tube flows.

Many shock tubes use a conical reducing section which is designed to be placed after the high pressure section so that the properties of the shocked flowfield will be amplified and also practically interference of the flow can be avoided when the diaphragm ruptures. The

area at the diaphragm is A_3' and at the end of the reducer is $A_3 = A_2$. To calculate the Mach number at point 3' we consider the area Mach number relation:

$$\left(\frac{A}{A^*}\right)^2 = \frac{1}{M^2}\left[\frac{2}{\gamma_4+1}\left(1+\frac{(\gamma_4-1)}{2}M^2\right)\right]^{\frac{\gamma_4+1}{\gamma_4-1}} \qquad (18)$$

Applying the above relation at points 3 and 3' we get the following expression:

$$\frac{A_3}{A'_3} = \frac{M'_3}{M_3}\left[\frac{2+(\gamma-1)M_3^2}{2+(\gamma-1)M'^2_3}\right]^{\frac{\gamma+1}{2(\gamma-1)}} \qquad (19)$$

for γ_4=1.4 the exponent of the above equation is equal to 3. Thus the following polynomial will provide the solution for M_3' (air is the driver and the driven gas):

$$\frac{A_3}{A'_3}[(\gamma_4-1)^3 M'^6_3+6(\gamma_4-1)^2 M'^4_3+12(\gamma_4-1)M'^2_3+8] = \frac{M'_3}{M_3}(2+(\gamma_4-1)M_3^2)^3 \qquad (20)$$

for γ_4=1.6667 (for gases such as helium and hydrogen) the exponent of equation (19) is equal to 2 and the polynomial now becomes:

$$\frac{A_3}{A'_3}[(\gamma_4-1)^2 M'^4_3+4(\gamma_4-1)M'^2_3+4] = \frac{M'_3}{M_3}(2+(\gamma_4-1)M_3^2)^2 \qquad (20a)$$

The Newton-Raphson method can be used to solve either polynomial using a close tolerance criterion to ensure accurate results. In our case a tolerance of 0.00001 was used.

For an adiabatic flow the total temperature (T_o) is constant. Therefore, the temperature relation between points 3 and 3' using total temperature relations is given by Anderson (1982) as:

$$\frac{T_3}{T'_3}=\frac{T_o/T_3}{T_o/T'_3}=\frac{2+(\gamma_4-1)M'^2_3}{2+(\gamma_4-1)M_3^2} \qquad (21)$$

Continuity equation between points 3 and 3' is:

$$\rho'_3 A'_3 U'_3 = \rho_3 A_3 U_3 \qquad (22)$$

also the speed of sound is defined as:

$$a^2=\frac{\gamma P}{\rho} \qquad (23)$$

Applying the previous equation into the continuity equation (22) we get a relation for the pressure drop through the reducer:

$$\frac{P_3}{P'_3}=\frac{A'_3}{A_3}\frac{M'_3}{M_3}\sqrt{\frac{T_3}{T'_3}}=\frac{A'_3}{A_3}\frac{M'_3}{M_3}\sqrt{\frac{2+(\gamma_4-1)M'^2_3}{2+(\gamma_4-1)M_3^2}} \qquad (24)$$

Using relations for the expansion wave in the high pressure region 4 (fig. 4.1a) we get by integration along the characteristic line C, the Riemann invariant $J_+=U+\frac{2a}{\gamma-1}$ which is constant through the wave (Anderson (1982)). Applying the previous relation between points 3' and 4 we get:

$$\frac{P'_3}{P_4}=\left[1-\frac{\gamma_4-1}{2}\frac{U'_3}{a_4}\right]^{\frac{2\gamma_4}{\gamma_4-1}} \qquad (25)$$

Since the flow is isentropic the following relations are true:

$$\frac{P'_3}{P_4} = \left(\frac{\rho'_3}{\rho_4}\right)^{\gamma} = \left(\frac{T'_3}{T_4}\right)^{\frac{\gamma}{\gamma-1}} \qquad (26)$$

Finally an expression can be obtained relating the bursting pressure ratio P_4/P_1 and the incident shock strength P_2/P_1:

$$\frac{P_4}{P_1} = \frac{P_4}{P'_3}\frac{P'_3}{P_3}\frac{P_3}{P_2}\frac{P_2}{P_1} =$$

$$\left(1 - \frac{\gamma_4 - 1}{2} M'_3 \sqrt{\frac{T'_3}{T_4}}\right)^{\frac{2\gamma_4}{1-\gamma_4}} \frac{A'_3}{A_3}\frac{M'_3}{M_3}\sqrt{\frac{2+(\gamma_4-1)M'^2_3}{2+(\gamma_4-1)M_3^2}}\frac{P_2}{P_1} \qquad (27)$$

where M'_3, T'_3, T_4 are known and P_2/P_1 is the desired incident shock strength.

4.5 Viscous Corrections

Corrections to the 1-D analysis are included to acount for friction and thermal resistance of the flow. The coefficient of friction for incompressible, fully developed isothermal flow in a constant area pipe is invariant along the length of the pipe. Therefore at any location L of the pipe the coefficient of friction is the average value along any segment of the pipe. For a compressible flow the coefficient of friction doesn't remain invariant along the length of pipe since the flow can never become fully developed and thus changes of momentum due to friction along the length of the pipe are appreciable. Thus to calculate the coefficient of friction for a compressible flow along the length of the apparatus, its length must be subdivided in multiple, short in length, segments between measuring points. A piecewise average coefficient of friction can then be obtained for this much shorter length segment as:

$$\tilde{C}_f = \frac{1}{L_2 - L_1} \int_{L_1}^{L_2} C_f \, dx$$

To obtain the piecewise average coefficient of friction for compressible flows the conservation of linear momentum has to be applied. The conservation of linear momentum for a constant area pipe with constant mass is the Fanno line solution:

$$\frac{dP}{P} + \frac{\gamma M^2}{2} 4C_f \frac{dx}{D} + (\gamma M^2)\frac{dU}{U} = 0$$

where: $\frac{P\gamma M^2}{2} = \frac{1}{2}\rho U^2$. After rearrangement and integration between two cross sections 1 and

2 we obtain: $$2\int_1^2 \frac{dP}{P\gamma M^2} + 2\int_1^2 \frac{dU}{U} = -\frac{4}{D}\int_{L_1}^{L_2} C_f dx = -\frac{4(L_2-L_1)\bar{C}_f}{D} \qquad (28)$$

From the above equation we can obtain the average coefficient of friction when the two integrals on the left hand side of the equation are evaluated between cross sections 1 and 2. When the cross sections are closely spaced the velocity and Mach number of the flowfield do not vary appreciably due to friction. On the other hand if one attempts to evaluate the integrals over a large segment of the pipe then the velocity and the Mach number of the flowfield vary significantly due to friction and therefore the average coefficient of friction does not offer a good estimate throughout the segment. A sketch of a control volume applicable to compressible flows is shown in the following sketch.

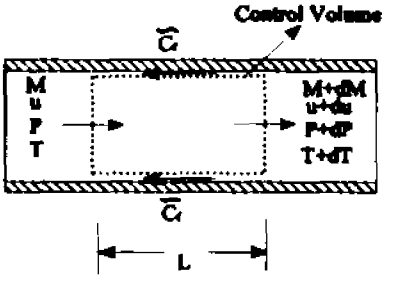

A piecewise average friction coefficient was calculated from experiments. The friction coefficient was calculated from the recorded pressure drop of the flowfield travelling at given short lengths in the shock tube. The Mach number of the incoming flow (M_2) is calculated from 1-D theory. In the present work nine pressure transducers were installed in the shock tube wall. The distance between neighboring pressure transducers was not more than 5 tube diameters. With the above set-up eight piecewise average friction coefficients were obtained concurrently at different segments of the shock tube. More details on the set-up and the

experimental procedure are given in chapter 6.1. Experiments revealed that the contribution of the second integral in equation 28 over the 5 tube diameters length was only a few percent of the total. Therefore, for a short length, the average friction coefficient can be conveniently approximated as follows without introducing a large error:

$$\tilde{C}_f = \frac{\Delta P}{\gamma P M^2} \frac{D}{2\Delta L}$$

The results are fitted in a second order polynomial with respect to the Mach number of the flow as for $1x10^7 < Re_D < 8x10^7$: $\tilde{C}_f = \frac{2.334 - 6.7155 M_2 + 5.116 M_2^2}{100}$.

The above expression, shown in figure 4.2, can also be expressed as a function of the Re_D number. The fitted curve and the piecewise average coefficient of friction obtained from experiments are shown on fig. 4.3.

The thermal resistance of the flow can be calculated with the use of the average friction and the Stanton number (St) as: $Q_w = St\ C_p(T - T_w)$.

The Stanton number is defined as: $St = \frac{\tilde{C}_f}{2} Pr^{-\frac{2}{3}}$. The Prandtl number (Pr) for air is taken to be equal to 0.7.

The flowfield near the shock wave is separated into three regions. Region 1 ahead of the shock wave at rest Region 1' behind the shock wave with induced flow U_1' while region 2 will be the section of length L where corrections will be applied. The above mentioned regions can be seen in the flow schematic shown below. Relative velocities with respect to the stationary shock wave are W_s for region 1 and $W_s - U_1'$ for region 1'. The continuity,

momentum and energy equations are similar to eq.(1-3). Thus for a given P_1'/P_1 (shock strength) eq. 1-3 will provide the properties of the flowfield.

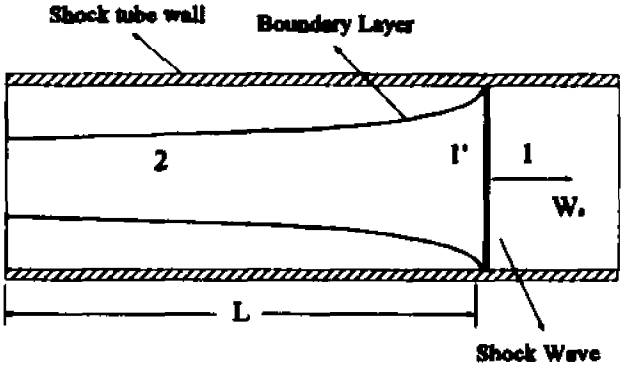

The three basic equations can be applied between regions 1' and 2. Since both regions are independent of the shock wave speed the relative velocities characterizing the three basic equations are the flow velocities. Thus continuity, momentum and energy equations with the addition of friction and thermal resistance terms become:

$$\rho_1 U_1' = \rho_2 U_2 \qquad (29)$$

$$P_1' + \rho_1 U_1'^2 = P_2 + \rho_2 U_2^2 \left(1 - \frac{2L}{D}\tilde{C}_f\right) \qquad (30)$$

$$C_p T_1' + \frac{U_1'^2}{2} = C_p T_2 + \frac{U_2^2}{2} + Q_w \qquad (31)$$

Solving the above equation together with the ideal gas equation we can get the properties of region 1' when the region 2 is known. The corrected velocity of the flowfield is:

$$U_1' = \frac{\gamma}{\gamma+1}\left[\frac{U}{\rho_2 U_2} \pm \sqrt{\frac{U^2}{\rho_2 U_2^2} - A}\right]$$

$$U = P_2 + \rho_2 U_2^2\left(1 - \frac{2L}{D}\bar{C}_f\right)$$

$$A = 4\frac{\gamma+1}{2\gamma}\left[\frac{P_2}{\rho_2} + \frac{\gamma-1}{2\gamma}U_2^2 - \frac{\gamma-1}{\gamma}Q_w\right]$$

The second order equation in velocity is to be expected since the flowfield upstream of region 2 is known. That is, it is not known if the flow upstream is supersonic or subsonic. For subsonic flow upstream the (-) sign in front of the square root should be used.

The effects of friction alone are shown in figures 4.4-4.7. It can be easily seen that, due to friction, there exists a pressure and temperature drop but an increase in velocity and the Mach number of the flow for the subsonic case. The plots show a variable length (L) where the friction force is applied. It varies from 0 (frictionless) to 40 diameters.

When the induced flow is supersonic there exists a shock strength, pressure and temperature increase while the flow velocity and Mach number decrease. Noticeable is also the chocking of the flow, singularity of the equations, in all the figures that occurs for a range of Mach numbers depending on the applied friction length.

Friction tends to accelerate a subsonic flow towards sonic conditions and decelerate a supersonic flow towards sonic conditions which corresponds to the familiar Fanno curve. The Fanno line is drawn for a set of initial conditions in the following sketch to illustrate the above.

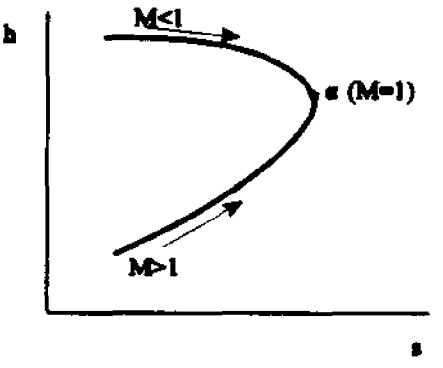

As is also shown in figures 4.6, 4.7 and the above sketch, friction tends to accelerate the flow to sonic conditions, M=1, when the flow is subsonic. A consequent decrease in temperature and pressure occurs during this process as shown in figures 4.4 and 4.5. When the flow is supersonic then deceleration of the flow occurs driving the flow towards M=1. The point of maximum entropy, α, divides the curve into subsonic and supersonic regions. Each point on the curve corresponds to a particular length L. As L gets larger the conditions at the exit approach point α, sonic conditions. At specific values of L the flow becomes sonic where a singularity in the solution is obtained. After this condition the flow becomes chocked and further increasing L will not affect the exit conditions without any revision at the exit of the section. If the maximum friction length is exceeded then the mass flux decrease. Thus the flow has to adjust in order to achieve sonic conditions at the exit of the section. To do so the mass flux decreases and the flow is chocked. The chocked mass flux is such that the predicted flow velocity remains real. To ensure that, the chocked mass flux should be:

$$(\rho U)_{sh} = \frac{P_2 + \rho_2 U_2^2\left(1 - \frac{2L}{D}\tilde{C}_f\right)}{2\sqrt{\frac{\gamma+1}{2\gamma}\left(\frac{P_2}{\rho_2} + \frac{\gamma-1}{2\gamma}U_2^2 - \frac{\gamma-1}{2\gamma}Q_w\right)}}$$

To calculate the range of the flow Mach numbers where the flow is chocked for various friction lengths the following equation is solved were cross section 2 represents the sonic conditions:

$$4\tilde{C}_f\frac{L}{D} = \frac{1-M^2}{\gamma M^2} + \frac{\gamma+1}{2\gamma}\ln\left(\frac{(\gamma+1)M^2}{2+(\gamma-1)M^2}\right) \qquad (32)$$

The above equation, if integrated between two cross sections, can also provide the average coefficient of friction.

The deviation from the inviscid case when both friction and heat resistance are included in the calculations can be seen on figures 4.8 through 4.10 for different friction lengths. Figure 4.8 presents the deviation from the inviscid case for the mean pressure field and mean flow velocity field. The deviation from the inviscid case for the mean temperature field and mean flow Mach number is shown in figure 4.9. It is clear from figure 4.10 that the effect of heat resistance in the range that the experiments were conducted was minimal and less than 0.05%. Thus in the present case figures 4.8 and 4.9 can also be seen as effects due to friction only since heat resistance effects contributed much less correction to the mean fields than the skin friction correction.

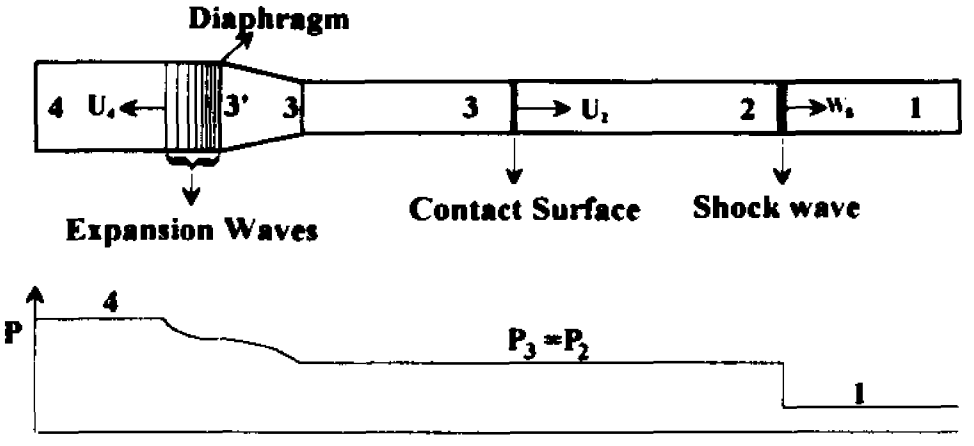

Fig a

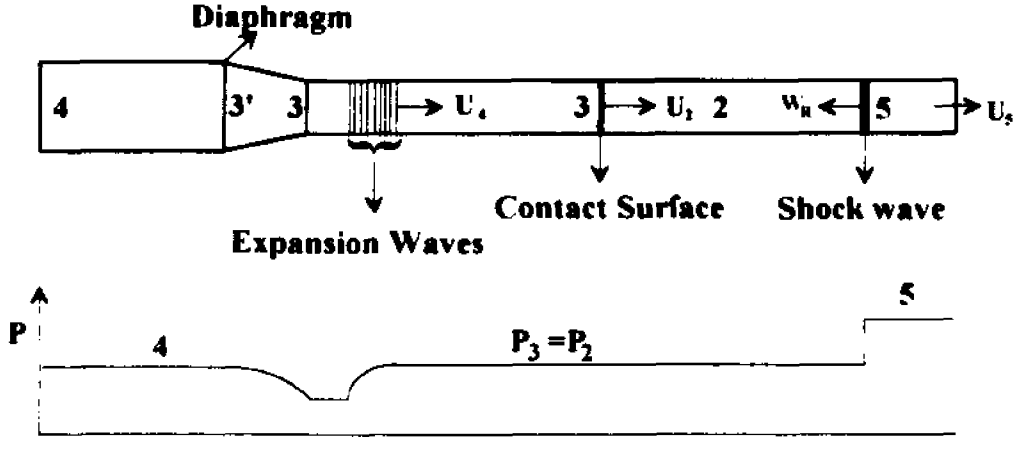

Fig b

Figure 4 1 Flow schematic in a shock tube

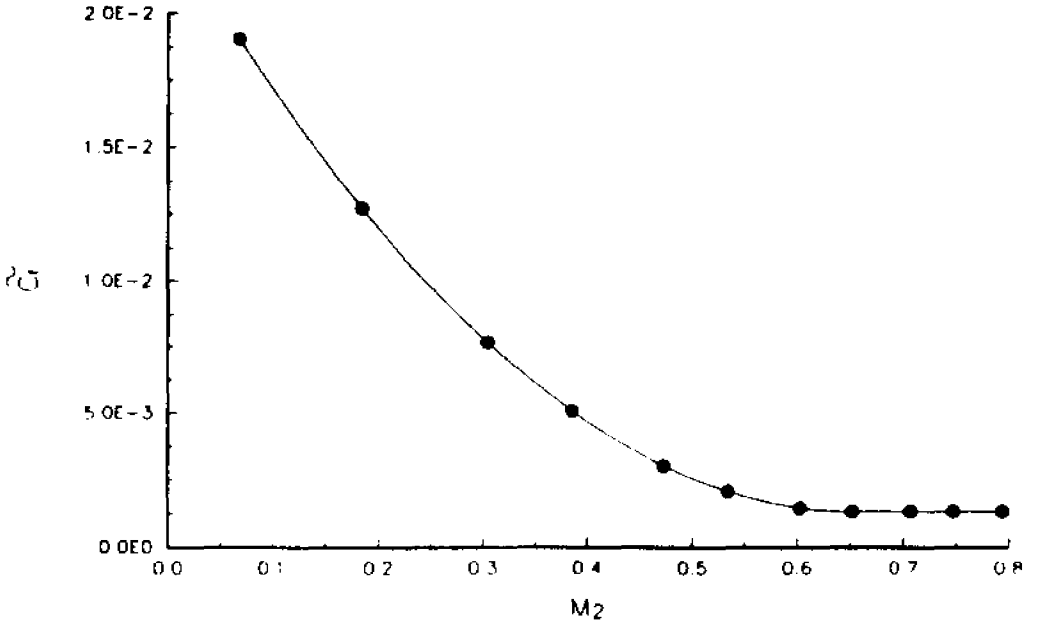

Figure 4.2: Average coefficient of friction vs mean flow Mach number.

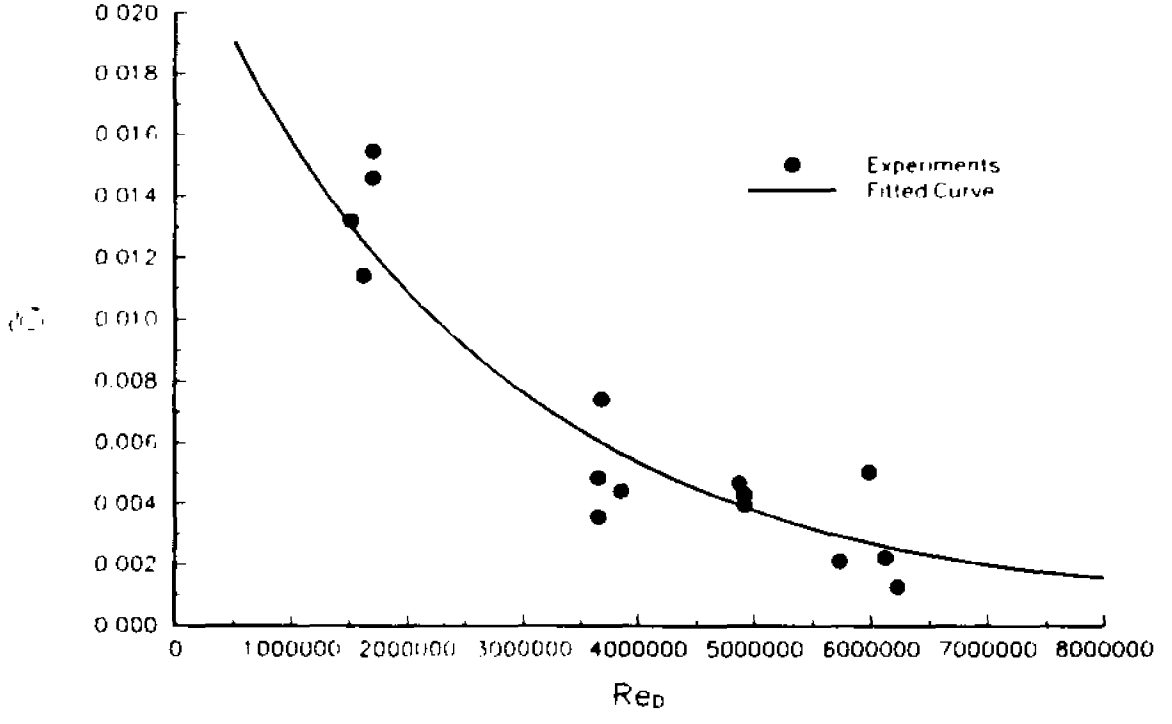

Figure 4.3: Experimental average coefficient of friction vs Re_D and fitted curve.

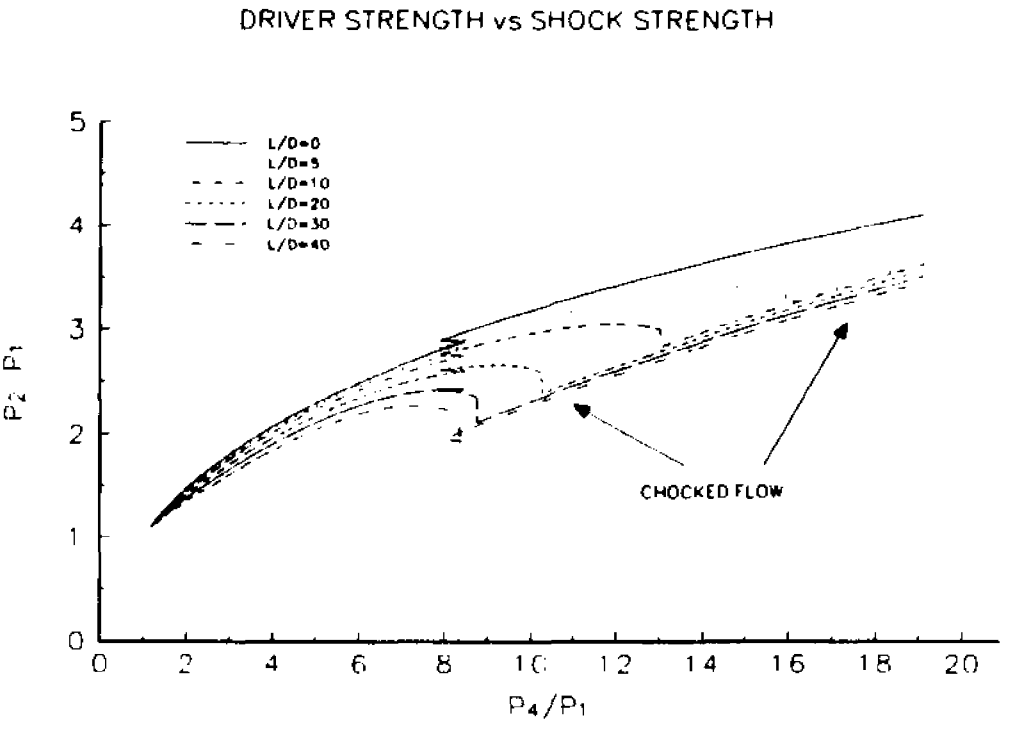

Figure 4.4: Friction effects on the mean pressure field.

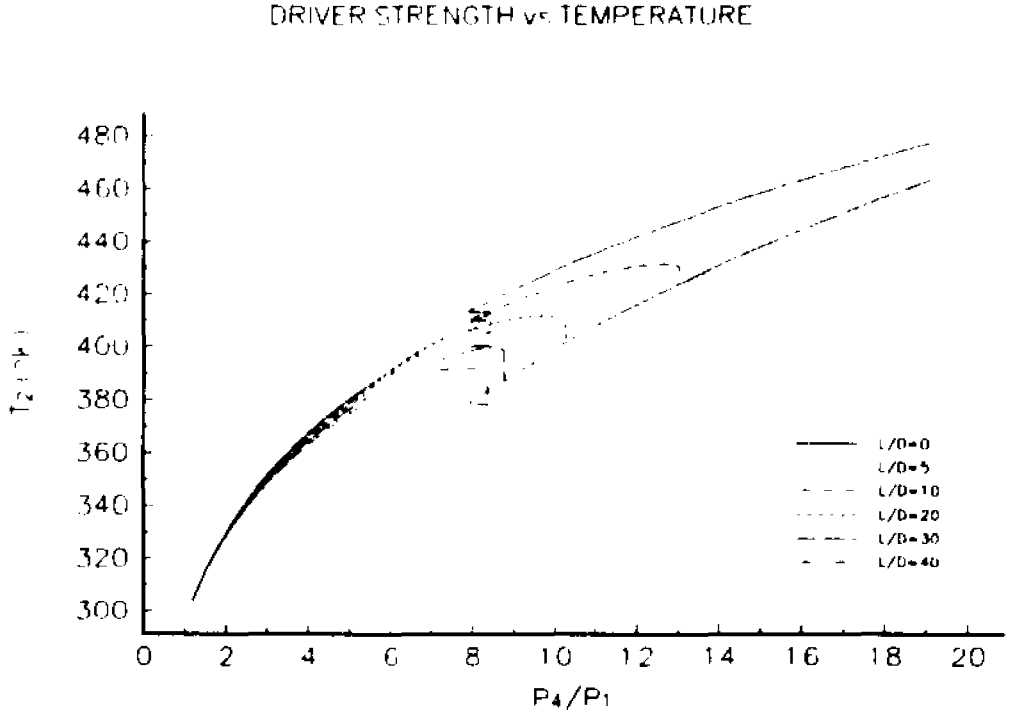

Figure 4.5: Friction effects on the mean temperature field.

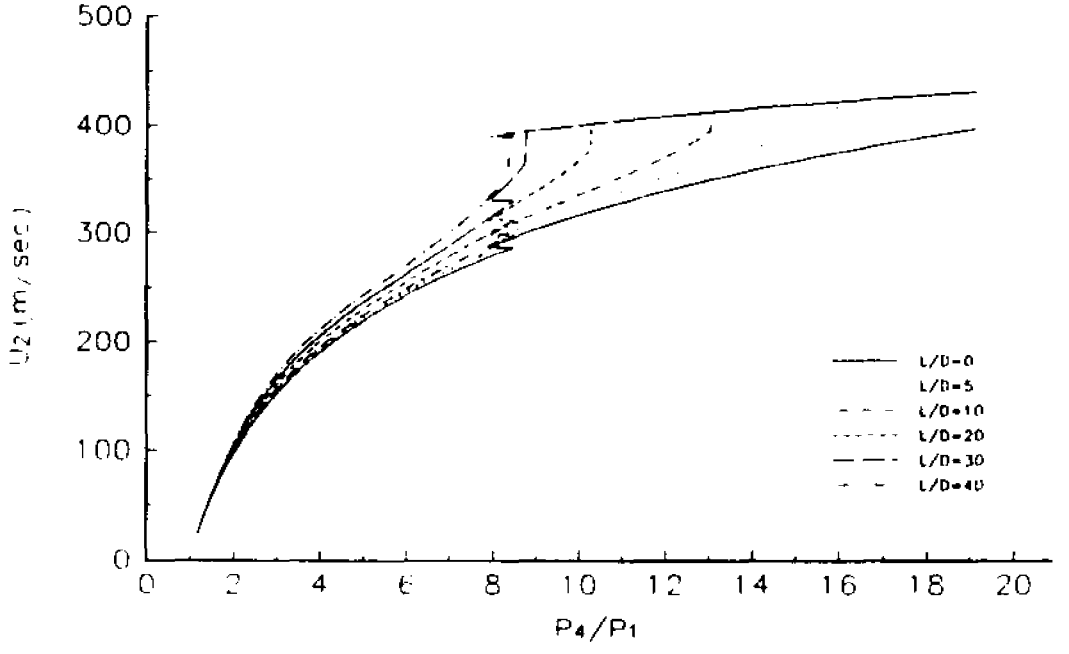

Figure 4.6: Friction effects on the mean velocity field.

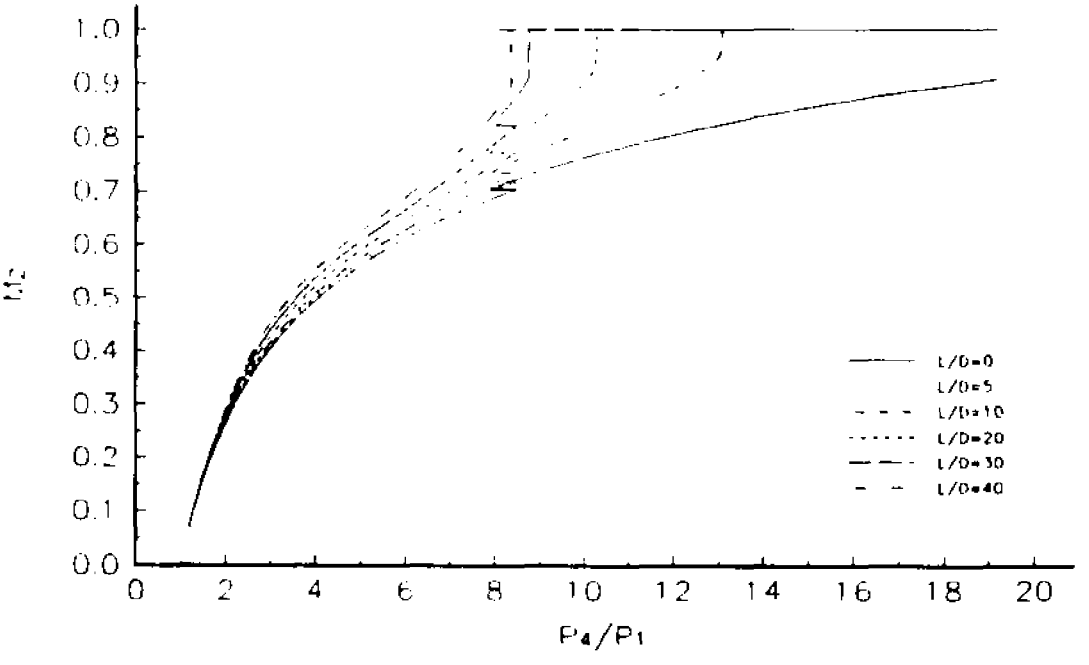

Figure 4.7: Friction effects on the mean Mach number of the flow.

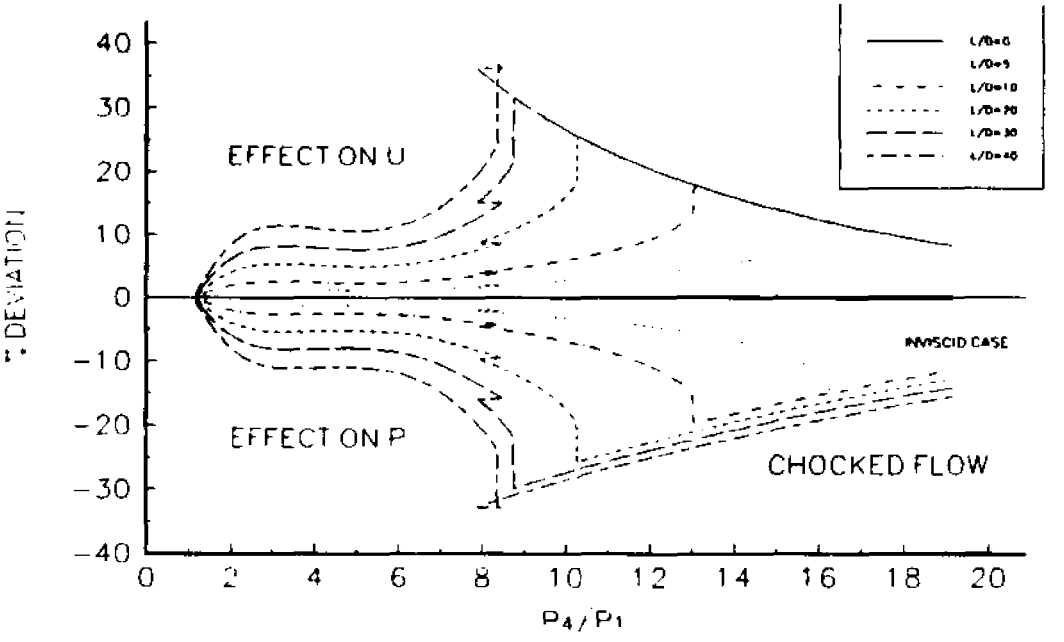

Figure 4.8: Deviation of the mean pressure and velocity field from the inviscid case.

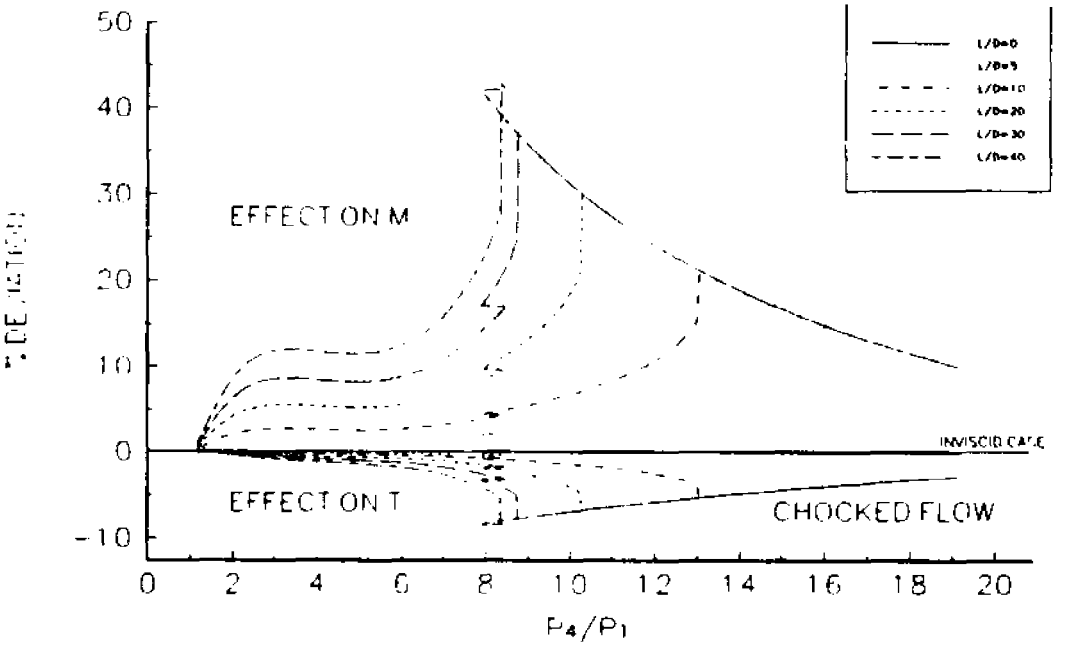

Figure 4.9: Deviation of the mean temperature field and Mach number from the inviscid case.

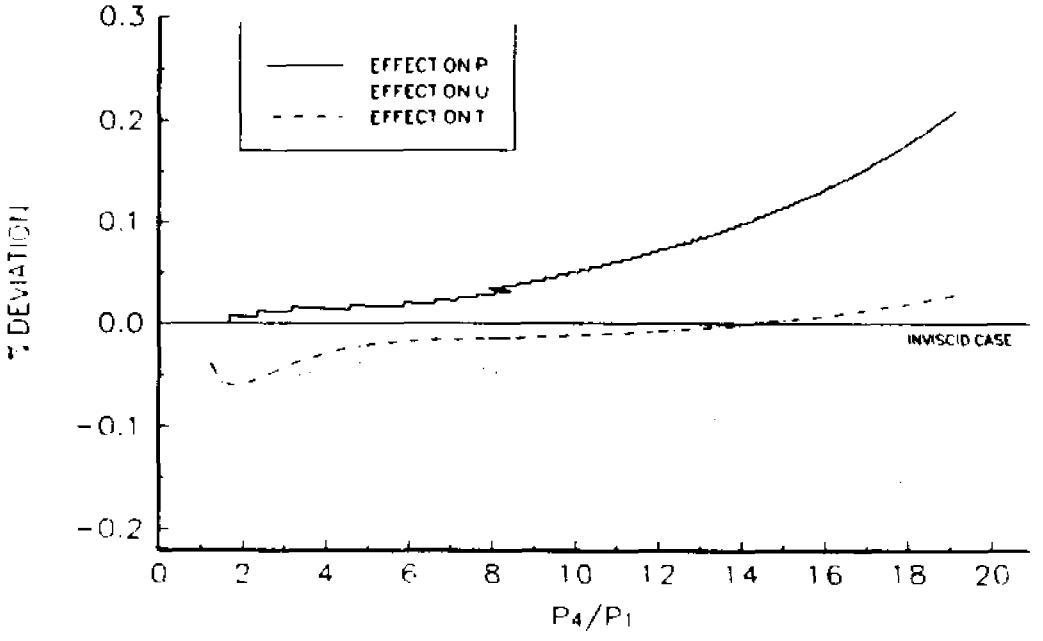

Figure 4.10: Deviation from the inviscid case of several mean fields from heat resistance effects.

5. EXPERIMENTAL SET-UP

NEW SHOCK TUBE FACILITY

The present experiments of decaying isotropic turbulence interaction with a normal shock wave were performed on the newly built shock tube facility of CCNY shown in figures 5.1 and 5.2. The shock tube is a simple piece of equipment that requires two lengths of straight uniform cross section tubing, separated by a diaphragm. When one side of the shock tube is pressurized enough so that the diaphragm ruptures, a shock wave is formed and travels downstream. Flow is induced behind the travelling shock. Additional turbulence can be introduced in the flow by installing a grid somewhere in the low pressure section. The shock wave travels towards the end wall of the tube and then is reflected from it where it interacts with the induced turbulent flow as shown in figure 2.1c. In the following sections, some historical aspects of shock tubes in general are presented as well as a complete description of its components.

5.1 Shock Tube

The potential of the shock tube as a research tool was understood in the early 1950's and many experimental and theoretical work was published to understand, describe, and analyze the basic operation of the shock tube and its wide range of applicability. The shock tube was not only used to produce shocked flows, but also to produce high temperature gases

by Resler, Lin and Kantrowitz (1952) as well as experimental analysis of the effects of collisional excitation of molecules by Charatis et al. (1957).

The amplification of the shock wave strength was realized by having an area reduction just in front of the diaphragm. These types of flows are called convergent shock tube flows and have been considered by Resler et al. (1952), Alpher and White (1958) and Bird (1959) to list a few. The experimental and theoretical work of Alpher and White (1958), for instance, extensively analyzed the shock tube parameters for different combinations of gases and area reduction ratios. Other fundamental works worth noting are the works on shock tube flows of Glass et al. (1953) and Hall and Glass (1958), on aerodynamic instrumentation of the shock tube by Hertzberg and Kantrowitz (1950), on the structure of the contact region by Goldsworthy (1959). Various theoretical works on the propagation of the weak shock waves and shock dynamics were conducted by Whitman (1956, 1957, 1958), Payne (1957), Chisnell (1957), Bird (1959), Lapworth (1959). The flow duration in shock tubes was analyzed by Roshko (1960) experimentally and analytically. Finally, the influence of the diaphragm opening on the shocked flows was extensively investigated by White (1958).

Experimental research on compressible turbulence often requires facilities in which a fluid or gas can be compressed adequately so that the effects of compression can be studied under well controlled conditions. The shock tube, as explained previously, has great capability in investigating the effects of sudden compression in homogeneous and isotropic turbulence.

This particular need has led to the development of a new Shock Tube Research Facility (STURF) which has been designed and constructed at The City College of New York.

The following are the distinguished features of this facility:

1. The ability to control the flow velocity and diminish the separation of the flow behind the shock wave after its reflection off the end wall, by introducing the porosity of the end wall.

2. The size of the facility, 12" in diameter and 70 ft long, provides an unprecedented platform for high spatial resolution measurements in ranges which have never been investigated before.

3. Simultaneous time-resolved measurements of pressure, temperature and velocity at multiple positions inside the working section.

4. Accessibility for non intrusive optical measurements by using laser techniques at various wavelengths.

Major part identification and layout of the shock tube is shown in Figure 5.1. The facility consists of:

1. The DRIVER section;

2. The conical reducer or CONE;

3. Two DRIVEN sections;

4. The WORKING section;

5. The VIEWPORT section;

6. The supporting FRAME.

The total length of the facility is 70 ft.

Details on the operation of the shock tube are discussed in Appendix A.

5.2 Driver

The dimensions of the driver are 16 ft long with 16" (OD) and 14.32" (ID). Four holes 1/4"x18 NPT (female) are drilled and tapped at the horizontal plane of the driver for the inlet of the supplied high pressure gas.

-Two holes, one 1/4"x18 NPT (female) for a pressure gauge indicator and one 1/4"x18 NPT (female) for a safety relief valve set at 3,000 psig are drilled and tapped on the top section. A pair of standard male/female flanges are welded and bolted on the left end of the driver. Finally, a 1.25" diameter hole is drilled on the top of the driver to accommodate the plunger mechanism. The plunger mechanism is welded on the driver at an angle of 18.25 degrees and is used to rupture the diaphragm at a set driver pressure (P_4). Thus a consistent shock strength (P_2/ P_1) is obtained repeatedly.

5.3 Cone

This is a transition piece to allow for a smooth change of the 14.32" (ID) of the driver to the 12" (ID) of the driven section in a 4 ft length. Thus, any effects due to the diaphragm rupture are eliminated when the shock wave passes through the cone. The types of flows where there is a reduction of the area in front of the diaphragm are called convergent flows. It is known from previous work of Alpher and White (1958) that convergent flows substantially amplify the shock strength because of the above mentioned area reduction in front of the diaphragm.

-The male flange on the right side is a standard one (20.5"x15"x2") ANSI B16.5 1968 rated for 1500 psi. This flange has undergone extensive machining in order to accommodate the diaphragm.

-The left hand side female flange (25.5"x16.125"x4") is not a standard one.

5.4 Driven sections

The two driven sections are 20 ft long and 12" (ID) with 12.75" (OD) standard pipe. The flanges are also standard male/female, to ensure an extremely smooth transition between the two sections, with one O-ring in between them sealing each other.

-Four pressure taps and one hot-wire tap are drilled and tapped on each driven section. The location of each of the taps is shown in Table I.

-A typical pressure tap requires welding of a 4"x4"x1/2" flat piece on each location and then drilling and tapping of 1/4" x18 NPT female through the extra plate and the wall of the pipe.

-A typical hot-wire tap is a flat plate 3"x5"x1/2" welded on the pipe. A slit 3" long and 3/4" wide, is machined on the plate and pipe. 8 threaded studs 3/8"x16 in diameter are installed on the plate only. A flat plate cover 3"x5"x1/2" are bolted with 3/8"x16 nuts to the hot-wire tap. A rubber gasket is used to seal the assembly.

5.5 Working section

The working section is used for the majority of the measuring locations in an

experiment. It is 8 ft long and is made of the same 12" (ID) Stainless Steel tube. Several hot-wire- and pressure-taps are machined in this section. Their locations are shown in figure 5.3 and are also listed in Table II. A pair of standard male/female circular flanges are welded on its ends. The female flange is machined so it can accept different grid models. The model consists of a stainless steel screen (wire cloth) sintered together with two stainless steel rings having 1/2 " thickness and they are sealed with silicon. More details on the grids are to follow.

5.6 Viewport section

The viewport section is the section used for non intrusive laser measurements and it is designed to fit on either end of the working section. The viewport is made of Stainless Steel and is 2 ft long.

-The right-hand side female flange is also machined to accommodate a "Rigimesh" or an assembly of several screens/filters. The "Rigimesh" or the screen/filter assembly is acting as the porous end wall.

-An additional blind (solid) flange is also available so that the facility can be pressurized for in situ calibration of the pressure transducers as well as to check for leaks.

-Three viewports are present in this section 90 degrees apart. Each viewport is 4.25" (OD) and 2.75" (ID). Fused silica windows specially coated with anti-reflect and UV coating are held in place by 8 1/4"x20 screws.

5.7 Diaphragms

The diaphragm is used to separate the high pressure side (driver) from the low pressure side (driven section). It is made out of aluminum and it is 18.5" in diameter and 1/8" thick. The diaphragms were scored in a cross shape (+) of various depths. Its strength to withstand the pressure of the compressed gas of the driver section depends on the depth of the scoring. Therefore the depth of this cross shaped scoring dictates the rupture pressure of each diaphragm. Thus the plunger was not needed to be used. A photograph of a ruptured diaphragm at P_4/P_1=7.6 can be seen in figure 5.4.

5.8 Turbulence and End-wall grids

To control the level of turbulence in the induced flow as well as the dominant mean length scales, several grids were used. The grid consists of a stainless steel screen which is sintered between two aluminum or stainless steel rings. The screens are woven with stainless steel rods in such a way that square meshes are formed. The denser the weaving, the smaller the size of the square mesh. Different sizes of meshes are available ranging from 1 mesh per inch to 20 meshes per inch. The diameter of the rods control the open area of the grid. Usually the solidity is in the range of 0.2 - 0.4 for grids used to generate turbulence and 0.7 - 0.8 solidity for grids used to reflect the shock wave off the porous end wall. The latter ones are used in conjunction with other denser screens (filters) at the end of the shock tube to imitate the porous end wall.

When the induced flow passes through the grid, the level of turbulence in the flow is substantially increased. It is clear that different grids, denser or coarser, will produce different levels of turbulence as well as different mean length scales. The dissipation of the turbulent flowfield will eventually depend on the grid size, since all turbulent quantities are measured and analyzed with respect to the non-dimensional downstream distance x/M, where M is the grid size (meshes per inch). Therefore, the decay of the turbulent quantities will be calculated at different downstream locations from the turbulence generating grid, even if the physical location of the instrument remains the same. Namely for the same downstream from the grid location x, the non-dimensional downstream distance x/M is different for different grid sizes.

5.9 Supporting frame

The whole structure is supported at an elevation of 48" above the ground level. The support of the driver section is sliding on stainless steel shafts which are mounted on I-beams through special bearings called dual roundway bearings manufactured by THOMPSON industries model RW-24-V. The working section is also sliding on stainless shafts and THOMPSON bearings model RW-16-V similar to those used in the driver's section. The two driven sections are tied on four support stands. The driver and the working sections are tied on the table with the use of metal hoops. The table, as well as the four stands, are constructed of 3"x3"x1/4" steel tubing.

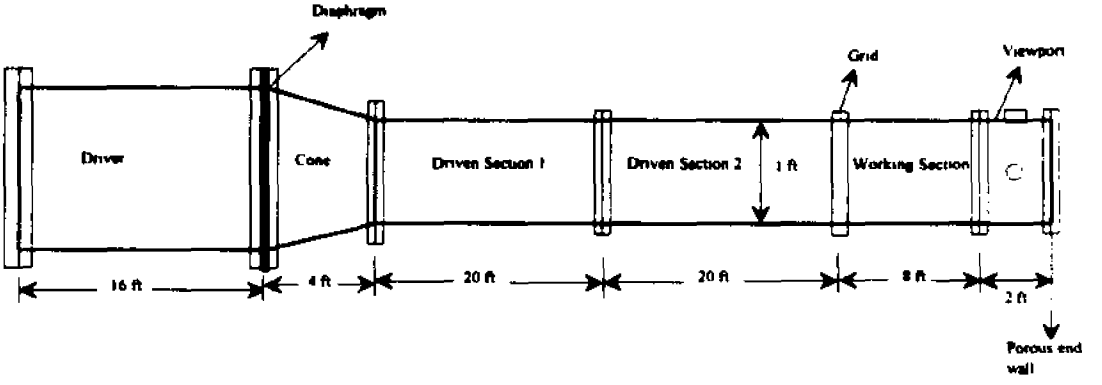

Figure 5.1: The new shock tube facility. (not to scale)

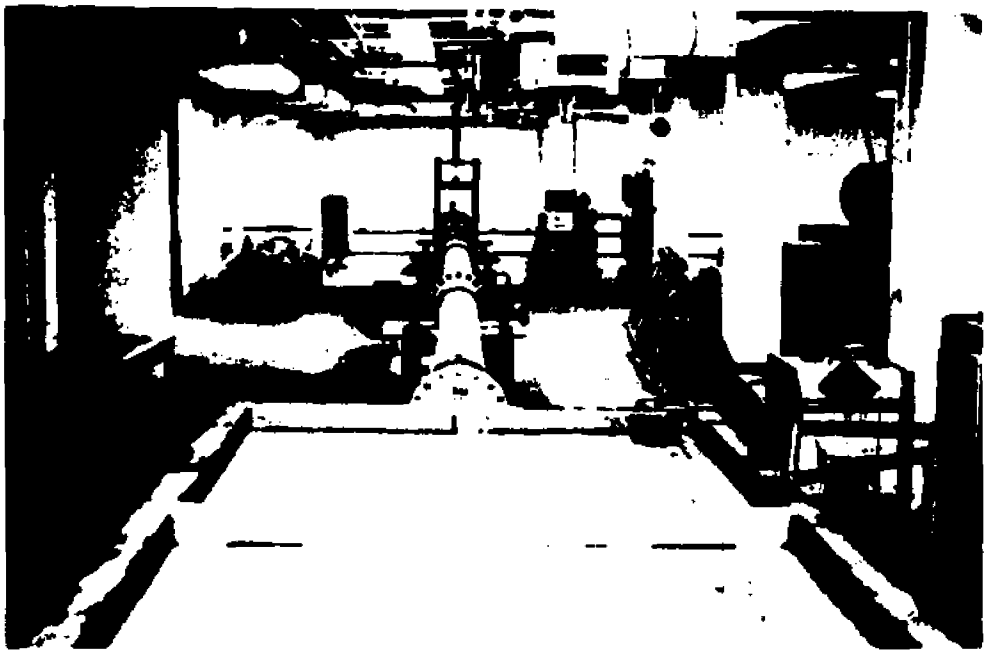

Figure 5.2: Photograph of the new shock tube facility.

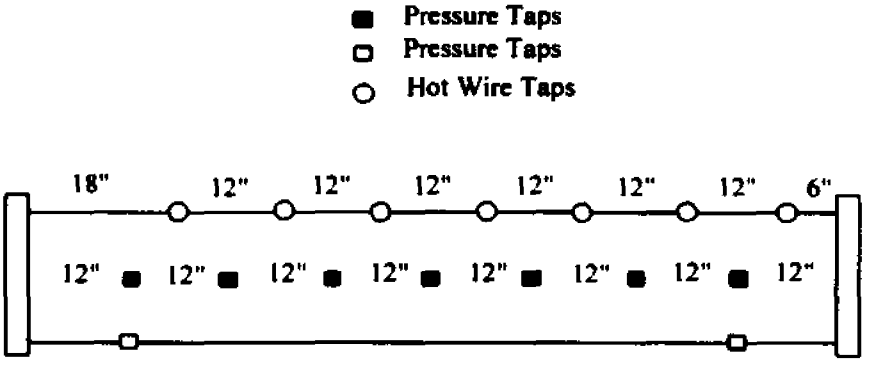

Figure 5.3: The working section and location of Pressure taps and Hot wire taps. (not to scale)

Figure 5.4: Photograph of a ruptured diaphragm

LOCATION	PRESSURE TAPS	HOT WIRE TAPS
DRIVEN SECTION 1	5 ft	15 ft
DRIVEN SECTION 1	10 ft	
DRIVEN SECTION 1	15 ft	
DRIVEN SECTION 1	16 ft	
DRIVEN SECTION 2	25 ft	35 ft
DRIVEN SECTION 2	30 ft	
DRIVEN SECTION 2	35 ft	
DRIVEN SECTION 2	36 ft	
WORKING SECTION	41 ft (2) 90 Degrees apart	41 ft
WORKING SECTION		41.5 ft
WORKING SECTION	42 ft	42 ft
WORKING SECTION		42.5 ft
WORKING SECTION	43 ft	43 ft
WORKING SECTION		43.5 ft
WORKING SECTION	44 ft	44 ft
WORKING SECTION		44.5 ft
WORKING SECTION	45 ft	45 ft
WORKING SECTION		45.5 ft
WORKING SECTION	46 ft	46 ft
WORKING SECTION		46.5 ft
WORKING SECTION	47 ft (2) 90 Degrees apart	47 ft

Table I: Location of pressure and hot wire taps
(distances from diaphragm measured in ft.)

PRESSURE TAPS		HOT WIRE TAPS	
DIAPHRAGM	GRID	DIAPHRAGM	GRID
41 ft (2) at 90^0	1 ft (2) at 90^0	41 ft	1 ft
		41.5 ft	1.5 ft
42 ft	2 ft	42 ft	2 ft
		42.5 ft	2.5 ft
43 ft	3 ft	43 ft	3 ft
		43.5 ft	3.5 ft
44 ft	4 ft	44 ft	4 ft
		44.5 ft	4.5 ft
45 ft	5 ft	45 ft	5 ft
		45.5 ft	5.5 ft
46 ft	6 ft	46 ft	6 ft
		46.5 ft	6.5 ft
47 ft (2) at 90^0	7 ft (2) at 90^0	47 ft	7 ft
		47.5 ft	7.5 ft

Table II: Location of pressure and hot wire taps in the working section.

6. DESCRIPTION OF EXPERIMENTS AND ASSOCIATED TECHNIQUES

When a shock tube is used as an apparatus to investigate shocked flows, the quality of the induced flow and of the shock wave are critical. Thus, a methodical check of the quality of the flow and the shock wave must be performed in order to establish well defined boundary and operating conditions.

- When dealing with a compressible flow the boundary and operating conditions, such as mean flow Mach number, incident shock Mach number, and mean velocity of the flowfield, depend on the downstream location from the diaphragm. The dependence of these properties on the downstream location is a direct result of the friction and heat resistance of the flowfield. In an incompressible, fully developed flow it would have been sufficient to calculate an average friction coefficient for the whole length of the pipe since the friction coefficient is invariant along the length of pipe. The situation is different for the present compressible flow case where the friction coefficient must be measured at various locations downstream of the diaphragm in order to establish the boundary and operating conditions of the flowfield at such locations.

- There are two vital quantities to be considered when one wishes to check for the homogeneity of the induced flow in the shock tube. Namely, the mean pressure and velocity fields should be constant ($d\bar{P}/dt \approx 0$ and $d\bar{U}/dt \approx 0$) before and after the

interaction with the reflected travelling shock wave.

- To check for the quality of the shock wave, one has to consider the inclination of the shock wave and its wiggles. That is, the travelling shock wave must be planar as well as perpendicular to the shock tube walls before and after reflection. To show and prove the homogeneity of the flow and the planar distribution of the shock wave, different experiments were carried out. Pressure measurement experiments revealed the distribution of the pressure field during the interaction with the shock wave throughout the working section. Radial time dependent distribution of the longitudinal velocity and temperature fields were sufficient to show the inclination of the shock wave and the homogeneity of the induced flow before and after its interaction with the shock wave. Finally, visualization of the shock wave and of the interaction was captured in another set of experiments.

- After the above experiments confirmed the quality of the flow and the shock wave, the two-dimensional velocity flowfield and temperature field were resolved simultaneously for multiple downstream locations for the decaying turbulent flowfield.

- Data were also acquired after the interaction of the turbulent flowfield with the shock wave using measurements obtained for the above mentioned fluctuating flowfields simultaneously and at multiple locations.

- Time dependent, simultaneous velocity measurements at six closely spaced locations can provide accurate information on the behavior of the integral length scales in the longitudinal and lateral direction for both cases i.e. decaying isotropic turbulent flowfield and shock wave compressed turbulent flowfield.

Details on the above experiments follow in the next sections. At the end of this chapter, the data acquisition technique and procedure, as well as a brief description of the instruments used in each set of experiments is offered. The calibration procedures used, for the instruments needed for each set of experiments are described in Appendix B.

6.1 FRICTION COEFFICIENT EXPERIMENTS

As mentioned earlier in this chapter the coefficient of friction for a compressible flow is not invariant to the length of the shock tube.

To measure the friction coefficient C_f at various locations in the shock tube nine high frequency response Kulite type XCQ-062-100 pressure transducers were installed in the wall of the shock tube. A brass fixture, shown in figures 6.1a and 6.1b was used to install the pressure transducers on the shock tube, flush with the inside wall. In the same figure the physical dimensions of the miniature pressure transducer are also shown. Each pressure transducer had its own power supply which consisted of 4 AA batteries generating a total differential of 6 volts.

Measurement of the friction coefficient was obtained for eight segments and for distances between neighboring transducers of no more than 5 shock tube diameters. Therefore a piecewise average distribution of the friction coefficient $\tilde{C}_f$ was obtained simultaneously at various downstream locations from the diaphragm. More details on the calculation of $\tilde{C}_f$ are offered in chapter 4.5.

All nine pressure measurements were sampled at 333 kHz per channel simultaneously using the first pressure transducer as a triggering device for the data acquisition as well as a measuring device. The output of each pressure transducer was amplified by a battery powered low noise pre-amp/filter so that the data acquisition board can resolve the pressure transducer signal at its optimum range (±10 V). The amplification depended on the pressure transducer's sensitivity and at the flowfield's operating conditions. The locations of the installed pressure transducers is given in table III.

6.2 PRESSURE MEASUREMENT EXPERIMENTS

Pressure measurements experiments were designed to show the distribution of the pressure field before and after the interaction with the shock wave throughout the length of the working section as well as the simultaneous azimuthal location of the shock wave for two azimuthal angles and two locations. One of the positions is located close to the turbulence generation grid at the beginning of the working section and the other is located close to the end of the working section. Their exact location and angle is given on Table IV. For the pressure experiments, 10 high frequency response Kulite pressure transducers type XCQ-062-100 were used to record pressure fluctuations. Installation of the miniature pressure transducers was achieved by using a home - made fixture made out of brass (shown in figures 6.1a and 6.1b). Each of the pressure transducers was driven by 4 AA batteries resulting to a total differential applied at the pressure transducer to be 6 volts. A switch was used to switch off power to the pressure transducer when it was not in use. The output from each pressure transducer was fed into the pre-amp to be filtered and amplified according to each transducer's sensitivity so that the maximum resolution of the data acquisition board can be obtained. All outputs were connected in the terminal box of the data acquisition board. All ten signals were sampled simultaneously at 333 kHz per channel. The transducers were used to record data and trigger the data acquisition. The trigger pressure transducer was placed 48 inches upstream of the grid. The remaining nine pressure transducers were installed throughout the working section. Their location is given on Table IV and the experimental set-up is shown in figure 6.2.

6.3 TOTAL PRESSURE MEASUREMENTS

Mach Number Experiments

This set of experiments were performed in order to acquire the time dependent Mach number of the flowfield at multiple locations before and after its interaction with the shock wave. Similar to the pressure measurement experiments, described in the previous section, this set of experiments utilizes the same miniature pressure transducers (Kulite type XCQ-062 - 100) for time dependent total pressure measurements instead of static pressure measurements. To achieve this type of measurements a new holder was designed to hold securely the miniature pressure transducer in the flowfield. Therefore total, time dependent, pressure measurements can be acquired.

Since for an isentropic and adiabatic flow the ratio of total to static pressure is proportional to the Mach number of the flow, the Mach number can be directly calculated when the total and static pressure of the flowfield is obtained. The above is expressed in: $\frac{P_0}{P} = \left[1 + \frac{1}{2}(\gamma - 1)Ma^2\right]^{\frac{\gamma}{\gamma-1}}$ where P_0 is the total pressure of the flowfield, P is the static pressure of the flowfield and Ma is the mean Mach number of the flowfield.

For this set of experiments three total probes were constructed in house. All have adjustable lengths and were made air proof. More details on the construction and physical dimensions of these probes are offered in Appendix C. The total pressure probes were designed to mount in the shock tube similar to the rake and the triple wire probes. Discussion on these experiments follows this section.

A total of eight time dependent pressure signals, five static and three total, were simultaneously acquired at various locations of the working section. The total pressure probes were installed in a staggered fashion to avoid any wake interference from the upstream probes to any downstream. The static pressure probes (fixtures) were installed in such a way so that at least two of them were on the same plane with the corresponding total pressure probes. The set-up of this experiment is shown in figure 6.3. The output of each pressure transducer (total or static) was amplified by a pre-amp/filter. All signals were acquired simultaneously at 333 kHz per channel. Table V presents the downstream location from the grid and the radial position of the pressure transducers.

Several experiments were performed with different grid sizes and different flowfield Mach numbers. A summary of the above mentioned experiments is offered in Table VI where the bulk parameters of each experiment are given.

6.4 FLOW QUALITY EXPERIMENTS

To assess the inclination of the shock wave and the homogeneity of the induced flow before and after its interaction with the shock wave, a unique instrument was constructed to obtain simultaneous time dependent measurements of velocity and temperature at various radial positions. This instrument (hot wire rake) also has the capability to check for the symmetry of the flow and the shock wave. The rake was constructed in house in order to perform this experiment. The rake assembly touches the bottom wall of the shock tube wall and extends out of the shock tube through a specially machined screw. The inside diameter of the shock tube is 12 inches. Five probes are equally spaced 2 inches apart and permanently attached on the rake's tube as shown in figures 6.4a and 6.4b. Each probe contains the ceramics, the prongs, the wiring and the hot wires. Details relevant to the construction of the rake assembly and its associated probes are given in Appendix C. Some pressure transducers were installed in the shock tube in order to obtain the mean pressure field of each experiment. Knowledge of the mean pressure field throughout the working section is used in the calibration of the hot wires as well as in the reduction of the hot wire measurements to time dependent velocity measurements. Essentially information on the temperature and pressure field will produce information on the density of the flowfield and therefore time dependent temperature and density corrections can be performed on the hot wire signals. The location of the installed pressure transducers in the working section and the location of the rake assembly with respect to the turbulence generation grid and the ruptured diaphragm is presented in Table VII.

Each probe is equipped with two Platinum/Tungsten wires; one 5 μm wire and one 2.5 μm wire. Each of the 5 μm Platinum/Tungsten wires (hot wires) were connected to the DANTEC anemometers operating in the constant temperature mode for time dependent measurements of the longitudinal velocity. The 2.5 μm wires (cold wires) operated in the constant current mode were connected to pre-amp/filters for time dependent temperature measurements. More information on the operation and calibration procedures of the probes are offered later on in Appendices B and C.

The rake assembly was placed at a hot wire tap 24 in. downstream of the grid as shown in figure 6.4b. The set-up of the above experiment is shown in figure 6.5.

Several turbulence generation grids were used in order to produce different levels of turbulence intensities and mean length scales in the flowfield. Consequently the non dimensional distance from the grid x/M varied according to the mesh size of the grid. For every grid the performed experiments produced flowfields ranging in mean flow Mach number from 0.3 to 0.7. The above mentioned experiments and the bulk parameters of the flowfield are summarized in Table VIII.

6.5 VELOCITY AND TEMPERATURE MEASUREMENTS

To resolve simultaneously two dimensional velocity components with hot wires, a cross wire (X-wire) arrangement was used. New three-wire probes (X-wire probes) were designed and built. Six different three-wire probe assemblies were used concurrently at different downstream locations, all adjustable to different lengths, each carrying 2 hot-wires in a X configuration and one cold-wire for simultaneous velocity and temperature measurements respectively. The three-wire probes were equipped with a 5 μm Platinum/Tungsten wire for time dependent velocity measurements and with a 2.5 μm Platinum/Tungsten wire for time dependent temperature measurements. For more details on the construction of the X-wire probes refer to Appendix C. To eliminate any wake effects from upstream probes on any downstream, all of the probes were staggered at different distances from the tube wall and 90 degrees apart from every other probe. Figure 6.6 shows the above arrangement of the three-wire probes and Table IX presents the downstream distance of the probes measured from the turbulence generation grid and from the diaphragm. The output signals from the cross wires were connected to the DANTEC anemometers and the output signals from the temperature wire were connected to the EG&G model 113 low noise, battery operated pre-amps/filters before their final connection on the terminal boxes as shown in figure 6.7. For more details on the hot-wire techniques see Briassulis et al. (1995) where estimates of uncertainties in the measurements are also given and in Appendix B.

Time dependent pressure fluctuations were obtained by 6 miniature high frequency Kulite pressure transducers installed on the shock tube wall.

During the different sets of experiments all of the above signals were acquired simultaneously with the ADTEK data acquisition system. The ADTEK AD830 board is a 12 bit EISA data acquisition system, capable of sampling simultaneously 8 channels at 333 kHz each channel. Three of those boards are currently available providing 24 simultaneously sampled channels at 333 kHz per channel.

The above mentioned setup allows for concurrent acquisition of 12 hot wire measurements, 6 temperature measurements and 6 pressure measurements at 6 locations downstream of the grid.

Various grids were used to generate the turbulent flowfield and the dominant mean length scales present. All the grids had about the same solidity but different mesh size. For each grid three different flowfield cases (shock strengths) were studied with the Mach number ranging from 0.3 to 0.7. Chocking of the flow was not present for the current Mach number range and solidity of the grids.

The bulk flow parameters of the experiments performed are presented in table X and include the grid size m, the mesh size M, the shock wave Mach number M_s, the flow Mach number M_{flow}, the mesh Reynolds number Re_M, the turbulent Reynolds number Re_λ and the solidity of the grids σ.

6.6 INTEGRAL LENGTH SCALES EXPERIMENTS

Simultaneous velocity measurements at six closely spaced locations will provide information on the correlation of the integral length scale (L_{11}) in the longitudinal and lateral direction with the new 9-wire hot wire probe. The new probe can be adjusted to different lengths with a 3/8" OD and 1/16" thick wall main tube made of 304 stainless steel designed to withstand the impact of a M_s=3 shock wave. Appendix C offers more details on the construction and physical dimensions of this probe.

The probe is carrying 9 wires, 6 hot wires for velocity measurements and 3 cold wires for temperature measurements. The hot wires are equally spaced 1 mm apart and thus the minimum length scales that can be correlated is of the order of 1 mm. The cold wire will provide time dependent information on the temperature field and therefore time dependent correction on the mass flux measurements (hot-wires) is possible. A sketch and a photograph of the 9 wire probe is given in Appendix C.

The 9 wire probe was placed in the centerline of the shock tube at several downstream distances from the grid. Using different grids (mesh sizes) several non-dimensional x/M downstream locations are obtained. Figure 6.8 shows the above arrangement of the 9 wire probe and the grid in the shock tube. Table XI summarizes the downstream location of the 9 wire probe and pressure transducers installed for time dependent pressure measurements in the she shock tube, with respect to the turbulence generation grid.

The hot wires were connected to the DANTEC anemometers and the temperature wires were connected to the pre-amp/filters for amplification before their final connection to

the terminal boxes, as shown in figure 6.9.

During the different sets of experiments all fifteen signals (6 for velocity, 3 for temperature and 6 for pressure) were acquired simultaneously with the ADTEK data acquisition system at 333 kHz each channel. For this experiment a pressure transducer installed upstream of the grid was acting as the trigger source for the data acquisition as well as for pressure measurement before the flow passes through the grid. Measurements obtained from this location can provide information on the possibility of chocking of the flow, passing through the grid, when compared with measurements acquired at latter locations as well as free stream pressure fluctuations.

Multiple experiments were performed for several turbulence generation grids and for different non dimensional distances downstream from the grid of the 9 wire probe. A summary of the above experiments as well as the bulk parameters of the flowfield is given in Table XII.

6.7 SHOCK AND FLOW VISUALIZATION

A CCD camera and a YAG laser are needed for this experiment. The specifications of the above equipment are given in the following section. To illuminate the flow, the laser light passed through a doublet and a cylindrical lens so that a thin laser sheet was produced. All lenses had to be specially coated to transmit the UV light. The CCD camera can record any light scattered from the focused area. Focusing of the scattered light is obtained by a Nikon 105mm f/4.5 UV Nikkor lens mounted on the camera. The camera was mounted on the shock tube in a specially designed case to eliminate any ambient light to enter the camera lens. The collected digitized images were analyzed by the software provided by Astromed. The software is capable of applying different filters on the digitized signal so enhancement of key characteristics of the image can be shown. More on the theory and related calculations of the scattered light is offered in Appendix D. Calibration procedure for the CCD camera is given in Appendix B.

To enhance the light scattered by the flow, liquid N_2 was injected perpendicular to the shock wave. Liquid N_2 when expanded produces for a short time condensation which adds adequate light scatterers into the flow. To illuminate the shock wave as it passes in front of the camera, a delay generator was used to synchronize the laser with the shock wave location. A pressure transducer signal, located at some pressure tap upstream from the camera, sends the signal to the delay generator and at the appropriate moment the delay generator sends a TTL pulse to trigger the laser and illuminate the flow. The above set-up can be seen in figure 6.10.

6.8 DATA ACQUISITION AND ELECTRONIC EQUIPMENT

During the different sets of experiments the signals were acquired simultaneously with the ADTEK data acquisition system. The ADTEK AD830 board is a 12 bit EISA data acquisition system, capable of sampling simultaneously 8 channels at 333 kHz each channel. Furthermore, the above boards can be connected together (up to 4 boards) making the total number of channels that can be sampled simultaneously at 333 kHz each to be 32. Three of those boards are currently available (24 channels total). When more than one board is installed in the PC, the first board controls the clock and therefore the other board or boards are driven by the first board (master - slave arrangement). The boards are installed in an IBM compatible PC with a 486 DX 33 MHz CPU with an EISA bus architecture capable of 32 bit data transfer and process. The PC has 16 MB RAM memory and under the present set-up 13.5 MB are available in the extended mode of the memory. The data to be acquired by the ADTEK board are stored in the extended memory of the computer. Therefore the maximum amount of data that can be acquired is the maximum available extended memory. Under the present configuration, 13.5 MB of available extended memory, a maximum of 6.25 million data points can be sampled in one shot. With the previous information known, sampling at 333 kHz and for 24 simultaneous channels the maximum sampling time is about 780 msec. Data stored in the extended memory are automatically downloaded to the hard disk, where they are permanently stored in binary form.

The signals are transferred in the ADTEK board via 3 terminal boxes. Each terminal box has eight high - low input channels and one input for the trigger channel. All the terminal

boxes have a common ground and they are all grounded on the computer's chassis.

Internal gain (2, 4, and 8 times signal amplification) is offered by the ADTEK boards as well as an online monitor of the incoming signal. Input on the board is allowed for voltages in the range of ± 10 volts.

For this work, several pre-amps are used to amplify the signals from the pressure transducers and the temperature wires (cold wires). The EG&G model 113 low noise, battery operated pre-amps/filters, are used. The pre-amps are capable of DC or AC coupling (input) on both high or low input. Amplification of signals up to 10000 times can be achieved using these pre-amps. Another feature of the pre-amps is that they can be used as filters (high pass, low pass or band pass filters) so any undesired frequencies can be filtered out. In the present experiments all signal were band passed form DC to 150 kHz.

Several anemometers are available for the Hot Wire Anemometry (HWA) technique. The constant temperature anemometers are made by DANTEC model CTA56C01 connected to model 56C17 bridge/power supplies.

The above anemometers can be used to measure and recheck the resistance of the Platinum/Tungsten wire, as well as to elevate the wire's temperature substantially so it can be used for measurements in a high subsonic compressible flow field. Details on the operation and calibration of the constant temperature anemometers are given in Appendix B.

For the shock/flow visualization experiment, a Spectra Physics GCR-14-S YAG pulsed laser was used to illuminate the flow. An Astromed Charge Coupling Device (CCD) with 16-bit resolution water cooled camera recorded the scattered light. The YAG laser has a 5 - 6 nsec pulse duration and a 10 Hz repetition rate emitting at the 4th harmonic of 266 nm

with a 30 mJ pulse energy.

The laser can be operated at either repetitive mode or one shot mode. One shot mode requires external triggering of the laser and it was used for the shock/flow visualization experiments. The Astromed CCD camera has a Thompson grade 0 chip, 578x385 pixel well and each pixel is capable of recording light emitted by 1 photon. This gives a minimum recording illumination value of 10^{-11} lux. The chip is specially coated for UV transmission and has a 30% quanta efficiency at 266 nm and close to 90% at 532 nm..

A 4 channel delay generator made by EG&G, model 9650, was used in order to synchronize, from an initial signal of a pressure transducer, the laser pulse with the passage of the shock in front of the CCD camera. Essentially, the signal from the pressure transducer is to be delayed by an appropriate time lapse and then sent to the laser via a TTL pulse to trigger the lamp and the Q switch of the laser.

A list of the equipment used for each experiment is given on Tables XIII and XIV.

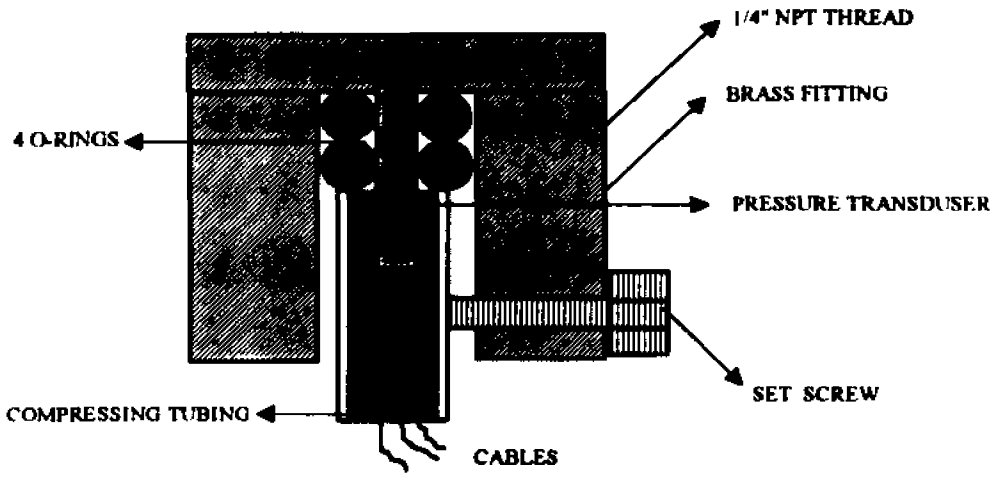

Figure 6.1a: Section AA of the pressure transducer fitting (not to scale)

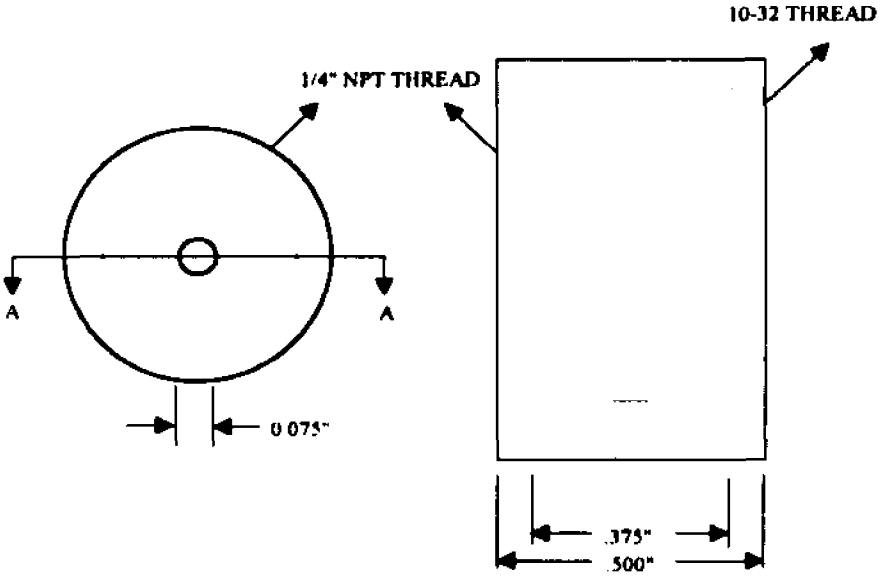

Figure 6.1b: Front and Side view of the brass pressure transducer fitting.

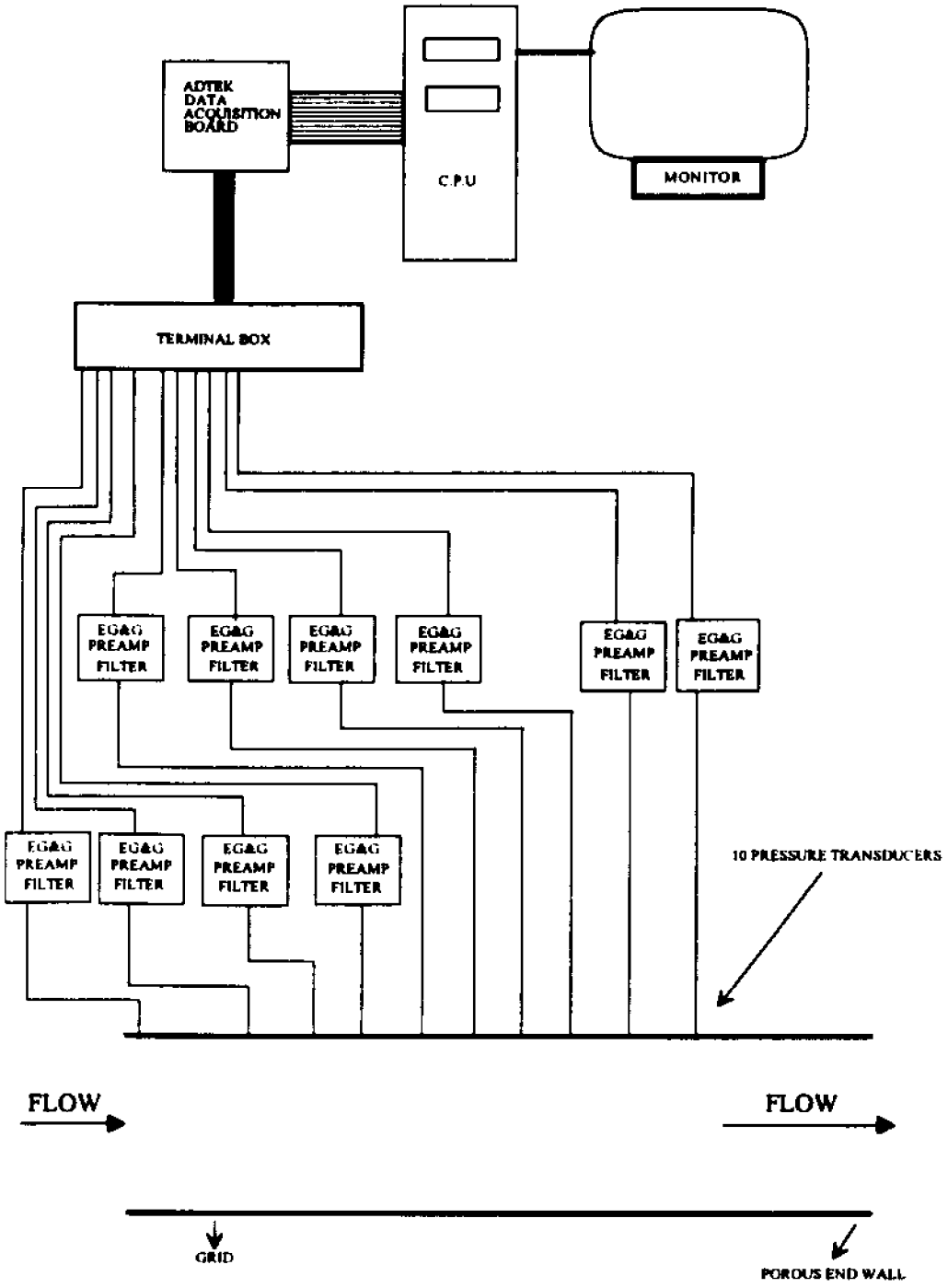

Figure 6.2: Experimental set-up and equipment used during the static pressure experiments.

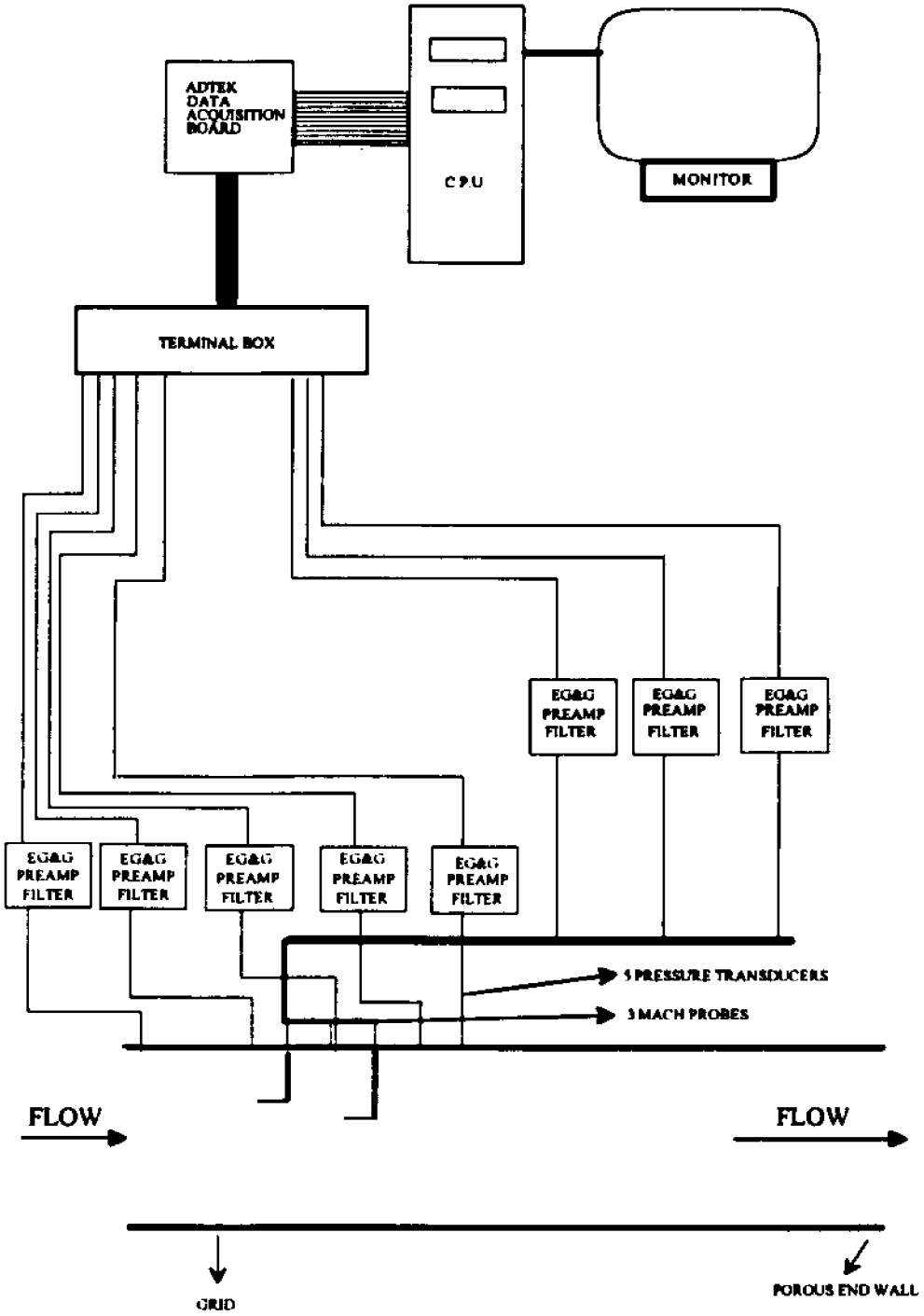

Figure 6.3: Experimental set-up and equipment used during the total pressure experiments (Mach number experiments).

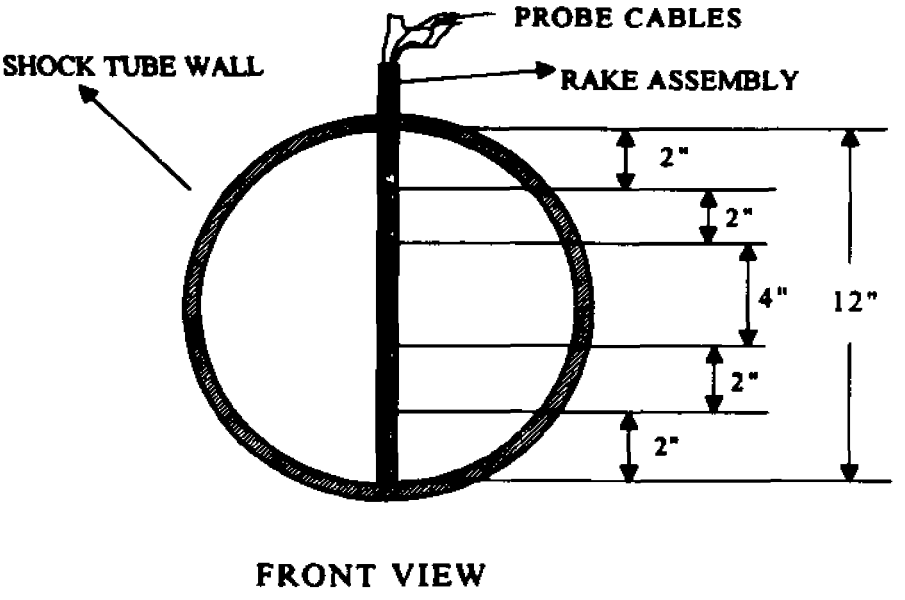

Figure 6.4a: Front view of the rake assembly in the shock tube.(not to scale)

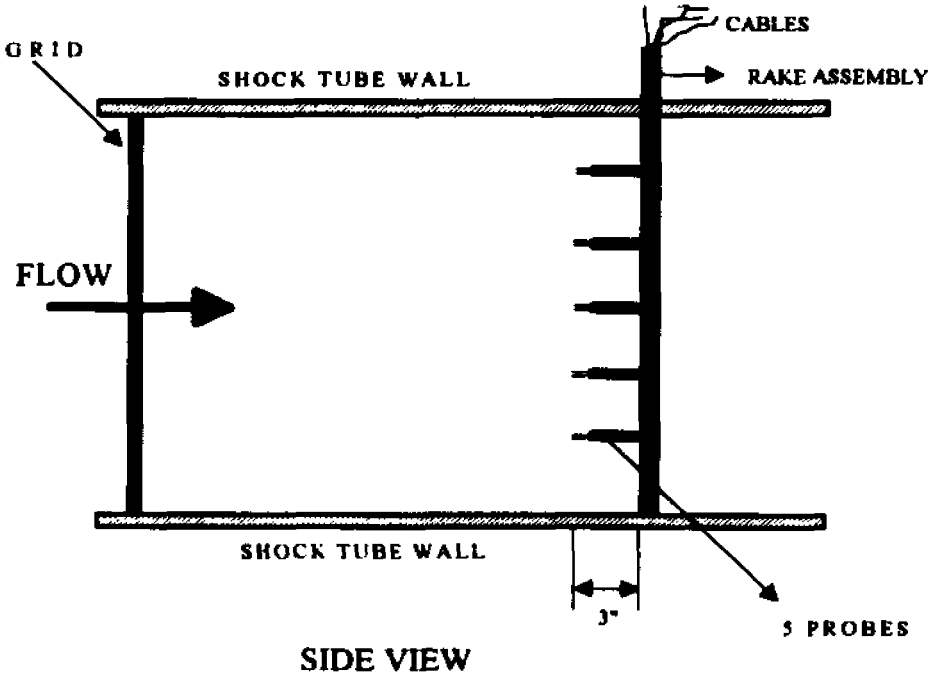

Figure 6.4b: Side view of the rake assembly in the shock tube.(not to scale)

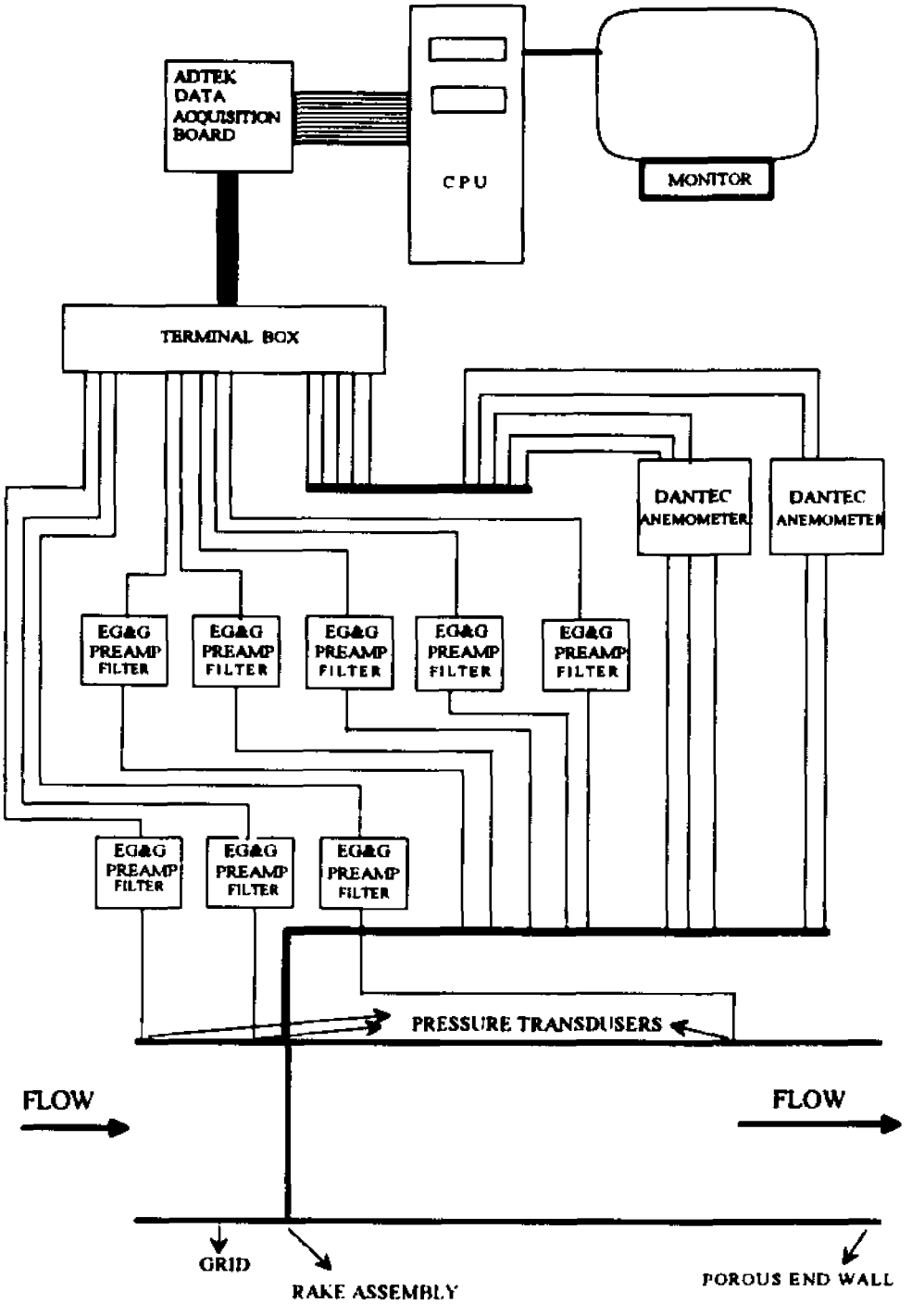

Figure 6.5: Experimental set-up and equipment used during flow quality experiments.

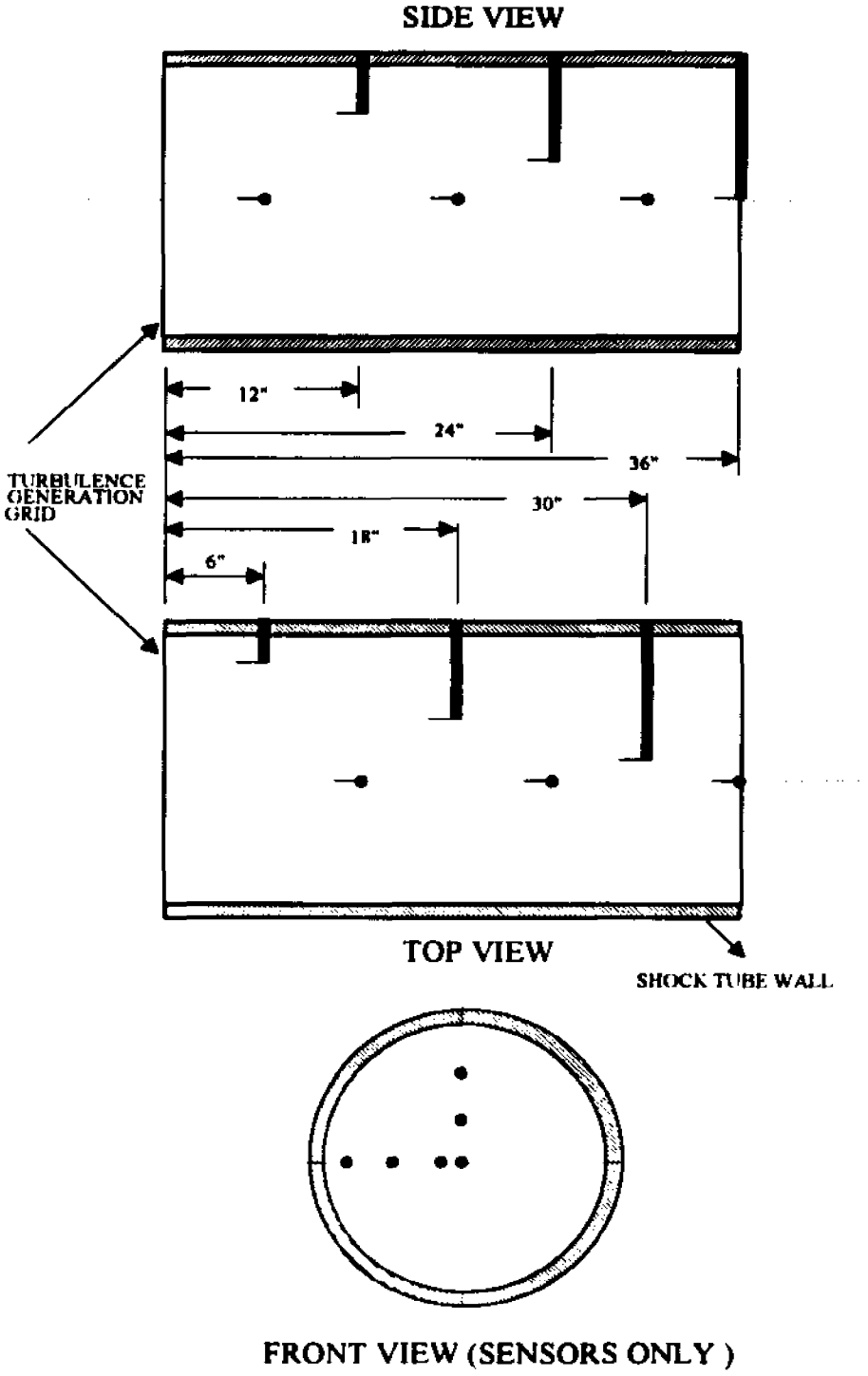

Figure 6.6: X-Wire probe location and arrangement in the shock tube. Side, Top and Front views of part of the working section are not shown to scale

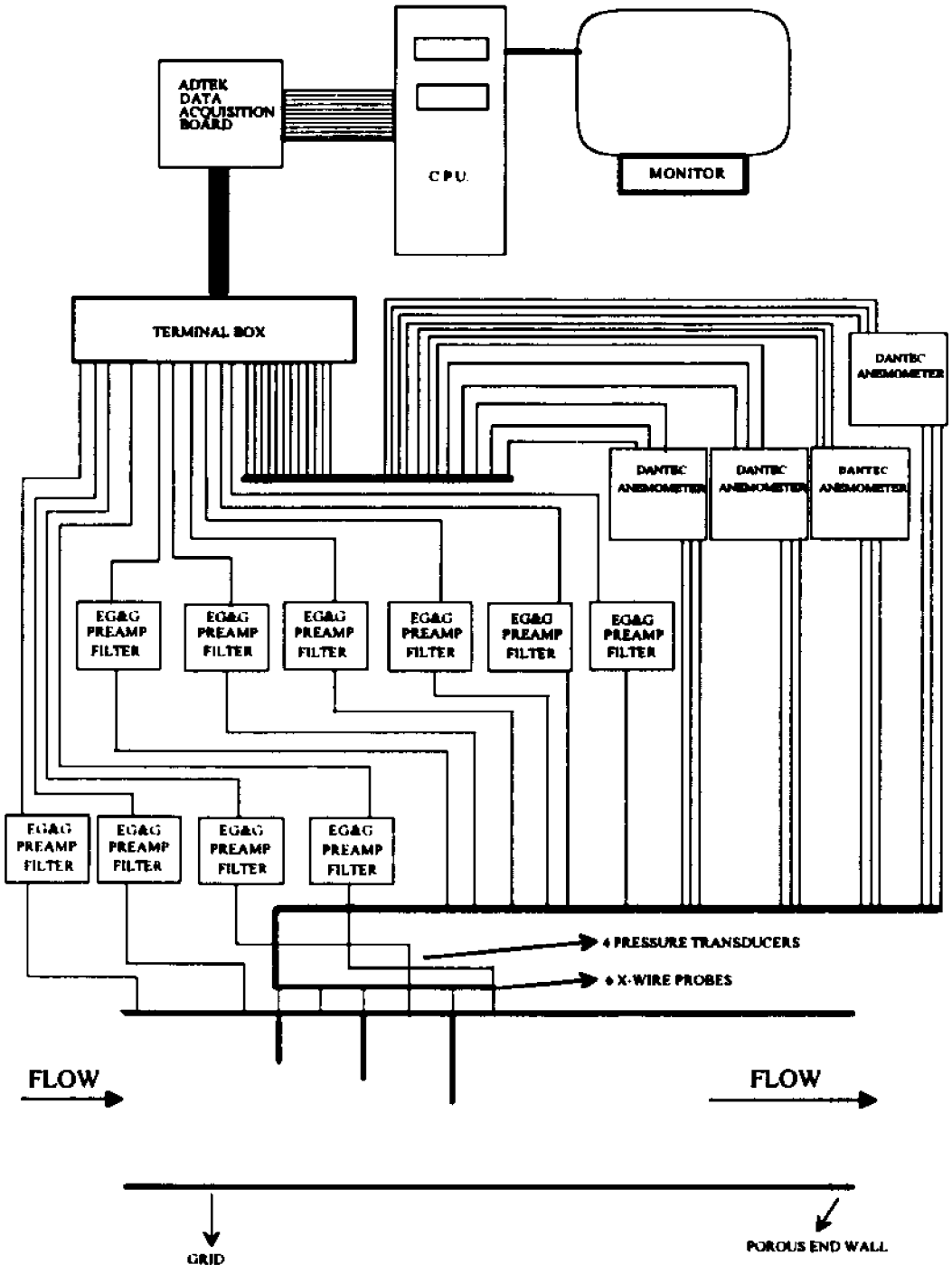

Figure 6.7: Experimental set-up and equipment used during the longitudinal and lateral velocity and temperature experiments.

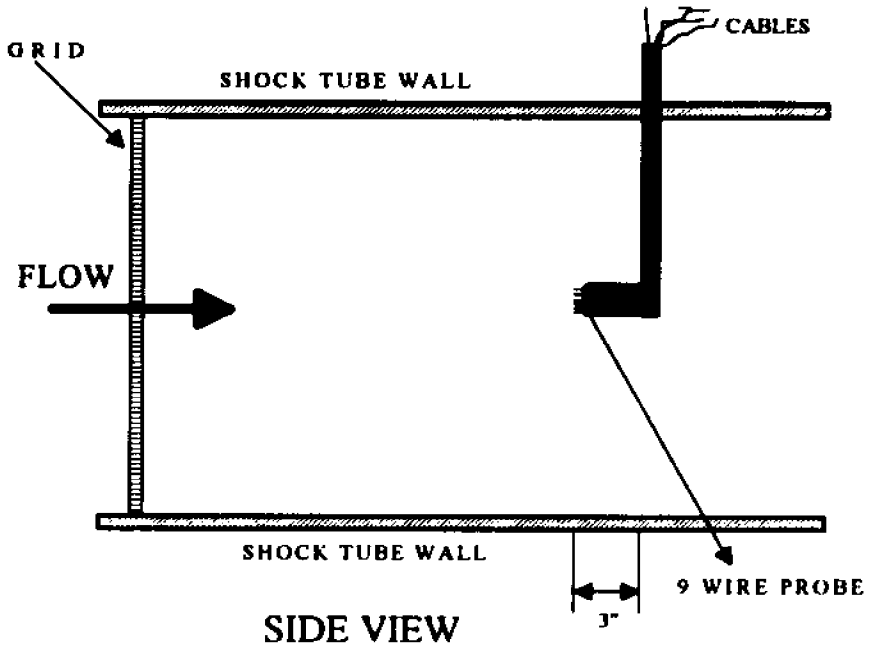

Figure 6.8: Side view of the 9 wire probe in the shock tube.(not to scale)

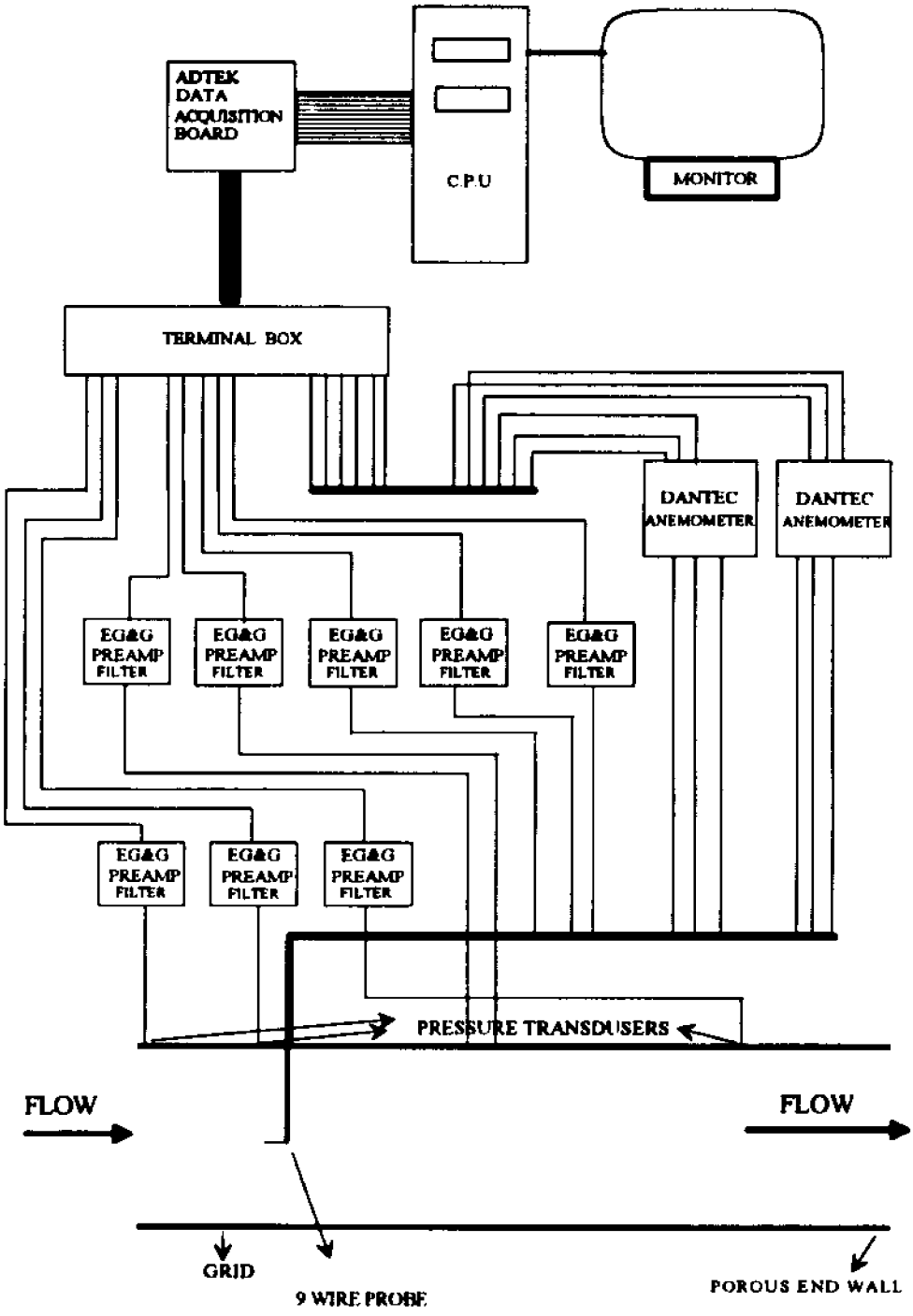

Figure 6.9: Experimental set-up and equipment used for the integral length scales experiments.

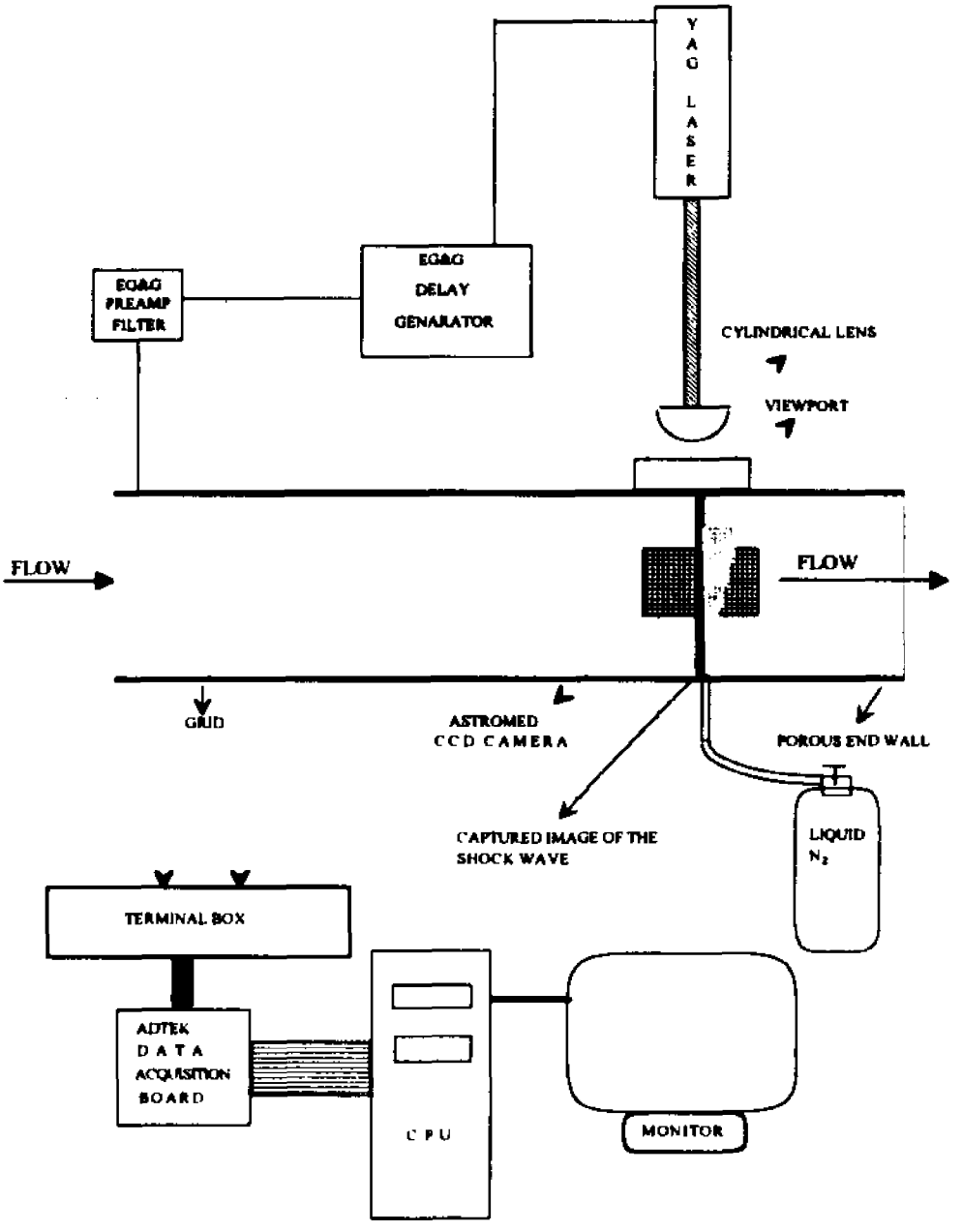

Figure 6.10: Experimental set-up and equipment used during the shock\flow visualisation experiments.

Pressure Transducer	Pressure Tap	Distance from Diaphragm
1	1	5 ft, 1.524 m
2	2	10 ft, 3.048 m
3	3	15 ft, 4.572 m
4	5	25 ft, 7.62 m
5	6	30 ft, 9.144 m
6	7	35 ft, 10.668 m
7	9	41 ft, 12.497 m
8	13	44 ft, 13.411 m
9	16	47 ft, 14.326 m

Table III: Location of installed pressure transducers with respect to the diaphragm during coefficient of friction experiments.

Distance from the Diaphragm	Distance from the Grid
36 ft	-4 ft
41 ft (2)	1 ft (2)
42 ft	2 ft
43 ft	3 ft
44 ft	4 ft
45 ft	5 ft
46 ft	6 ft
47 ft (2)	7 ft (2)

Table IV: Location of installed pressure transducers during pressure experiments.(distances in feet)

Distance from Grid	Radial Position (r/D)
-4 ft, -1.22 m	0.5 (wall) (Trigger)
1 ft, 0.3048 m	0.5 (wall)
1 ft, 0.3048 m	0.333
1.5 ft, 0.4572 m	0.166
2 ft, 0.6096 m	0.5 (wall)
2 ft, 0.6096 m	0
3 ft, 0.9144 m	0.5 (wall)
4 ft, 1.22 m	0.5 (wall)

Table V: Location of installed dynamic and static pressure transducers during dynamic pressure experiments.

Grid (Meshes/in)	M (mm x mm)	σ	M_{flow}	Re_M	P_0/P (inc.flow)
5x5	5.08x5.08	0.37	0.313	49842	1.0705
5x5	5.08x5.08	0.37	0.4652	74537	1.1599
5x5	5.08x5.08	0.37	0.5815	93062	1.265
4x4	6.35x6.35	0.44	0.3416	68216	1.084
4x4	6.35x6.35	0.44	0.441	88324	1.1428
4x4	6.35x6.35	0.44	0.5381	107645	1.2177
3x3	8.47x8.47	0.39	0.280	74582	1.056
3x3	8.47x8.47	0.39	0.447	119495	1.1472
3x3	8.47x8.47	0.39	0.5413	144438	1.2206
2x2	12.7x12.7	0.38	0.3025	120816	1.0655
2x2	12.7x12.7	0.38	0.449	179853	1.1484
2x2	12.7x12.7	0.38	0.570	228054	1.2465
1.33x1.33	19.1x19.1	0.26	0.335	201221	1.081
1.33x1.33	19.1x19.1	0.26	0.4637	279342	1.1661
1.33x1.33	19.1x19.1	0.26	0.6011	361692	1.2766

Table VI: Bulk flow parameters of the total pressure experiments performed.

PRESSURE TRANSDUCERS		RAKE ASSEMBLY	
Distance from Diaphragm	Distance from Grid	Distance from Diaphragm	Distance from Grid
36 ft	-4 ft	42 ft	2 ft
41 ft	1 ft		
47 ft	6 ft		

Table VII: Location of installed pressure transducers and rake assembly during radial velocity and temperature experiments.(distances in feet)

Grid (Meshes/in)	M_{flow}	Re_M	P_2/P_1	U_2 (m sec)	P_4/P_1
2x2	0.237	92502	1.429	85	2.701
2x2	0.503	198729	1.959	192	4.742
2x2	0.607	250060	2.674	250	7.803
1.33x1.33	0.3215	189854	1.495	116	2.837
1.33x1.33	0.510	303545	1.966	195	4.742
1.33x1.33	0.6275	383595	2.531	255	7.463
1x1	0.3421	269890	1.525	124	2.837
1x1	0.5545	434720	1.898	210	4.809
1x1	0.6604	540128	2.599	270	7.326

Table VIII: Bulk flow parameters of the flow quality experiments performed.

PRESSURE TRANSDUCERS		X WIRE PROBES	
Distance from Diaphragm	Distance from Grid	Distance from Diaphragm	Distance from Grid
36 ft	-4 ft	41.0 ft	1.0 ft
41 ft	1 ft	41.5 ft	1.5 ft
42 ft	2 ft	42.0 ft	2.0 ft
44 ft	4 ft	42.5 ft	2.5 ft
		43.0 ft	3.0 ft
		43.5 ft	3.5 ft

Table IX: Location of installed pressure transducers and X wire probes during longitudinal and lateral velocity and temperature experiments.(distances in feet)

Grid (Meshes/in)	M (mm x mm)	σ	M_{flow}	Re_M	Re_λ
5x5	5.08x5.08	0.37	0.371	59654	222
5x5	5.08x5.08	0.37	0.477	86315	250
5x5	5.08x5.08	0.37	0.576	102421	325
4x4	6.35x6.35	0.44	0.354	68208	223
4x4	6.35x6.35	0.44	0.446	105389	277
4x4	6.35x6.35	0.44	0.594	132921	355
3x3	8.5x8.5	0.39	0.321	81687	224
3x3	8.5x8.5	0.39	0.474	124203	316
3x3	8.5x8.5	0.39	0.564	215043	654
2x2	12.7x12.7	0.38	0.346	137319	267
2x2	12.7x12.7	0.38	0.436	169025	405
2x2	12.7x12.7	0.38	0.592	261667	737
1.33x1.33	19.1x19.1	0.26	0.368	200371	270
1.33x1.33	19.1x19.1	0.26	0.504	295721	550
1.33x1.33	19.1x19.1	0.26	0.607	398661	680
1x1	25.4x25.4	0.38	0.376	256903	296
1x1	25.4x25.4	0.38	0.529	438727	582
1x1	25.4x25.4	0.38	0.708	577040	735

Table X: Bulk flow parameters of the three wire probe experiments performed.

Pressure Transducers	NWP Set A	NWP Set B	NWP Set C
-4 ft, 1.22 m	1.75 ft, 0.5334 m	1.25 ft, 0.381 m	0.75 ft, 0.229 m
1 ft, 0.3048 m			
2 ft, 0.6096 m			
3 ft, 0.9144 m			
4 ft, 1.22 m			

Table XI: Location of installed pressure transducers and the nine wire during different sets of correlation experiments.

Grid (Meshes/in)	Mesh size M (mm x mm)	Incident Shock M_s	Reflected Shock M_r	Flow Mach # M_{flow}	Re_M	Re_λ
8x8	3.18x3.18	1.27	1.18	0.371	37138	162
8x8	3.18x3.18	1.342	1.25	0.461	53506	195
8x8	3.18x3.18	1.486	1.392	0.592	63458	246
5x5	5.08x5.08	1.27	1.18	0.371	59654	222
5x5	5.08x5.08	1.367	1.26	0.477	86315	250
5x5	5.08x5.08	1.469	1.388	0.576	102421	325
4x4	6.35x6.35	1.254	1.175	0.354	68208	223
4x4	6.35x6.35	1.337	1.242	0.446	105389	277
4x4	6.35x6.35	1.489	1.393	0.594	132921	355
3x3	8.47x8.47	1.227	1.166	0.321	81687	224
3x3	8.47x8.47	1.364	1.258	0.474	124203	316
3x3	8.47x8.47	1.456	1.372	0.564	215043	654
2x2	12.7x12.7	1.248	1.17	0.346	137319	267
2x2	12.7x12.7	1.328	1.231	0.436	169025	405
2x2	12.7x12.7	1.486	1.392	0.592	261667	737
1.33x1.33	19.1x19.1	1.267	1.179	0.368	200371	270
1.33x1.33	19.1x19.1	1.394	1.278	0.504	295721	550
1.33x1.33	19.1x19.1	1.504	1.405	0.607	398661	680
1x1	25.4x25.4	1.274	1.184	0.376	256903	296
1x1	25.4x25.4	1.42	1.291	0.529	438727	582
1x1	25.4x25.4	1.622	1.475	0.708	577040	735

Table XII: Bulk flow parameters of the nine wire probe experiments performed.

Experiment	Pre-Amps	Anemometers	C.C. Circuit
Pressure and Friction Exp.	10	X	X
Dynamic Pressure Exp.	8	X	X
Radial Velocity and Temperature	3 for Pressure 5 for Temperature	5	5
U and V Velocity and Temperature	4 for Pressure 6 for Temperature	12	6
Length Scale Correlation	6 for Pressure 3 for Temperature	6	3

Table XIII: Equipment used for pressure, velocity and temperature experiments.

Experiment	Pre-Amps	C.C.D. Camera	Laser	Delay Generator
Shock/Flow Visualization	1 (Trigger)	1 (Astromed)	1 (YAG)	1 (EG&G)

Table XIV: Equipment used for shock/flow visualization experiments.

7. DATA REDUCTION

The acquired data were automatically stored in binary form. Several programs, compiled in BASIC, were written in order to convert the binary data in ASCII readable form. Three conversion programs were necessary, since data is stored differently when one uses one data acquisition card (up to 8 channels), differently when 2 are used (up to 16 channels) and differently when all three cards are used (up to 24 channels). Thus, the number of data acquisition cards used determines the corresponding conversion program. When all the data are converted and stored in ASCII form, they can then be processed using programs written in the FORTRAN language.

All unprocessed signals were visually inspected for the existence of spikes or noise and for the duration of flow before and after the reflected shock wave. The amount of useful data after the interaction with the shock wave depends on the downstream distance from the grid as well as on the flow velocity. As it can be seen on figures 7.1 and 7.2, the duration of the useful data is affected by the grid reflection of the end wall reflected shock and by the arrival of the expansion waves, created in the driver, arriving at the measuring location after their reflection on the driver end wall.

In the first case (figure 7.1) the shock reflected from the end wall passes over (through) the measuring location and continues to move towards the grid. After it meets the grid, most of it goes through but part of it gets reflected back and moves toward the measuring location. When that second reflection arrives at the measuring location, the flow is further compressed and therefore, the data cannot be considered as useful for analysis.

Such data acquired after the second shock passes, maybe used in the future for analysis of variable compression flow field.

On figure 7.2, the effect of the arrival of the expansion waves is evident. The mean pressure and pressure fluctuations of the measured flowfield drop when the expansion waves arrive. Again, when the expansion waves arrive at the measuring location the data cannot be considered for analysis in this work. Instead this data has excellent potential for further analysis on the effects of the expansion fan on the fluctuating flowfield.

Formulas and expressions applicable for statistical and frequency analysis to be performed on the acquired data are offered in Appendix E.

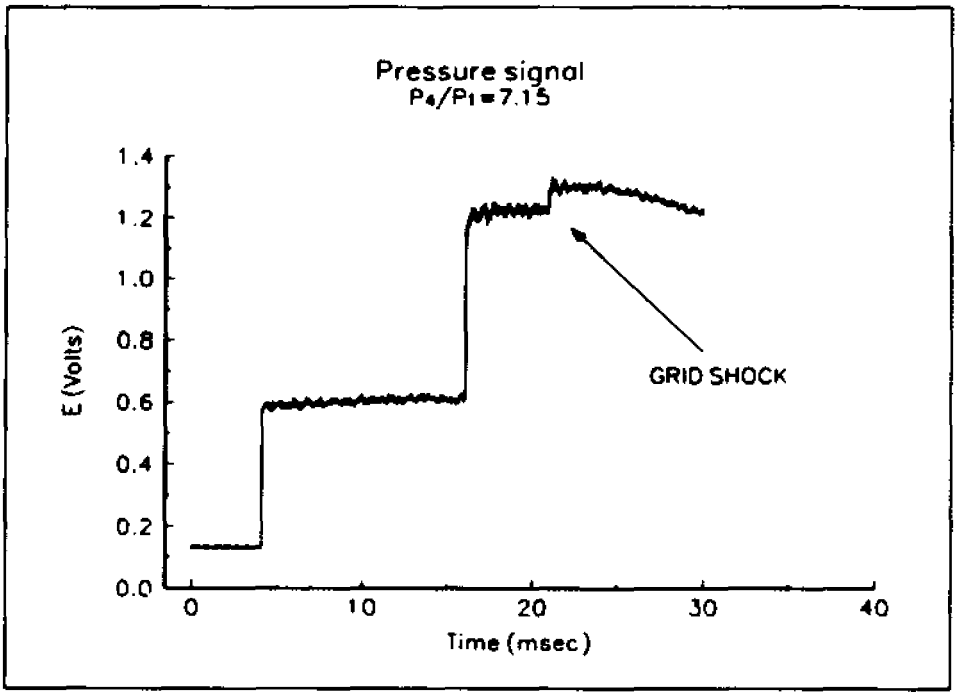

Figure 7.1: Time resolved pressure field showing the effects of the grid shock.

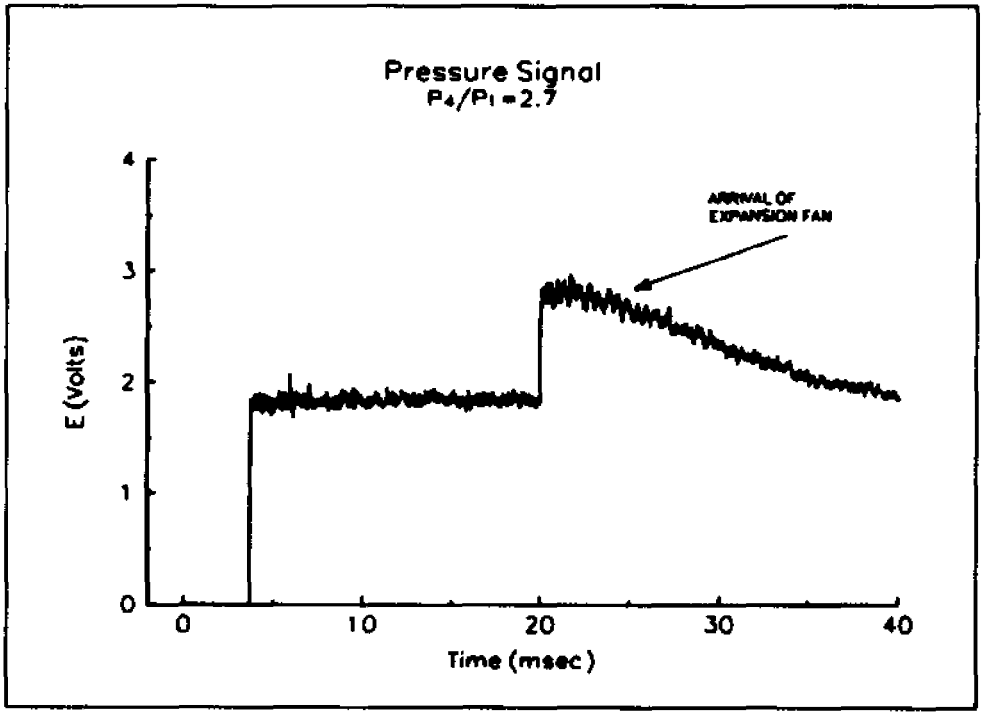

Figure 7.2: Time resolved pressure field showing the effects of the expansion fan.

8. RESULTS & DISCUSSION

The following discussion is divided in several sections, focusing in four major divisions of experiments.

I. First the operating conditions of this shock tube will be discussed by incorporating 1-D theory modified accordingly to include skin friction and heat resistance applicable to compressible flow. Estimation of the coefficient of friction was calculated for various flow conditions and at multiple locations of the shock tube.

II. The homogeneity of the flow and the planform shape of the shock wave will then be discussed (section 8.2) from results obtained from data acquired using pressure transducers installed on the wall of the shock tube as well as in the free stream, hot-wires and an optical technique to visualize the shock wave and the induced flow.

III. When the operating conditions of the shock tube are well established, then the results of the pressure flowfield (section 8.3) and the decay of isotropic turbulence for several flowfield conditions (section 8.4) will be presented. In the following section (8.5) results are presented on the interaction of a planar shock wave with decaying isotropic turbulence.

IV. Finally the behavior of the longitudinal and lateral integral length scales will be discussed for both cases (before and after interaction of the flow with the shock wave) and for various values of the flowfield parameters.

8.1 OPERATING CONDITIONS

Results from two predictive tools (1-D theory and numerical simulation) will be presented in the following sections as well as results from experiments performed in order to estimate a piecewise average friction coefficient for compressible flow throughout the length of the shock tube, using high frequency pressure transducers.

8.1.1 COMPARISON OF THEORY AND EXPERIMENTS

Theoretical analysis of the shock tube mean flowfield presented in Chapter 4, produced some interesting results. In particular, the effect of shock tube convergent flows is evident in figure 8.1.1. Namely, notice the amplification of the incident and reflected shock wave Mach number that is achieved by the addition of the conical section after the diaphragm. To obtain a non-zero as well as a non separated flow field behind the reflected shock, the solid end flange was replaced by an open flange fitted with several screens resulting in an effective porosity of 25%-50% depending on driver strength (P_4/P_1). The difference in the effective opening area is due to the fact that at higher driver strengths the flow becomes chocked at the porous end wall. Although the geometric area is approximately 50%, the effective porosity is decreased. The effect of the porous end wall on the reflected shock wave Mach number for different porosities is presented in figure 8.1.2.

Some experimental results are compared with the theoretical calculations without the presence of a turbulence generation grid, in figures 8.1.3 and 8.1.4. In particular, in figure

8.1.3 the driver strength (P_4/P_1) is plotted against the shock strength (P_2/P_1) and reflected shock strength (P_5/P_1). It is obvious that the calculated shock strength is in agreement with the experimental shock strength. The same cannot be claimed when the calculated reflected shock strength is compared with the experimental reflected shock strength. The theoretical values are higher than the actual. The reason for such a disagreement is that for higher driver strengths the ratio of mass flux exiting the shock tube to the mass flux of the induced flow is less than the mass flux ratio for a lower driver strength. As explained previously the flow becomes chocked at the end wall for high driver strengths and thus the effective opening area decreases. Therefore, one reflected shock strength curve cannot accurately describe the whole range of driver strengths. Figure 8.1.4 presents the shock strength with the theoretical and experimental shock velocities. The incident shock velocities seem to agree at low shock strengths but at higher shock strengths the theory predicts lower shock velocities, of the order of 10%. As was seen earlier in Chapter 4, the effect of friction, for subsonic cases, on the shock wave speed is greater for the stronger shocks than for the weaker shocks.

In order to assess the overall performance of the facility several qualification tests have been carried out. In one of them the wall pressure was measured at several locations simultaneously. Figure 8.1.5 shows several pressure signals obtained by high frequency response subminiature Kulite pressure transducers. The first transducer located at a distance x/D=9 from the diaphragm triggered the data acquisition for all the others. As can be seen from this figure the pressure rise behind the shock is not very steep at locations closer to the diaphragm because of the initially strong viscous effects. However for x/D>20 the pressure rise is very steep, even in this case of weak shock with Mach number, M_s=1.3, and overshoots

the transducer's response. It is obvious that the shock wave and the flow need some initial development time/distance before they reach their final strength. This development time/distance depends strongly on Reynolds number and M_s. The initial passage of the shock is followed by a long period of constant mean pressure before the arrival of the expansion waves which have reflected on the left end wall of the driver. The reflected expansion waves reduce the mean pressure by about 40%. After their passage the flow maintains a relatively long period with constant pressure for about 15 to 20 ms. At x/D=24 the arrival of the shock wave reflected off the end wall of the working section can be seen, while at the other stations the arrival of weak expansion waves emanated from the cone is evident.

Similar pressure traces obtained at a higher driver pressure which produced a shock with M_s=1.6 are shown in figure 8.1.6. Both figures (8.1.5 and 8.1.6) indicate several time intervals with remarkably steady mean pressure. The fluctuations evident in all pressure signals are due to turbulence in the boundary layer. In incompressible flows pressure fluctuations beneath the boundary layer are related to the local skin friction C_f. In compressible boundary layer flows, like that in the present facility, this relation is yet to be established.

In addition to the previously discussed comparison of 1-D theory and experiments, a comparison of the experimental time dependent pressure traces with a 1-D MacCormick scheme numerical solution of the unsteady differential equations for mass, momentum and energy transport was made by Agui (1995). Frictional losses as well the presence of the cone and the porous end wall of the shock tube were also included. The results of the comparison between the time-dependent pressure predicted by the developed model and actual pressure

measurements obtained at 10 different locations of the present facility is shown in figures 8.1.5a and 8.1.5b. Both types of results i.e. experimental and numerical have been obtained for a porous wall of 30% open area ratio and initial pressure ratio P_4/P_1=2.7. The experimental data of pressure have been interpolated to produce the x-t diagram shown in fig. 8.1.5a. The model predicts the arrival time of the incident and reflected shock waves as well as the magnitude of pressure quite satisfactorily. The incident and reflected shock, as well as the reflected expansion waves are clearly shown in both figures. There is also evidence of the transmitted expansion waves through the reflected shock.

Figure 8.1.6a shows the x-t diagram of the measured pressure data obtained in a flow with M_s=1.6 and pressure ratio P_4/P_1=7.8. The numerically simulated results are shown in figure 8.1.6b. It should be noted that the location of the diaphragm is at x/L=0.22 where the cone starts. The cone effects are clearly shown in this figure and are also depicted in the experimental data of figure 8.1.6a. Experimental information about the arrival of shock and expansion waves obtained from the pressure signals of figure 8.1.6 has also been plotted in figure 8.1.6b. It appears that the agreement between experimental observation and theoretical predictions for both incident and reflected shock is good. The experimental data suggest a shock speed which is always less than the theoretical one. In most facilities this is the case.

The x-t diagram of density as predicted by the model is shown in figure 8.1.6c. Now the contact surface is clearly shown since it is characterized by the change in temperature / density while pressure and velocity remain unaltered across it. The x-t diagram of temperature is shown in figure 8.1.6d.

8.1.2 COEFFICIENT OF FRICTION EXPERIMENTS.

The experimental set-up and the formulation to estimate the coefficient of friction are discussed in Chapters 6 and 4 respectively. Specifically in Chapter 4 the average coefficient of friction as a function of Re_D and M_2 is given. The need for a piecewise estimate of $\check{c}_f$ in compressible flows is apparent and discussed in more detail in Chapter 4.

The boundary layer that forms on the wall of the shock tube and initially extends from the leading edge of the expansion waves to the foot of the shock wave causes the shock wave and expansion waves to decelerate. The effects of the unsteady boundary layer on the flow are very complicated. These effects, in the absence of shock or expansion wave reflections off the end walls, have been known for a long time (Walker and Dennis, 1972). The piecewise average $\check{c}_f$ at various locations in the shock tube are shown in figure 8.1.7. High skin friction values were measured at locations near the diaphragm. The piecewise average $\check{c}_f$ decreases with increasing mean Mach number of the flow and Reynold's number to a value of about 0.002.

As seen on this figure the average friction coefficient reaches very high values close to the diaphragm. The high values near the diaphragm can be explained since the flow and the shock wave are still developing and thus acceleration of the shock wave and flow result in strong viscous effects. The friction coefficient can be assumed to be constant after x/D>35. The working section, where most of the measurements were acquired, is located at x/D=44 and ends at x/D=52 and thus the coefficient of friction remains constant throughout the length of the working section for all investigated flow conditions.

A comparison between experimental and theoretical values of shock speed W_s is plotted in figure 8.1.8. The experimental data have been obtained from the pressure signals calculating the time passage of the shock between two pressure taps. Again the experimental data appear to be about 8% smaller than the theoretical ones in the case of P_4=145 psig while in the lower driver pressure case P_4=25 psig the difference is about 20% at locations closer to the diaphragm and about 13% away from it. This is a result of the stronger viscous effects present in the low Mach number case.

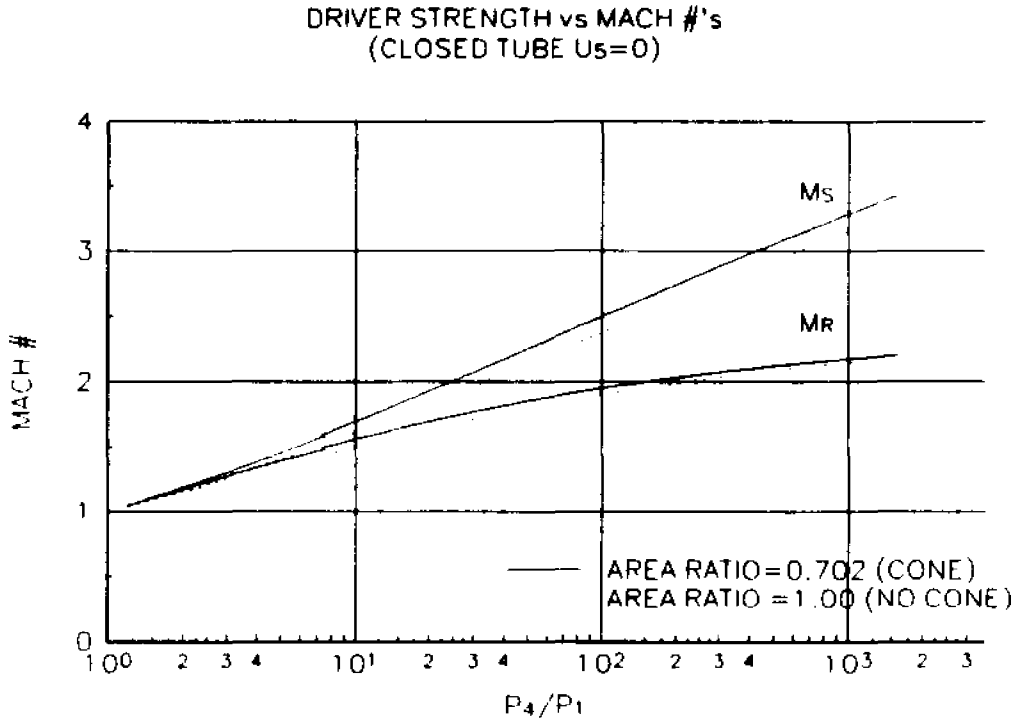

Figure 8.1.1: Theoretical effect of the cone on the shock Mach number

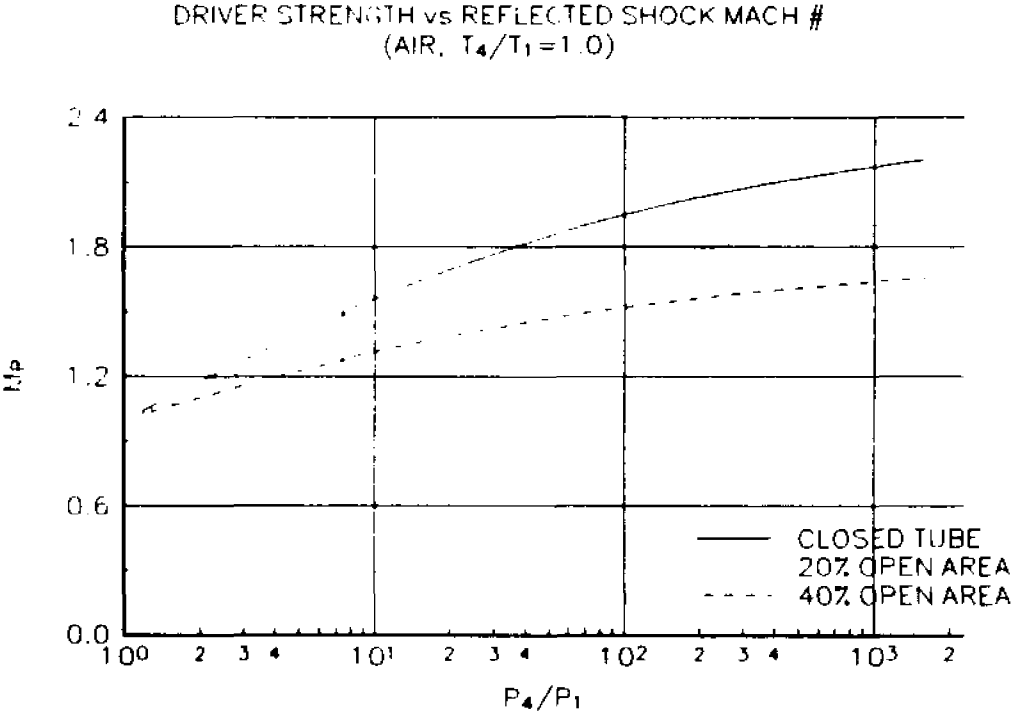

Figure 8.1.2: Effect of the porous end wall on the reflected shock wave.

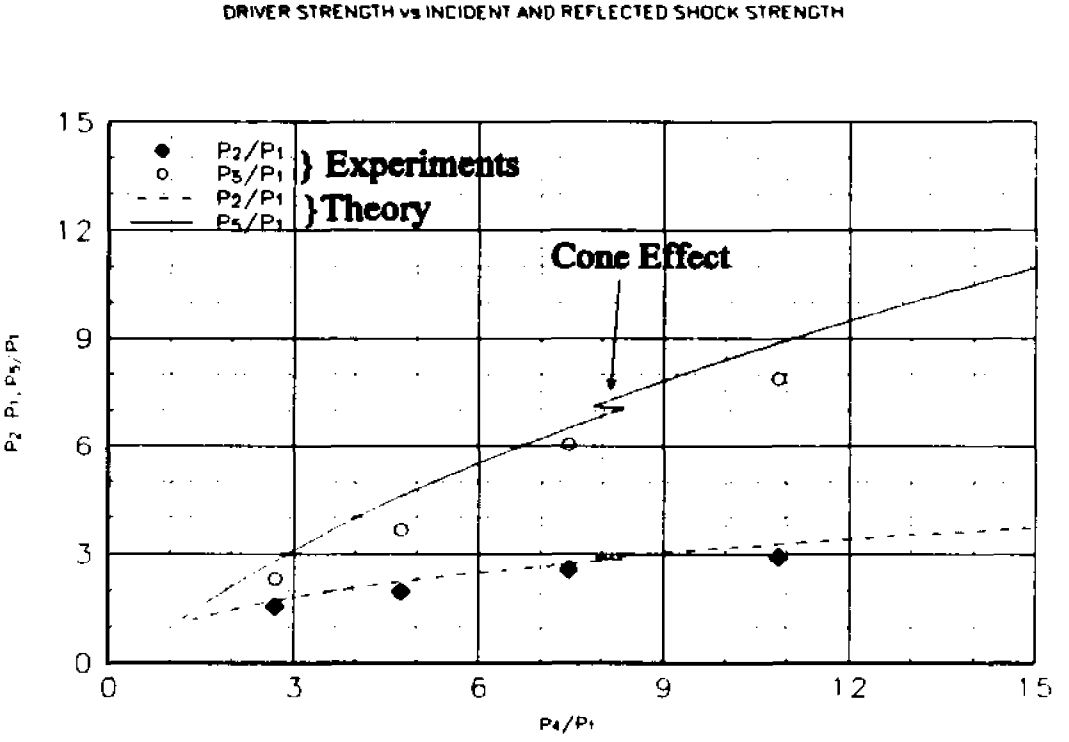

Figure 8.1.3: Comparison of experimental and theoretical pressure ratios.

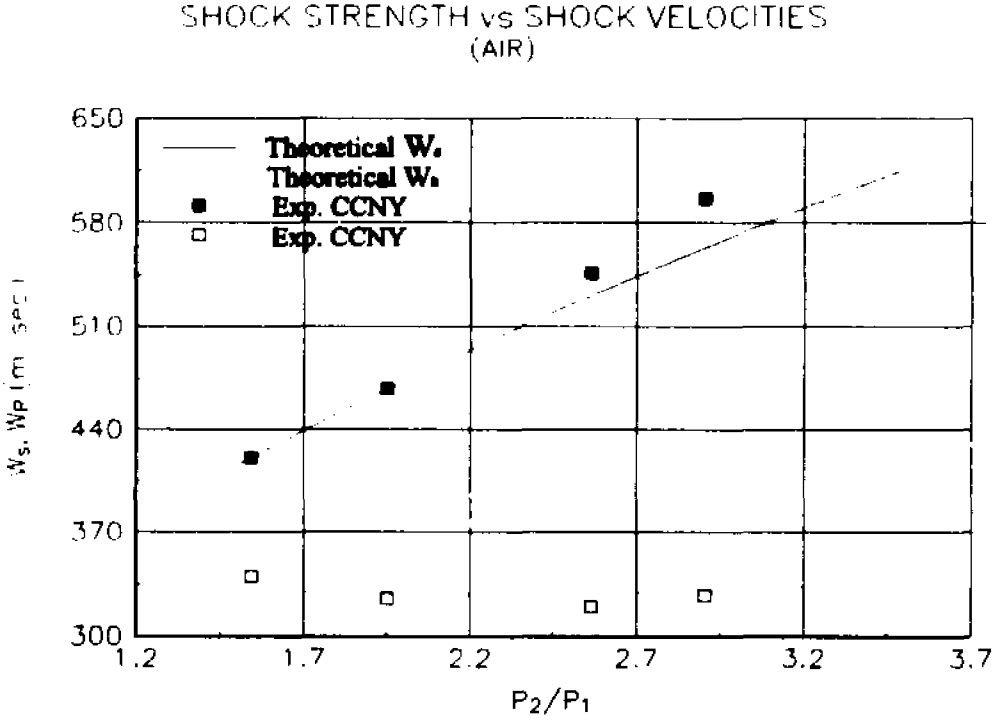

Figure 8.1.4: Shock strength vs. shock velocities.

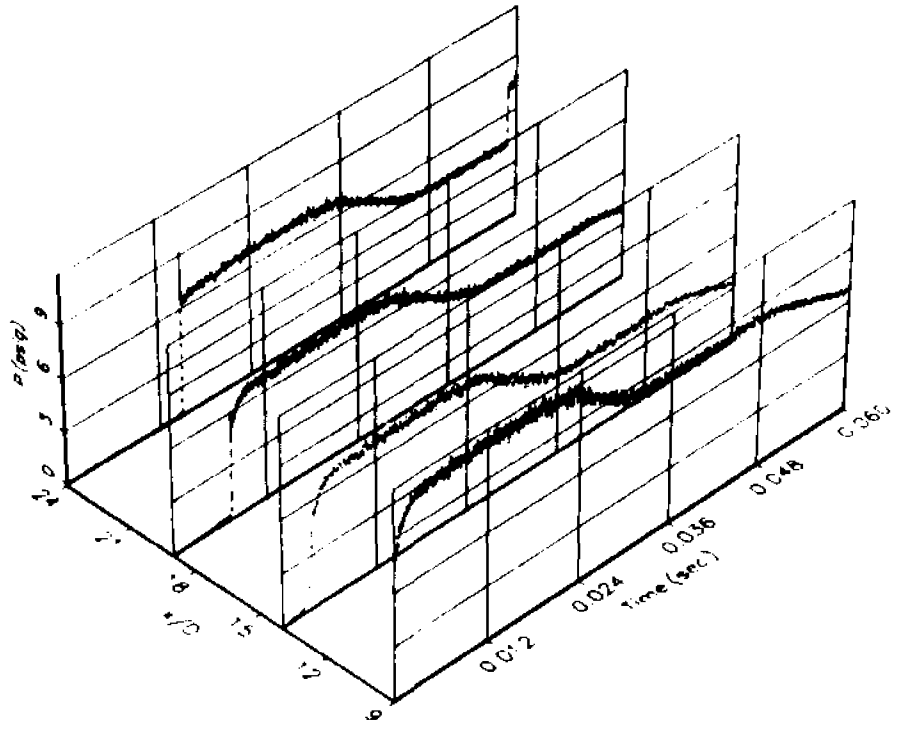

Figure 8.1.5: Simultaneous pressure signals at 4 different locations for P_4=25 psig

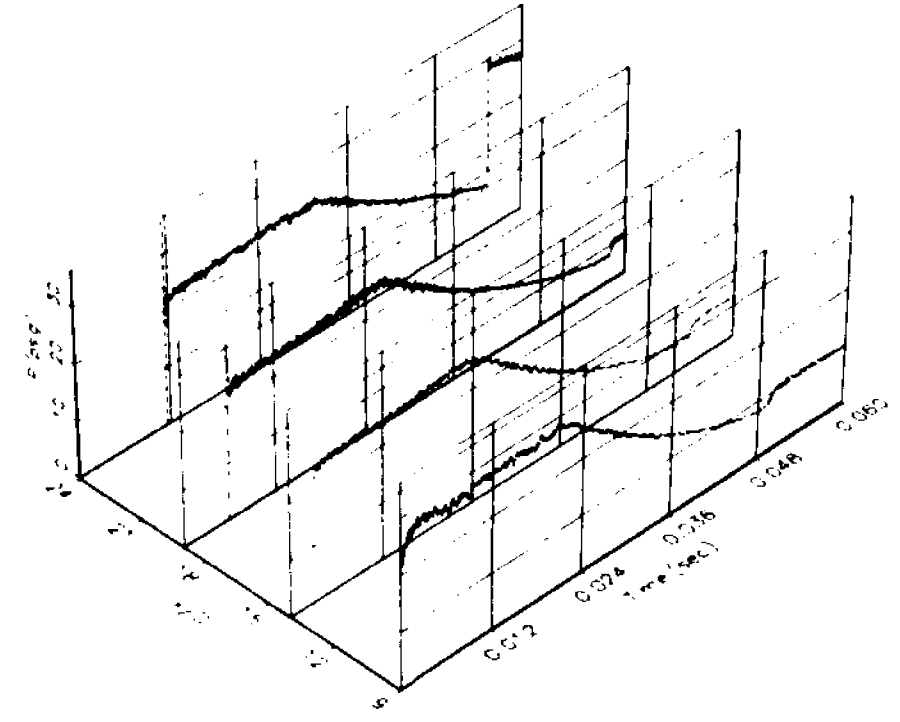

Figure 8.1.6: Simultaneous pressure signals at 4 different locations for P_4=100 psig

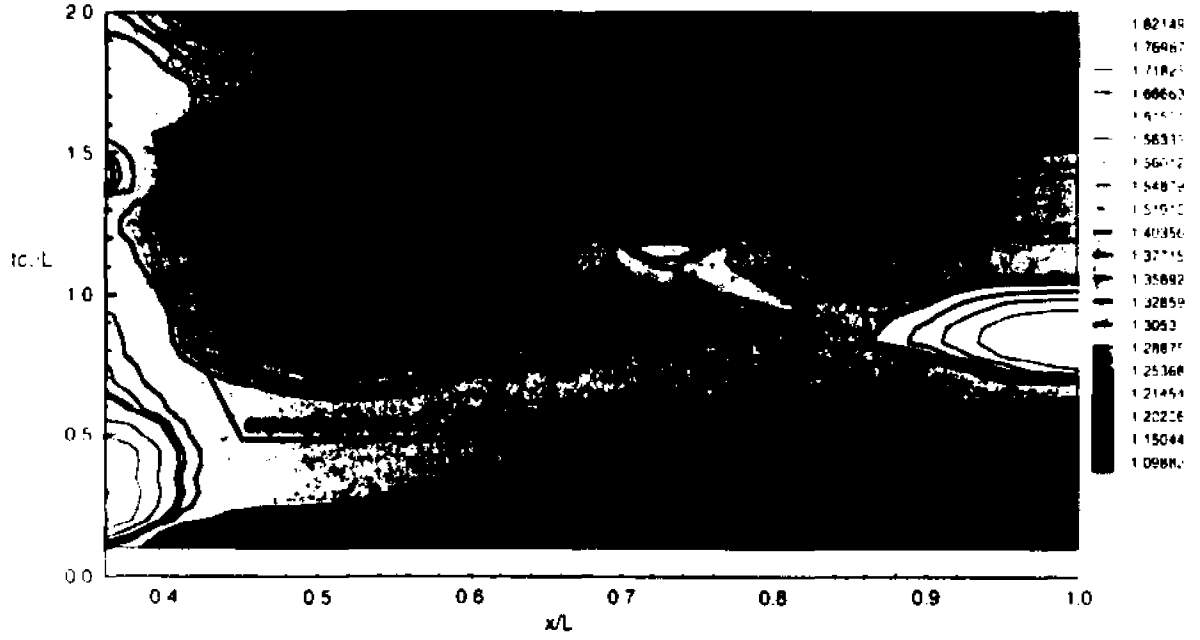

Figure 8.1.5a: x-t diagram: Experimental pressure data for P4/P1=2.7

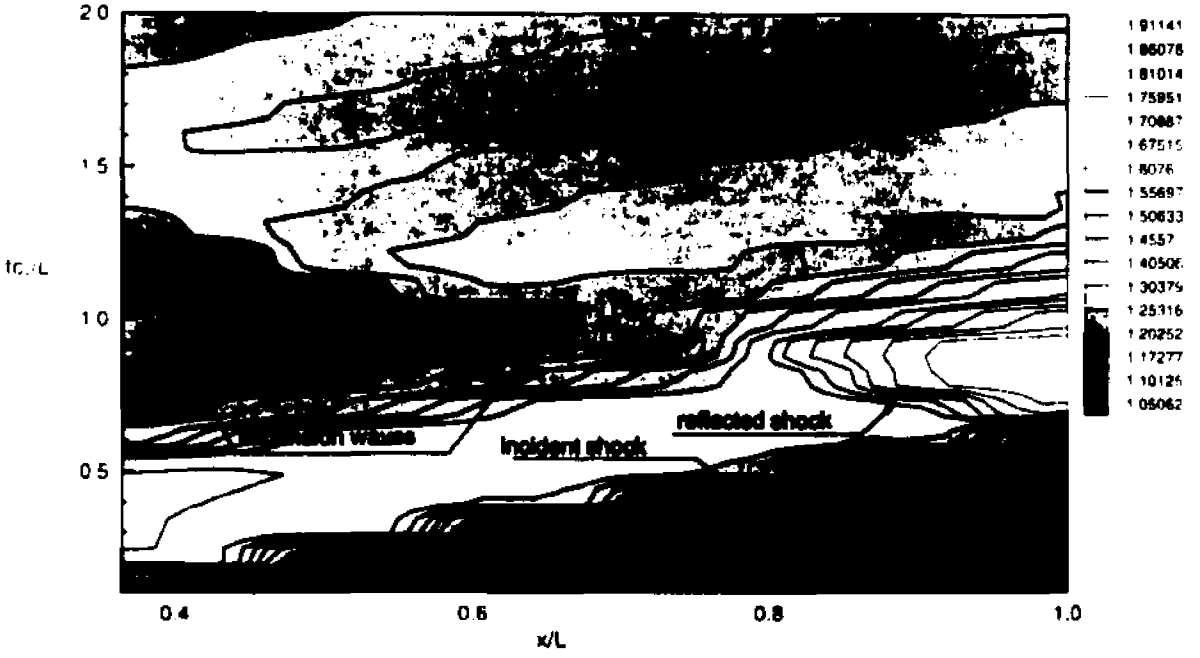

Figure 8.1.5b: x-t diagram: Theoretical pressure data for P4/P1=2.7

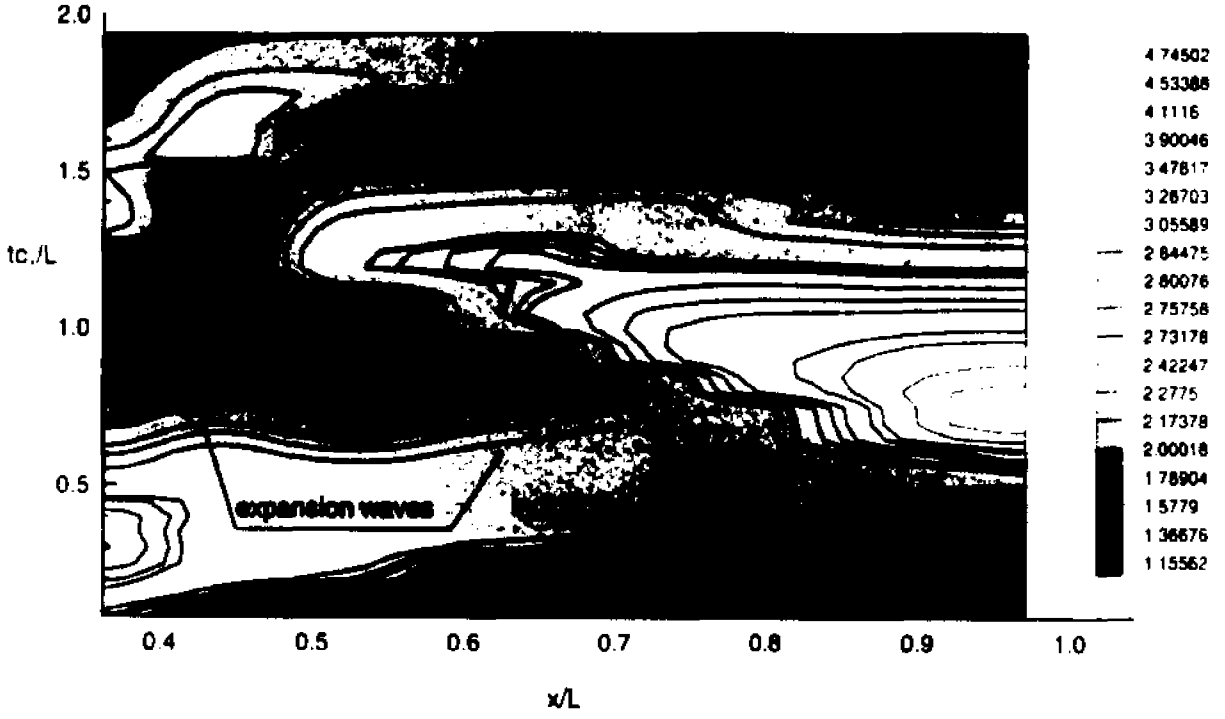

Figure 8.1.6a: x-t diagram: Experimental pressure data P4/P1=7.8

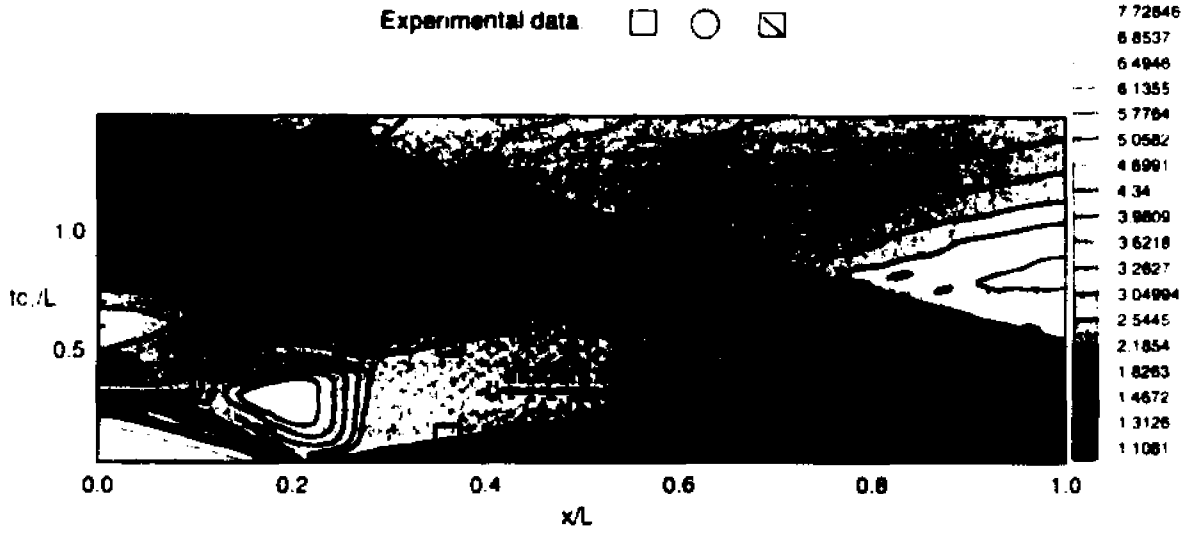

Figure 8.1.6b: x-t diagram: Theoretical pressure data P4/P1=7.8

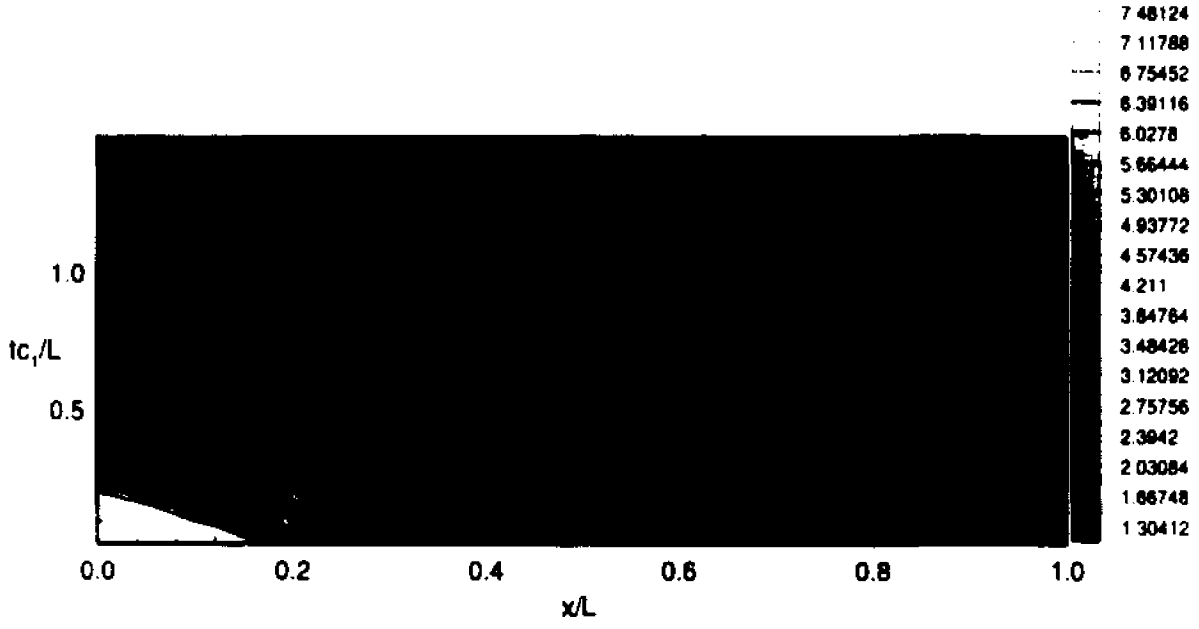

Figure 8.1.6c: x-t diagram; Theoretical density data P4/P1=7.8

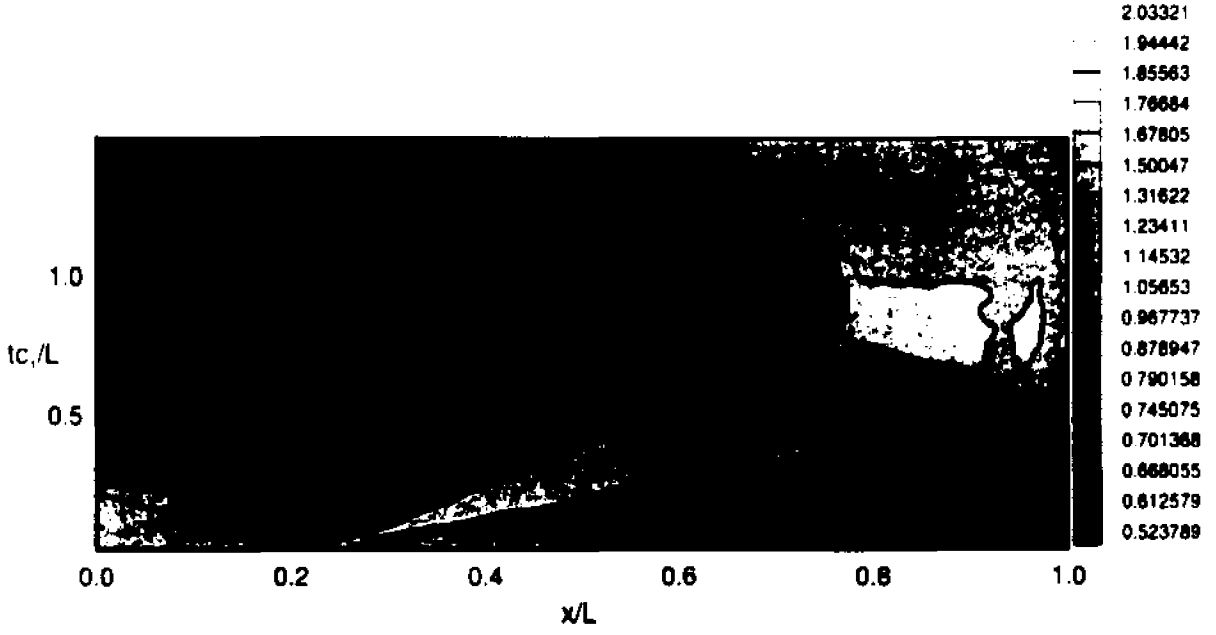

Figure 8.1.6d: x-t diagram; Theoretical temperature data P4/P1=7.8

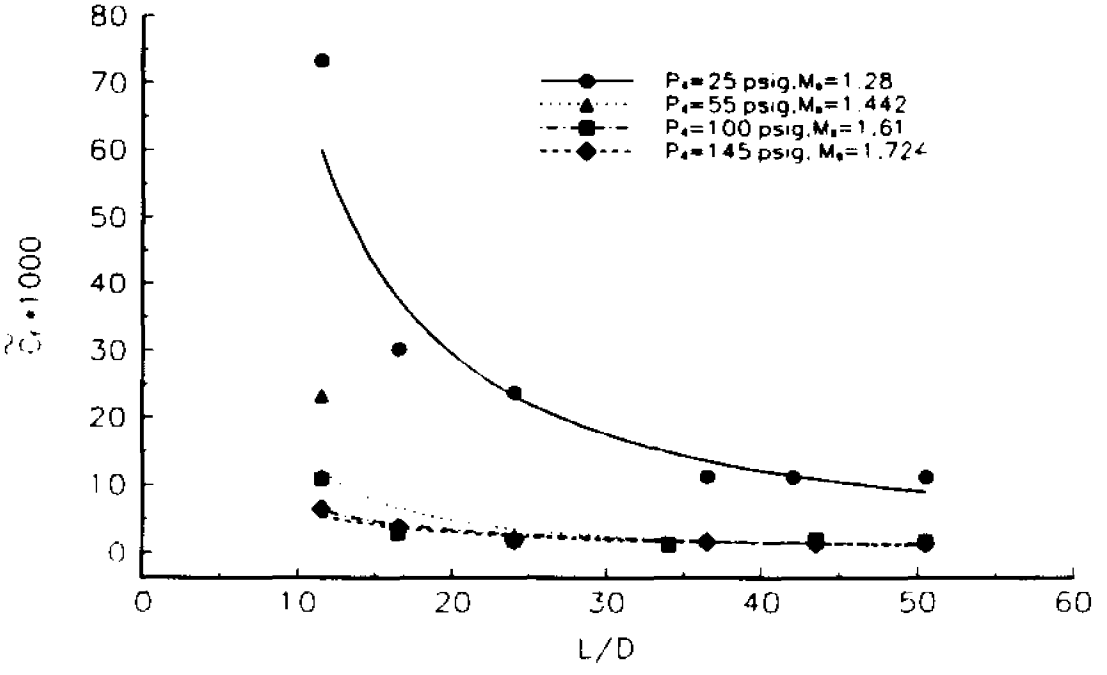

Figure 8.1.7: Local friction coefficient for various shock strengths.

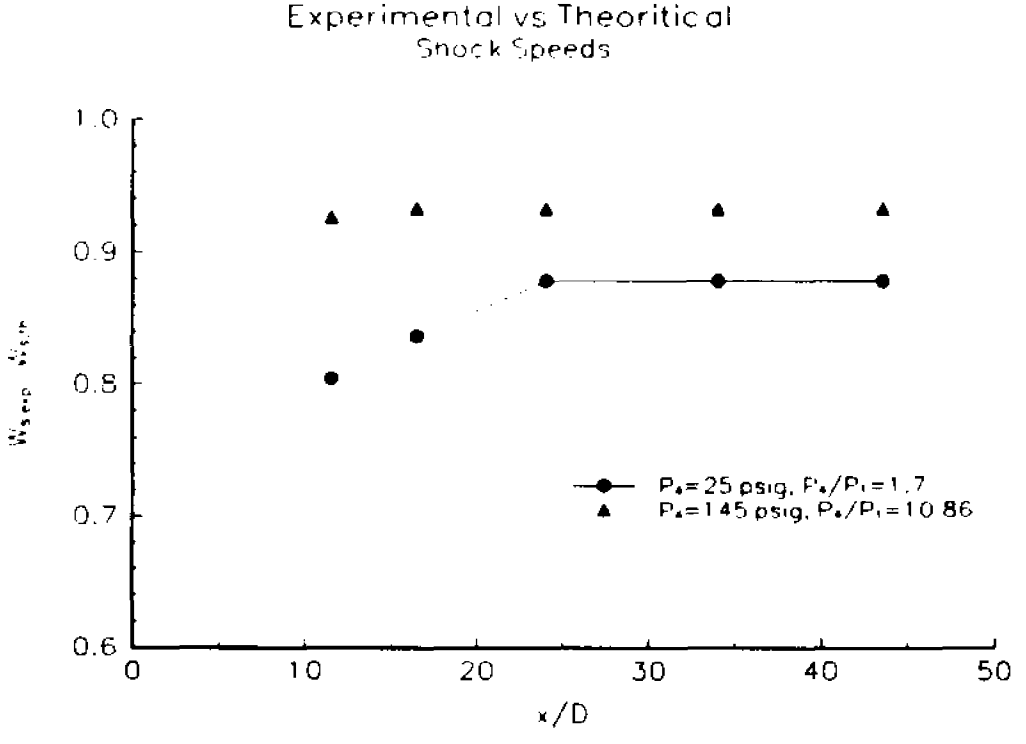

Figure 8.1.8: Comparison of experimental and theoretical shock speeds.

8.2 FLOW QUALITY AND VISUALIZATION EXPERIMENTS

The results presented in this section will establish the flow quality in the shock tube facility using three different techniques. One is shock/flow visualization, which is a non intrusive optical technique, that was used to check for the planform of the shock wave. Two other techniques were also used independently. Simultaneous velocity and temperature data acquisition using a hot-wire rake and the usage of the new total pressure probes (Mach probes) for gathering the time dependent Mach number of the flow as well as to check for the homogeneity of the flow.

8.2.1. SHOCK/FLOW VISUALIZATION

First the shock wave was visualized in order to check its inclination and planform by using a non intrusive optical technique using a YAG laser emitting at the UV range and a UV sensitive CCD camera.

Figures 8.2.1 and 8.2.2 present two pictures of the shock wave and the induced flow behind it for two different flow conditions and shock wave strengths. It was visualized by introducing liquid N_2 in the flow to increase the scattered light, since the elastic scattering of UV light by the air molecules of the flow was rather weak for the present density changes. As opposed to supersonic wind tunnels where the low temperature environment causes substantial condensation of water vapor which subsequently introduces adequate light scatterers for flow visualization, the high temperature of the flow in shock tubes precludes

the presence of the same materials for stronger light scattering. The CCD camera was mounted at an angle to the incoming shock wave because of the construction of the optical port and that is why the shock wave is shown at an angle. It can be seen from the above mentioned figures that for both Mach numbers and shock strengths presented here that the shock wave is planar. In these two pictures the vertiacl distance is 28 mm and the horizontal distance is 25 mm. The effect of the incident shock wave strength can also be seen from this two pictures. Specifically for the lower shock strength (P_2/P_1 = 1.5, M_{flow} = 0.35), shown in figure 8.2.1 it appears that the width of the shock wave is larger than that of the higher shock strength (P_2/P_1 = 2.2, M_{flow}=0.6) shown in figure 8.2.2. The width of the flowfield behind the weaker shock wave (fig. 8.2.1) can be estimated from the picture to be approximately 6-7 mm and for the stronger shock wave to be 3-4 mm. The liquid nitrogen vapor evaporates behind the shock wave due to the higher temperature of the induced flowfield. The response of the liquid nitrogen depends in the temperature can be seen from the above mentioned figures. The structure of the shock front can be located in front of the liquid nitrogen (bright band).

Theoretically the shock wave thickness is proportional to the mean molecular free path, Λ, and inversely proportional to the mean density of the flowfield and shock strength, P_2/P_1.

8.2.2 HOT-WIRE RAKE EXPERIMENTS

The first objective of the present investigation was to establish the flow quality with well defined boundary conditions. The homogeneity of the flow was checked by the

measurements provided by the hot-wire rake. The special hot/cold wire rake was constructed to reveal the planarity of the incident and reflected shock waves as well as the quality of the flow downstream of the turbulence generating grid. Data were acquired simultaneously at several radial positions and results from analysis of the above flow quality experiments are presented here. The bulk parameters of the hot-wire rake experiments are presented in Table VIII.

Time dependent flow velocity fluctuations and temperature profiles are shown in figures 8.2.3, 8.2.4 for various radial locations at the same downstream distance. The flow velocity and temperature remains constant throughout the diameter of the tube for both incident and reflected flowfields.

The arrival of the reflected shock wave as well as the velocity flowfield before and after the interaction with the shock wave appear in figure 8.2.3. Three velocity signals are shown at different radial positions. It is obvious that the shock wave arrives at the same time in all probes and therefore independently verifying that the shock wave is planar and not inclined.

Similar results are offered in figure 8.2.4 for three temperature profiles at three different radial positions. Again the arrival of the incident and reflected shock wave is the same for all probes.

The mean velocity and temperature $\bar{U}$ and $\bar{T}$, shown in figure 8.2.5 and 8.2.6, were uniform within 5% of its mean value over 85% of the tube cross section. The fluctuating fields and particularly $\overline{u^2}$ and $\overline{q^2}$ were uniform within 12%.

8.2.3 TOTAL PRESSURE EXPERIMENTS (Mach Number Experiments)

An alternate method was used to investigate the flow quality as well as to obtain the time dependent flow Mach number at multiple locations in the flowfield simultaneously. The time dependent Mach number of the flowfield was acquired at three locations in the shock tube's working section simultaneously. To obtain the time dependent Mach number of the flowfield two pressure transducers were used simultaneously. One was measuring the time dependent total pressure in the freestream and the other the time dependent static pressure at the wall. Both measurements were obtained at the same plane (i.e. downstream location). Although pressure fluctuations at the wall can not be assumed equal to pressure fluctuations in the free stream, the mean static pressures can comfortably be assumed equal at those locations by virtue of the thin boundary layer approximation. The bulk parameters of the total pressure experiments are presented in Table VI.

Figure 8.2.7 presents the time dependent static and total pressure fluctuations obtained at the same downstream location. The alignment in time of the arrival of both shock waves (incident and reflected) at these two different radial locations provides another indication of the planform of the shock wave. The static pressure was averaged before and after the arrival of the reflected shock wave and with the use of $\frac{P_0}{P} = \left[1 + \frac{1}{2}(\gamma - 1)M_{flow}^2\right]^{\frac{\gamma}{\gamma-1}}$, where P_0 is the total pressure of the flowfield and P is the static pressure of the flowfield, the time dependent Mach number (M_{flow} or M_2) of the flowfield was obtained. Figure 8.2.8 presents just that. It is evident from this figure that Mach number fluctuations are amplified by the interaction

of the induced flowfield with the reflected shock wave.

Three time dependent Mach number traces obtained simultaneously at different downstream locations are shown in figure 8.2.9. The signals are displaced and refer to the induced flowfield before any interaction with the shock wave. It is clear that Mach number fluctuations are very similar for all three signals, and so are the quality of the flow and the resolution of high frequencies from the probe.

With a turbulence generation grid placed at the beginning of the working section the mean Mach number of the flowfield was investigated at various dimensionless downstream distances x/M. This is shown in figure 8.2.10 for three different flowfields at several non dimensional downstream distances. It can be seen that for all the non dimensional distances that data were obtained, (up to x/M=120) the mean Mach number remained within 3%. Similar conclusions can be drawn for the flowfield after the interaction with the shock wave. The mean Mach number of the compressed flowfield remained constant within 5% at all tested x/M.

A comparison of the mean Mach numbers of the flowfield obtained using all three different techniques is shown in figure 8.2.11. The data were obtained independently by the hot wire rake and by the Mach probes. They are plotted along with the theoretical prediction for several shock strengths and for both cases. Both cases, incident and reflected, agree well with the theoretical prediction. Since the hot wire measurements and the total pressure measurements were obtained from different experiments the above results confirm the consistency of the experimental techniques as well as the quality of the flowfield.

The deviation of experimental values from theoretical predictions is shown in figure

8.2.12. At the lowest Mach numbers the experimental value is approximately 5% greater than the theoretical one, while for higher Mach numbers the experimental values are about 2% lower than the theoretical. The deviation, even though small, for both cases is attributed to the frictional losses present. For the lowest Mach number flow with a higher coefficient of friction, as shown in the previous section, it is expected that the Mach number predicted from theory would be lower since frictional losses tend to increase the mean Mach number of the flow. For the higher Mach number flows with much lower coefficient of friction the theoretical prediction is expected to be closer to the experimental. This is realized since the deviation for the total pressure probes is less than 2% and most probably can not only be attributed to frictional losses but to probe resolution as well. The resolution of the total pressure probe is of the order of 40 to 50 viscous scales, while the resolution for the hot wires is of the order of 7-26 viscous scales. More on the estimate of the resolution of the hot wire probes appears in chapter 8.4 where the viscous scales are also discussed. The hot wires indicate an almost perfect agreement of the experimental mean Mach number to that predicted from theory.

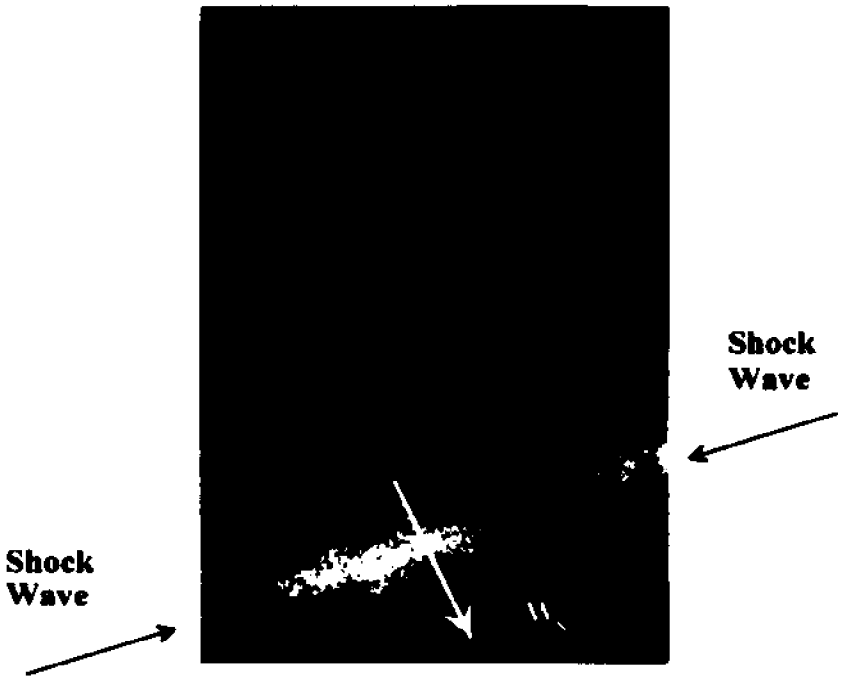

Figure 8.2.1: Shock wave visualization for P_2/P_1=1.5

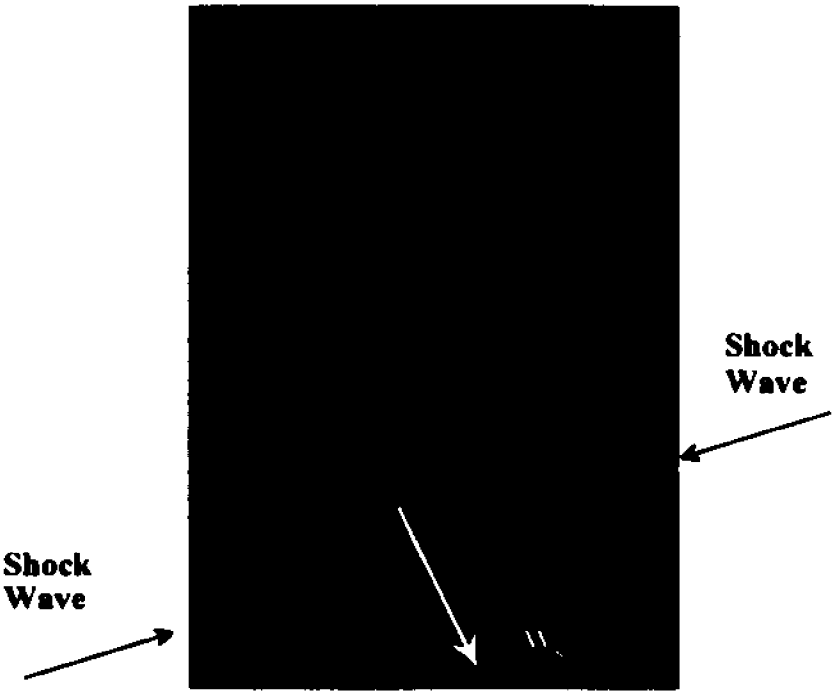

Figure 8.2.2: Shock wave visualization for P_2/P_1=2.2

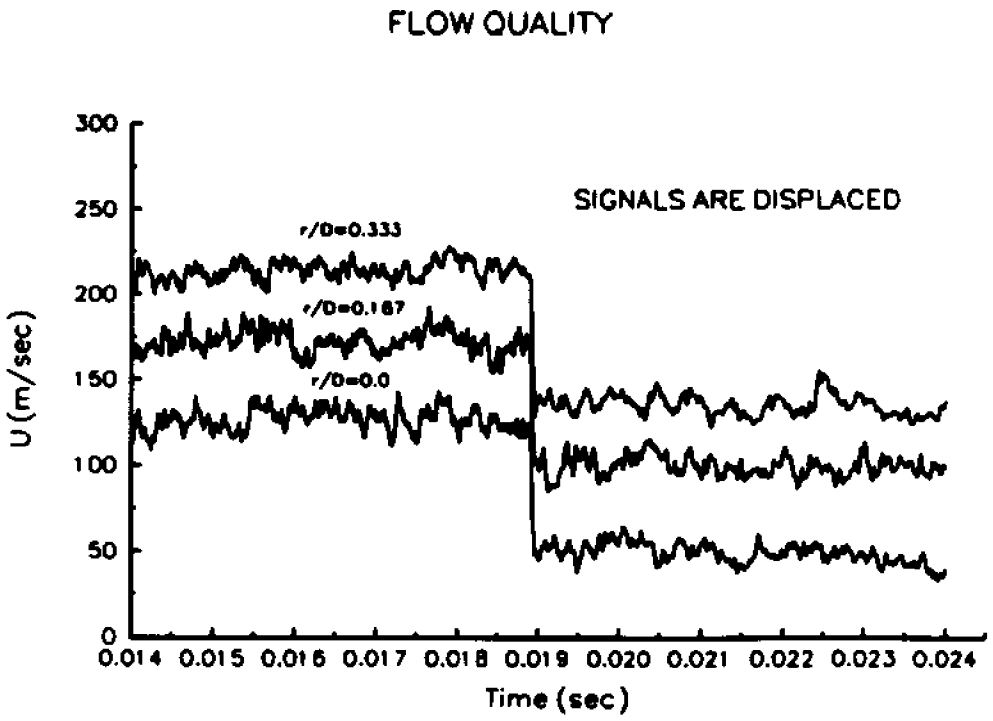

Figure 8.2.3: Time dependent velocity traces at different radial locations in the shock tube.

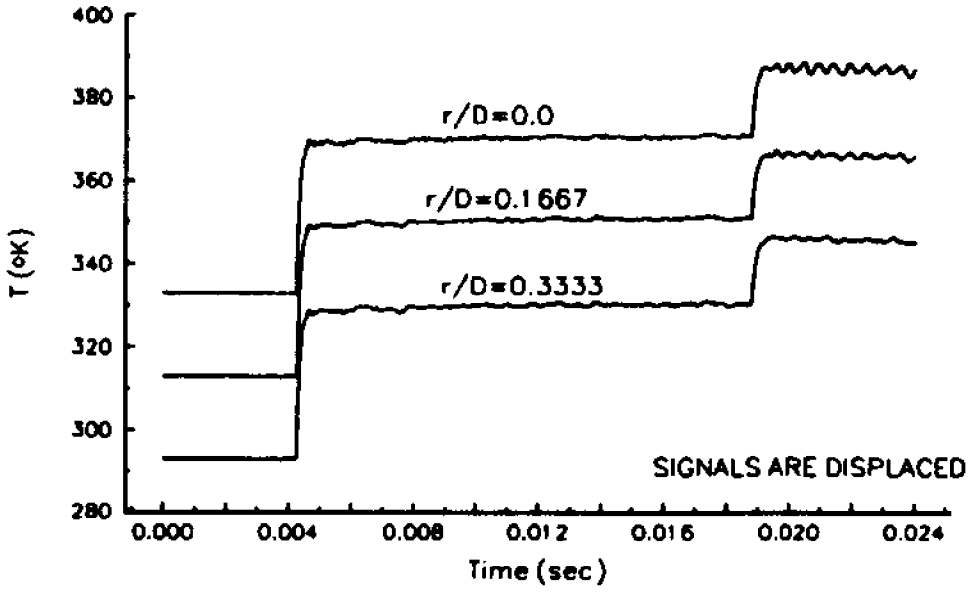

Figure 8.2.4: Time dependent temperature traces at different radial locations in the shock tube.

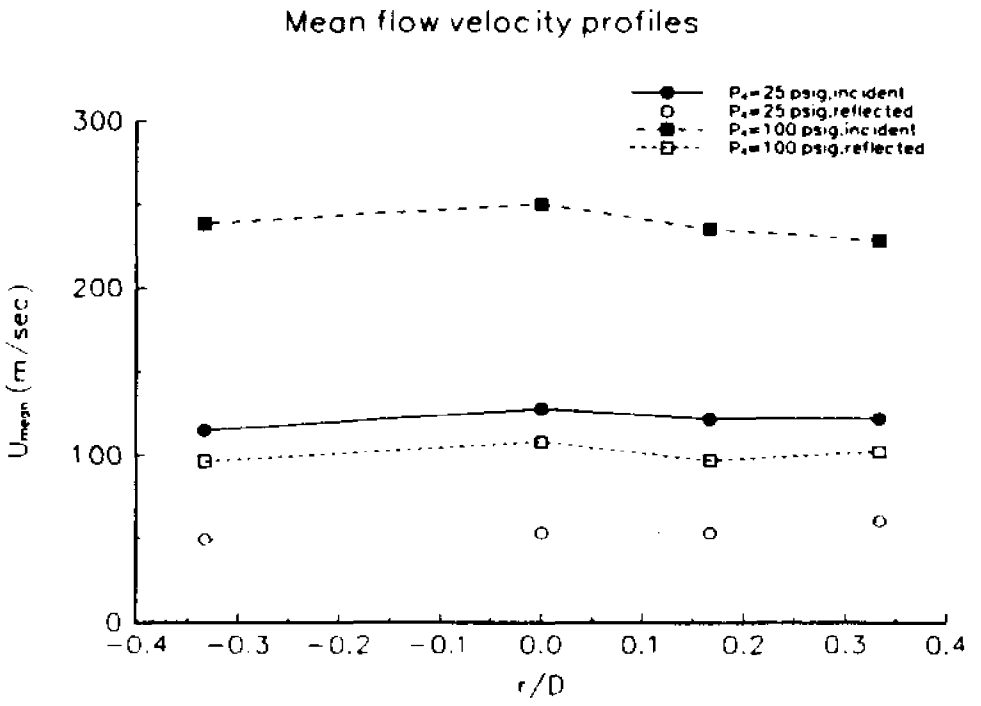

Figure 8.2.5: Mean flow velocity profiles for various radial positions.

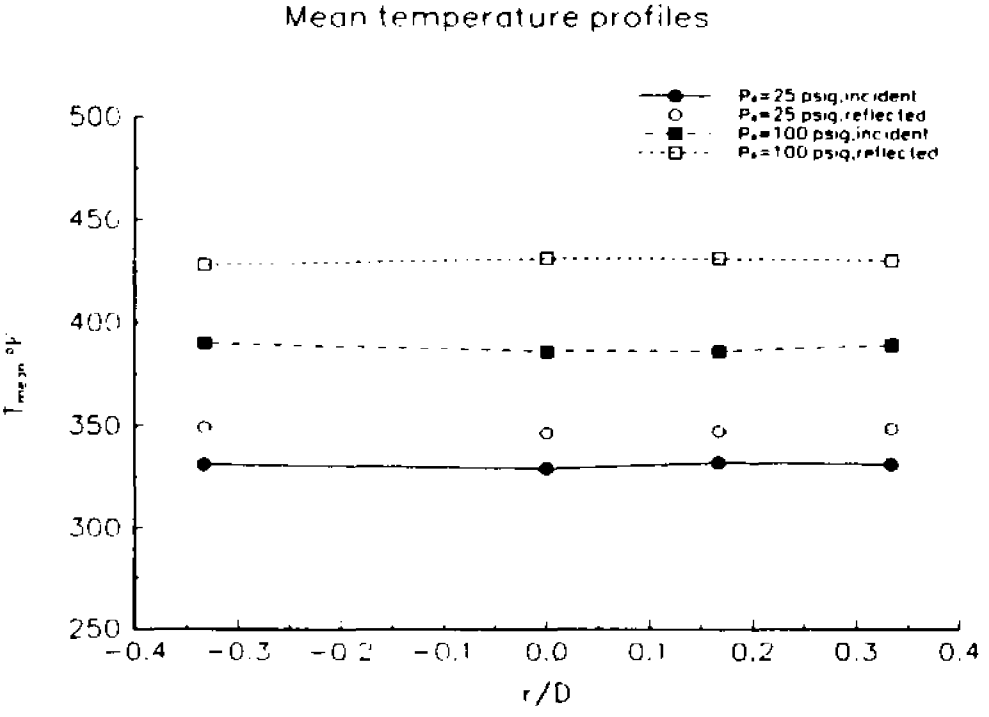

Figure 8.2.6: Mean temperature profiles for various radial positions.

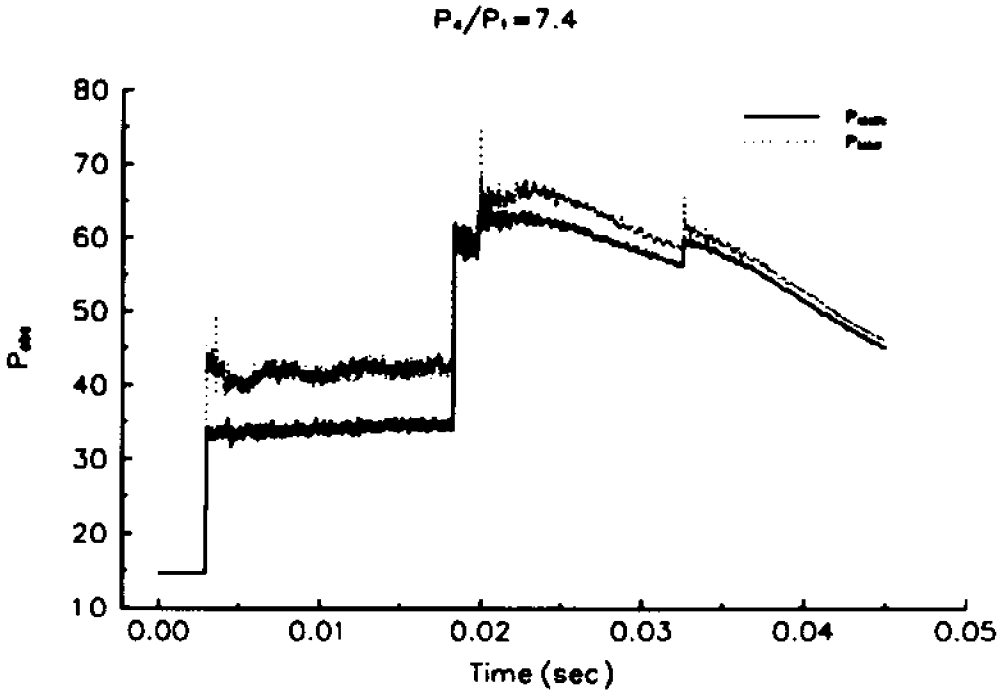

Figure 8.2.7: Time dependent total and static pressure signals at the same x/M.

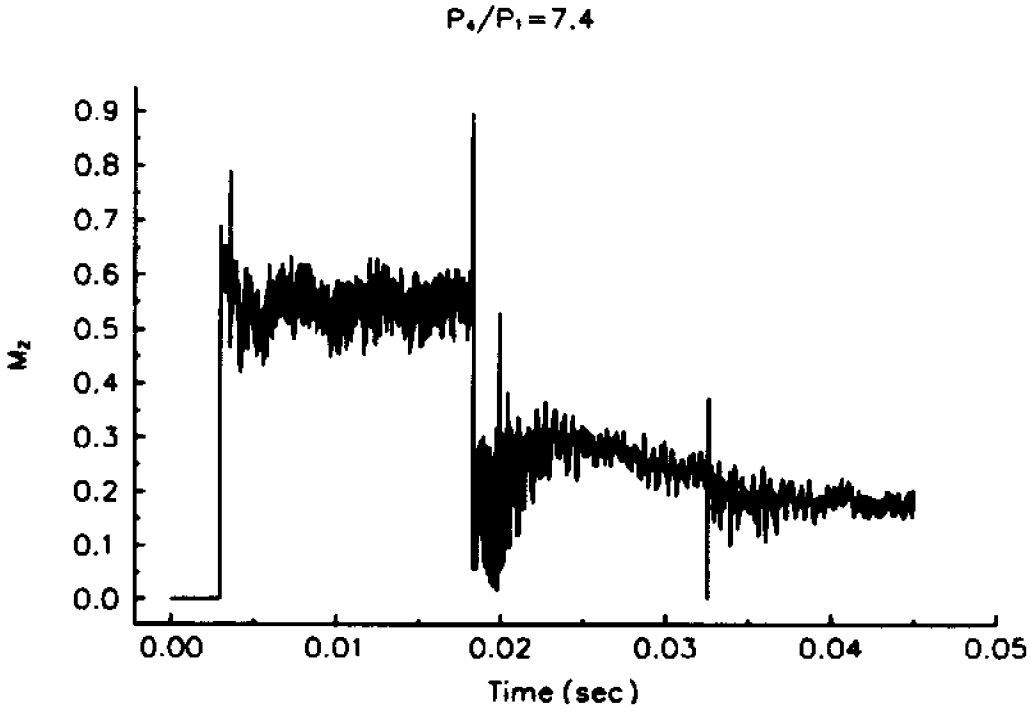

Figure 8.2.8: Time dependent flow Mach number.

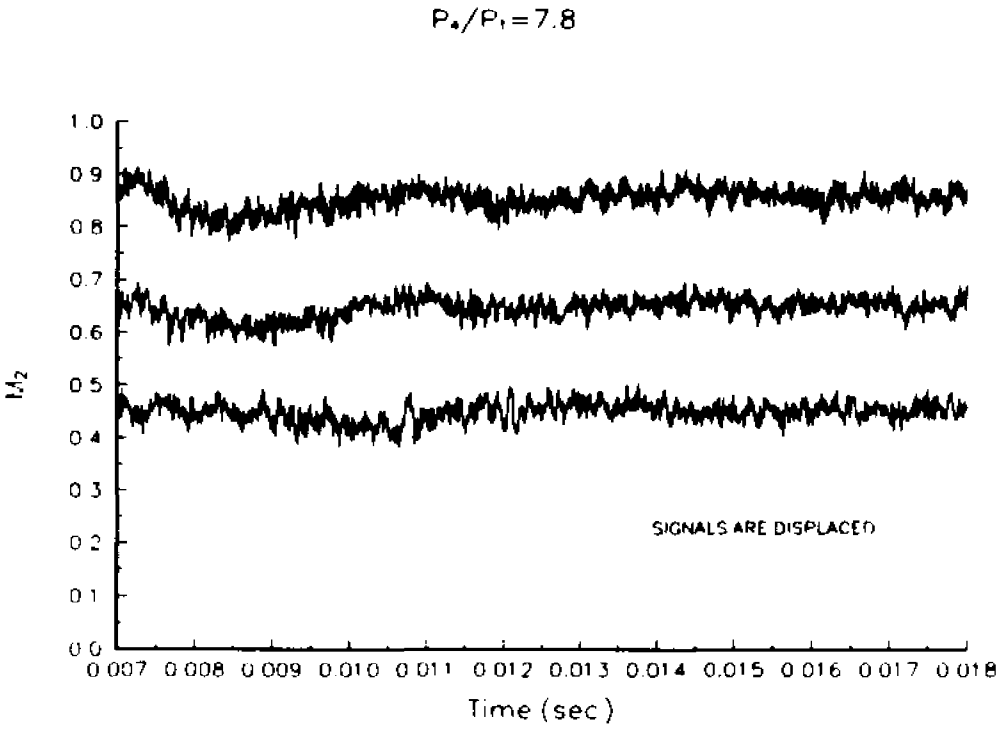

Figure 8.2.9: Time dependent flow Mach number traces for different downstream positions.

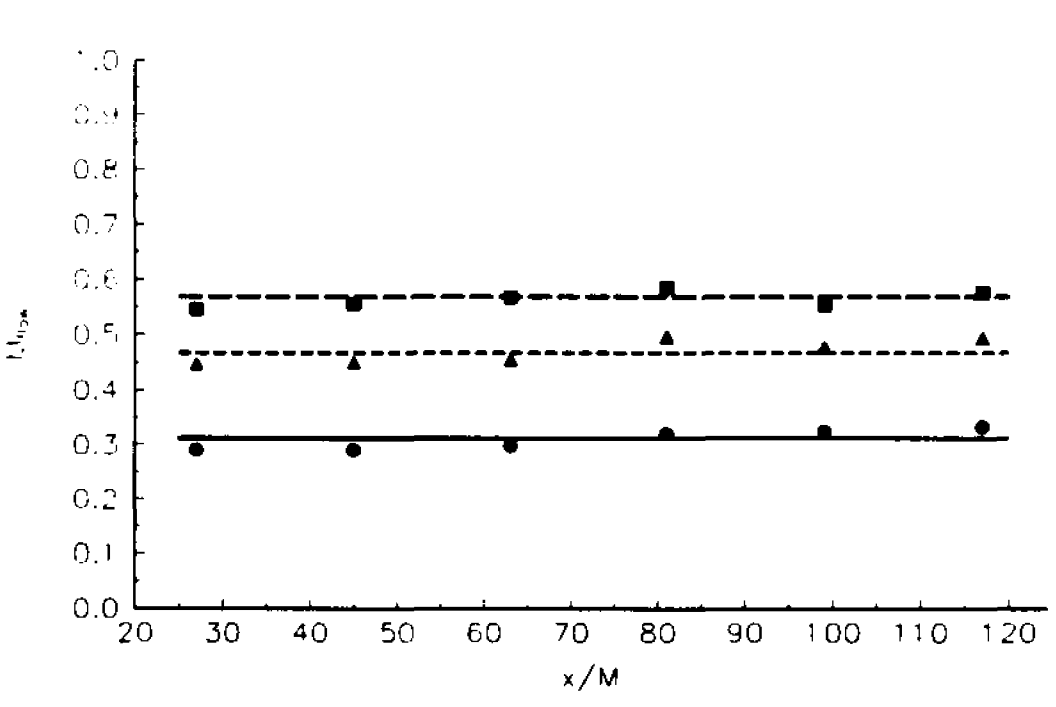

Figure 8.2.10: Mean flow Mach number profiles for different x/M locations.

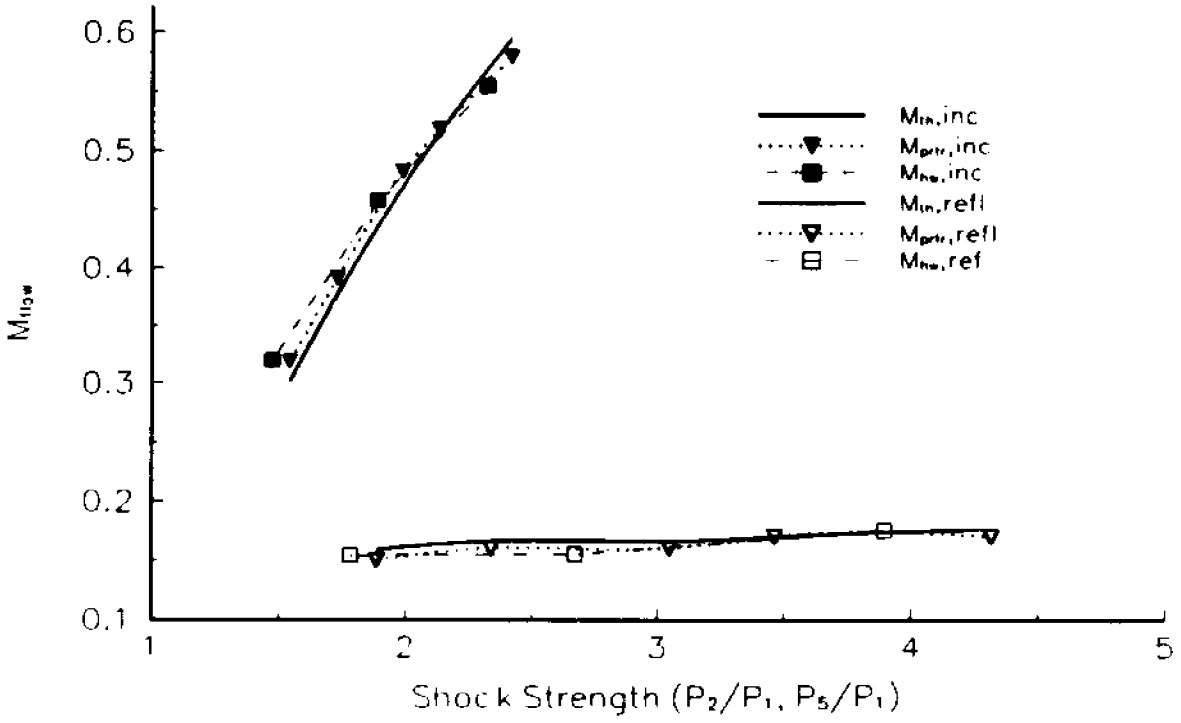

Figure 8.2.11: Comparison of the mean flow Mach numbers using different techniques.

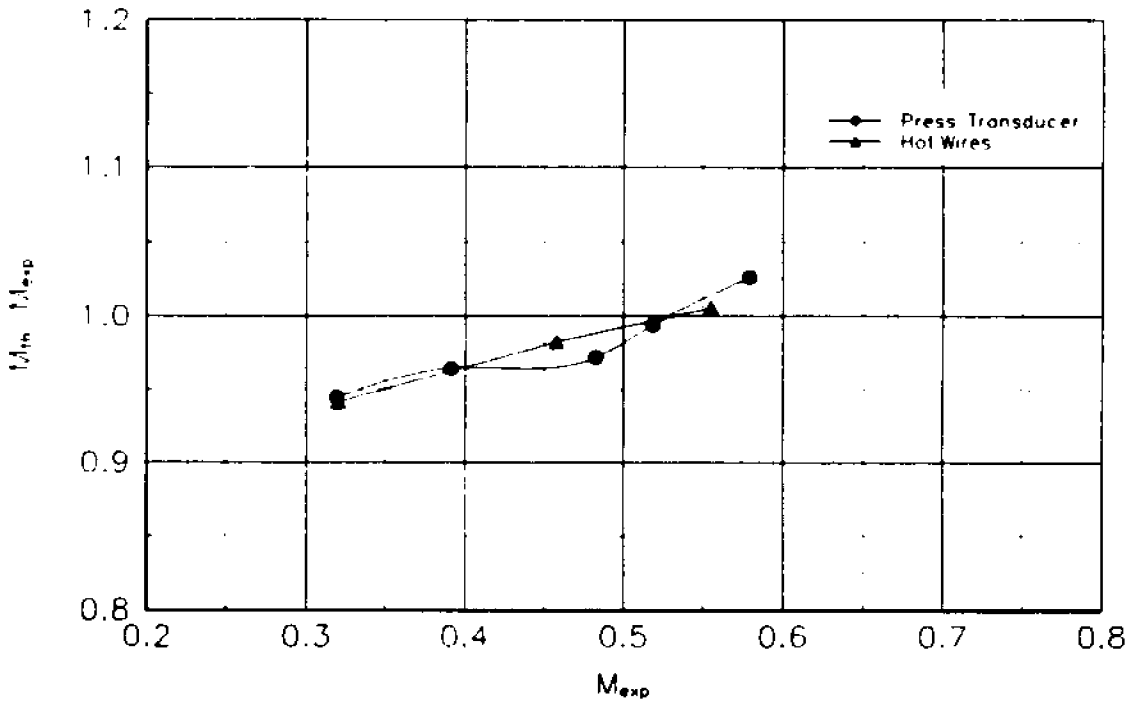

Figure 8.2.12: Deviation of the experimental values from theoretical predictions.

8.3 TIME RESOLVED STATIC PRESSURE EXPERIMENTS

For the experiments presented here, 4 different grids have been used (bulk parameters of these experiments are shown in table XV). All results were obtained with the same pressure and opening rupture characteristics of the aluminum diaphragms.

The characteristics of the travelling shock wave, as well as its interaction with the flow, can be seen on figure 8.3.1. The fluctuations of the grid generated turbulent flow after the incident shock can be easily seen to be amplified after its interaction with the reflected shock. In the same figure, the grid generated shocks as well as the arrival of the expansion fan can be identified, defining the extend of the useful signal for post processing. A slight increase in pressure can be attributed to velocity decrease with time at a given location, which means that the boundary layer growth has increased as the shock wave has well passed that measuring location.

Figures 8.3.2 and 8.3.3 show the effect of grid size, as well as the mean pressure profiles throughout the working section. It can be easily seen that the finer grid (4x4), for the same driver strength produces a lower shock strength than the coarser grid (2x2) does. The same figures show the constant mean pressure profiles throughout the length of the working section. The effect of the grid size is more evident in figure 8.3.4, where for nearly the same shock strength (P_2/P_1) the reflected shock strength (P_5/P_1) was very much affected due to compression of the flow. It is evident that the finer the grid size is, the lower the reflected shock strength (P_5/P_1) would be. The boundary layer displacement thickness is greater in the case of finer grids than in the cases of coarser grids resulting in a slight pressure decrease in

the free stream. Worth noting is also the fact that mean pressures remain constant for either the incident case or the reflected case.

It is very interesting to observe, in the previous figure, that the mean pressure behind the reflected shock is not the same in all experiments with the same incident shock strength (P_2/P_1). It is obvious that there exists a substantial grid dependence of pressure as a result of the strong interaction of the reflected shock wave with the grid generated turbulent field. It appears that the reflected shock strength (P_5/P_1) is attenuated more after the interaction with turbulence generated by finer grids. Thus the pressure jump due to further compression from the reflected shock is less than the value predicted by the inviscid theory. This pressure loss depends on Re_M and seems to be inversely proportional to $(Re_M)^n$ with n equal to 1/8. The dependence of the non dimensionalized pressure loss ($\Delta P/\gamma P M_2^2$) is shown in figure 8.3.5 where M_2 is ranging from 0.3 to 0.7.

The non-dimensional rms pressure values are presented in figure 8.3.6. The rms values are non-dimensionalized with the change in pressure due to compression, P_5-P_2. The effect of higher turbulence due to finer grids are evident. The finer grid produces repeatedly higher rms values due to the higher turbulent flow generated by the grid.

Amplification of pressure fluctuations is not the same for all distances away from the grid. Figure 8.3.7 shows the effect of amplification of pressure fluctuations for three different grids. The 10x10 grid generated higher pressure fluctuations than the other two grids (4x4, 2x2) and thus amplification was higher. From the same picture one can also depict the amplification of pressure fluctuations at relatively large downstream distances. It is interesting to point out that at large non-dimensional distances (non-dimensionalized with the

grid size) x/M=720 the pressure fluctuations are still amplified.

Amplification of pressure fluctuations at various wavenumbers k_n has also been evaluated from the frequency spectra and it is shown in figure 8.3.8. To obtain the wavenumber spectrum of the pressure fluctuations from the available frequency spectra the following dispersion relation was used: $\omega - n\Omega = 0$. This relation is valid under the assumption that vorticity fluctuations are simply advected by the mean flow.

Had the acoustic mode been solely responsible for the pressure fluctuations present in the flow, then the following dispersion relation, for acoustic waves, would have been used: $\omega - n\Omega = \pm ck$ where c is the propagation speed of the acoustic wave (Mc.Kenzie and Westphal, 1968).

Although the entropy and acoustic modes are triggered by the interaction, the vorticity mode remains to be the most dominant and thus the first dispersion relation is valid since the other two modes do not substantially modify the flowfield.

It can be seen, from figure 8.3.8, that the amplification is not the same throughout the whole range of wavenumbers. In fact in the wavenumber range of 1 to 10 there is no considerable amplification after the passage of the shock. A finite decrease in the amplification of the wavenumbers is evident from figure 8.3.8 as the value of $(k_n \cdot M)$ increases. The smaller eddies (small scale structures, high wavenumbers) seem not to be considerably amplified. The large eddies are substantially amplified. The last two statements suggest that the compression effects of the shock wave on the scales are not felt uniformly in the resolved range of scales.

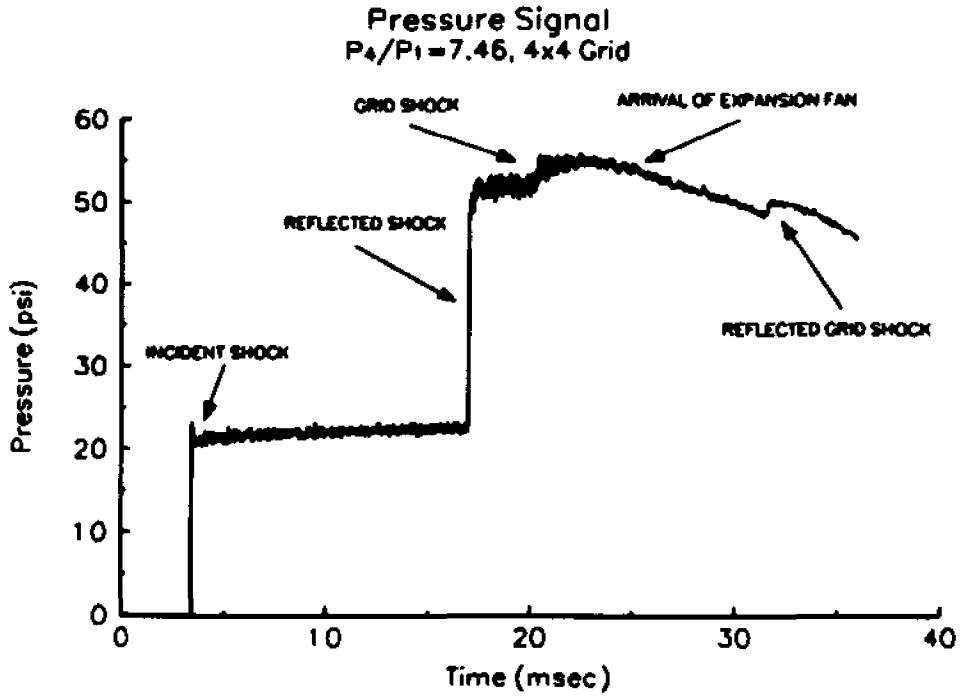

Figure 8.3.1: Typical time resolved pressure signal.

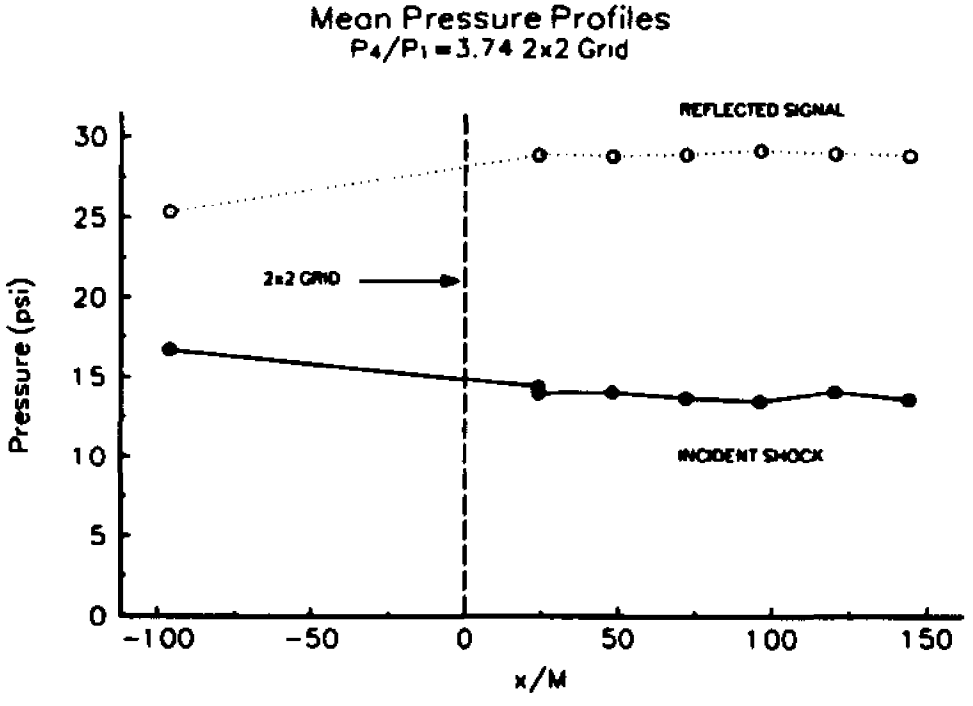

Figure 8.3.2: Mean pressure profiles for 2x2 grid.

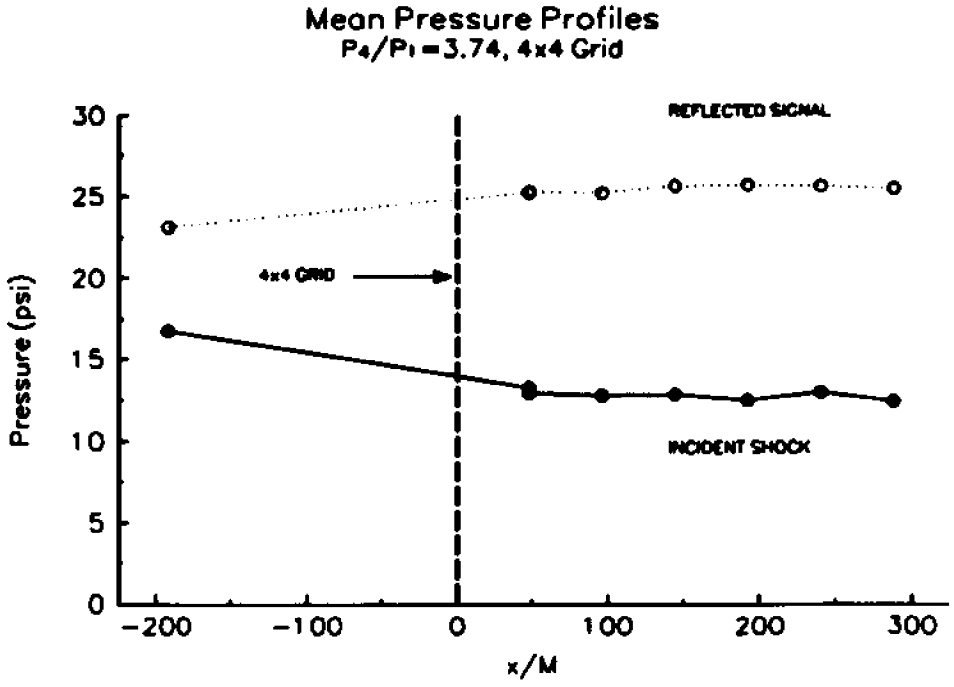

Figure 8.3.3: Mean pressure profiles for 4x4 grid.

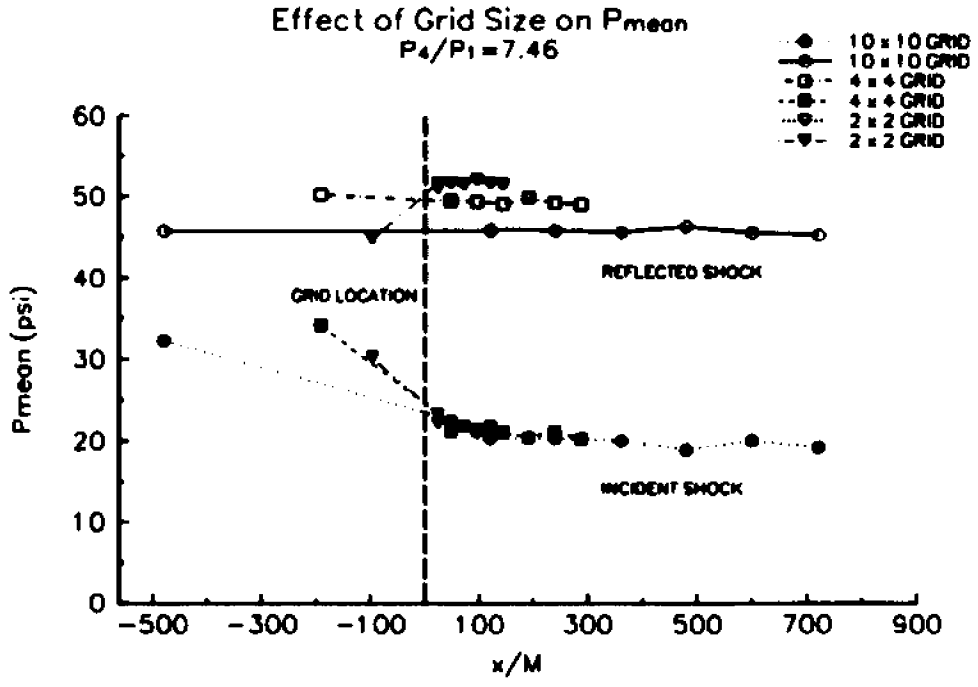

Figure 8.3.4: Mean pressure profiles for various grids.

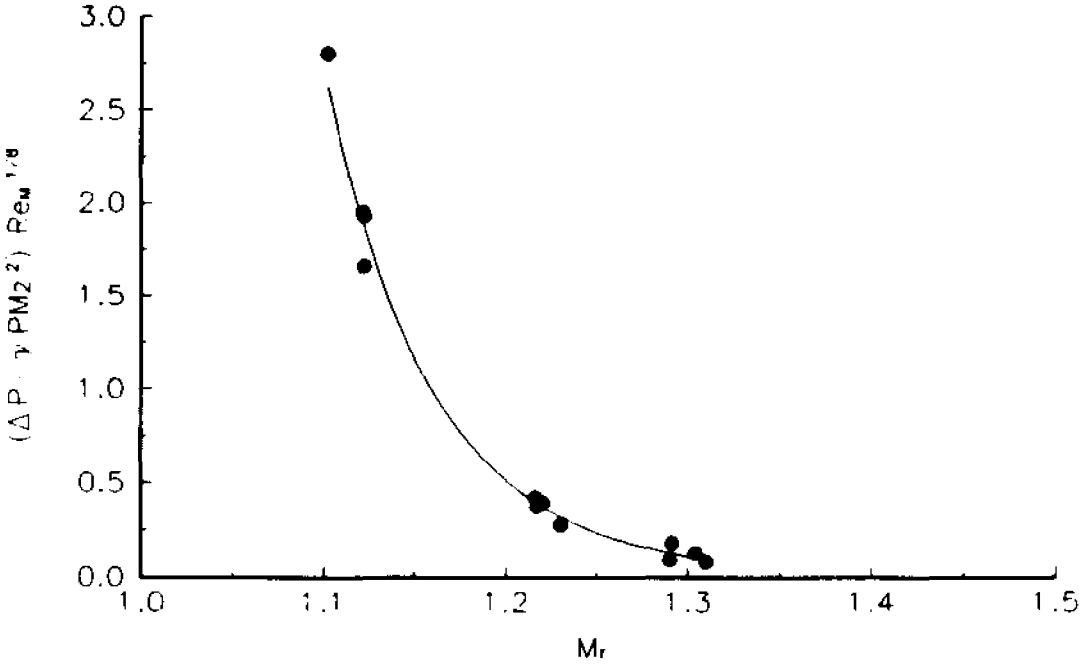

Figure 8.3.5: Shock attenuation vs M_r

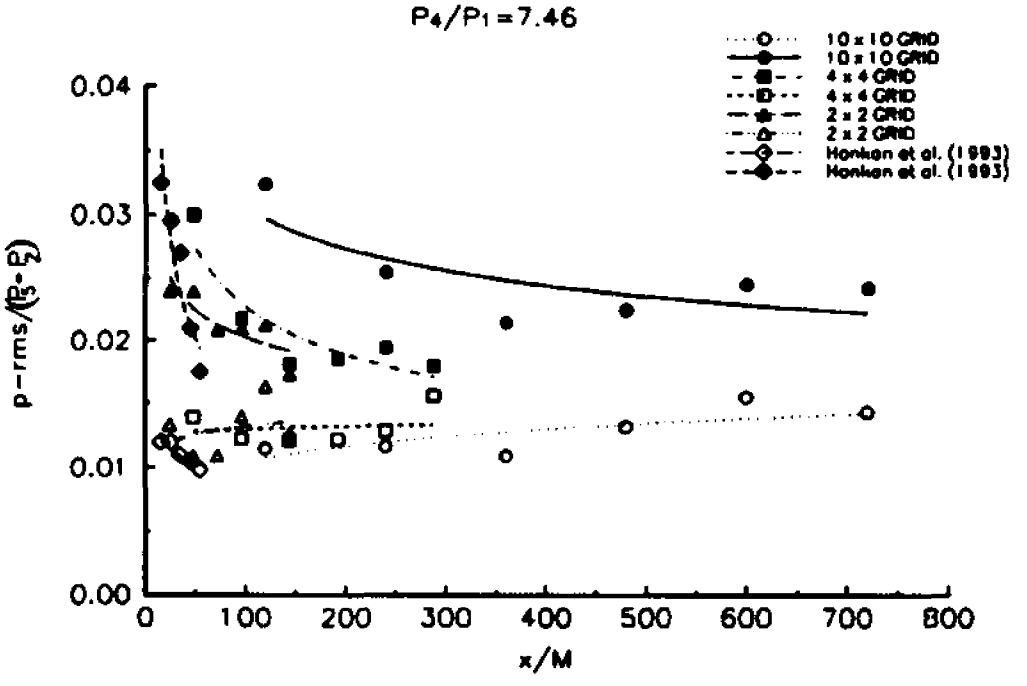

Figure 8.3.6: Pressure R.M.S. for various grids.

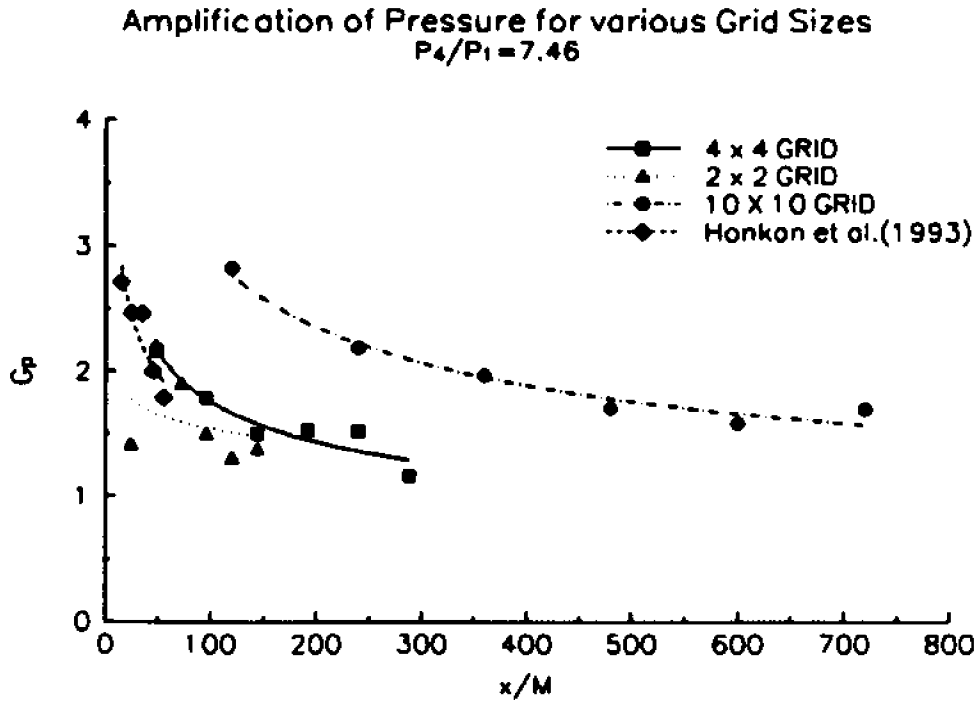

Figure 8.3.7: Amplification for various grids.

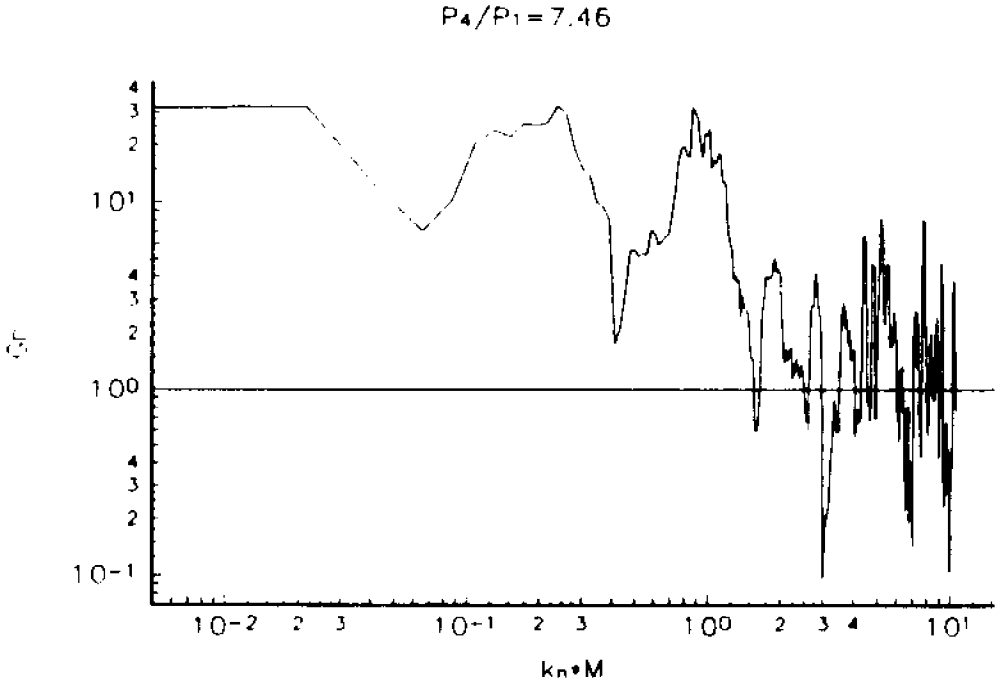

Figure 8.3.8: Amplification of pressure fluctuations vs wavenumber.

Grid	W_s	W_r	P_2 (psi)	P_5 (psi)	T_2 (°K)	T_5 (°K)
2x2	406	295.9	6.3	9.3	327	345
2x2	467.7	274.3	14	29	360.5	430
2x2	520.5	272.8	22	51	391.7	509.5
2x2	563.88	272.8	27	71.5	410.6	560.5
4x4	406	298.5	6.2	9.4	327	345
4x4	461.35	285.9	12.9	25.6	356	417
4x4	515.2	278.1	21	49	388	498.3
4x4	554.6	279.6	25.5	67	405	545.5
8x8	409.3	288.3	7.2	11.2	331	355
8x8	461.35	281.94	13.5	27	358	423.5
8x8	507.5	274.3	20.5	47.5	386	494
8x8	534.2	287.5	25	65	403	542
10x10	401.2	267.1	7	11.5	330.5	355
10x10	461.35	280.4	13.5	27.3	358	423.8
10x10	507.5	274.3	20	45.5	384	489
10x10	534.2	276.6	22.5	52.5	394	513

Table XV: Table of Pressure Experiments conducted at different grid sizes.

8.4 DECAY OF ISOTROPIC TURBULENCE

A fundamental understanding of compressible turbulence in the absence of shock wave interactions is necessary for the development of supersonic transport aircraft, combustion processes, as well as high speed rotor flows. Compressibility effects on turbulence are significant when the energy associated with dilatational fluctuations is large or when the mean flow is compressed or expanded. The present experimental work is a fundamental study of compressibility effects in grid generated turbulence for flows with Mach numbers ranging from 0.3 to 0.6. The measurements were carried out inside the induced flow behind a travelling shock wave in a shock tube facility. It should be mentioned that this section does not consider the interaction of the flow with the shock wave going through a turbulence generating grid which causes sudden compression of the flowfield. The bulk parameters of all tested flowfields are present in Table X.

The flow isotropy was verified directly and indirectly. Direct verification provided by computing the anisotropy tensor b_{ij}.

$$b_{ij} = \frac{\overline{u_i u_j}}{\overline{u_i u_i}} - \frac{1}{3}\delta_{ij}$$

where u_i is velocity fluctuations and δ_{ij} is the Kronecker delta.

The present data suggest a rather low degree of anisotropy which although not perfect is within well established margins. For comparison it should be mentioned that for boundary layers and close to the wall b_{11}=0.45 and b_{12}=0.15. Indirect evidence of isotropy was provided by considering the skewness of velocity fluctuations and the skewness of velocity derivative

(Tavoularis et al., 1978, Tavoularis and Corrsin, 1981(a), 1981(b), Mohamed and LaRue, 1990). The anisotropy tensor b_{ij}, shown in figure 8.4.1, established the isotropic nature of the flow. Anisotropy of the present flowfield is compared with one of the latest and most complete studies in this matter offered by Tsinober et al (1992) in incompressible flows.

Figure 8.4.2 presents the skewness of velocity fluctuations for three mean flow Mach numbers. It appears that S_u remains constant and close to zero for all measured downstream locations. The skewness of velocity derivative has been found experimentally to depend on the turbulent Reynolds number, Re_λ. Tavoularis et al., (1978) presented a comprehensive study of values of the skewness of velocity derivative for a variety of flowfields and Re_λ. From this study, if one considers the data obtained from isotropic grid turbulence, it can be observed that $S_{\partial u/\partial x}$ decreases for $Re_\lambda>5$. Typical values for $S_{\partial u/\partial x}$ are shown for three different flow cases in figure 8.4.3 together with values obtained from various turbulent flowfields. The values obtained are lower than the $S_{\partial u/\partial x}$ value at $Re_\lambda \approx 5$ and between 0.2 and 0.4. Determination and calculation of the skenwess of velocity derivative is given in Appendix G at the end of this work.

The typical decaying, with x/M, of the turbulent kinetic energy data was fitted with the power law $\frac{\overline{u^2}}{\overline{U^2}} = A\left[\frac{x}{M} - \left(\frac{x}{M}\right)_0\right]^{-n}$. In this fitting the decay coefficient A, the virtual origin $(x/M)_0$, and the decay exponent n were determined so that the residual deviation from the original data was minimized. The present work documents the effects of the mesh size/mesh Reynolds number as well as the flow Mach number on the above mentioned variables. The

importance of this parameters is evident when one studies the following equation:

$$\epsilon = \frac{3}{2} nA \left[\frac{x}{M} - \left(\frac{x}{M} \right)_0 \right]^{(-n-1)} \left[\frac{\overline{U}^3}{M} \right]$$

The dissipation rate ϵ can be computed once the coefficients of the power law are known. This provides an alternate method of calculating ϵ. Several expressions for calculating ϵ are given in Appendix E.

Figure 8.4.4 demonstrates the power law decay behavior of all the measured data as it is described by $M_t^2 = B \left[\frac{x}{M} - \left(\frac{x}{M} \right)_0 \right]^{-n}$ where B is the decay coefficient of the Mach number fluctuations, $(x/M)_0$ is the virtual origin and n is the decay coefficient. The results of six experiments are plotted in logarithmic scales in this figure. They include 3 different grids at three different pressures/mean flow Mach numbers. Several conclusions can be drawn from the data. First the exponent n and the constant B depend on the grid, Mach number or Re_M and second that the region where isotropy starts, depends more on the grid than on the flow Mach number or Re_M.

The effect of Re_M or M and Mach number on the coefficient A is shown in figure 8.4.5. Reynolds number variation was produced by changing the mesh size under a constant velocity.

For the lowest tested velocity flowfield ($U \approx 120$ m/sec), which corresponds to a mean flow Mach number of 0.30, the decay coefficient A increases in a non-linear fashion with increasing mesh size M as shown in figure 8.4.5. As the Mach number increases, A is substantially decreased from the previous case and furthermore it appears to be independent

of mesh size. The same holds for the highest tested Mach number, where the decay coefficient is further suppressed. It can be concluded that the decay coefficient A decreases when the Mach number increases.

The virtual origin $(x/M)_0$ strongly depends on the mesh size/Re_M. For all cases it was observed that the virtual origin approaches the grid as the mesh size/Re_M increases as shown in figure 8.4.6. The effects of the Mach number can be seen in figure 8.4.7. The virtual origin is mainly affected at the highest Mach number only, while for the medium and low cases remains unaffected. Possible physical explanations for the behavior of the virtual origin can be found in the recent work of Briassulis and Andreopoulos (1996 b). At the highest Mach number and the associated compressibility effects the virtual origin moved further away from the grid. It is interesting to observe, in the same figure, that the above mentioned effect is diminished for the largest mesh size. Namely the virtual origin for the 18mm mesh is the same for all Mach numbers.

The decay exponent n, shown in figure 8.4.8, is substantially affected by the Mach number of the flowfield. It is clear from the above figure that n is decreasing with increasing Mach number. The effect of the mesh size on the decay exponent can also be observed. It behaves similarly to the decay coefficient A. Namely for the lowest Mach number it increases with increasing mesh size/Re_M. That means that for finer grids, small mesh size, there exists larger dissipation rates. At a first glance the above statement appears to contradict previous views based on fixed n fitting of the data, but if we consider the equation providing the alternate method of calculating ϵ, then the dissipation rate ϵ is inversely proportional to a constant $\{nA(x/M-(x/M)_0)\}^{(n+1)}$. Thus ϵ will increase if n decreases.

When the Mach number increases the opposite trend can be seen. The decay exponent is decreasing with increasing mesh size for the medium shock strength and it remains more or less constant for the highest shock strength at $n \approx 0.3$.

A typical decay of velocity fluctuations, as fitted by the power law, for a 5.08 mm mesh size is shown in figure 8.4.9. The velocity fluctuations are higher at higher Mach numbers and Re_M. The effect of higher velocity fluctuations can not simply be attributed to the increase of the mean Mach number and the associated compressibility effects of the flow but also to the increase of Re_M. A 4-fold increase in pressure which corresponds to 100% change in Mach number and Reynolds number results in a 3 fold increase in the Mach number fluctuations M_t, presented later on, throughout the entire flowfield. Most probably this increase in M_t and $(u/U)^2$ can be attributed to both parameters, i.e. M_{flow} and Re_M.

Spectral analysis of the longitudinal velocity field was performed for several experiments and for multiple locations downstream of the turbulence generation grid. A typical power spectrum obtained from such analysis is shown in figure 8.4.10. The Kolmogorov's spectrum law (-5/3) as is frequently called, was verified for the better part of the power spectral curve, thus confirming the resolution and capabilities of the probe measuring scales at the inertial subrange.

Figure 8.4.11 shows the dissipation rate of kinetic energy ϵ for one grid at different flow Mach numbers. It appears that ϵ as well as the kinetic energy increase with increasing Mach number in all investigated subsonic flows. The dissipation rate of kinetic energy was also independently verified by calculating the total energy supply. This was done by integrating the wavenumber spectrum for each signal. Results of this integration are plotted

in this figure as scattered values. The total dissipation of kinetic energy, obtained by integration, was found to be very similar to the ϵ obtained by the power law and thus presenting the proof of the validity of both methods. It remains unclear whether this effect is a Mach number effect or it is due to Reynolds number increase or both.

The dissipation rate of kinetic energy (ϵ) for a coarser grid is shown in figure 8.4.12. It can be seen that ϵ is higher for coarser grids and higher Re_M. A comparison of ϵ obtained from the power law with the ϵ obtained from the integration of the wavenumber spectrum is also shown for six downstream distances from the grid. Once again both methods offer similar values for the dissipation of kinetic energy.

The dissipation rate of kinetic energy ϵ for various mesh sizes is shown in fig. 8.4.13 at the highest tested Mach number flowfield. For the highest Mach number the coarser grid and higher Re_M did not produce higher dissipation rates as was implied from figure 8.4.12. Namely figure 8.4.13 suggests that coarser grids produce lower dissipation rates, ϵ, when compressibility effects are high. In the absence of high compressibility effects, which are typical in the highest tested Mach number flowfields and the reverse influence of the mesh size on ϵ non-dimensionalized by the mean velocity and mesh size is shown in figure 8.4.14. In this figure the lowest tested flowfield of M_{flow}=0.35 is plotted for various mesh sizes. The reverse trend is observed for $\epsilon M/U^3$ in the absence of strong compressibility effects. Since the mean flowfield velocity U is equal for all plotted cases the effect presented in this figure is mainly due to the Mesh size M and Re_M. In this case the coarser grid with the largest mesh size and highest Re_M shows the largest non dimensionalized dissipation rate of kinetic energy. For even higher Re_M and mean Mach number flowfields, presented in figure 8.4.15, the effect

of compressibility is rather striking where, once more, the opposite trend of the dependence of $\epsilon M/U^3$ to the mesh size is shown. For the medium tested Mach number flowfield case the effect of the grid's mesh size becomes obvious when figure 8.4.16 is studied. For this case the mean Mach number was constant and only the mesh size was changing. It can be summarized from this figure that the coarser grids with the greater mesh sizes and highest Re_M flowfield produce a lower dissipation rate ϵ. The dissipation rate of kinetic energy for the medium tested Mach number follows the trend that exists for the highest tested Mach number and therefore suggest that the presence of compressibility effects are felt in this flowfield too. The difference and the influence of the compressibility effects for both flowfields can be estimated upon closer investigation of figures 8.4.13 and 8.4.16. For almost a 4-fold increase in the mesh size and Re_M the dissipation rate decreased 10 times for M_{flow}=0.6 and approximately 5 times for the M_{flow}=0.475 flowfield. Thus verifying that higher Mach number flowfields introduce higher compressibility effects.

As Mach number increases it has been found that the dissipative length scale increases. A typical result is shown in figure 8.4.17 for the flow at three different Mach numbers and for the same mesh size. It is interesting to observe that for the highest mean flow Mach number the dissipation length scale increased much more than for the medium case. Higher compressibility effects and higher Re_M are the only logical parameters than can cause such a drastic increase. The effect of the grid's mesh size on the dissipation length scale is shown in figure 8.4.18. The dissipation length scale L_ϵ increases with increasing mesh size and Re_M. From this figure it can be seen that for the same mean Mach number a 5-fold increase in L_ϵ occurs for a 3-fold increase in the mesh size/Re_M. The pivotal effect that the grid size exerts

on the length scales in the flowfield should be clear by now. It is apparent from both previous figures that the dissipation length scale strongly depends on x/M.

The effect of Mach number on the Taylor's microscale computed from $\epsilon = 15\nu\overline{\left(\frac{\partial u}{\partial x}\right)^2} = 15\nu\frac{u^2}{\lambda^2}$ is shown in figure 8.4.19 for three different Mach numbers and for the same mesh size. The Taylor's microscale appears to increase with increasing Mach number. Increase of the Taylor's microscale is also observed for the flowfield produced by coarser grids. This is shown in figure 8.4.20 where four different grid sizes at the same Mach number are plotted. It is clear that the coarser the grid, larger mesh size, the greater the Taylor's microscale. The dependance (increase) with increasing x/M is evident, as shown earlier for the dissipation length scale, is also shown for the Taylor's microscale.

As the Mach number increases the Kolmogorov's length scale (η) decreases as it can be seen in figure 8.4.21 for M=5.08 mm. This result was expected since the dissipation rate of kinetic energy increases with increasing Mach number. Thus from the definition of $\eta = \left(\frac{\nu^3}{\epsilon}\right)^{\frac{1}{4}}$ the previous result was obtained.

The effect of the different mesh sizes on the viscous scales can be shown for a constant velocity flowfield but with different mesh size turbulence generating grids. Experimental results showed that the Kolmogorov's length scale increases as the mesh size increases. Figure 8.4.22 presents four different mesh sizes for a decaying flowfield at a constant mean Mach number of 0.6. Similar results are obtained for the rest of the tested flowfields.

The last two figures (8.4.21 and 8.4.22) can verify the influence of the compressibility effects on the viscous scales. Since η increases as the mesh size and Re_M increase, then one might expect figure 8.4.22 to show an increase of η when Re_M is increased by increasing the velocity of the flowfield only (mean flow Mach number). The latter trend is shown in figure 8.4.21 to be incorrect and rather high compressibility effects associated with the corresponding flowfields are credited for such behavior of η. Namely for the case of the viscous scales, compressibility effects appear to suppress their size. The above mentioned measurements indicate values of η ranging from 0.015 to 0.06 mm. The size of the probes expressed in terms of Kolmogorov's length scales appears to be $\eta_w=l_w/\eta=13$ for the greatest scales and 52 for the smallest scales. The scales at error start at about half of these values, 7 and 26 respectively. Based on these values, which determine the upper limit of the valid part of the spectrum, estimates of the spectral power density of the spatially filtered scales have been obtained from Wyngaard's (1968) work for subsonic flows. It appears that the spatially filtered scales amount to about 15% of the total spectral density of velocity fluctuations for measurements close to the grid where η is small and less than 4% for measurements where η is larger. The high resolution of the hot wire probes allows us to conclude that the results obtained in regard to the compressibility effects on the viscous scales are not biased. Other measurements obtained with lower resolution (40-50 viscous scales resolution of the Mach probes) high frequency pressure transducers produced inconsistent and biased results especially when the analysis of the viscous scales was sought.

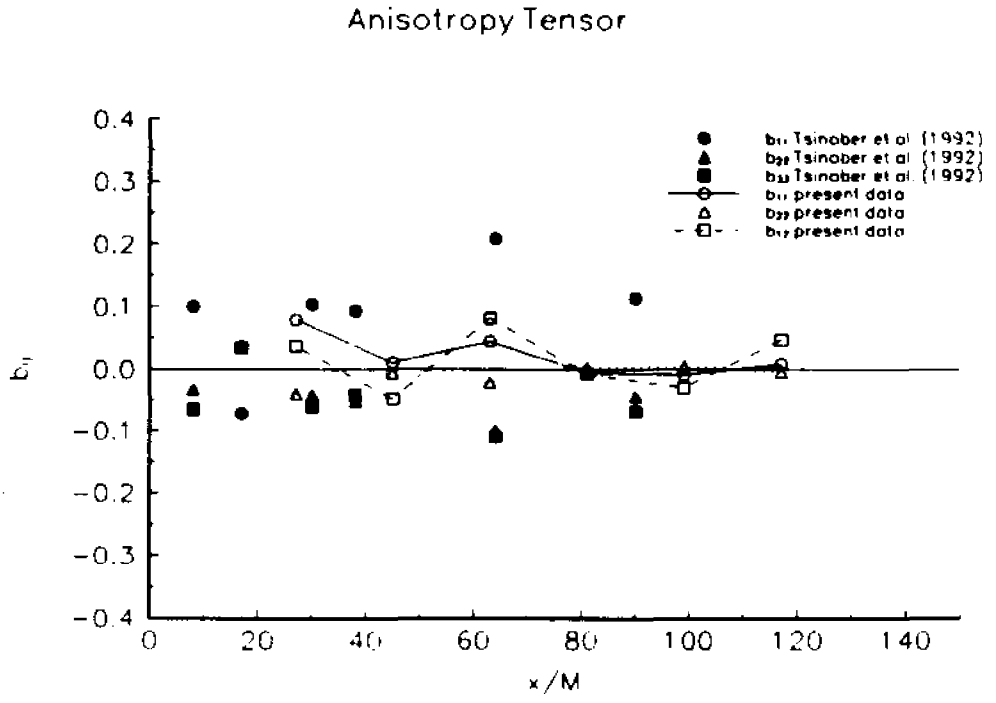

Figure 8.4.1: Anisotropy Tensor b_{ij} vs x/M

M = 5.08 mm

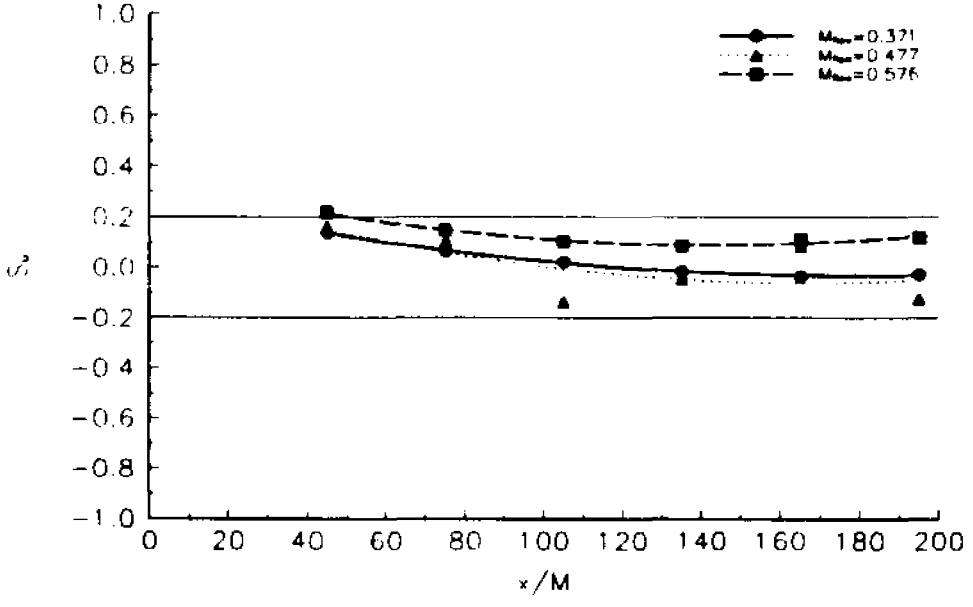

Figure 8.4.2: Skewness of velocity fluctuations for three different flowfields.

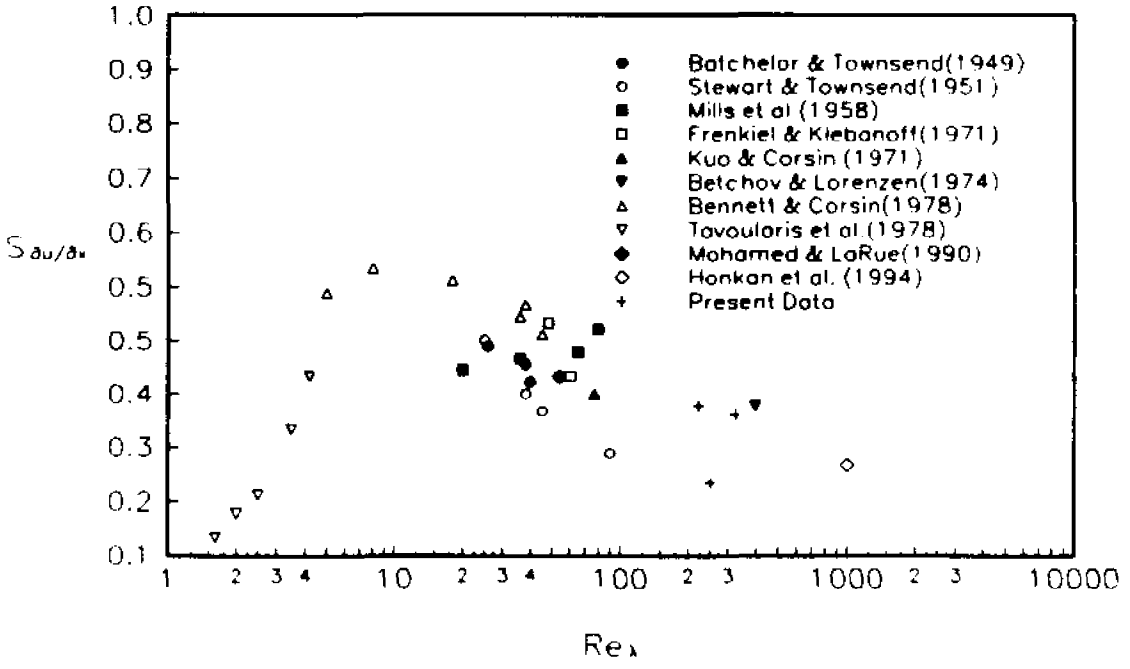

Figure 8.4.3: Skewness of the derivative of velocity fluctuations for different flowfields.

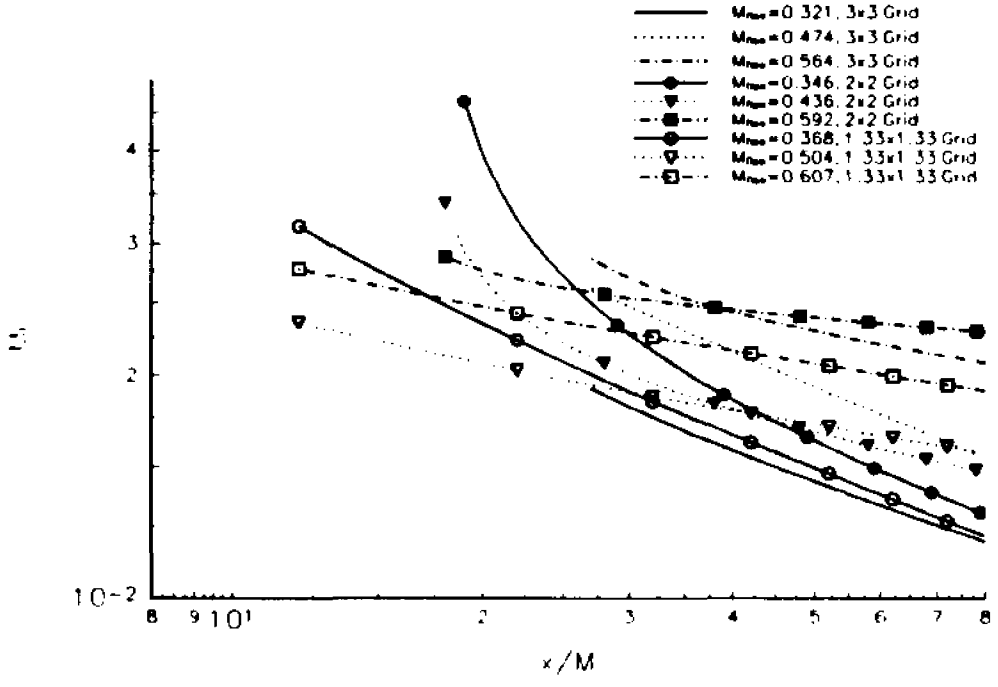

Figure 8.4.4: Mach number fluctuations for various experiments

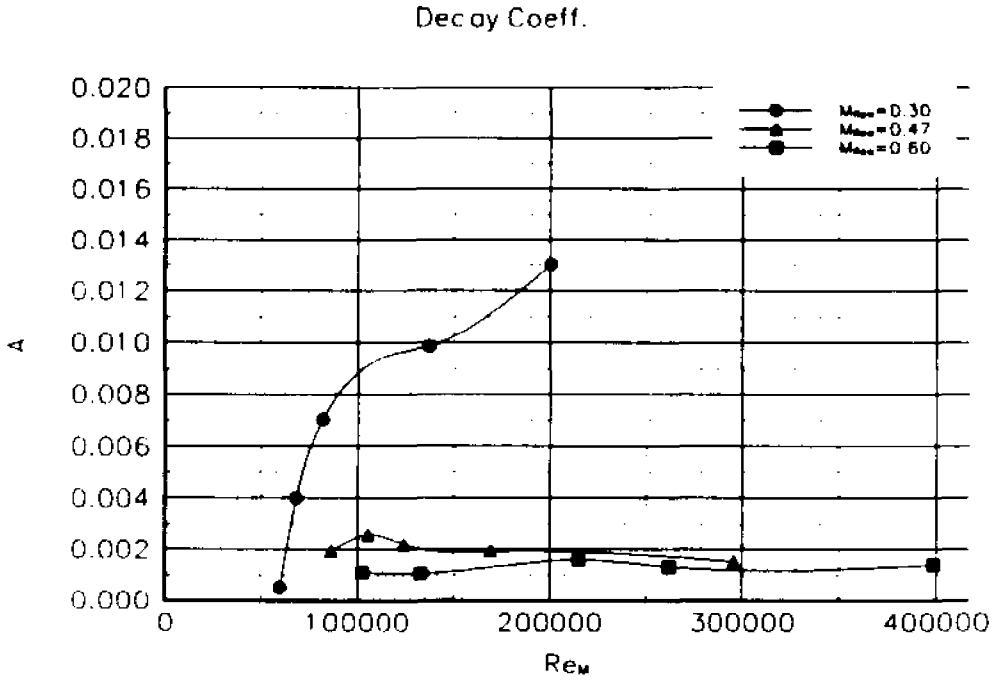

Figure 8.4.5: Decay coefficient A vs Re_M for 3 different Mach numbers

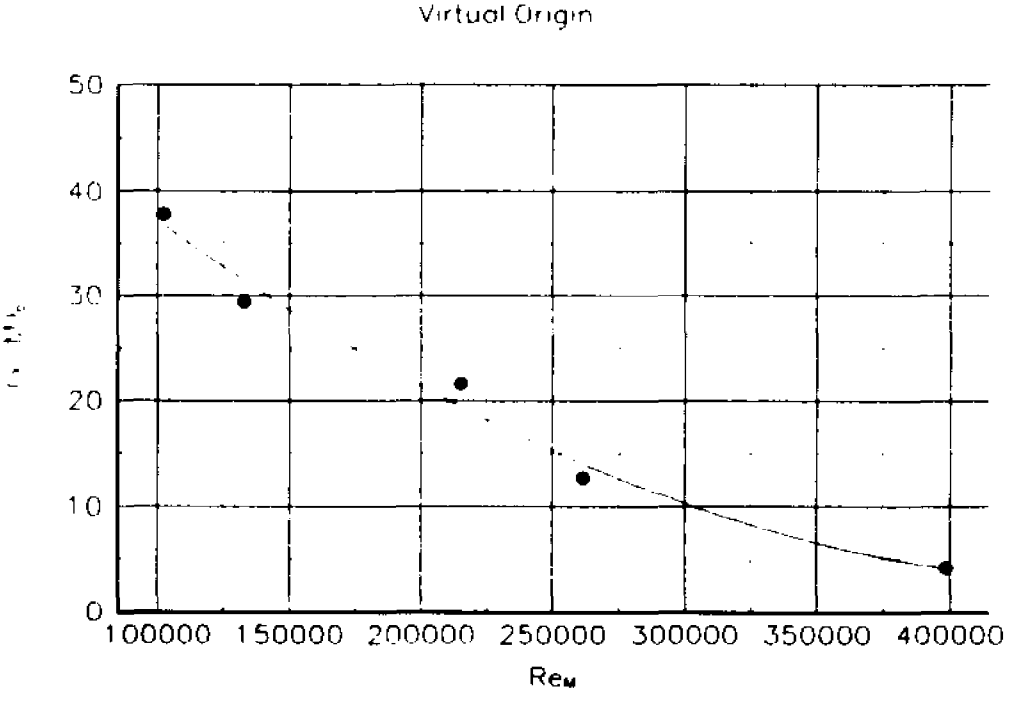

Figure 8.4.6: Virtual origin vs Re_M for M_{flow}=0.6

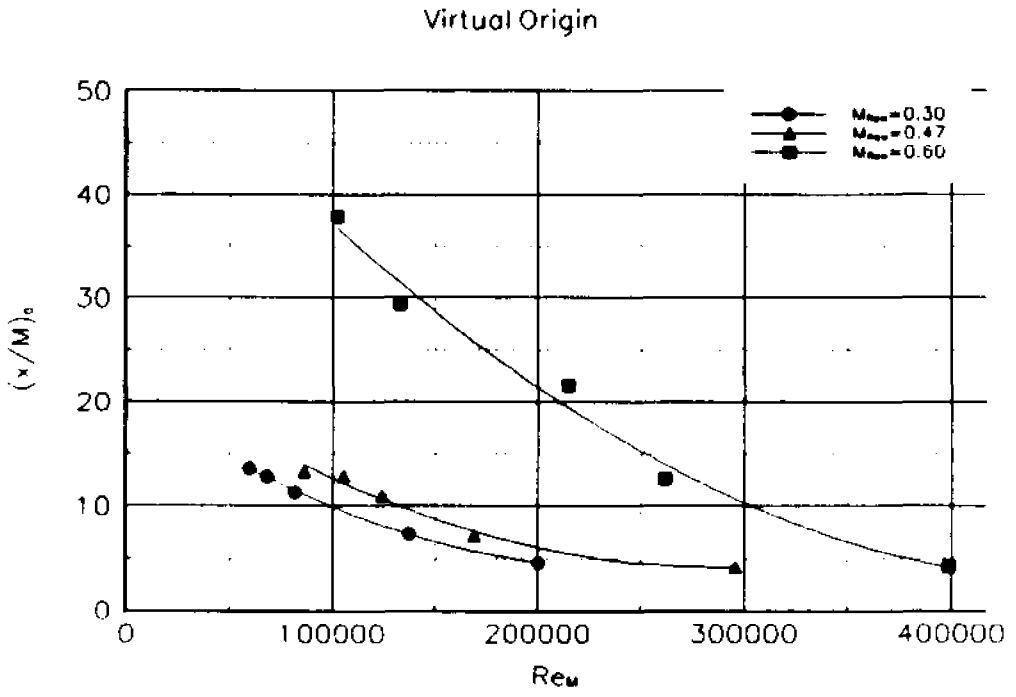

Figure 8.4.7: Virtual origin vs Re_M for 3 different Mach numbers

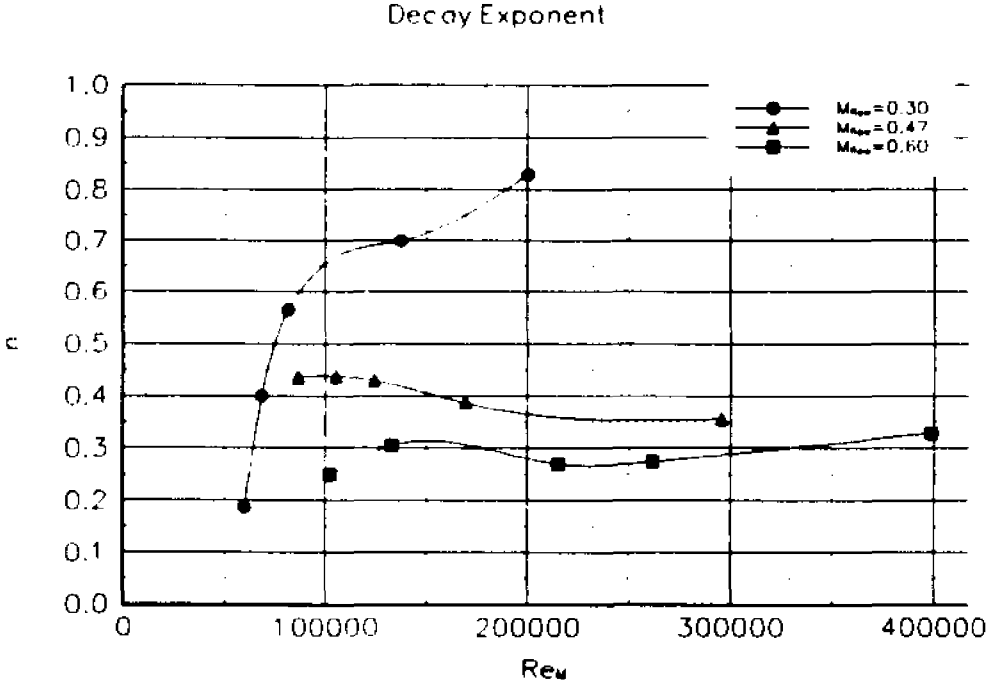

Figure 8.4.8: Decay exponent n vs Re_M for 3 different Mach numbers

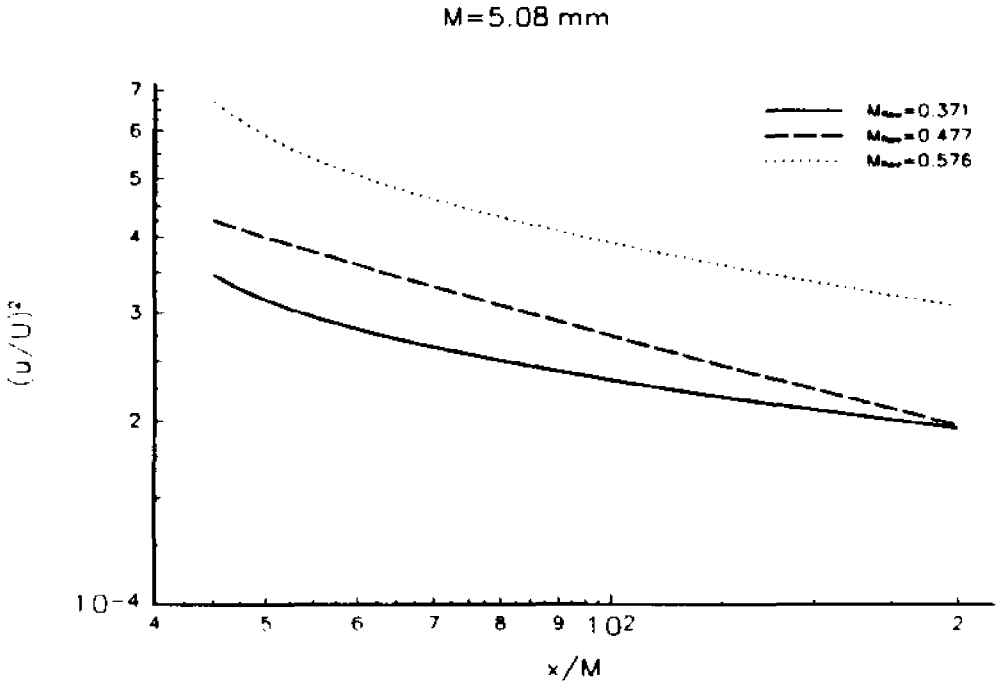

Figure 8.4.9: Decay of velocity fluctuations for various Mach numbers

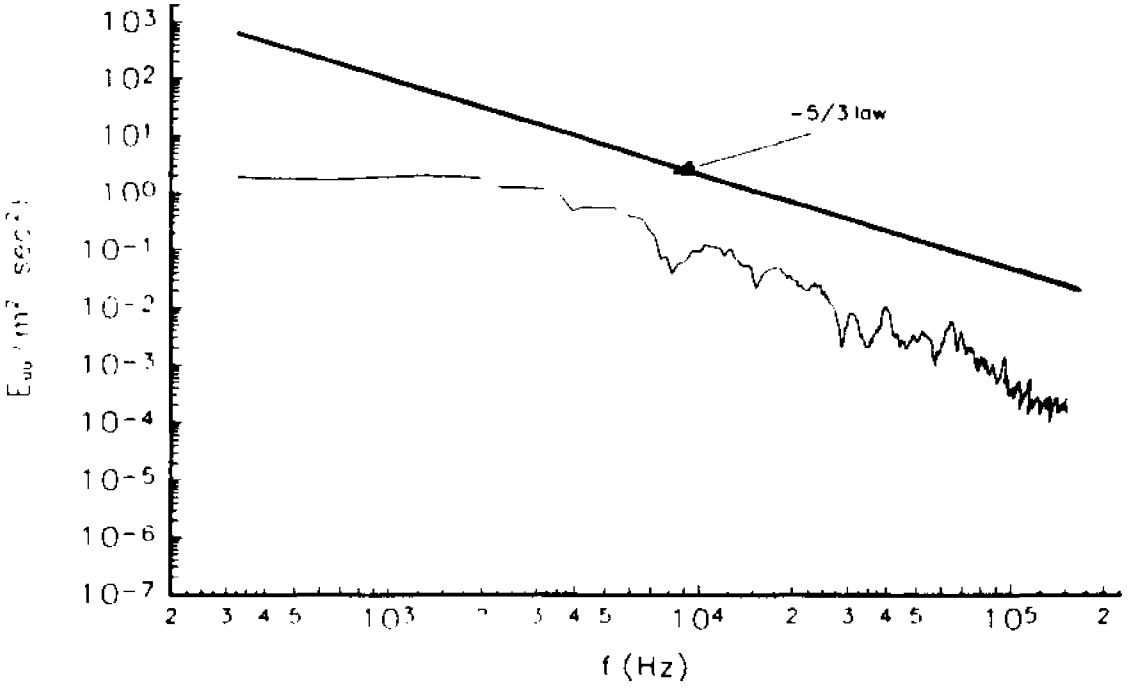

Figure 8.4.10: Typical power spectrum of velocity fluctuations.

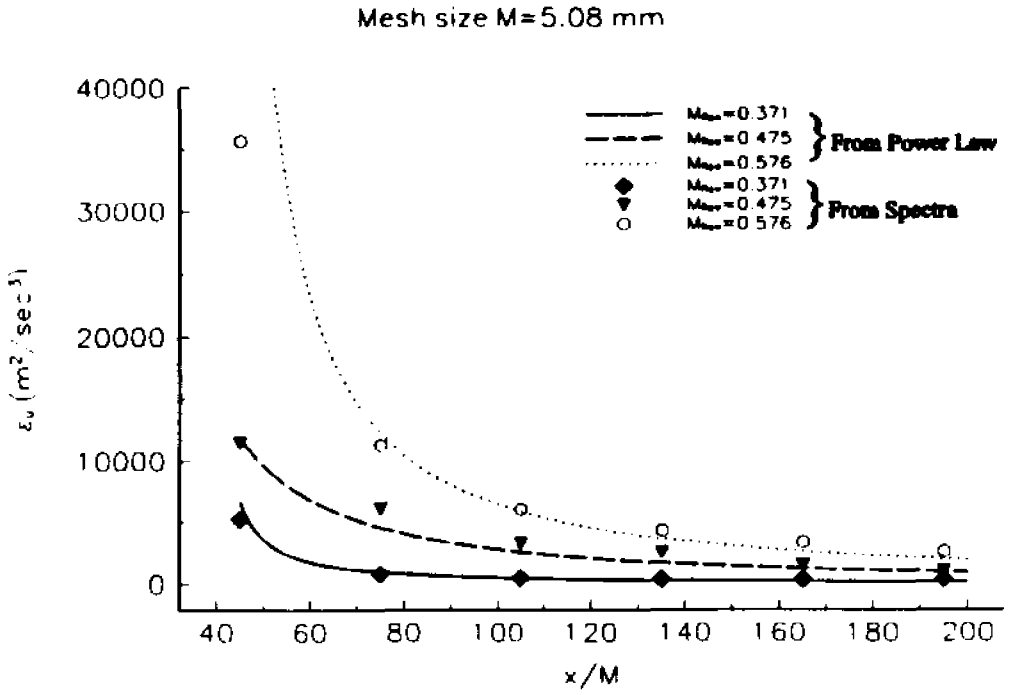

Figure 8.4.11: Dissipation rate of kinetic energy vs x/M for 3 different Mach numbers

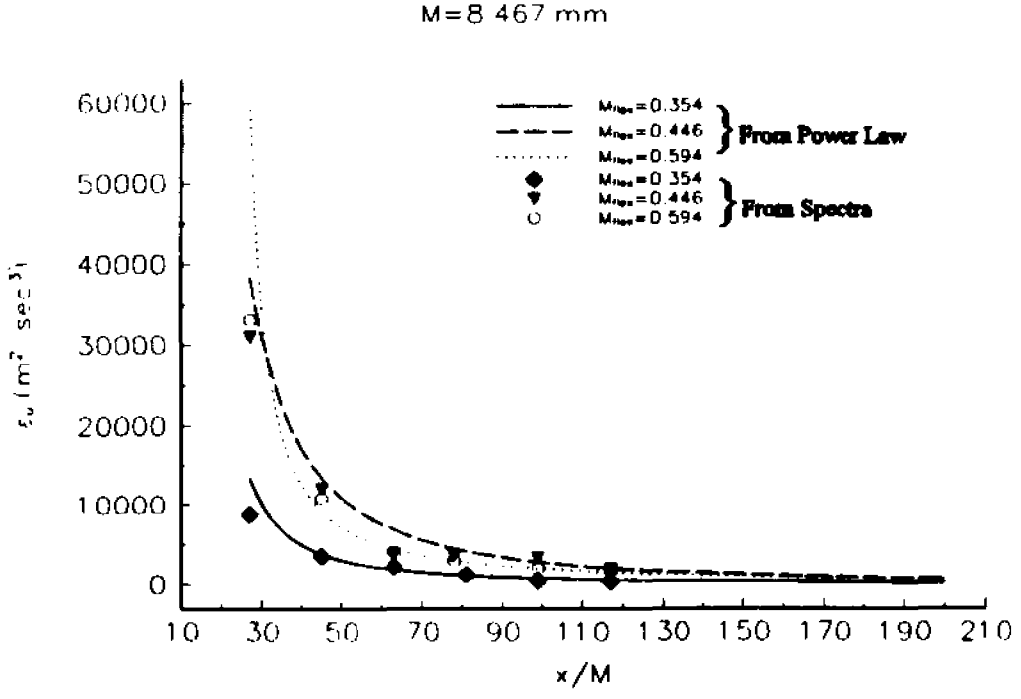

Figure 8.4.12: Dissipation rate of kinetic energy for M=8.47 mm mesh

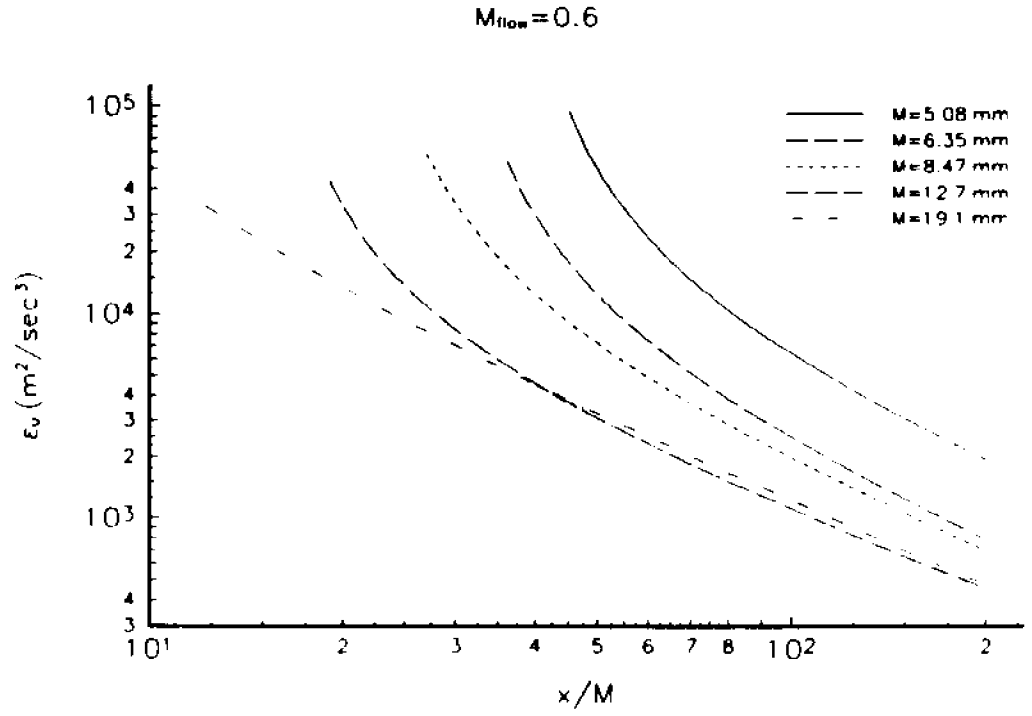

Figure 8.4.13: Dissipation rate of kinetic energy for various mesh sizes.

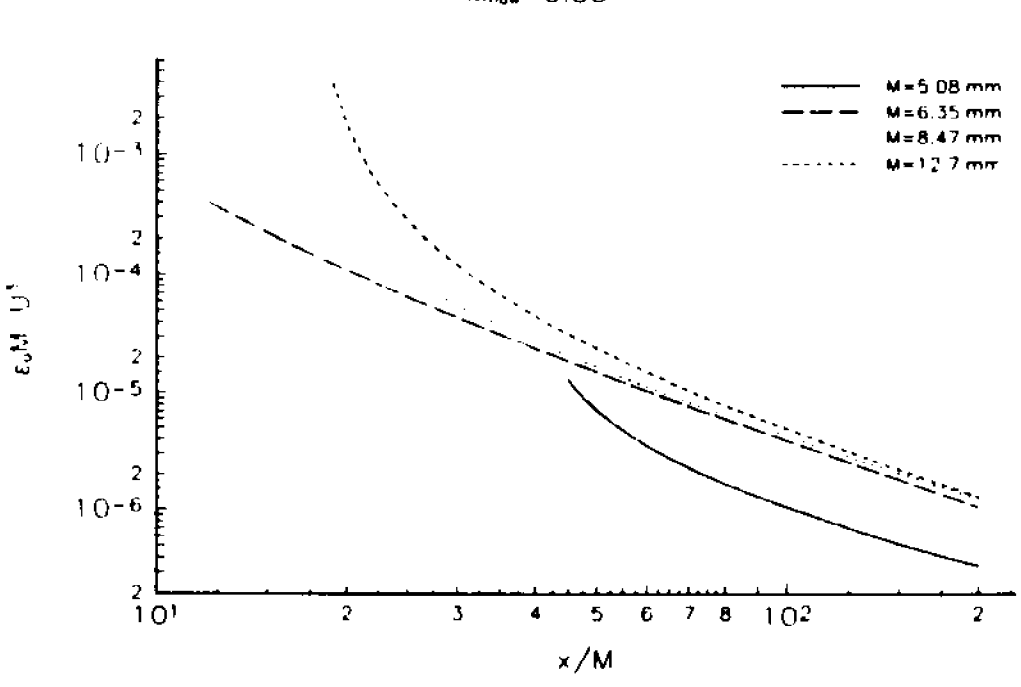

Figure 8.4.14: Non dimensional ϵ for M_{flow}=0.35 and various mesh sizes.

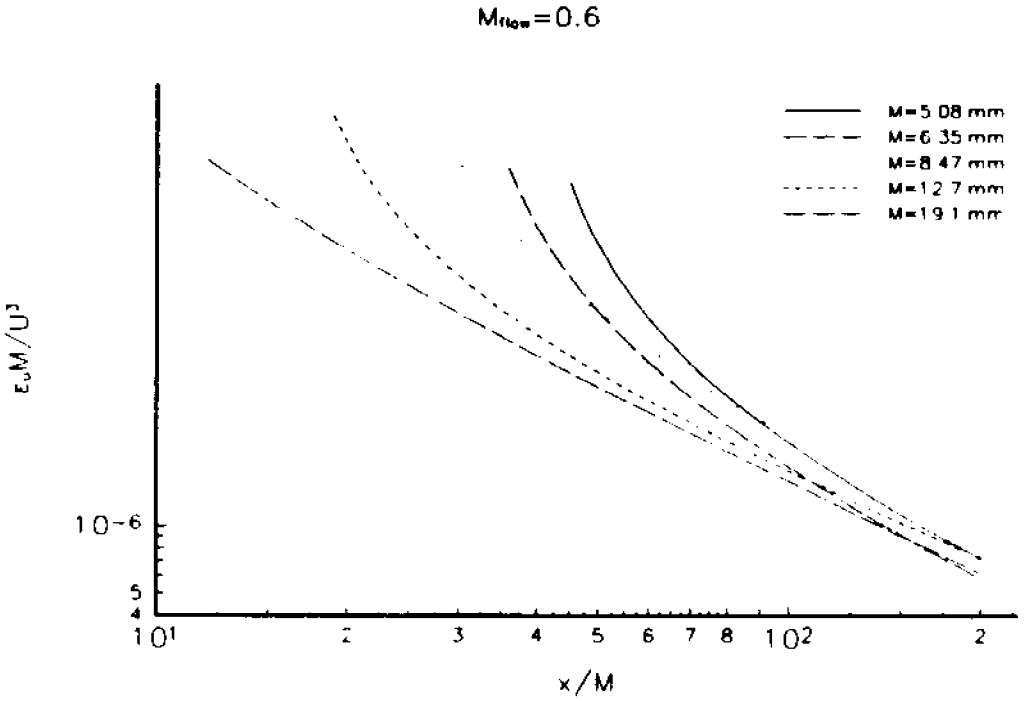

Figure 8.4.15: Non dimensional ϵ for M_{flow}=0.6 and various mesh sizes.

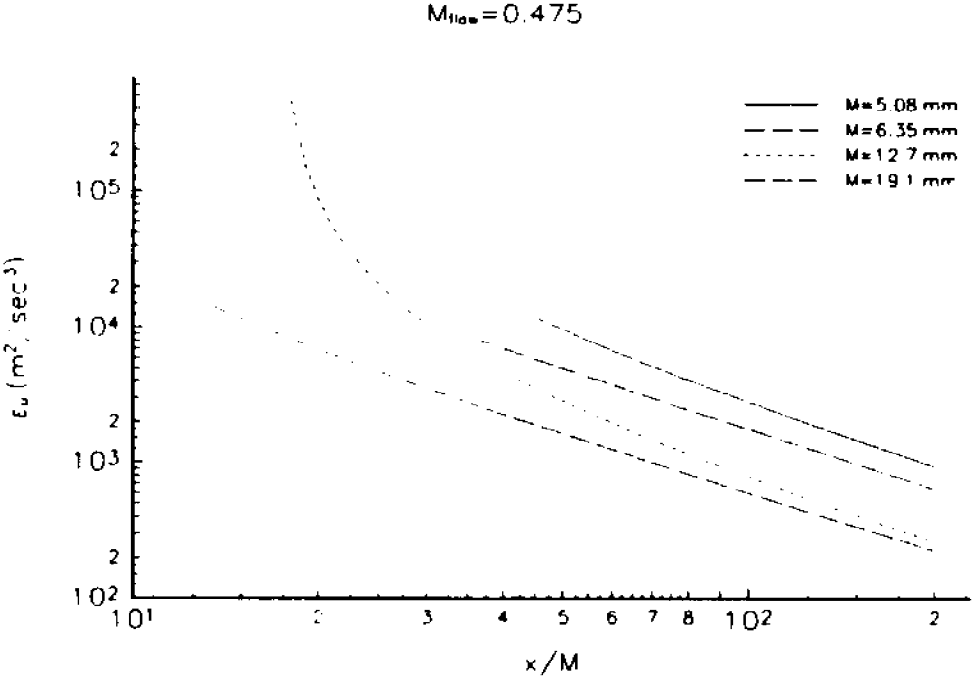

Figure 8.4.16: Dissipation rate of kinetic energy for various mesh sizes at M_{flow}=0.475

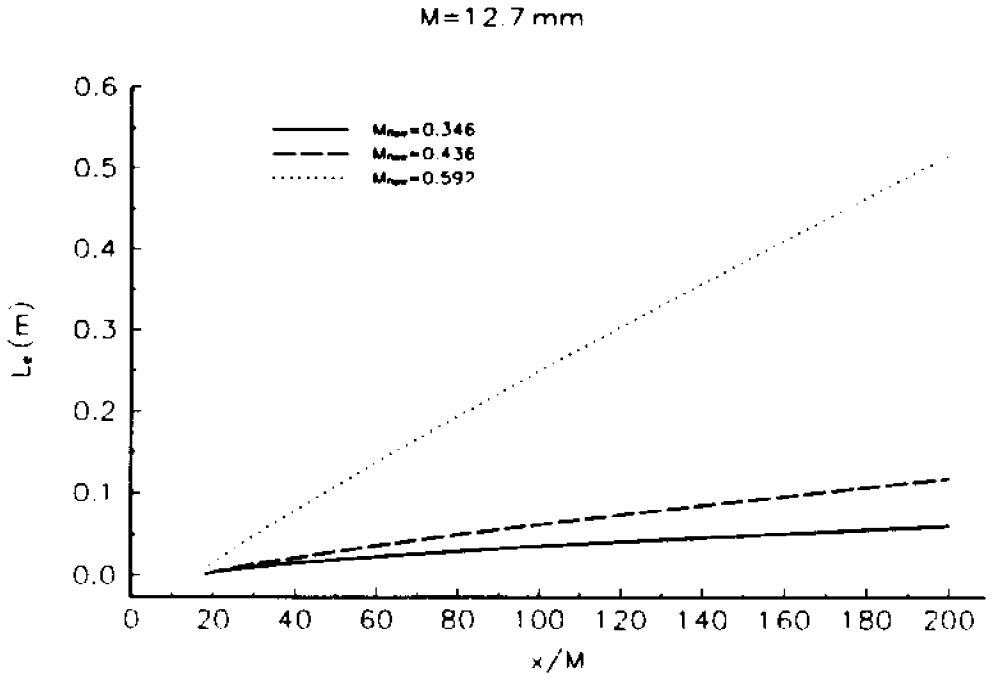

Figure 8.4.17: Dissipative length scale for three mean flow Mach numbers.

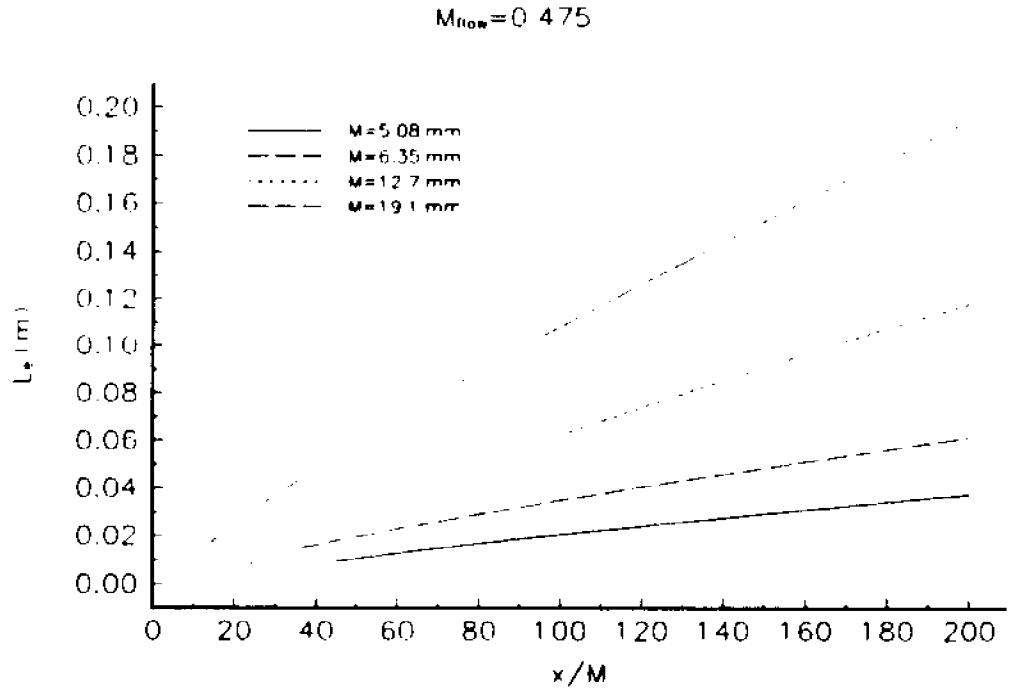

Figure 8.4.18: Dissipative length scale for several mesh sizes.

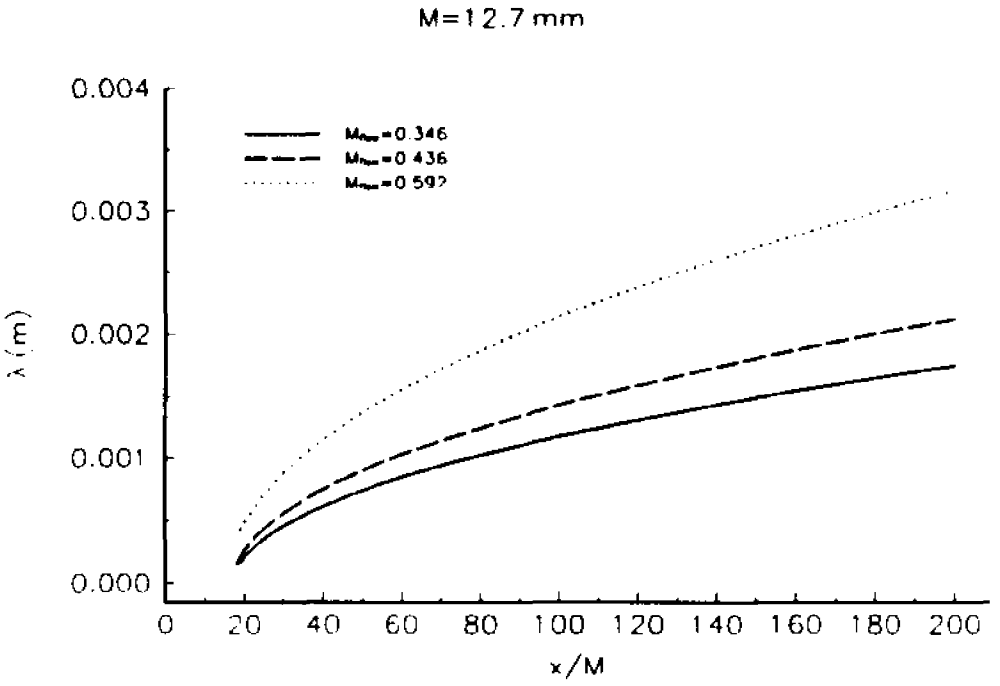

Figure 8.4.19: Taylor's microscale for three mean flow Mach numbers.

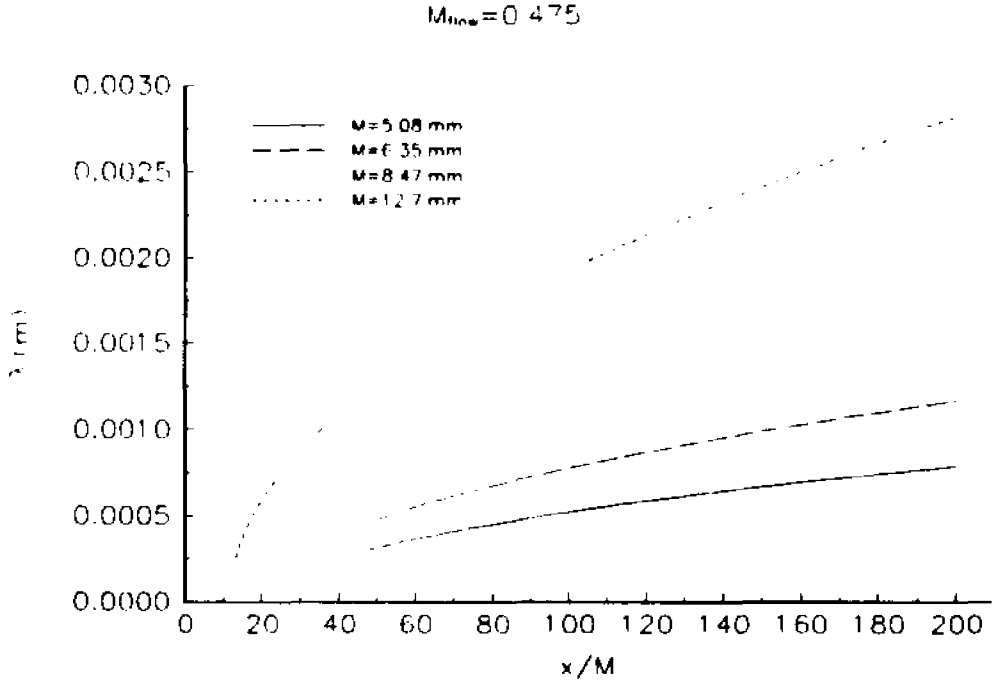

Figure 8.4.20: Taylor's microscale for several mesh sizes.

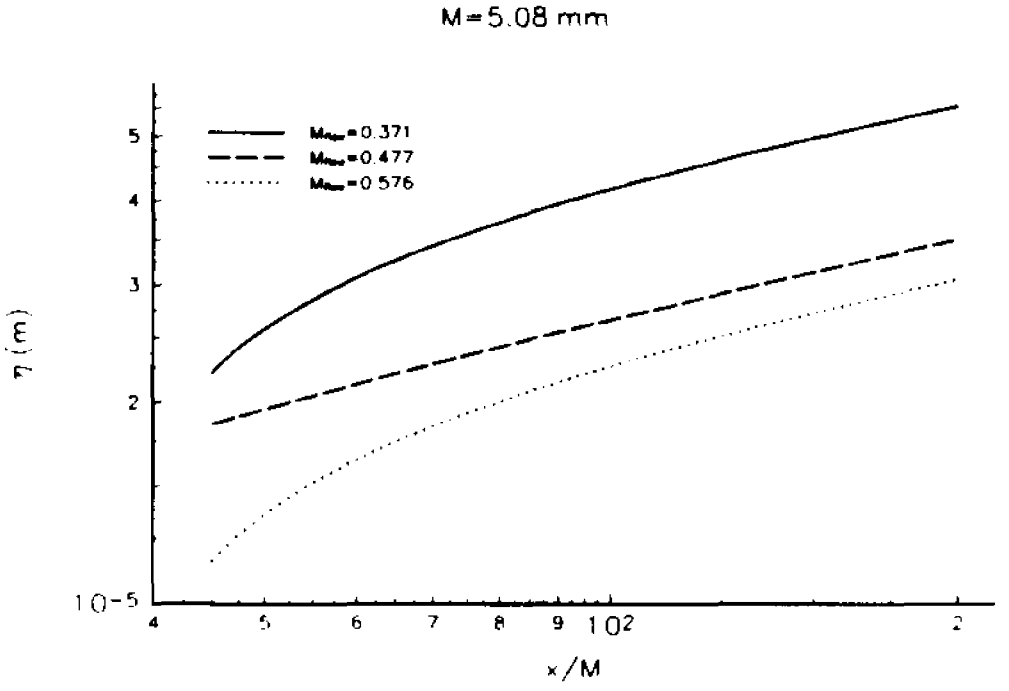

Figure 8.4.21: Kolmogorov's length scale for three mean flow Mach numbers.

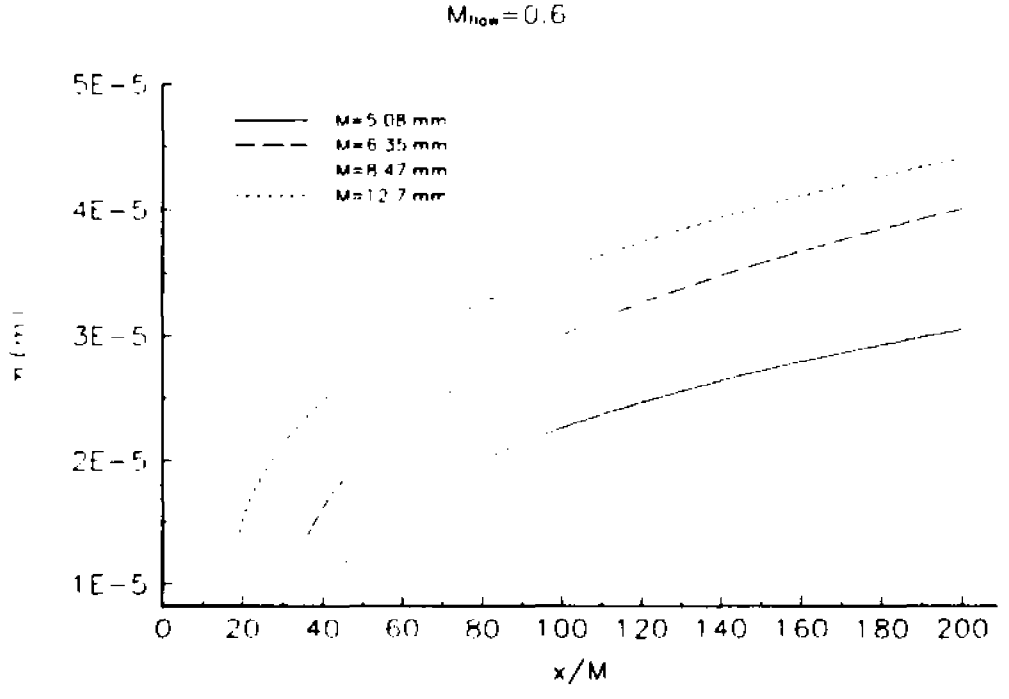

Figure 8.4.22: Kolmogorov's length scale for various mesh sizes.

8.5 INTERACTION OF TURBULENCE WITH A PLANAR SHOCK WAVE

Several grids were used in the present experiments so that the Reynolds number based on the mesh size, Re_M, as well as the dominant length scales present in the flow can be varied. The mesh Reynolds number ranged from 60,000 to 600,000 while the mesh size ranged from 5mm to 25mm. Measurements were obtained at three different driver pressures/shock strengths. The bulk parameters of all flow cases are shown in table X.

Figure 8.5.1a shows the decay of the Mach number fluctuations downstream of the 2x2 (2 meshes per inch) grid. It can be seen that the experimental data obey very closely the power law decay described by: $M_t^2 = B\left[\frac{x}{M} - \left(\frac{x}{M}\right)_0\right]^n$. It is also clear that M_t increases with the mean flow Mach number M_{flow}, i.e. the driver pressure. A 4-fold increase in pressure which corresponds to 100% change in the flow Mach number results in a 3 fold increase in the Mach number fluctuations throughout the entire flow field. After the passage of the shock the flow field changes. Velocity fluctuations in the longitudinal direction increase and Mach number fluctuations (shown in figure 8.5.1b) are changed also but not very drastically because the amplification of velocity fluctuations u is offset by an increase in mean temperature due to the compression. Thus M_t after the interaction is sometimes higher and sometimes lower than that before the interaction.

Figure 8.5.2a demonstrates the power law decay behavior of all the measured data as it is described by the above mentioned equation. The results of these six experiments are also

discussed in section 8.4. The results presented in this figure were obtained for the decaying isotropic turbulent flowfield without the presence of any shock wave interaction and are offered again here in order to compare with data obtained after the flow interacted with the shock wave.

The results after the passage of the shock are shown in figure 8.5.2b. The large region of linear behavior in this log-log plot indicates that the flow follows the same power law decay with different values of n, B and $(x/M)_0$. This is an indication that there is a quick return to isotropy of the flow after the axisymmetric character of the shock wave interaction.

Determination of the virtual origin $(x/M)_0$, decay exponent n and decay coefficient B was accomplished by fitting the experimental data to the power law, given earlier, so that the standard mean square deviation is minimized (see Mohamed and LaRue, 1990). Figure 8.5.3 shows a typical variation of the decay exponent, n, before and after the interaction with the shock wave of $M_s \approx 1.37$ for various mesh sizes of grids. The results show that n is a function of the mesh size (M), i.e. initial conditions before the interaction and that these values are substantially less than one. The effect of the shock interaction is very dramatic and depends on the M_s, M_{flow} and initial conditions.

Figure 8.5.4 presents the ratio of the decay coefficient, after the interaction with the shock to that before the interaction, n_d/n_u. It can be seen that this ratio is always greater than one for all investigated cases. In the lowest subsonic flow interaction with a shock wave traveling at $M_s \approx 1.2$, this ratio appears independent of initial conditions. This is in agreement with Mohamed and LaRue, 1990, where it was found that n was independent of Re_M, grid solidity σ and mesh size M . In the case of $M_{flow} \approx 0.475$ this ratio is very high at small Re_M

and decreases to 1.25 at high Re_M where it remains independent of it. At higher Mach numbers this ratio increases dramatically with Re_M. Thus n_d/n_u depends on initial conditions, flow Mach number M_{flow} and shock strength M_s.

From the previous section, 8.4, it was shown that the velocity fluctuations are higher for higher mean Mach number flowfields. The opposite trend is evident after interaction in figure 8.5.5 where the flowfield is compressed by the reflected shock wave. Namely, after the interaction of the flow with the reflected shock wave, the lower Mach number flow possesses the higher velocity fluctuations. Similar results are observed for the other coarser grids (larger mesh sizes). The effect of the grid size on velocity fluctuations can be verified from figures 8.5.5 and 8.5.6. It appears that there exists higher velocity fluctuations in flowfields produced by finer grids with lower Re_M.

From the information on the decay of velocity fluctuations and the use of the power law, the dissipation of kinetic energy for the compressed by the shock wave flowfield can be obtained by:

$$\epsilon = \frac{3}{2} nA \left[\frac{x}{M} - \left(\frac{x}{M} \right)_0 \right]^{(-n-1)} \left[\frac{\overline{U_u^2} \overline{U_d}}{M} \right]$$

where the subscripts u and d refer to the mean flow upstream and downstream of the shock wave respectively. In general it can be concluded that the dissipation rate of kinetic energy (ϵ) is drastically decreased after the interaction of the flowfield with the reflected shock wave. Typical results of ϵ are shown in Figures 8.5.7 and 8.5.8 for two different grids at the highest Mach number tested.

When the dissipation rate of kinetic energy is non-dimensionalized by the mesh size

and the incident mean flow velocity, U, then the dependance of $\epsilon M/U^3$ on the shock strength/mean flow Mach number can be shown in figure 8.5.9. For the flowfield compressed by the reflected shock wave the non-dimensionalized dissipation rate appears to be inversely proportional to the mean flow Mach number. That is the higher the shock strength/M_{flow} of the reflected shock wave the less the dissipation rate of kinetic energy.

From the analysis of the dissipation rate of kinetic energy the dissipative length scale, L_ϵ, can be calculated as $-\overline{U}\frac{\partial \overline{q^2}}{\partial x} = \epsilon = \frac{(\overline{q^2})^{\frac{3}{2}}}{L_\epsilon}$. In general experiments have shown that the dissipative length scale increases after the flow has been compressed by reflected shock wave as seen in figure 8.5.10 and depends on x/M. As turbulence decays with larger x/M, the dissipative length scale (L_ϵ) increases substantially. It is also shown that at larger x/M, where the length scales have grown to larger sizes the dissipative length scale was amplified the most.

The dependance of the dissipative length scale on the mean Mach number of the flow is shown in figure 8.5.11. The grid's mesh size was kept constant and the only parameter that was varied was the mean Mach number of the flow. It is clear that as the mean Mach number of the flow increases the dissipative length scale also increases. Furthermore the dissipative length scale depends on the downstream distance x/M for all tested cases regardless of the mean flow Mach number and their associated compressibility effects. Namely L_ϵ increases with increasing x/M. It is interesting to observe that the independence of the dissipative length scales on compressibility effects and mean flow Mach number is clearly distinguishable

after x/M>70. Prior to that, where the scales are sufficiently small, things get complicated and compressibility effects dominate the behavior of the dissipative length scales.

The effect of the mesh size as well as the effect of the sudden compression of the flowfield by the reflected shock wave on the Taylor's microscale (λ) are the principal parameters in such type of flows where energy is transferred instantaneously to the flowfield. In all cases the Taylor's microscale, obtained by $\epsilon = 15\nu\overline{\left(\frac{\partial u}{\partial x}\right)^2} = 15\nu\frac{u^2}{\lambda^2}$, increases due to the compression of the flow by the reflected shock as shown in figure 8.5.12. It is obvious that λ depends on x/M and this amplification is greater at larger x/M where the microscale has grown. Once again it appears that energy is more easily transferred to larger scales from the sudden compression of the flowfield by the planar shock wave. The effect of the turbulence generating grid on the length scales is of great importance for the study of the flowfield. One indication is offered from the decaying isotropic flowfield as described in the previous section. As observed in the decaying flowfield the grid is the principal control parameter of the length scales present in the flowfield. The effect of the grid's mesh size on the Taylor's microscale for the flowfield compressed by the shock wave is shown in figure 8.5.13 for several grids and the same mean Mach number flowfields. The figure shows the coarser grids to introduce larger scales than the finer grids. The dependance of λ on x/M is clearly shown in the above mentioned figure.

The hot wire probes that were used were able to resolve 7-26 Kolmogorov's length scales. Previous experiments (Andreopoulos and Muck, 1987, and Smits and Muck, 1987) report resolutions of 300-1000 viscous length scales. Even though the present resolution is

not ideal, physical constraints on the construction and operation of the probes do not allow us to achieve a better resolution. Nevertheless the current resolution achieved is the highest reported for such type of flow measurements. Resolution of 7-26 Kolmogorov's length scales yielded an excellent understanding of the bulk characteristics of the behavior of such scales. The Kolmogorov's length scale (η) defined as $\eta = \left(\frac{\nu^3}{\epsilon}\right)^{\frac{1}{4}}$, increases after the flowfield has been compressed by the reflected shock wave. This is shown in figure 8.5.14 where it is clear that η increases as x/M increases (i.e. as turbulence decays and length scales grow).

Figure 8.5.15 presents the effect of the grid's mesh size on the viscous scales. Similarly to the isotropic decaying flowfield (without any interaction) the viscous scales of the interacted flowfield are greater for flowfields generated by larger mesh sizes/higher Re_M.

The effect of the sudden compression of the flowfield attenuates or amplifies certain parameters of the flowfield. The following discussion considers the ratio of a certain flowfield property before interaction of the field with the shock wave to that after interaction.

The effect of the shock strength on the velocity fluctuations is shown in fig 8.5.16. For high shock strength (high Mach number) compressibility effects control the velocity fluctuations and instead of amplification of turbulent kinetic energy there exists an attenuation of turbulent kinetic energy (fig. 8.5.16). In the same figure it is also important to point out that the lower shock strength produces the highest amplification in velocity fluctuations. A 2 fold increase in velocity fluctuations was found for the flowfield compressed by a weak shock while for the medium case amplification of the order of 1.4 is evident.

Attenuation of the dissipation rate of kinetic energy is of the order of 0.3 for all the grids tested at the highest Mach number. A 3-fold decrease of the dissipation rate of kinetic energy is found for the interacted (compressed) flow as shown in figure 8.5.17. It is interesting to observe that at this high mean Mach number which produced flowfields with the greatest compressibility effects, the grid's mesh size appears to be inconsequential to the attenuation of the dissipation rate of kinetic energy

The effect of the shock strength / mean flow Mach number on the attenuation of the dissipation rate was found when the mesh size was kept constant and data presented for experiments of different mean flow Mach numbers is shown in figure 8.5.18. It is clear that the higher the mean flow Mach number/compressibility effects, the greater the attenuation of the dissipation rate of kinetic energy. A 3-fold attenuation of ϵ is observed for high (M_{flow}=0.7) and medium (M_{flow}=0.5) shock strengths and a 2-fold attenuation for the lowest case (M_{flow}=0.3). The attenuation of ϵ after the interaction of the flowfield with the reflected shock wave was also independently calculated by integrating the wavenumber spectrum before and after the interaction. The ratio of the two integrals is shown in the same figure (scattered points). It is clear that both methods present the attenuation of the dissipation rate of kinetic energy after interaction with the shock wave.

Typical spectra of the velocity fluctuations before and after the interaction of the flowfield with the shock wave is shown in figure 8.5.19a. The energy of the spectra of the compressed flowfield by the shock wave was found to be higher than the energy associated with the flowfield before the interaction. The ratio of the two spectra will provide information on the change of the time scale through the interaction. The time scale was found

to increase after the interaction with the shock wave. The frequency spectrum can not provide information on the change of the length scales since the frequency spectrum depends on the individual reference frame of the flowfield. If we consider the deceleration of the flowfield after its compression from the shock, then the frequency spectrum applying Taylor's hypothesis can be converted into the wavenumber spectrum. The wavenumber spectrum is independent of the reference frame and it can provide information on the length scales.

Figure 8.5.19b presents the wavenumber spectrum of velocity fluctuations for various wavenumbers before and after the interaction with the shock wave. The integration of each curve for the whole range of wavenumbers yields the dissipation rate of kinetic energy, ϵ. It can be observed that if the two integrals under each curve are obtained then the resulting ϵ is substantially reduced after the interaction. An interesting and important observation can be made from the above figure. Namely the wavenumber spectrum of velocity fluctuations is not attenuated throughout the range of the wavenumbers. In fact for the specific case the wavenumber spectrum is amplified around $k \approx 600$ and $k \approx 1400$ (1/m), suggesting that the effect of the shock wave compressing the flowfield is not felt uniformly across the range of wavenumbers, and therefore nor across the range of the length scales of the flowfield.

Figure 8.5.20 shows the amplification, growth, of the dissipative length scales defined as:

$$G_L = \frac{L_{\epsilon,d}}{L_{\epsilon,u}}$$

where $L_{\epsilon,d}$ and $L_{\epsilon,u}$ are the dissipative length scales downstream and upstream of the shock respectively. At each location x/M, L_ϵ and turbulence intensity are different. The results

suggest that at large x/M where L_e is indeed large and velocity fluctuations are small, L_e is amplified more. The data also indicate that G_{L_e} is increased with shock strength/M_{flow}.

The present high resolution measurements allowed for acurate analysis of the viscous scale level. Experiments performed using high frequency pressure transducers resolving 40 to 50 viscous scales presented inconclusive results and therefore, especially, the results on viscous scales were severely biased. Figure 8.5.21 shows the amplification of the viscous scales defined as:

$$G_\eta = \frac{\eta_d}{\eta_u}$$

It is interesting to observe that G_η is considerably smaller than G_{L_e} and that it behaves somehow differently. G_η decreases with downstream distance and shock strength. The different behavior of G_{L_e} and G_η clearly suggest that the result of the shock interaction is not felt uniformly across all the length scales of the flow. Larger eddies are amplified or attenuated (expanded or compressed) more than smaller eddies. Both length scales L_e and η depend on the dissipation rate ϵ which in all experiments has been found to be reduced after the interaction to about 0.3 of the upstream value. The DNS of Lee et al. (1993) indicate a moderate increase in ϵ after the shock interaction. This difference between the present experimental results and those of DNS leads to different, qualitatively, description of the effect of the shock interaction on the length scales. In order to further assess the behavior of length scale independently from the dissipation rate ϵ, the Taylor's microscale $\lambda_g = \left[\frac{\overline{u^2}}{\overline{\left(\frac{\partial u}{\partial x}\right)^2}}\right]^{\frac{1}{2}}$ has

been computed from the time derivative of u velocity after invoking Taylor's hypothesis. The amplification ratio $G_\lambda = \frac{\lambda_{behind}}{\lambda_{ahead}}$ is plotted in figure 8.5.22 together with the amplification of the same scale λ_ϵ obtained from: $\epsilon = 15\nu\frac{\overline{u^2}}{\lambda_\epsilon^2}$

The data clearly indicate that Taylor's microscale increases after the interaction.

Amplification of the Taylor's microscale (λ) is presented in figure 8.5.23. It appears that the microscale is amplified more for flowfields produced by coarser grids with higher Re_M. A 2-fold increase is observed for most of the experiments.

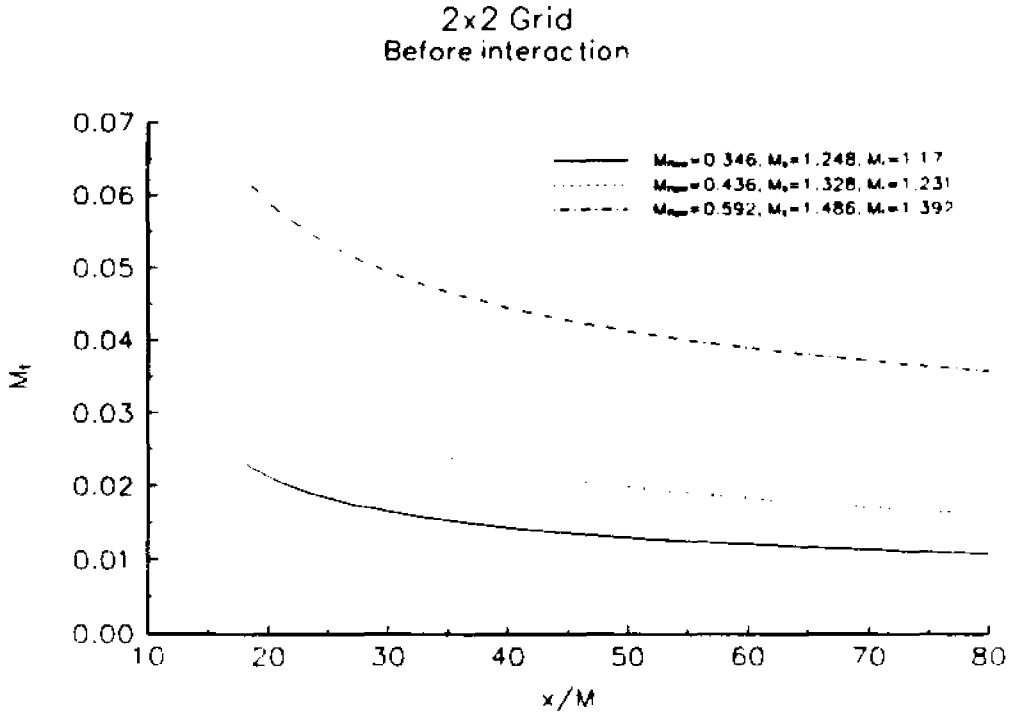

Figure 8.5.1a: Mach number fluctuations before interaction with the shock wave.

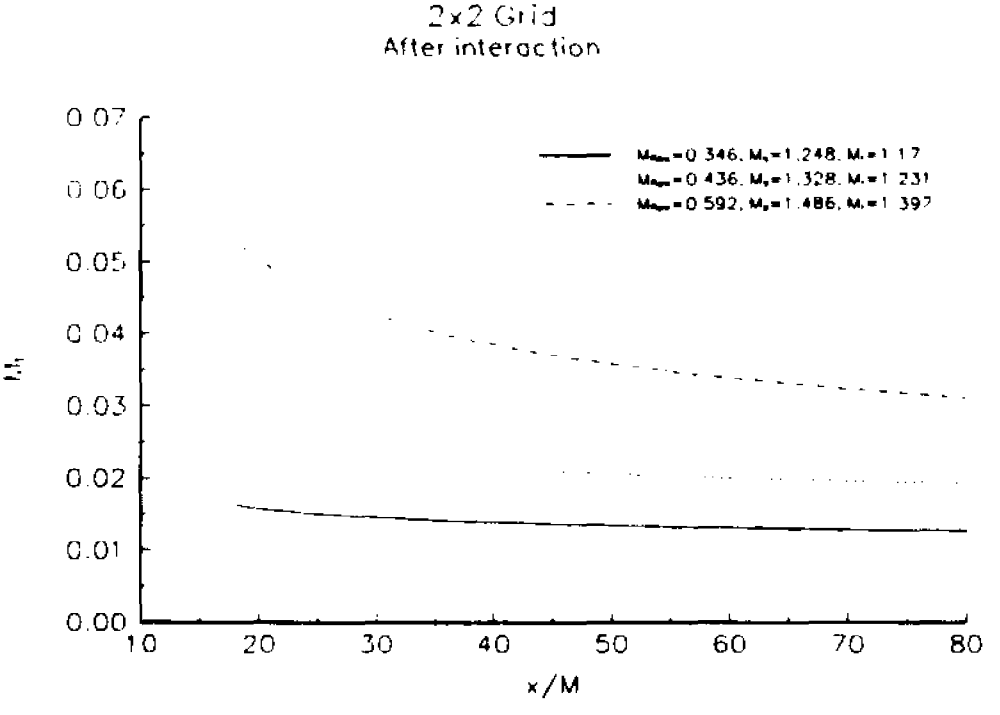

Figure 8.5.1b: Mach number fluctuations after interaction with the shock wave.

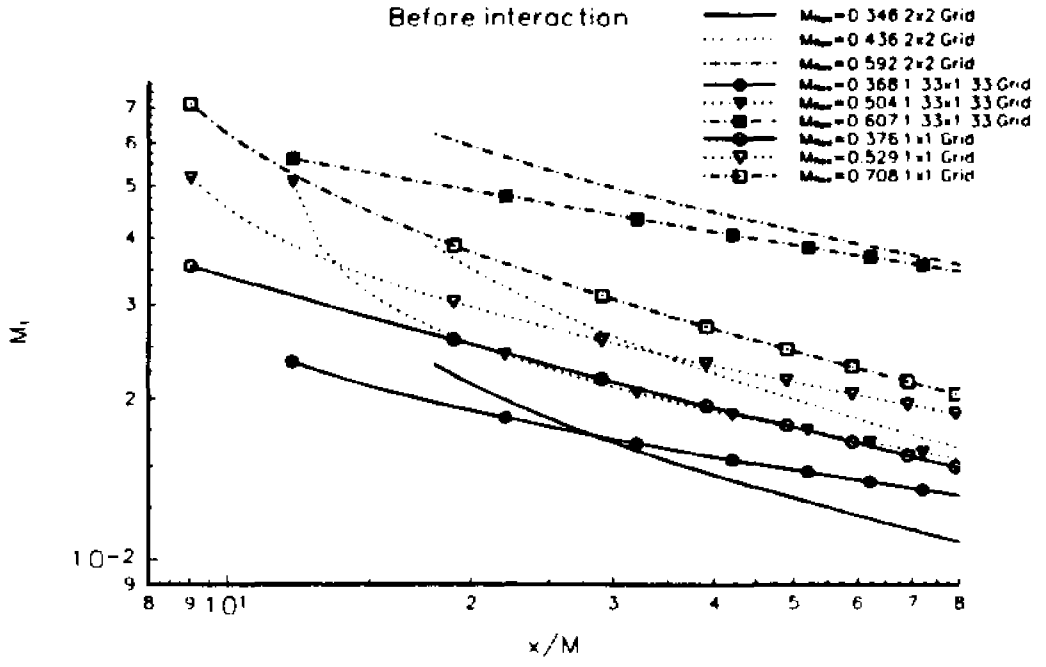

Figure 8.5.2a: Mach number fluctuations before interaction with the shock wave.

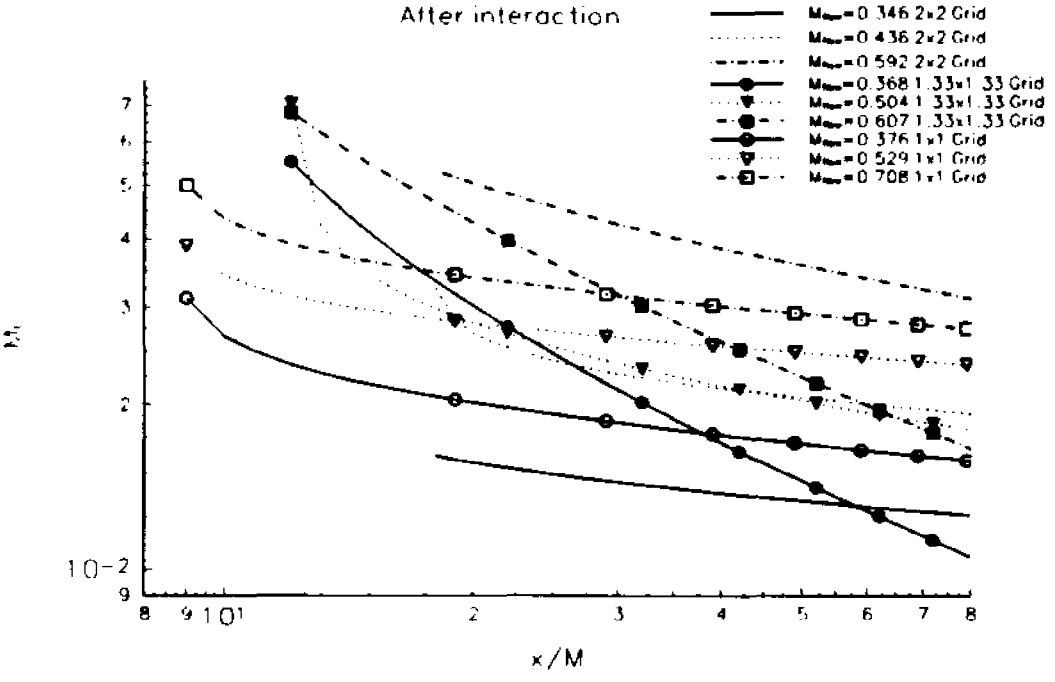

Figure 8.5.2b: Mach number fluctuations after interaction with the shock wave.

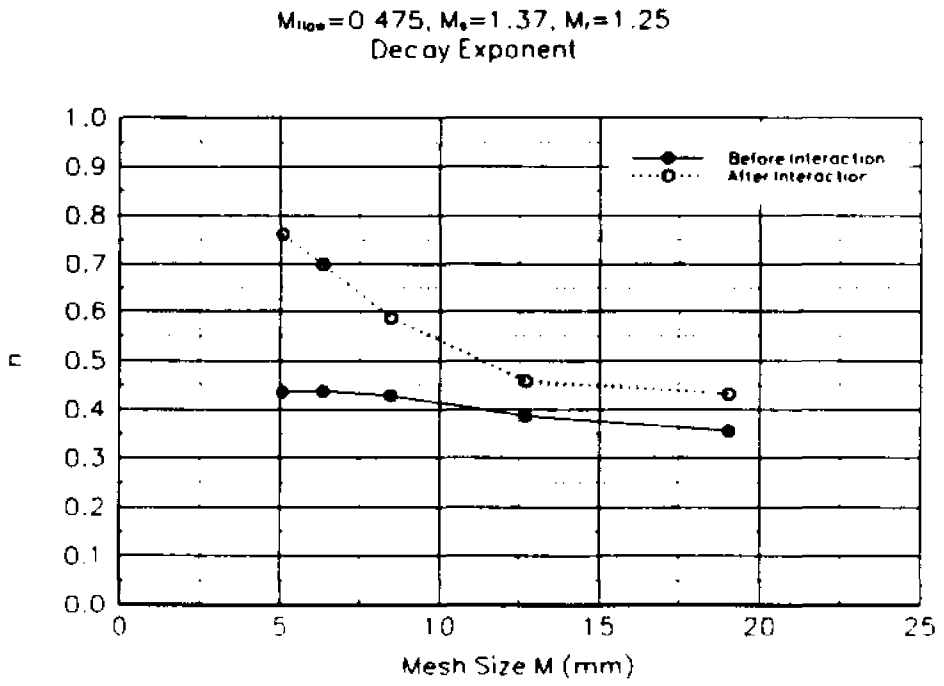

Figure 8.5.3: Turbulence decay exponent for various mesh sizes.

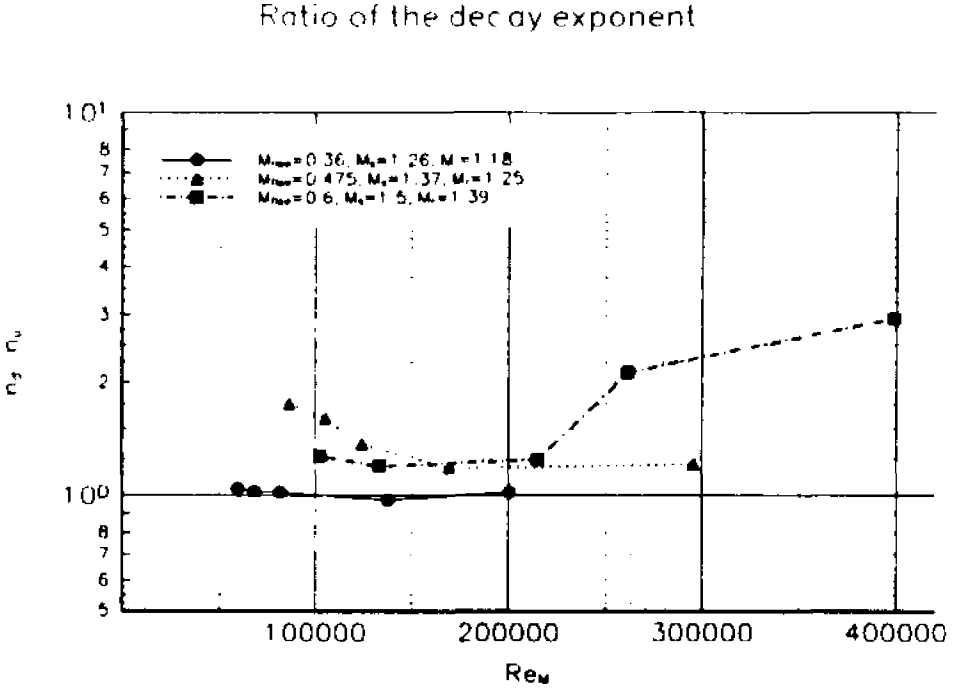

Figure 8.5.4: Ratio of the decay exponent for various experiments.

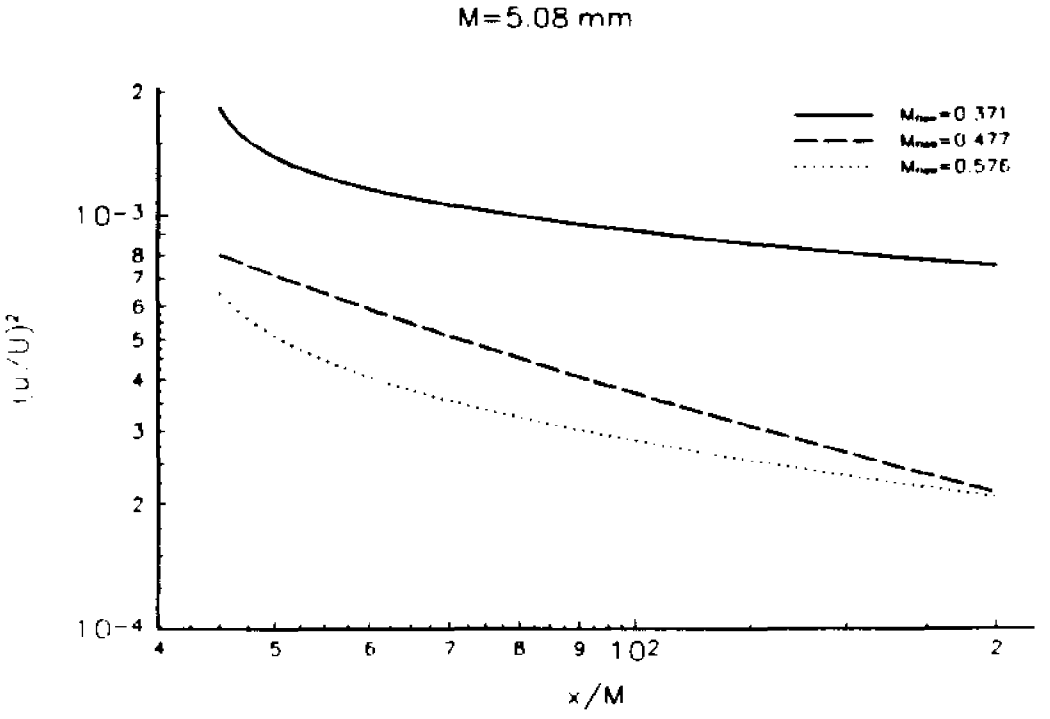

Figure 8.5.5: Decay of velocity fluctuations for three Mach numbers at M=5.08 mm.

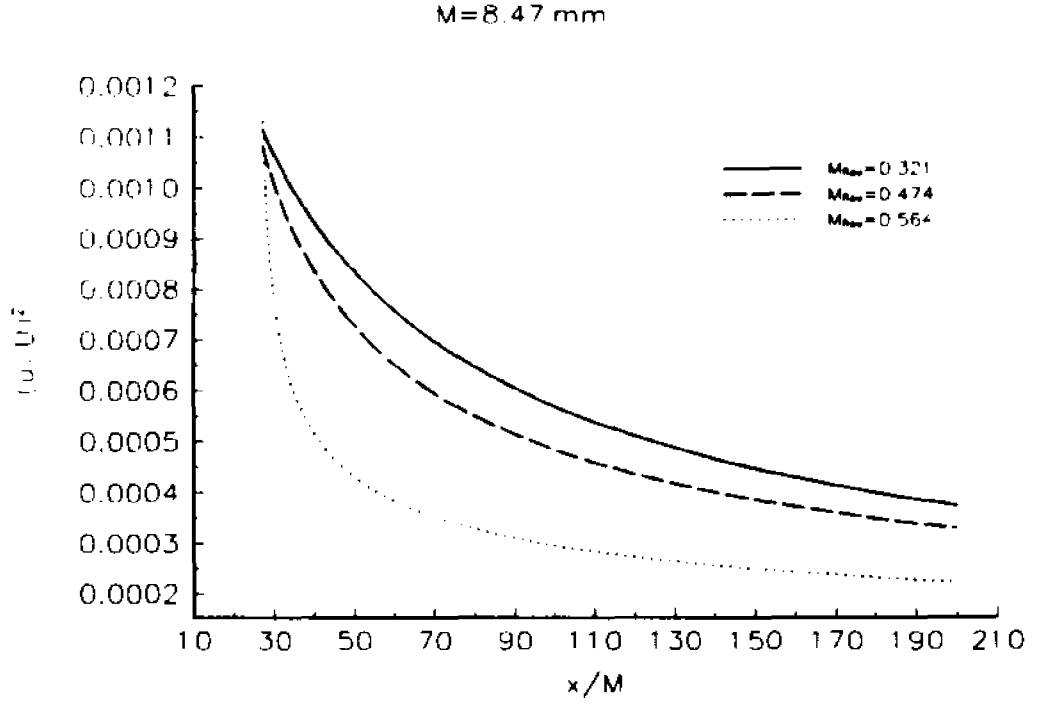

Figure 8.5.6: Decay of velocity fluctuations for three Mach numbers at M=8.47 mm.

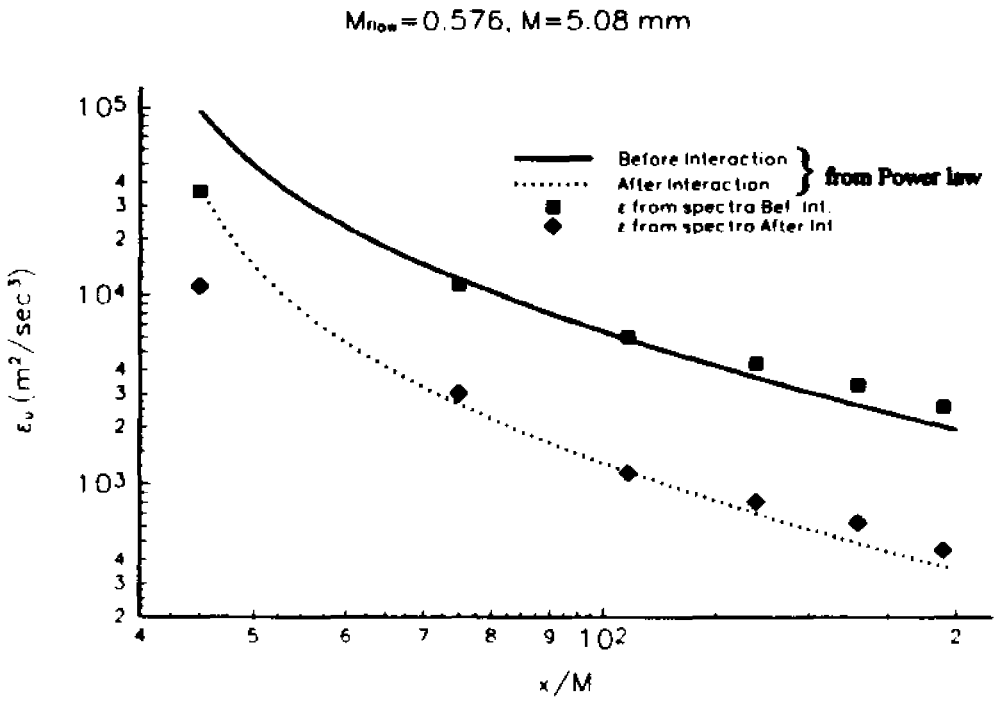

Figure 8.5.7: Dissipation rate of kinetic energy before and after interaction at M=5.08mm.

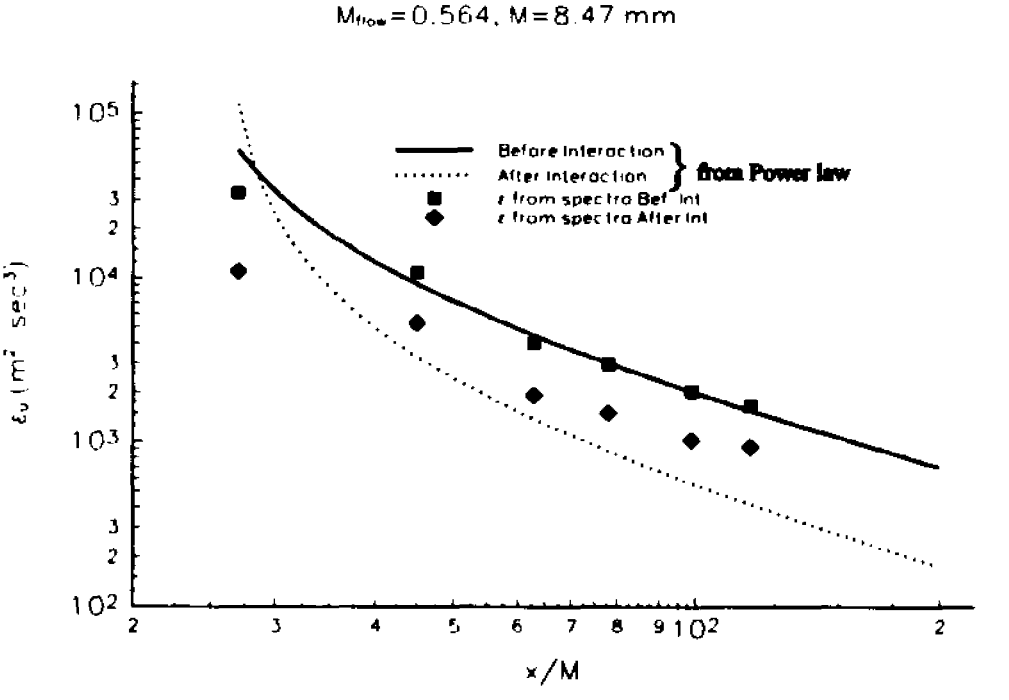

Figure 8.5.8: Dissipation rate of kinetic energy before and after interaction at M=8.47mm.

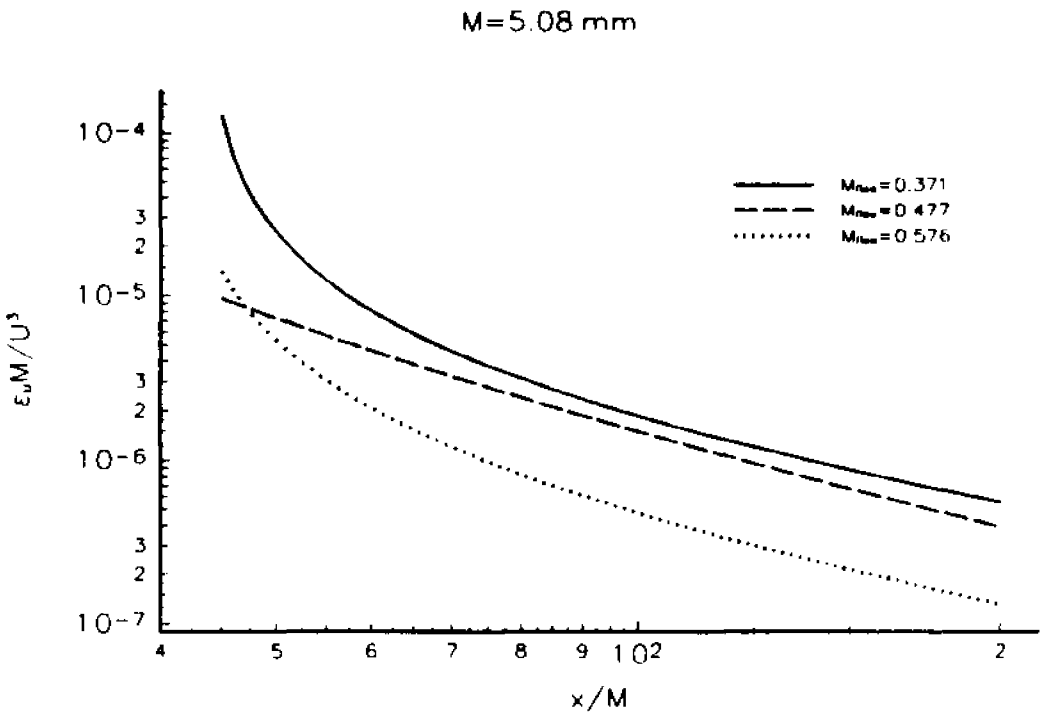

Figure 8.5.9: Non dimensional ϵ for three Mach numbers at M=5.08 mm.

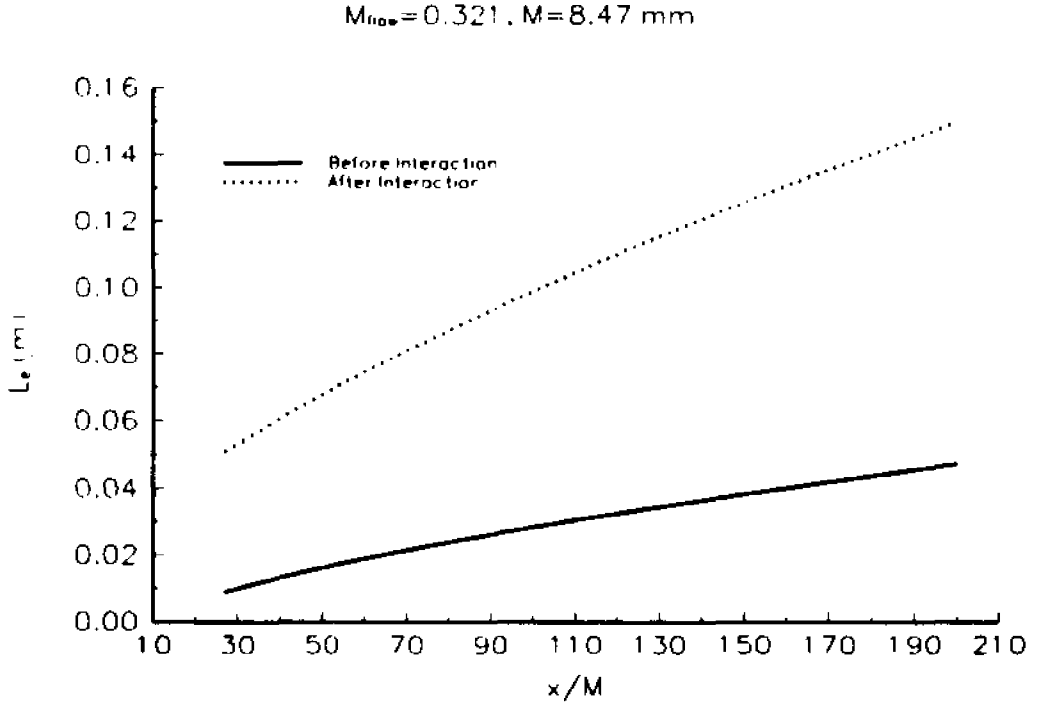

Figure 8.5.10: Dissipative length scale before and after interaction at M=8.47 mm.

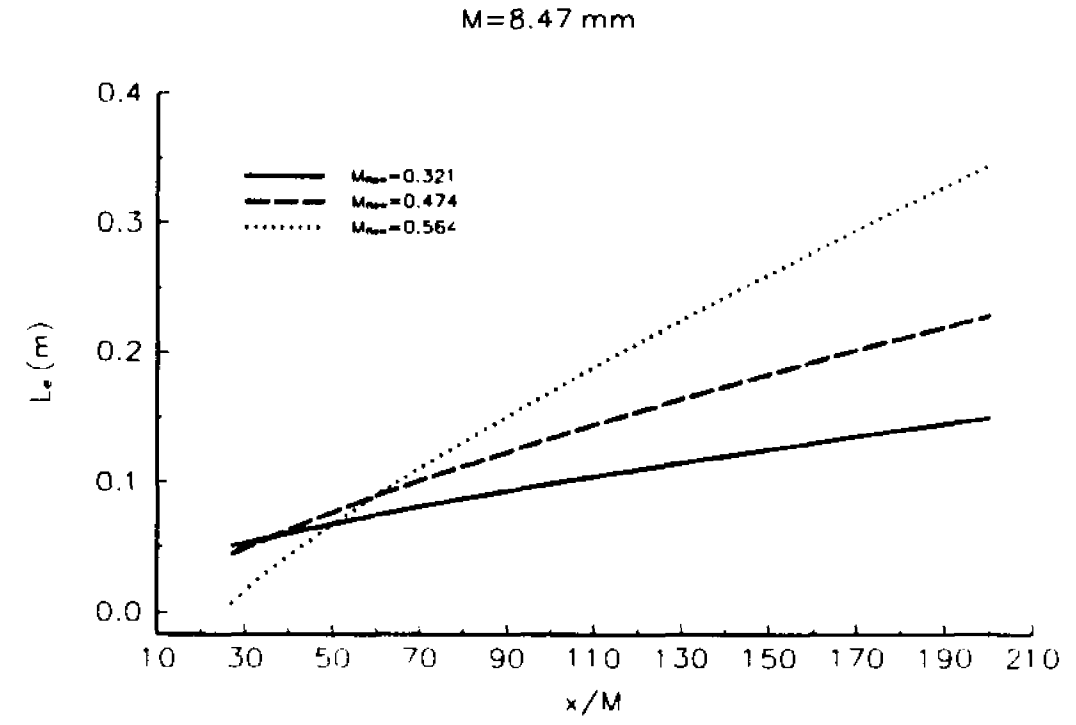

Figure 8.5.11: Dissipative length scale for three Mach numbers at M=8.47 mm.

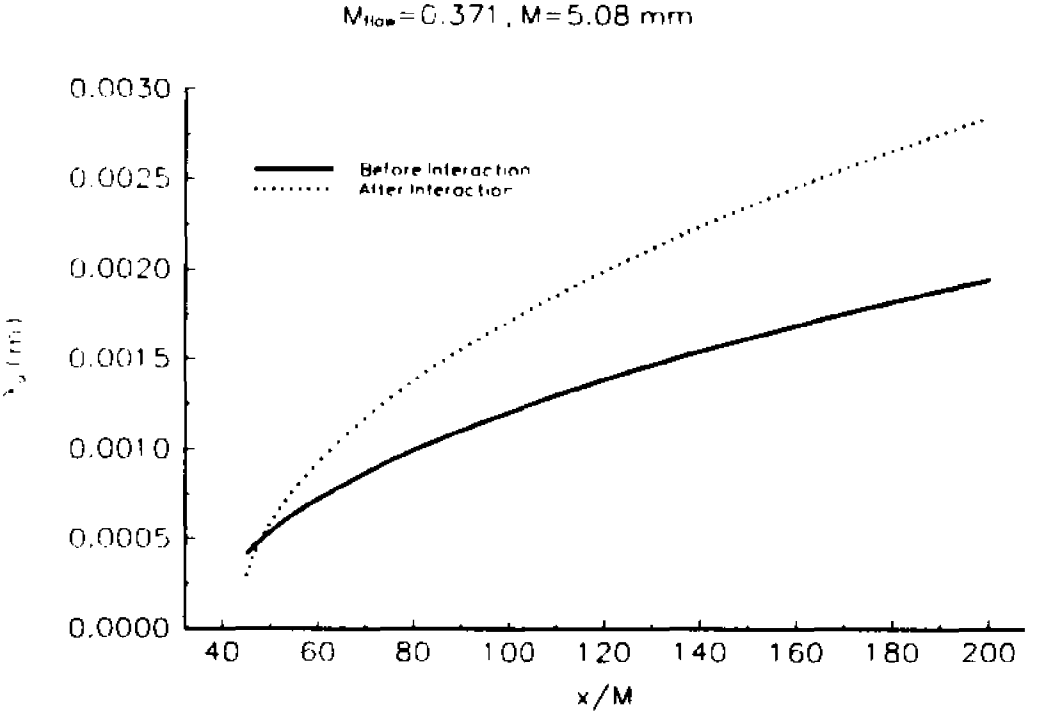

Figure 8.5.12: Taylor's microscale before and after interaction at M=5.08 mm.

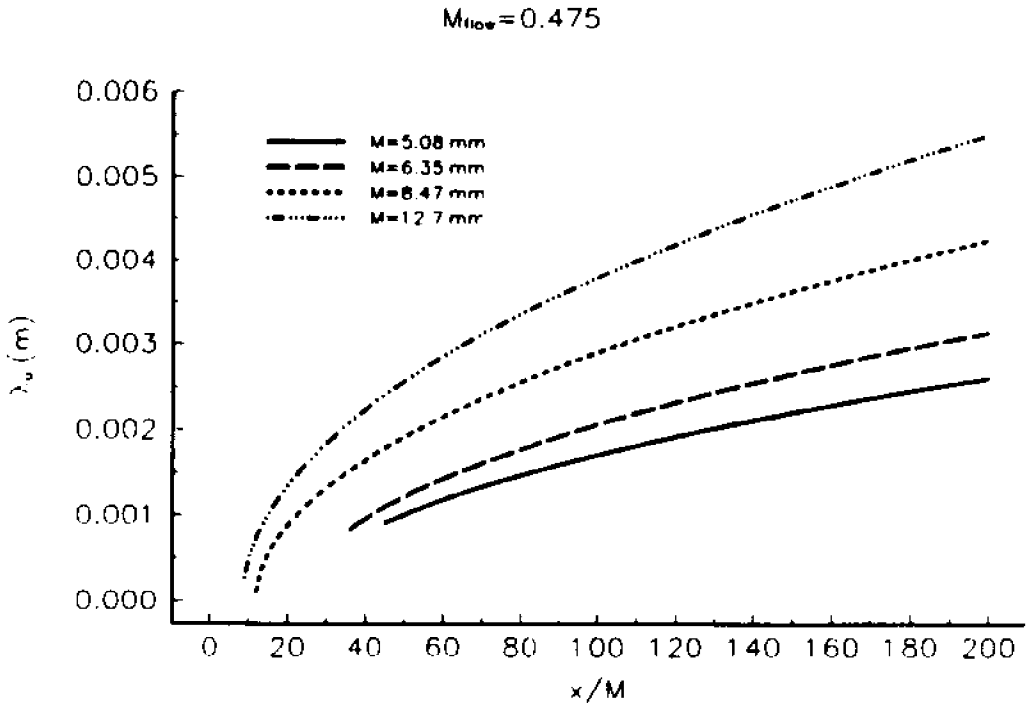

Figure 8.5.13: Taylor's microscale at M_{flow}=0.475 for several mesh sizes.

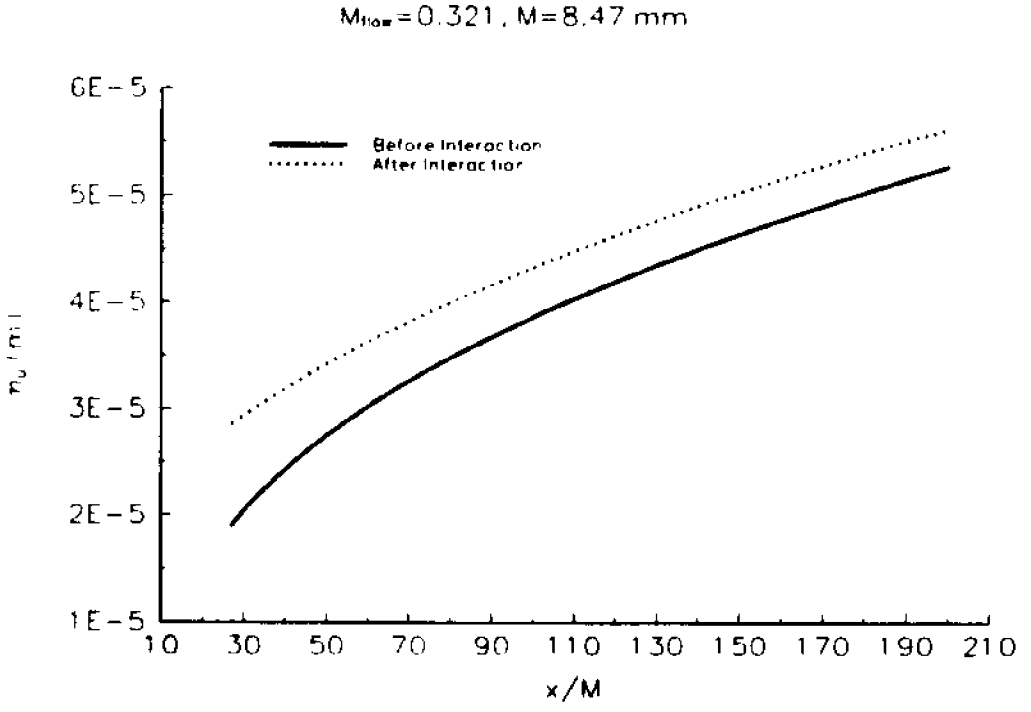

Figure 8.5.14: Kolmogorov's length scale before and after interaction at M=8.47 mm.

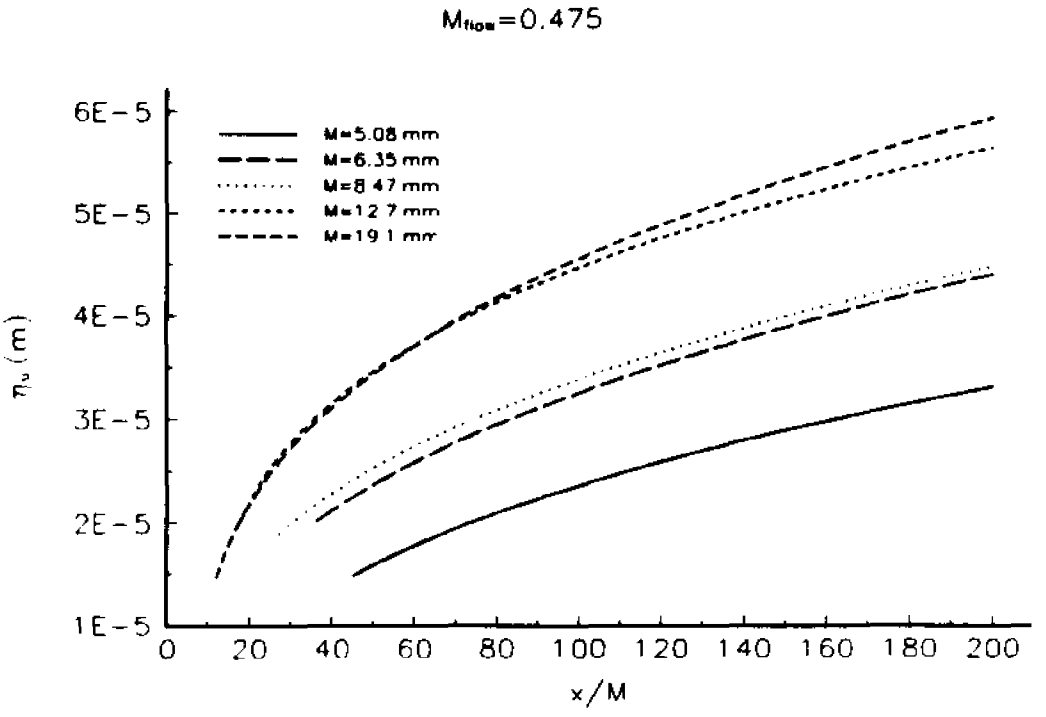

Figure 8.5.15: Kolmogorov's length scale for several mesh sizes at M_{flow}=0.475.

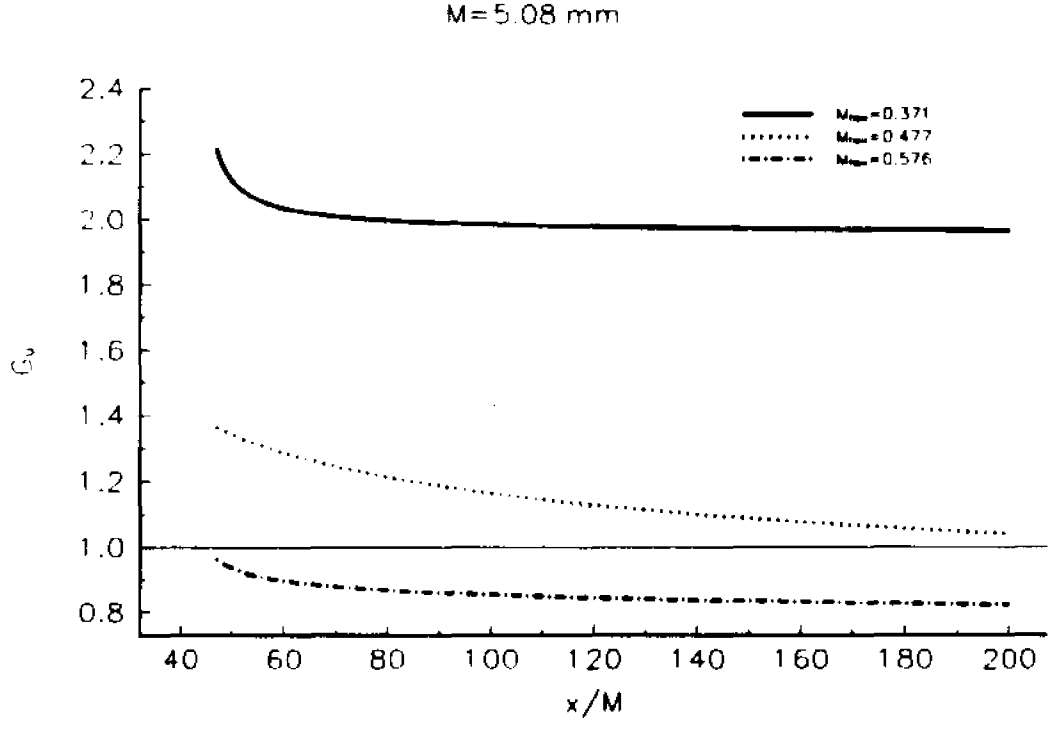

Figure 8.5.16: Amplification/Attenuation of velocity fluctuations.

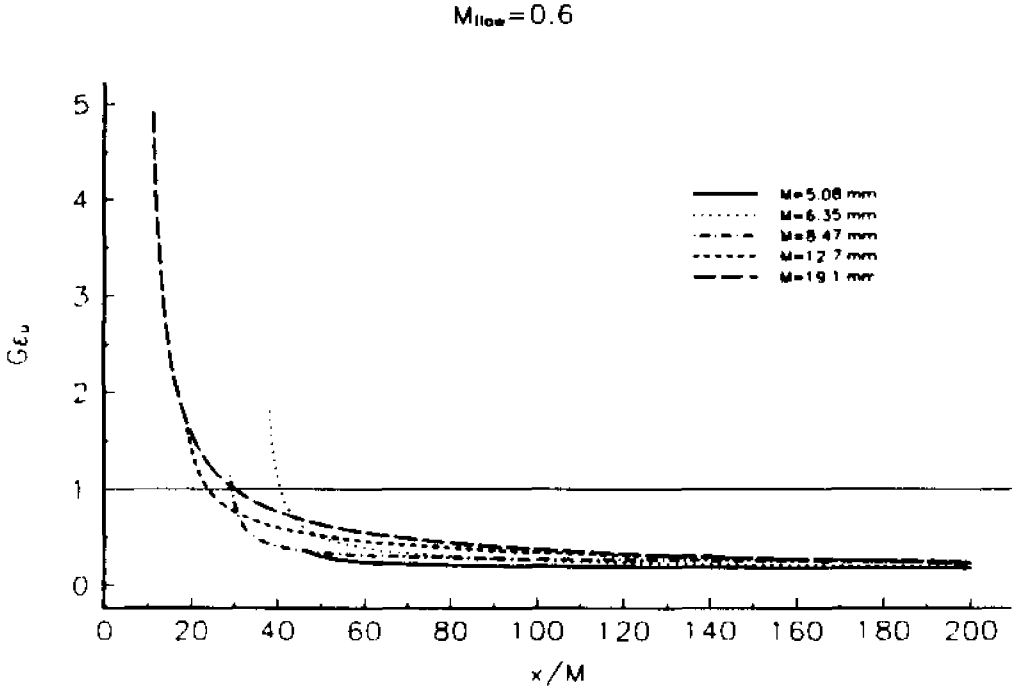

Figure 8.5.17: Attenuation of dissipation rate of kinetic energy.

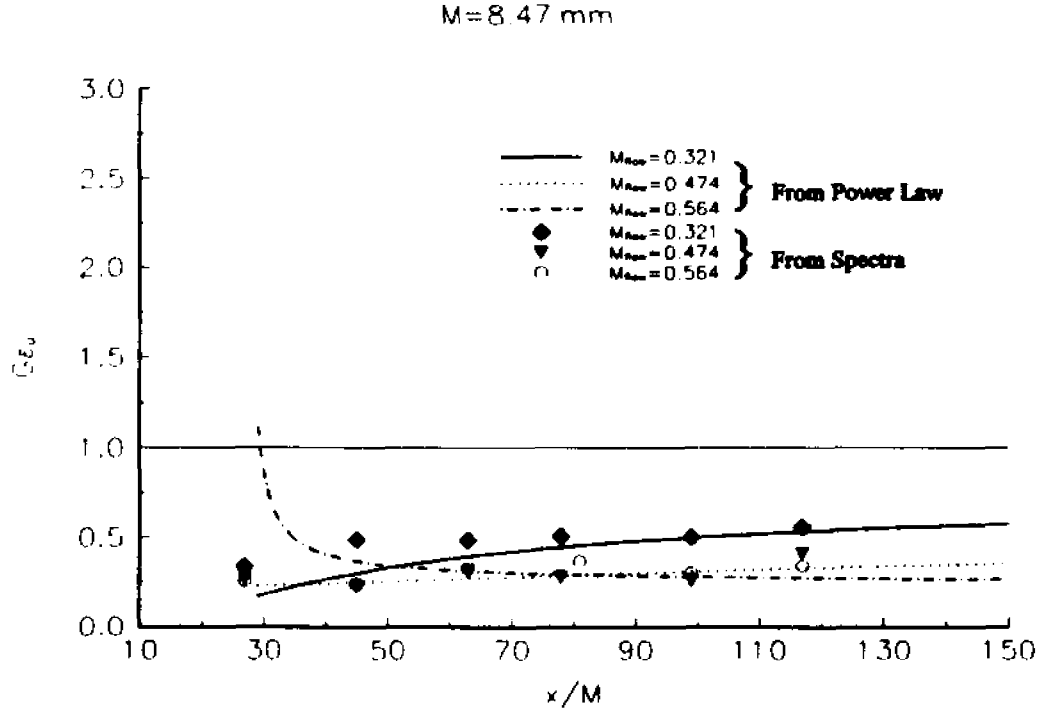

Figure 8.5.18: Attenuation of dissipation rate of kinetic energy for three Mach numbers.

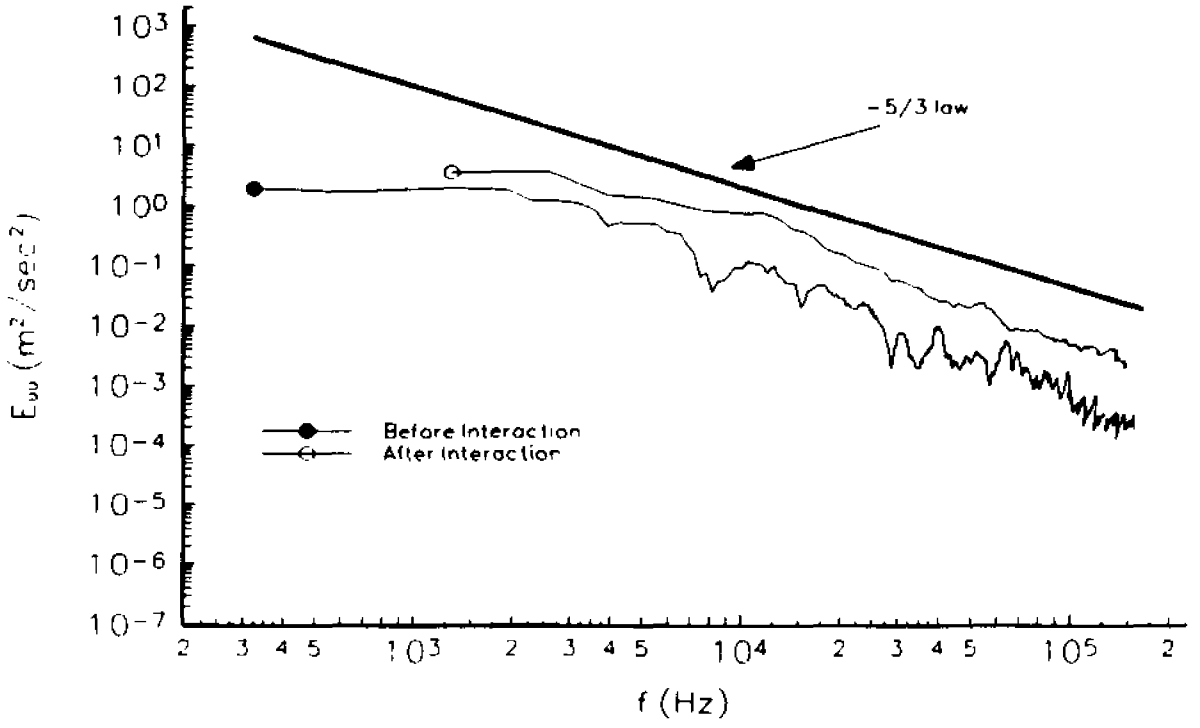

Figure 8.5.19a: Typical spectrum of velocity fluctuations before and after interaction

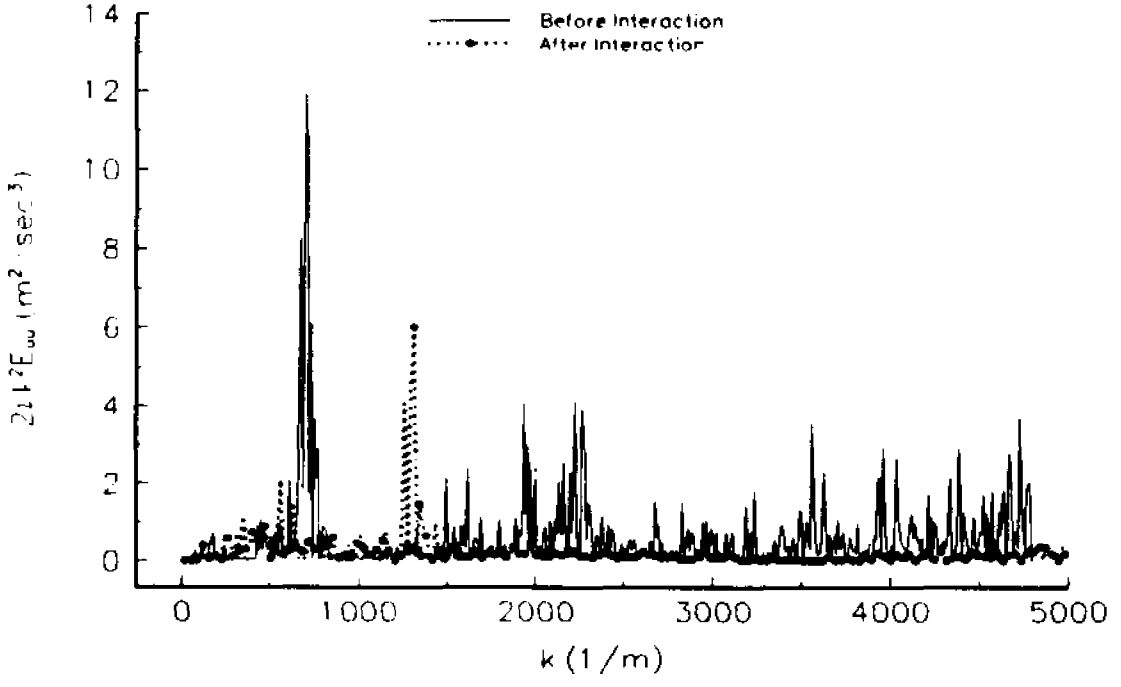

Figure 8.5.19b: Typical wavenumber spectrum of velocity fluctuations for various wavenumbers before and after interaction

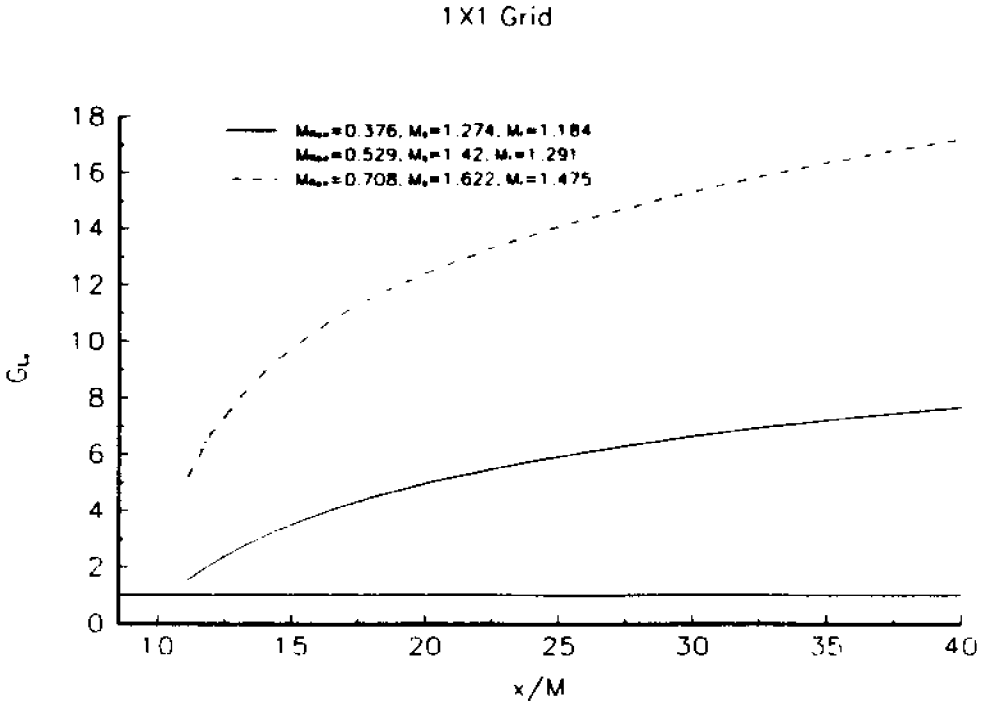

Figure 8.5.20: Amplification of the dissipative length scale.

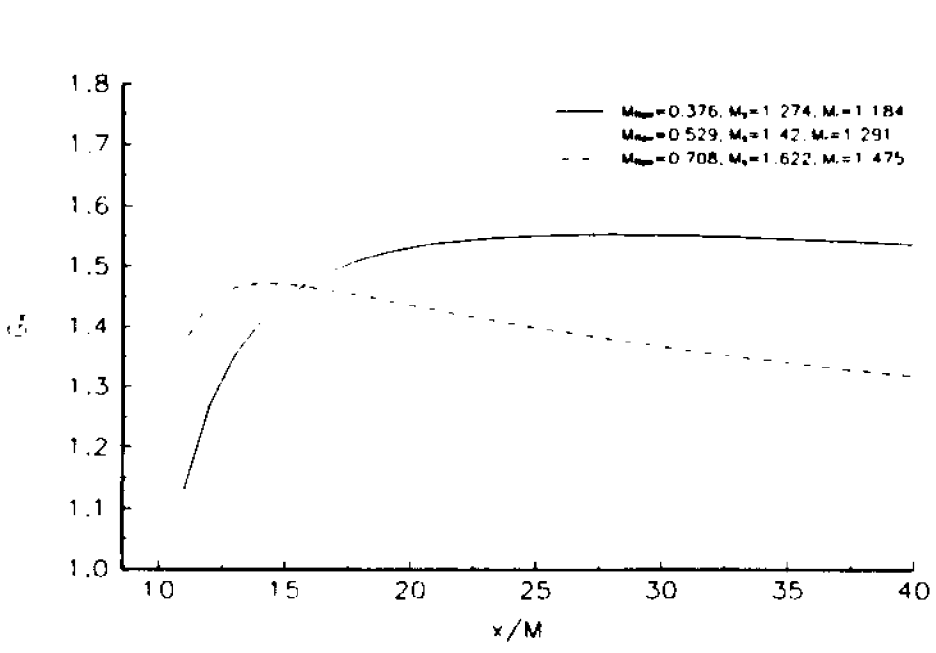

Figure 8.5.21: Amplification of the viscous length scale.

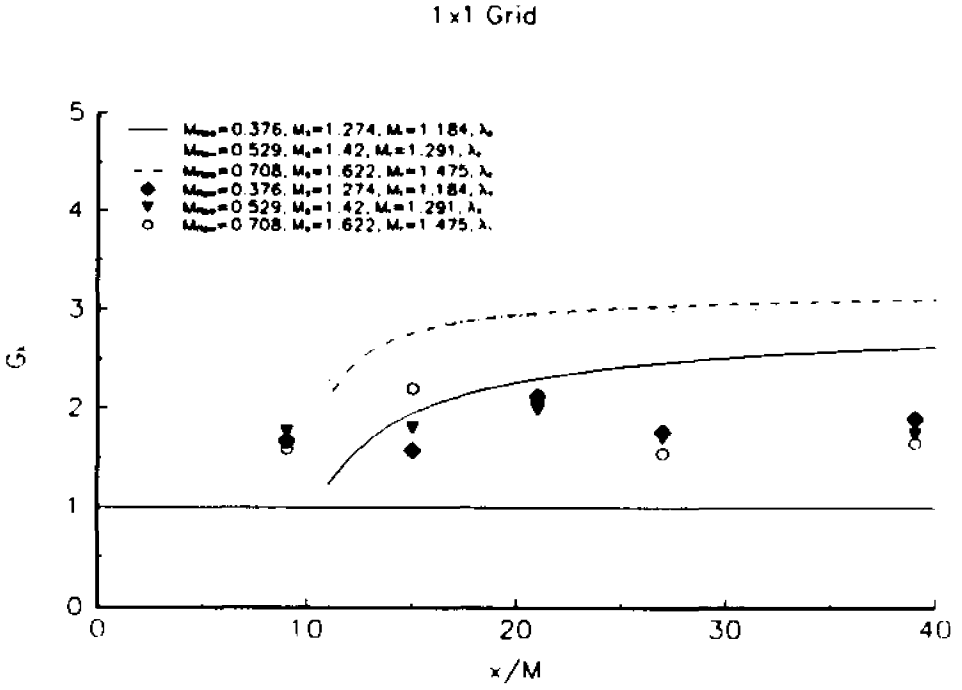

Figure 8.5.22: Amplification of the Taylor's microscale.

$M_{flow}=0.335$

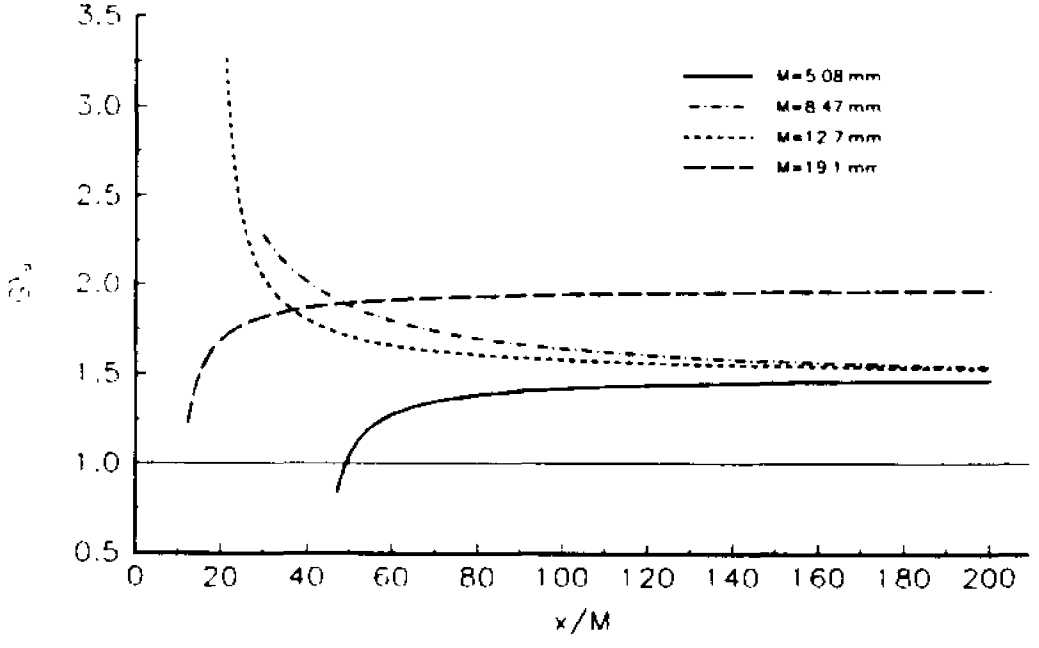

Figure 8.5.23: Amplification of the Taylor's microscale for several mesh sizes.

8.6 INTEGRAL LENGTH SCALES

In order to estimate the integral length scales in the longitudinal ξ_1 and normal ξ_2 directions the auto-correlation coefficients

$$r_{ij}(\xi_k) = \frac{\overline{u_i(x)u_j(x+\xi_k)}}{\sqrt{u_i^2(x)}\sqrt{u_j^2(x+\xi_k)}}$$

were evaluated by two point measurement in the ξ_2 direction and from auto-correlations in the ξ_1 direction after invoking Taylor's hypothesis. The integral length scales were obtained by integrating the correlation curve and then applying Taylor's hypothesis.

Figure 8.6.1 shows the $L_{11}(\xi_1)$ in the longitudinal direction before the interaction with the shock wave for the three different flow cases. There exists some scatter in the data in each particular case which is attributed to the various grids used. It can be seen, in the above mentioned figure, that the integral length scale increases with downstream non-dimensional distance, x/M, for all investigated cases. It is also evident that L_{11} in the case of M_{flow} =0.475 is higher than in the case of M_{flow} =0.36. However when the flow Mach number increases to M_{flow} =0.6 and therefore stronger compressibility effects are present, then the integral length scale drops.

After the interaction with the shock wave the distribution of $L_{11}(\xi_1)$ is more complicated (see fig. 8.6.2). All the scales are reduced considerably. However the reduction of the larger scales, at greater x/M locations, is greater than the reduction of smaller scales. This is also shown in figure 8.6.3 where the attenuation ratio

$$G_{L_{11}} = \frac{L_{11,a}(\xi_1)}{L_{11,b}(\xi_1)}$$

is plotted. At large x/M where the initial scales were the largest the reduction is dramatic. Thus once again it is found that amplification or attenuation is not the same for all initial length and velocity scales. It is interesting to observe that the stronger the shock strength the greatest the attenuation of the longitudinal length scales.

The two point correlation $r_{11}(\xi_2)$ in the lateral direction ξ_2 of the longitudinal velocity fluctuations is shown in figure 8.6.4. These data were obtained by a specially designed cross correlation probe of six parallel wires and three temperature wires separated from each other by 1mm. Not all the curves cross the zero line and therefore it is very difficult to integrate them in order to obtain the classically defined integral length scale in the lateral direction. However the slopes of these curves are indicative of their trend. It is rather obvious that the length scales before interaction are reduced with increasing flow Mach number. This behavior is very similar to that of $L_{11}(\xi_1)$. After the interaction, however the length scale $L_{11}(\xi_2)$ increases in the first two lower Mach number cases and decreases for the strongest interaction.

In order to investigate the effect of initial conditions on this correlation at the highest flow and shock Mach number where the lateral scales are shown to reduce (fig. 8.6.4) various grids were used. The data shown in figure 8.6.5 indicates that the correlation increases substantially in the case of the finest grid, 8x8 with the lowest Re_λ, after the interaction. However the coarser grid, 2x2 grid with the highest Re_λ=737, shows the greatest attenuation in the lateral integral scale of turbulence after the interaction.

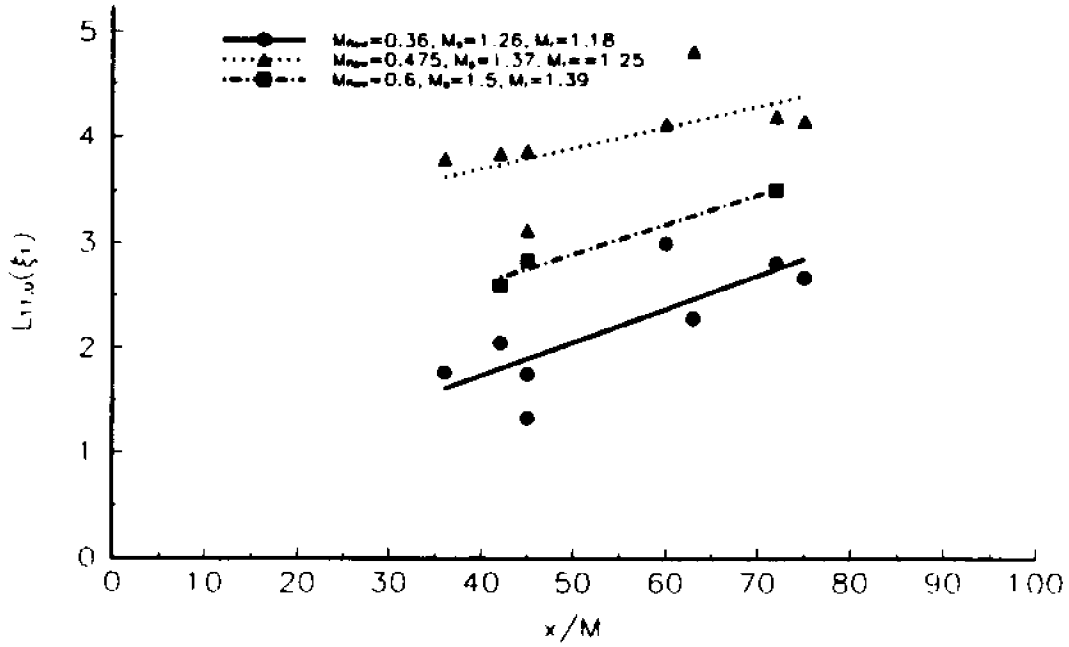

Figure 8.6.1: Longitudinal integral length scale for various experiments before interaction with the shock wave.

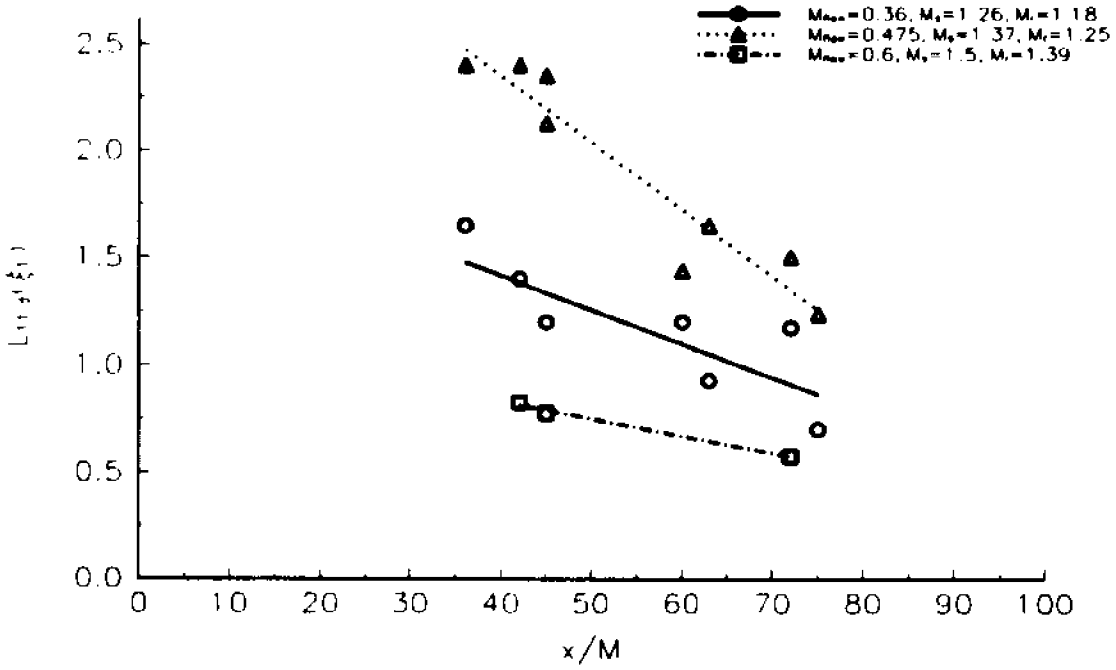

Figure 8.6.2: Longitudinal integral length scale for various experiments after interaction with the shock wave.

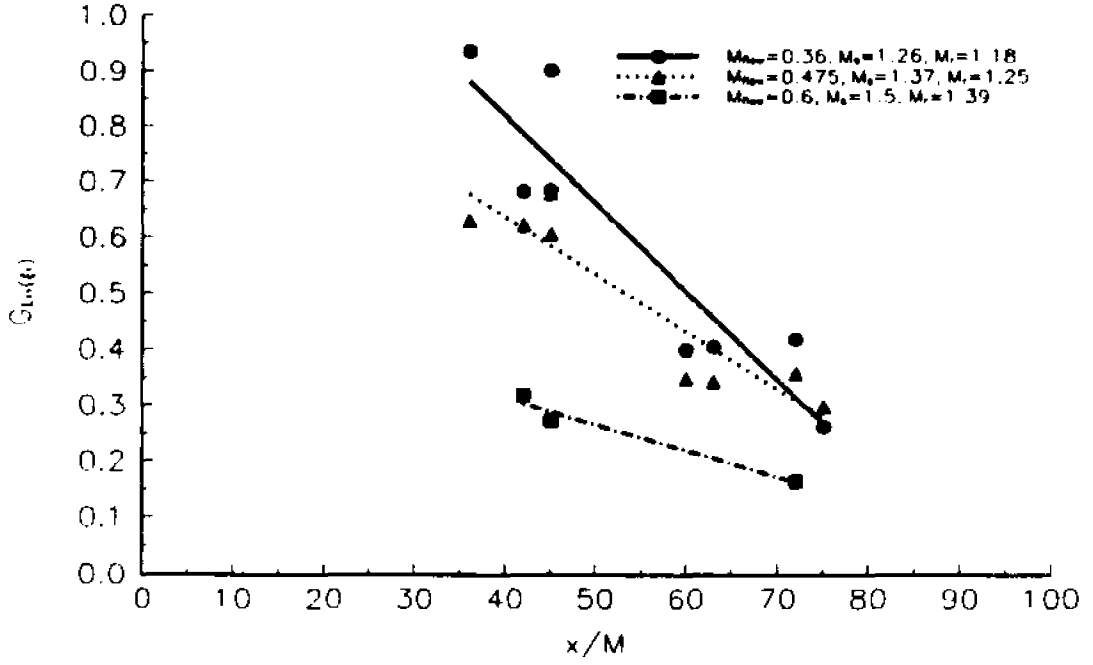

Figure 8.6.3: Ratio of the longitudinal integral length scales for various experiments.

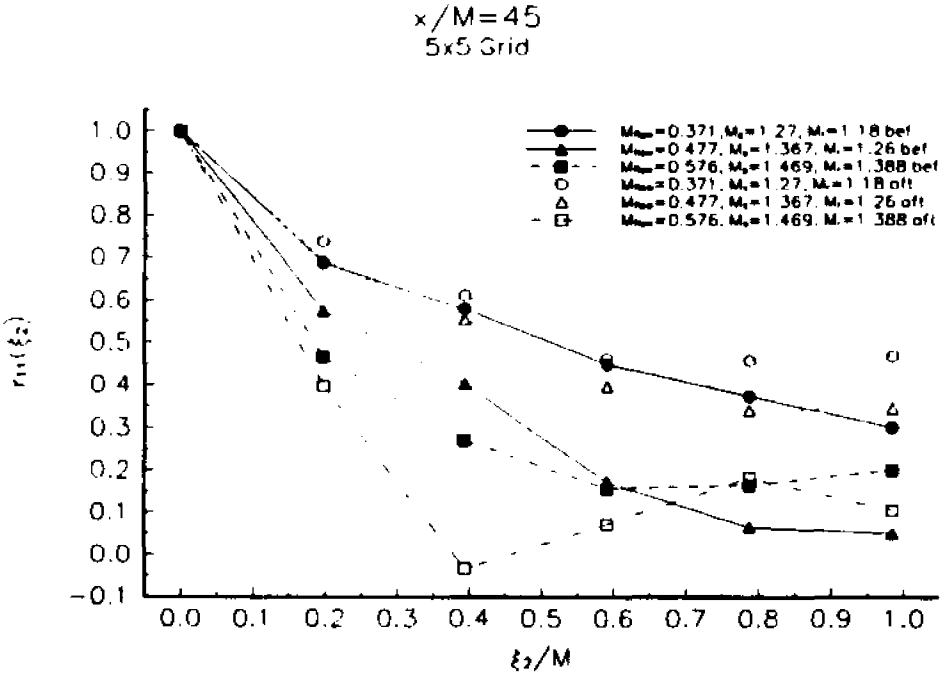

Figure 8.6.4: Space correlation in the lateral direction for three different flow cases.

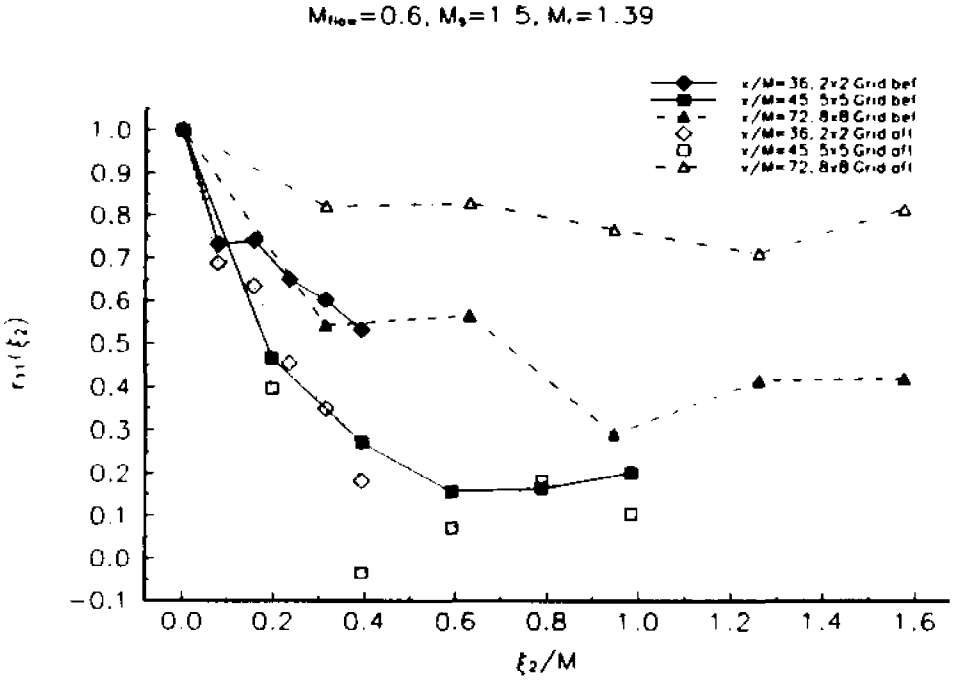

Figure 8.6.5: Space correlation in the lateral direction for three different downstream locations.

9. CONCLUSIONS

An experimental study of the interaction of a normal shock wave with decaying grid generated nearly isotropic turbulence has been performed using time resolved pressure, velocity, temperature and Mach number measurements in a shock tube. Spatial resolution of the order of 7-26 Kolmogorov viscous length scales was achieved in the measurements of turbulence. A variety of turbulence generating grids provide a wide range of turbulence scales with flow Mach numbers ranging from 0.3 to 0.7 and shock Mach numbers from 1.2 to 1.6.

The conclusions are separated into three major divisions. One concerning results obtained from the analysis of the pressure flowfield before and after its interaction with the shock wave and the other two refer to the decaying turbulent flowfield without any interaction with the shock wave and the second on the interaction of the decaying turbulent flowfield with the planar shock wave.

Analysis of the acquired data revealed that the amplification of the pressure fluctuations after the interaction of the normal shock wave with the flowfield depend on the grid's mesh size (initial turbulence level) and shock strength. Furthermore, spectral analysis confirmed that there exists amplification in the wavenumbers after the interaction and this amplification is not constant for the whole range of wavenumbers resolved.

The major conclusions of the pressure flowfield study is that pressure fluctuations and their amplification after the passage of the shock wave depend strongly on the mesh size for a given shock strength.

The finer grid (smaller mesh size) produces higher pressure fluctuations on the flowfield. After the interaction of the induced flow with the shock wave, the higher pressure fluctuations are the ones that are amplified the most.

There exists a substantial grid dependence of pressure as a result of the strong interaction of the reflected shock wave with the grid generated turbulent field. The reflected shock strength (P_y/P_1) attenuates more after the interaction with turbulence generated by finer grids. The non dimensionalized pressure loss ($\Delta P/\gamma P M_2^2$) depends on Re_M and seems to be inversely proportional to $(Re_M)^n$ with n equal to 1/8.

Spectral analysis of the pressure fluctuations indicate different amplification at various wavenumbers. Results indicated that the pressure fluctuations of the larger eddies are amplified the most while the pressure fluctuations of the smaller eddies are not significantly amplified.

High spatial resolution measurements of decaying isotropic turbulence were also carried out in the shock tube facility. The experimental data verified the isotropy of the flow directly and indirectly.

It can be concluded that the decay coefficient , A, obtained from the power law, decreases when the Mach number increases.

The virtual origin $(x/M)_0$ strongly depends on the mesh size/Re_M. For all cases it was found that the virtual origin approaches the grid as the mesh size/Re_M increases.

The decay exponent n is substantially affected by the mean Mach number of the flowfield. It is found that n decreases with increasing Mach number. The effect of the mesh size on the decay exponent was also found to behave similarly to the decay coefficient, A.

Namely for the lowest Mach number it increases with increasing mesh size/Re_M. That means that for finer grids, small mesh size, there exists larger dissipation rates.

Compressibility effects present for the highest tested flowfield (M_{flow}=0.6) and the medium flowfield (M_{flow}=0.475) do not permit to draw general conclusions on the behavior of the dissipation rate of kinetic energy with respect to mesh size/Re_M. But when compressibility effects are substantial then the coarser grids with the greater mesh sizes and highest Re_M flowfield, produced a lower dissipation rate ϵ. The opposite was found for the lowest tested flowfield (M_{flow}=0.3) where compressibility effects were absent or not substantial. It was found that ϵ as well as the kinetic energy increase with increasing Mach number in all investigated subsonic flows.

As Mach number increases it has been found that the dissipative length scale increases. The dissipative length scale also increases with increasing mesh size and Re_M.

The Taylor's microscale (λ) appears to increase with increasing Mach number. It is clear that the coarser the grid, larger mesh size, the greater the Taylor's microscale.

The Kolmogorov's length scale (η) decreases as the Mach number increases. Experimental results showed that the Kolmogorov's length scale increases as the mesh size increases.

Table XVI, presented at the end of this section, summarizes the conclusions for the parameters that were investigated in this work and their response to an increase of the mean flow Mach number and an increase in the mesh size/Re_M. In this table three symbols are used: (↑) represents that the parameter increases with increasing M_{flow} or increasing mesh size/Re_M, (↓) represents that the parameter decreases with increasing M_{flow} or increasing

mesh size/Re_M and finally (↕) represents that the parameter because of compressibility effects does not present a specific trend with increasing M_{flow} or increasing mesh size/Re_M.

A summary of the results of a nearly homogeneous nearly isotropic compressible turbulent flow interacting with a normal shock wave in the shock tube facility are now presented.

It is clear that M_t increases with the mean flow Mach number M_{flow}, i.e. driver pressure, and decrease with coarser grids but due to high compressibility effects M_t after the interaction sometimes is higher and sometimes is lower than before the interaction.

The results show that the decay exponent, n, is a function of the mesh size i.e. initial conditions before the interaction, and that its value is substantially less than one. The effect of the shock interaction is very dramatic and produces a dependance of n on the M_t, M_{flow} and initial conditions. The decay exponent after interaction is greater than the one obtained before interaction for all investigated cases.

After the interaction of the flow with the reflected shock wave, the lower Mach number flow possesses the higher velocity fluctuations. It appears that there exists higher velocity fluctuations in flowfields produced by finer grids with lower Re_M.

In general it can be concluded that the dissipation rate of kinetic energy (ϵ) is decreasing after the interaction of the flowfield with the reflected shock wave.

Experiments have shown that the dissipative length scale (L_ϵ), the Taylor's microscale (λ) and the Kolmogorov's length scale (η) increases after the flow has been compressed by reflected shock wave and there exist a strong dependance of all the length scales on x/M. The effect of the mesh size on the above mentioned scales was found to be consistent for all tested

flowfields. Experiments performed with a large variety of mesh sizes revealed that the coarser grids introduce larger scales than the finer grids.

The integral length scales in the lateral direction are amplified at small Mach numbers and attenuated at large Mach numbers but their behavior depends on the initial conditions. That is, even at large Mach numbers amplification of lateral integral length scales has been observed in the case of fine grids.

Integral length scales in the longitudinal direction were reduced after the interaction in all investigated flow cases. The integral length scales in the lateral direction increased at low Mach numbers and decrease during stronger interactions. It appears that at the weakest of the present interactions the eddies are compressed in the longitudinal direction drastically while their extent in the normal direction remains relatively the same. As the shock strength increases the lateral integral length scale increases while the longitudinal decreases. At the strongest interaction of the present cases the eddies are compressed in both directions. However, even at the highest Mach number case the issue is more complicated since amplification of the lateral scales has been observed in fine grids. Thus the outcome of the interaction strongly depends on the initial conditions.

The present results clearly show most of the changes, either attenuation or amplification occur at large x/M distances where the length scales of the incoming flows are high and turbulence intensities low. Thus large in size eddies with low velocity fluctuations are affected the most by the interaction with the shock.

Table XVII summarizes in a similar fashion as before the conclusions for the parameters that were investigated in this work and their response to an increase of the mean

flow Mach number and an increase in the mesh size/Re_M.

	INCREASING M_{flow}	INCREASING Re_M/M
A	⇓	⇕
$(x/M)_0$	⇑	⇓
n	⇓	⇕
u	⇑	⇕
M_t	⇑	⇕
ϵ	⇑	⇕
$\epsilon M/U^3$	⇑	⇕
L_ϵ	⇑	⇑
λ	⇑	⇑
η	⇓	⇑
$L_{11}(\xi_1)$	⇕	⇓
$L_{11}(\xi_2)$	⇓	⇕

Table XVI: Summary of conclusions for the decaying isotropic flowfield.

	INCREASING M_{down}	INCREASING Re_M/M	SHOCK WAVE INTERACTION
A	⇕	⇕	⇑
$(x/M)_0$	⇑	⇓	⇑
n	⇕	⇕	⇑
u	⇓	⇓	⇕
M_t	⇑	⇕	⇕
ϵ	⇕	⇓	⇓
$\epsilon M/U^3$	⇓	⇓	⇑
L_ϵ	⇑	⇑	⇑
λ	⇕	⇑	⇑
η	⇕	⇑	⇑
$L_{11}(\xi_1)$	⇕	⇑	⇓
$L_{11}(\xi_2)$	⇓	⇓	⇕

Table XVII: Summary of conclusions for the interaction of a decaying isotropic flowfield with a planar shock wave.

APPENDICES

APPENDIX A

OPERATION OF THE SHOCK TUBE FACILITY

An effort has been made to incorporate as many as possible standard, commercially available, components in the design of the facility. The facility, in a very simplistic description consists of several pipe sections flanged properly to allow for no leak operation. The driver and the cone have been designed to withstand maximum pressure of 2,200 psig while the driven and working section are designed for 1,000 psig. The material is High Strength Carbon Steel A106 for the driver, the cone and the flanges. Stainless Steel T304L grade for all the rest of components including the pipes are used.

A thin, scored ⅛" thick aluminum diaphragm is placed in the flange between the driver and the cone. Compressed air or any type of high pressure gas can be supplied to the driver. In this work the gas that was used was compressed air that was supplied from a reciprocating compressor. The diaphragm ruptures suddenly at a given pressure or with the assistance of the plunger. This rupture (sudden burst) creates a shock wave travelling downstream towards the working section where several measurements were carried out. At the end of the experiment the ruptured diaphragm is replaced by a new one by sliding the driver 18" to the left. The driver is sliding on two guiding shafts/rods with the help of two special linear bearings. A similar sliding mechanism is also used for the working and viewport section. This is necessary since several models (turbulence generation grids) were supported in the first flange of the working section and needed to be replaced from time to time.

APPENDIX B

CALIBRATION TECHNIQUES

B.1 PRESSURE TRANSDUCERS CALIBRATION

To calibrate the pressure transducers, the solid end plate was installed on the shock tube. All the pressure transducers were installed on the shock tube and then the shock tube was pressurized at different pressures. The pressure inside the tube was recorded by reading a pre-calibrated pressure gauge.

Data was acquired for a wide range of pressures and the signal output of each transducer was acquired at the time of pressure stabilization in the shock tube.

The stored binary data was converted to ASCII form using a basic program. The data was read and then averaged. The averaged signal output is then stored in a file and with the corresponding static pressure recorded from the pressure gauge for further use.

The calibration revealed that the response of each transducer to the pressure difference was linearly varying. The output voltage of the transducers is plotted against the static pressure and it can be seen on figure B1. The sensitivity of each transducer can be easily found as the slope of the fitted line of the previous figure.

Recalibration of the pressure transducers was performed several times at different time periods from each other. Each calibration set was found to be identical to the original calibration set presented in figure B1.

B.2.1 TEMPERATURE (COLD WIRE) CALIBRATION

The cold wire, when placed in a flow, it measures both velocity and temperature fluctuations. In order to use the cold wire as a temperature measurement device, the sensitivity of the wire to velocity fluctuations must me minimal , i.e. $\frac{\partial E}{\partial U} \approx 0$. The total resistance of the 2.5 μm wire, prongs and wiring is measured using a multimeter. The resistance (0.6 Ω in average) for each prong and the Teflon coated wiring attached to it, is subtracted from the total resistance in order to obtain the wire resistance.

The temperature wire is chosen to be longer and 2.5 μm for two reasons. A long wire will minimize end conduction effects since the length to diameter ratio of the cold wire is between 600 to 800 (Bradshaw 1971). Thus the length of the cold wire must meet the previous criterion.

When a 2.5 μm Platinum/Tungsten wire is placed in a high speed flow then under certain conditions it becomes insensitive to velocity fluctuations and therefore the 2.5 μm wire is best suited for temperature measurements as it will be evident from the discussion that follows. To calculate the corresponding sensitivities due to temperature and velocity fluctuations of the 2.5 μm under the prescribed conditions the following expressions are used.

The temperature sensitivity on the flow velocity of the temperature wire can be found by using the suggestion of Wyngaard (1971) as:

$$\frac{\partial T}{\partial U} = \frac{I^2 R_w \left(\frac{1}{4} Re_d^{n}\right)}{\pi k_f l U_1 (0.24 + 0.56 Re_d^{n})^2}$$

where I is the supplied current, R_w is the resistance of the wire, Re_d is Reynolds number based on the diameter of the wire, k_f is the thermal conductivity of air, l is length of the wire and U_1 is the mean flow velocity. A typical value for the 2.5 μm Platinum/Tungsten wire in a 200 m/sec flow will result a $\frac{\partial T}{\partial U} = 1.179 \times 10^{-5} \frac{°C}{m/sec}$. Typical values that were used in the previous calculation are: I=0.3mA, l=1.5 mm, R_w=20Ω, k_f=0.025 $(A^2\,\Omega)/(m\,°C)$. The temperature sensitivity $\left(\frac{\partial E}{\partial T}\right)$ is needed to find the output fluctuation due to the mean velocity $\left(\frac{\partial E}{\partial U}\right)$. That is $\frac{\partial E}{\partial U} = \frac{\partial E}{\partial T}\frac{\partial T}{\partial U}$ and $\frac{\partial E}{\partial T} = \alpha I R_w$ where α is the temperature resistivity of the Platinum/Tungsten wire equal to 0.0039 (1/°C).

A typical value for $\left(\frac{\partial E}{\partial T}\right)$ is 24×10^{-3} mV/°C. Therefore, the velocity sensitivity is

$$\frac{\partial E}{\partial U} = \frac{\partial E}{\partial T}\frac{\partial T}{\partial U} = 2.829 \times 10^{-7} \frac{mV}{m/sec}.$$

A second calculation of the wire sensitivities is needed at low speed flows since the cold wires are placed in flowfields with various flow velocities. This way an upper bound of the wire sensitivities can also be established. For a minimum flow velocity of 20 m/sec the temperature sensitivity of the wire to mean velocity is: $\frac{\partial T}{\partial U} = 2.35 \times 10^{-4} \frac{°C}{m/sec}$ resulting

in a maximum velocity sensitivity of the wire of $\frac{\partial E}{\partial U} = 5.6 \times 10^{-6} \frac{mV}{m/sec}$.

In view of the above calculations, $2.8 \times 10^{-7} < \frac{\partial E}{\partial U} < 5.6 \times 10^{-6} \frac{mV}{m/sec}$, the 2.5 μm can be safely assumed to be insensitive to velocity fluctuations in the above range of conditions.

The output voltage can be converted easily now using a conversion factor similar to the above $\left(\frac{\partial E}{\partial T} \right)$ with the corresponding operating conditions of each cold wire (i.e. constant current, R_w, l_w). The above value for the temperature sensitivity can be used without the introduction of a significant error. A typical temperature calibration can be seen in figure B2. The 1-D inviscid total temperature of the flow is plotted against the calculated mean total temperature using the above calibration value. The recorded shock strength of each experiment was used to identify the 1-D total temperature. The data collapsing on a straight line supports the insensitivity claim of the temperature wire to velocity as well as the validity of the calculations.

The calibration of the cold wires for the rake assembly, the three wire probes and the nine wire probe were performed using the above procedure.

B.2.2 FREQUENCY RESPONSE AND COMPENSATION

Hot-Wire Anemometry (HWA) has been extensively used in the past for turbulence measurements in incompressible flows. Kovasznay (1950) described first the use of HWA

in supersonic flows and Morkovin (1956, 1960) addressed several of the problems associated with density fluctuations inside the flow. The recent review paper by Stainback and Nagabushana (1993) discusses some of the major issues associated with the use of hot-wire Anemometry (HWA) in compressible flows. Smits, Muck and Hayakawa (1983) and Smits and Muck (1987) demonstrated the use of constant temperature anemometry in obtaining reliable time-dependent information of the turbulence structure in supersonic boundary layers and shock-wave interactions. The present work describes several HWA techniques applicable in shock-tube turbulence research. The flow under investigation is an interaction of a plane shock-wave with homogeneous and nearly isotropic turbulence. In many occasions, like the present one, a shock-tube setup fits much better the research requirements than a regular supersonic wind tunnel. However the application of HWA techniques in this type of turbulence measurements is not straight forward, particularly when time-dependent measurements are required.

The frequency response of the hot-wire as it was measured during the passage of the shock wave was found to be of the order of 100 kHz. The cold wire signal had a flat frequency response up to 8 kHz at 150 m/s, a value which is close to that suggested by Antonia et al (1981) for 2.5 μm wires. This frequency limit is rather low for the present applications. For frequencies above the cut-off frequency, it is necessary to compensate the thermal lag up to the frequencies of interest. The frequencies under consideration are those present in the flow before and after the shock wave as well as those associated with the passage of the shock wave itself. This differentiation is necessary since velocities in the induced flow behind the shock are substantially lower than shock propagation velocities.

In practice, if end conduction effect can be eliminated by increasing the l/d ratio, the amplitude response of the cold wire, in general, falls as $[1+(f/f_o)^2]^{-n}$ for frequencies higher than the wire cut-off (3dB) frequency f_o. Therefore a typical compensator should be able to provide response which increases as $[1+(f/f_o)^2]^n$. The exponent n usually takes a value of n=1/2 which makes the cold-wire behaving like a low-pass filter and it can be estimated from measurements of the frequency response function which is defined as the output of the system to a unit impulse. The present experimental set-up is the ideal platform for this type of measurement since the passage of the shock wave can be considered as a step function in temperature. Figure B3 shows a plot of the modulus of the frequency response function or amplitude response for two different cold wires. The present data have shown that n can take values in the range 0.3 to 0.5, with most of the values closer to 0.44 .

If a standard RC type of electronic frequency compensation circuit is used to boost the frequency response up to 40 kHz, the time constant of the compensation has to be adjusted by trial and error and it had to be set somehow a priori before each experiment since it depended on the flow velocity. A value of n=0.5 is usually used.

It can be realized that the capture of both the incident and the reflected shocks can not be obtained with one setting of the compensating time constant because the speed of the reflected shock is smaller than that of the incident shock. One setting, which provides adequate compensation to capture one case, may over or under-compensate the second one. However when the focus of the present investigation is the effect of the reflected shock on the flow induced by the incident shock, the amount of compensation can be adjusted to capture the reflected shock wave. This amount of compensation however is usually small to

capture the incident shock and therefore the total temperature signal immediately after the incident shock may look slightly undercompensated. As a result the computed velocity signal could be also undercompensated in this region because the temperature signal was used to correct the hot-wire voltage for temperature contamination.

In general analog compensation is time consuming and requires a knowledge of the time constant of the wire (see also, Barre et. al., 1993). These two drawbacks make the use of digital techniques more appealing.

In the case of digital compensation the Inverse Fast Fourier Transform of the transfer function corresponding to the amplitude response, shown above, was convoluted with the signal in the time domain. This type of compensation was carried out off-line and provided more flexibility in determining the right amount of power needed to increase the frequency response of the cold wire. In addition to the time constant the exponent n was also adjusted by trial and error.

A correctly compensated signal should follow, as closely as possible, a step function response. However, even under the most favorable operating conditions of the wires and the circuitry, conductivity of the fluid will prevent the temperature signal from appearing like an ideal step function. In addition, adjustment of the two parameters f_o and n can cause overcompensation of the signal i.e. substantial overshooting of the signal beyond the step function response indicating higher order response. In the case of digital compensation overshooting may also be a result of substantial side-lobe leakage because of the finite Fourier transforms and finite time windows used. No Hanning window or any type of time history tapering was used in the present work since overshooting of the signal was avoided

by proper adjustment of f_o and n.

Figure B4 shows a digitized record of an uncompensated total temperature signal together with several compensated signals corresponding to different values of the exponent n. The frequency response of this particular wire falls off as -0.45 and therefore the correct compensation corresponds to n=0.45. In general compensation improved the frequency response of the cold-wire by a factor of 5 or more.

As was mentioned earlier the purpose of frequency compensation for thermal lag in shock tube applications is to restore energy in the frequency band $f > f_o$ of the two flow regimes i.e. before and after the passage of the shock and of the two shock waves i.e. incident and reflected so that the temperature signal is aligned in time with that of velocity. The two flow regimes and the two shock waves have characteristic velocities which may be considerably different in each of these four cases. In some of the present applications, for instance, the flow velocities before and after the shock and the shock wave velocities differed from each other by a factor between 1.5 and 3. If only one f_o is used throughout the whole signal then some mismatch between the applied compensation characteristics and those of the original cold-wire system should be expected. Off-line digital compensation techniques allow for piece-wise adjustment of f_o and therefore the effects of potential mismatching are reduced.

The flexibility which is inherent with digital off-line data processing makes this technique more attractive. However, analog compensation should not be discarded because it is known from the work of LaRue and Libby (1978) and Weir et al. (1981) that if the cold-wire is not correctly compensated, the velocity statistics do not change considerably.

In the present flow temperature fluctuations are only 2% of the mean temperature. This level of fluctuations is relatively low and therefore the effect of any possible "mismatched" compensation on velocity statistics is small. This is not only true in the analog compensation but also in the digital one, as will be demonstrated later where some results of the qualification tests are shown. The major function of compensation is to align in time the temperature jumps with those of the hot-wire signals and to correct instantaneously the later for temperature contamination.

To demonstrate the present technique in practice measurements of turbulence intensities have been obtained in the flow behind a grid where the decaying turbulence interacts with a shock wave. The induced flow after passing through the grid has the features of a nearly homogeneous and nearly isotropic turbulent flow and it is subjected to an interaction with the reflected shock off the end wall and travelling in the opposite direction. Figure B5 shows a typical velocity signal obtained by the present technique. The main characteristics of the interaction are a sudden decrease in velocity with considerable increase in turbulent fluctuations, and a sudden increase in temperature and pressure, features which are typical of a suddenly compressed flow.

The effect of compensation on measured statistical quantities has been investigated systematically by varying the two parameters n and f_o independently. Three different values f_o were used corresponding to the cut-of frequency of the shock wave ($f_{o,s}$), that of the flow upstream of it ($f_{o,u}$) and that of the flow downstream of the shock ($f_{o,d}$). The values of $f_{o,s}$ have been directly estimated from the rise of the cold-wire signal after the passage of the shock, while estimates for the other two have been indirectly obtained from the correlation

$f_o \sim U^{0.24}$ as suggested by Antonia (1981) and the known velocity ratios U_2/W_2 and U_1/W_1. Figure B6 shows the effect of the exponent n, which describes the amount of applied compensation, on the rms value of the fluctuations of the longitudinal velocity component before and after the passage of the shock wave. The values of n vary from n=0 (no compensation) to n=1. The results of figure B6 clearly indicate that the application of compensation has practically no effect on the velocity r.m.s. values. The values of rms remain unaffected by the substantial changes in n as well as in cut off frequency f_o. There is however a more pronounced effect of compensation on the statistics of static temperature. Figure B7 shows the dependence of θ_{rms} on the exponent n for various values of f_o. As is expected compensation increases the level temperature fluctuations by artificially restoring energy at high frequencies. There is some considerable change in the r.m.s. level of temperature fluctuations for values of n between 0.4 and 0.5 and some enormous increase of θ_{rms} for n=1. The present work indicated that values for n>0.75 are rather unrealistic, and that value of n between 0.4 and 0.5 should be used. In this range of n, the effect of f_o is also very small.

The effect of compensation on higher order statistics like the skewness of velocity fluctuations, S_u and the skewness at velocity derivative fluctuation $S_{\partial u/\partial x}$ has also been investigated. Both quantities are useful in qualifying the present flow as isotropic.

The approach to isotropy can be assessed by considering S_u (see Mohamed and LaRue 1990) while according to the analysis of Taylor (1938) $S_{\partial u/\partial x}$ represents the average rate of production of mean square vorticity by vortex stretching. The skewness of velocity

fluctuations S_u was found to be close to zero (see Honkan and Andreopoulos, 1992). Batchelor and Townsend (1949) indicated that $S_{\partial u/\partial x}$ is a function of turbulent Reynolds number $Re_\lambda=(u_{rms}\lambda)/\nu$ where λ is the Taylor microscale. Specifically, he suggested that $S_{\partial u/\partial x}$ decreases with increasing Re_λ. In the present experiments Re_λ has values between 600 and 1000, depending on the grid size and therefore $S_{\partial u/\partial x}$ may reach values lower than 0.2 which was found by Mohamed and LaRue (1990) for Re_λ=50.

Figure B7 shows the effect of compensation on the skewness $S_{\partial u/\partial x}$. The values of $S_{\partial u/\partial x}$ before the interaction are very moderately decreased for n=0.5 while they drastically change for n=1. The values after the interaction are much less sensitive to the amount of compensation applied to the temperature signal. These data also show that the effect of f_o is very limited in the range $0.4<n<0.5$.

The results shown in figures B6, B7, and B8 clearly demonstrate that the effect of any mismatched compensation on velocity statistics is small. Most likely, the main reason for this behavior is the low level of temperature fluctuations of the present flow.

B3 1-D HOT WIRE CALIBRATION

The 1-D hot wire that was used on the rake assembly was calibrated in the shock tube. Since the pressure measurements and calibration signals were very reliable, they were used as a pointer to calculate the shock wave velocities, incident and reflected (W_s, W_R). Flow velocities (U_2, U_5) as well as total temperature were calculated from the 1-D inviscid theory, by matching the shock strengths (P_2/P_1) and (P_5/P_1) and shock wave speeds (W_s, W_R).

No turbulence generation grid was used during calibration. Several diaphragm ruptures creating various shock strengths were recorded for different driver strengths. The turbulence level of a typical calibration was about **1.0%** so it can be adequately considered for calibration. Calibration signals consist of a pressure signal, a hot wire signal and a temperature signal. Figures B9, B10 present a typical calibration set of unprocessed signals.

The shock strengths can be directly found from values based on the mean recorded pressure before and after the reflected shock. The hot wire voltages (E_2, E_5) are also found as the mean voltages before and after the reflected shock. The above values together with the total temperature (T_o) will produce two calibration points (one before and one after the reflected shock). The functional relation of the Nusselt and Reynolds numbers for the hot wire probe leads to the following relation:

$$\frac{E_i^2}{T_w - T_\infty} = A\left[\frac{T_\infty}{T_r}\right]^a + B\left[\frac{T_\infty}{T_r}\right]^b (\rho U)_i^n$$

where T_w (should be calculated from the overheat ratio applied to the wire from the anemometer) is the wire temperature, T_o is the total temperature of the flow and T_r is the

reference temperature (usually T_r is the ambient temperature $T_{amb}=T_1$). The overheat ratio applied to a hot wire is defined as: over $= \frac{R_w}{R_0} - 1 = \alpha(T_w - T_0)$ where the subscript (0) refers to ambient conditions and α is the temperature resistivity of the Platinum/Tungsten wire equal to 0.0039 (1/°C). The factors $(T_{oi}/T_r)^a$ and $(T_{oi}/T_r)^b$ represent the dependence of the total temperature to the thermal conductivity K and viscosity μ respectively. The subscript (i) represents the value for upstream or downstream of the reflected shock. The exponents a, b, and n were suggested by Kovasznay (1950) to be equal to a = b = 0.768 and n = 0.45. The same values were used in this work. A typical calibration curve is shown on figure B11. The straight line suggests that the data collapses in one curve and that the calibration technique is valid.

The single wires of the rake assembly and those of the nine wire probe were calibrated in the same manner.

B4 CROSS ("X") WIRE CALIBRATION

Calibration of two wires arranged in an X configuration demands the determination of the angle (ψ) formed between the incident flow and the normal to the wire. An estimation of the wire angle ψ can produce large error in the analysis of the collected data. To accurately determine the wire angle, a calibration fixture was constructed to accommodate all 6 probes simultaneously at a height where boundary layer effects of the wind tunnel are

not present. The calibration fixture is able to accurately pitch the probes up to $\pm 50^{o}$ with respect to the incoming flow. The fixture was placed in the low speed wind tunnel and data at several angles was acquired for pitch calibration of the probes. A photograph of this fixture placed in the wind tunnel with all six probes installed on it is shown in figure B12. Estimation of hot wire constants was also attempted at the highest flow velocity of the wind tunnel (11 m/sec). Pitch calibration was performed for nine different pitch angles (-15, -10, -5, 0, 5, 10, 15, 20, 25 degrees with respect to the incoming flow). When data is acquired the wire angle can be rechecked according to the following:

$$\left[\frac{E^2-E_o^2}{(E^2-E_o^2)_{\Delta\psi=0}}\right]^{\frac{1}{n}}\cos\Delta\psi = \tan\psi_{eff}\ \sin\Delta\psi$$

where $\Delta\psi$ is the pitch angle, ψ_{eff} is the effective wire angle and as an initial approximation will be equal to ψ, E_0 is the calibration intercept at $\Delta\psi=0$ and E is the output of the bridge.

The above equation has to be plotted for both wires. The left hand side of the equation should be plotted as the Y-axis and sin $\Delta\psi$ as the X-axis. Then two effective wire angles (ψ_{eff}) were obtained, thus the mutual angle will be the addition of those two. Any deviation from a straight line will indicate that there is some prong interference or any departure from the cosine law (U_{eff} = Ucosψ). The mutual angle of two X wires of a three wire probe is shown in figure B13. It can clearly be seen from this figure that no prong interference is evident. The results are satisfactory and there is no need to use any other complex calibration scheme. King's law was applied to obtain the effective cooling velocity.

$$E^2 = A + BU_{eff}^n$$
where
$$U_{eff}^2 = U_N^2 + k^2 U_T^2$$

The normal velocity component is equal to $U_N = U\cos\psi$ and the tangential velocity component is equal to $U_T = U\sin\psi$. In the previous relations the angle $\psi = \psi_{eff} \pm \Delta\psi$ depending on the orientation of the hot wire. After velocity and pitch calibration in the tunnel are completed and found to be satisfactory, the probes were placed in the shock tube for high speed calibration as it was done with the single wire. Again, when calibration of the cross wires is attempted the turbulence generation grids were not installed. Similar techniques as there were applied for the single wire were applied for the cross wire high speed calibration. Figure B14 presents a typical high speed calibration for a pair of X wires.

The temperature wire (Cold Wire) was calibrated as it was calibrated for the rake assembly and the nine wire probe's cold wires (Section B2).

B5 CCD CALIBRATION

The optics involved with the CCD are very simple and straight forward. There is no aperture involved with the CCD camera since electronic apertures may introduce noise and. thus, many of the captured features of the interaction may be considerably masked. The focusing lens that was used was a Nikon 105mm f/4.5 UV Nikkor lens and prior to any experiment the exact focal length was set on the lens and checked by capturing a photograph

of a graph paper (printed grid on the graph paper must be clear with no distortion of the lines) at the desired radial position in the shock tube. The f-stop that was used was the minimum (f4.5 ie largest aperture) so that maximum light can enter the lens. A drawback of this is that the depth of field is drastically reduced and therefore the focusing position must always be carefully checked before any experiment, using the above mentioned graph paper. Light is continuously captured and recorded by the camera unless otherwise instructed (stop the operation). A few laser shots have to be captured with no flow in the shock tube in order to obtain the laser light recorded on the chip due to its reflection from the shock tube walls. Since the viewport section was painted black the reflection of the laser sheet was minimal.

The above mentioned images were added and averaged, thus, an average ambient light illumination and reflection picture was formed. The averaged ambient light and laser reflection picture was subtracted from the shock captured images. The processed image is free of any unwanted outside effects. This procedure assumes that all the calibration images are recorded at a constant incoming light intensity, therefore the incoming light is recorded at the same pixels all the time. For further information on the pixel manipulation and filtering of images, the reader can refer to the Astromed manuals.

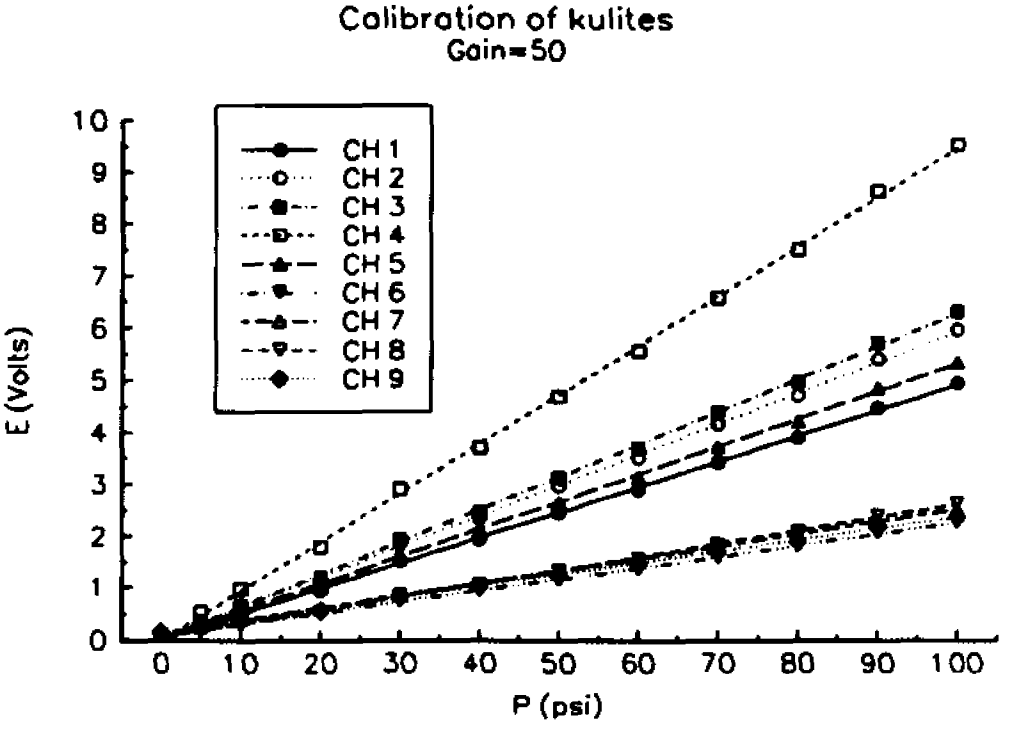

Figure B1: Pressure transducer calibration

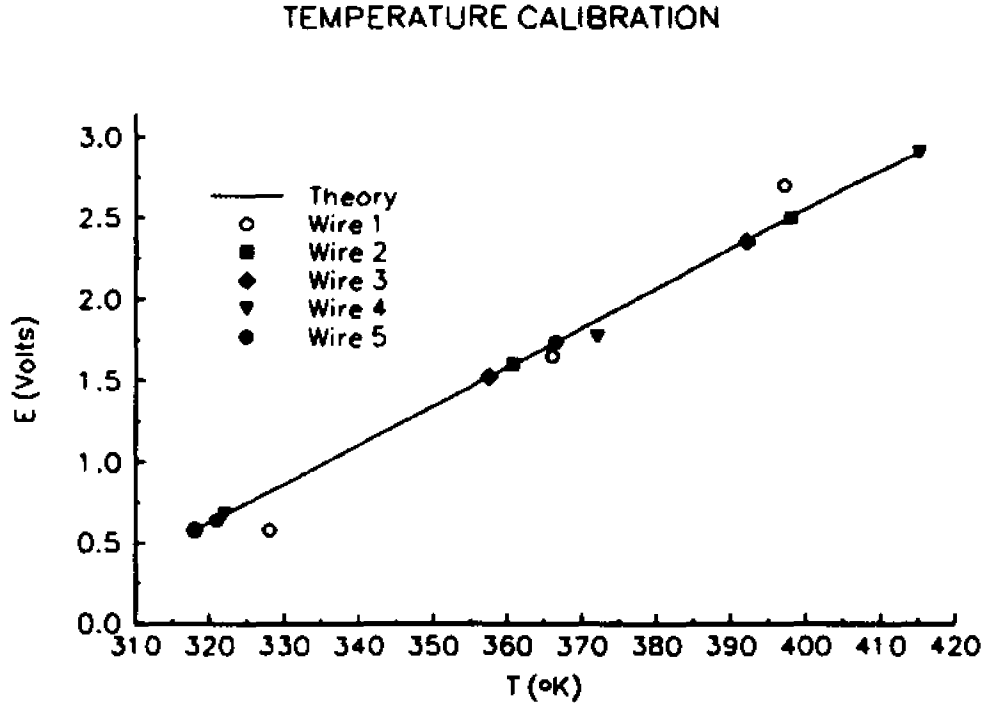

Figure B2: Temperature calibration

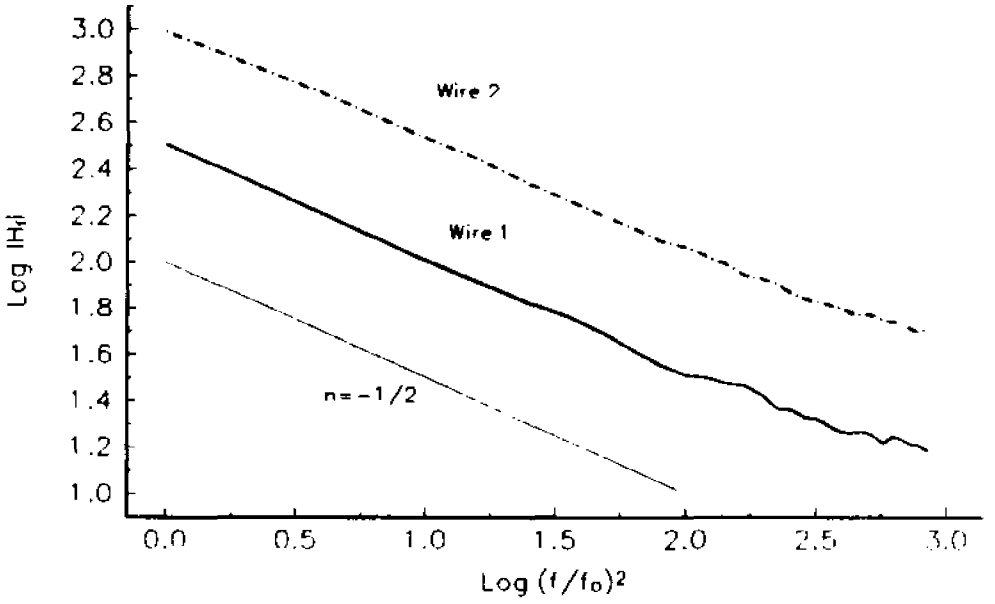

Figure B3: Measured frequency response function H_f of cold wires.

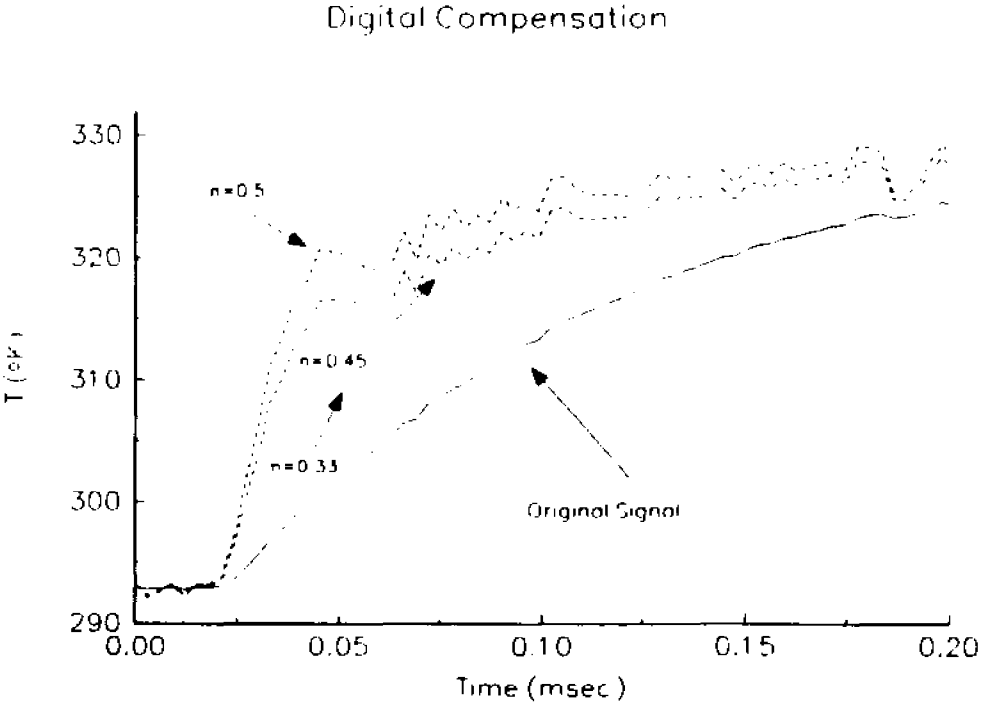

Figure B4: Compensation effect on the temperature signal.

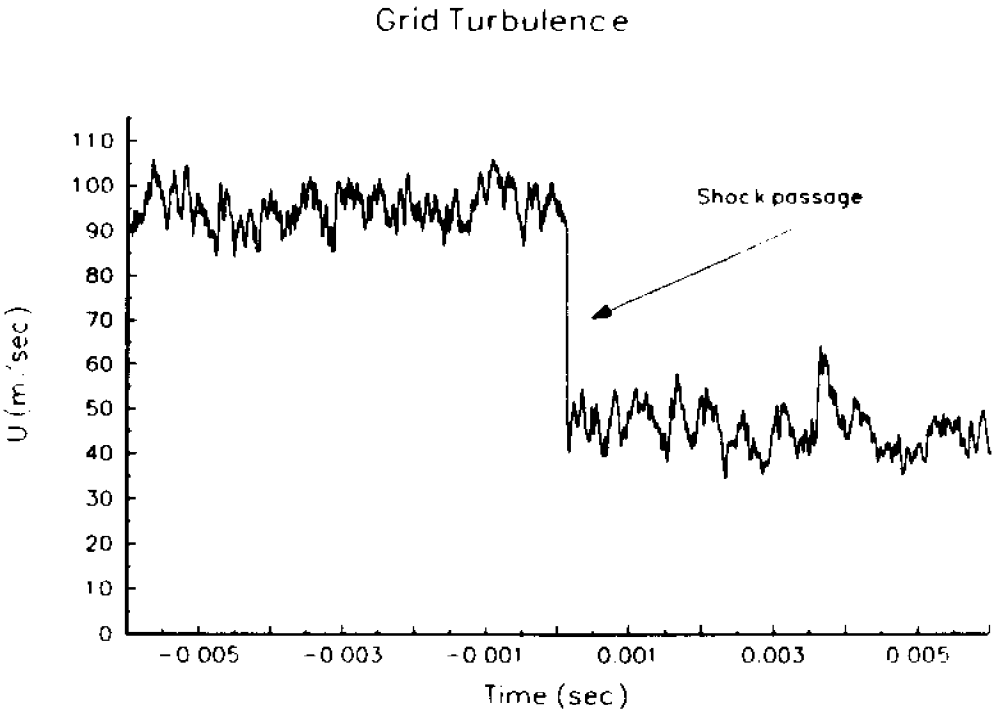

Figure B5: Velocity signal before and after interaction with the reflected shock wave in a flow downstream of a grid.

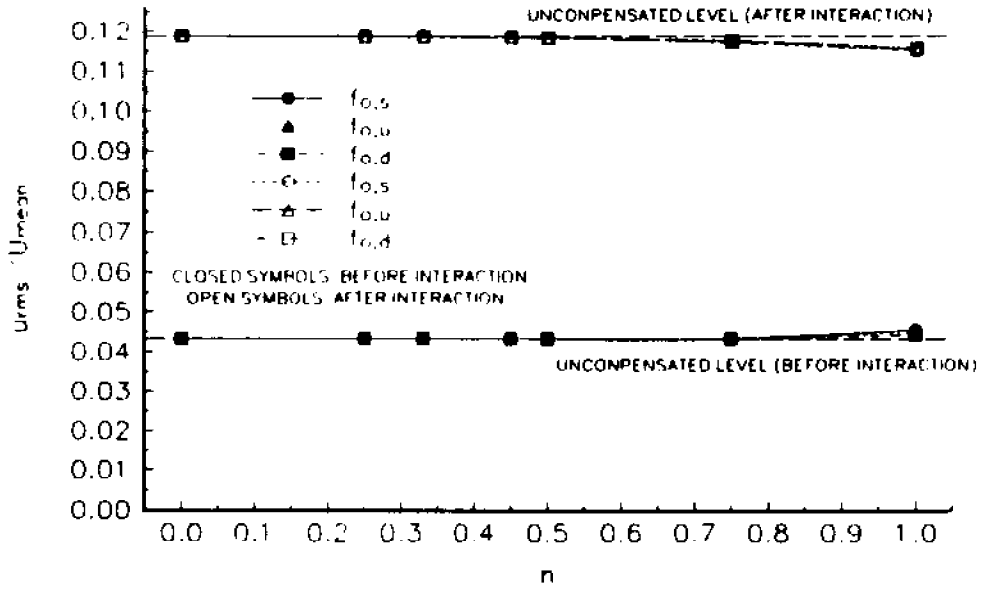

Figure B6: Compensation effect on u_{rms}

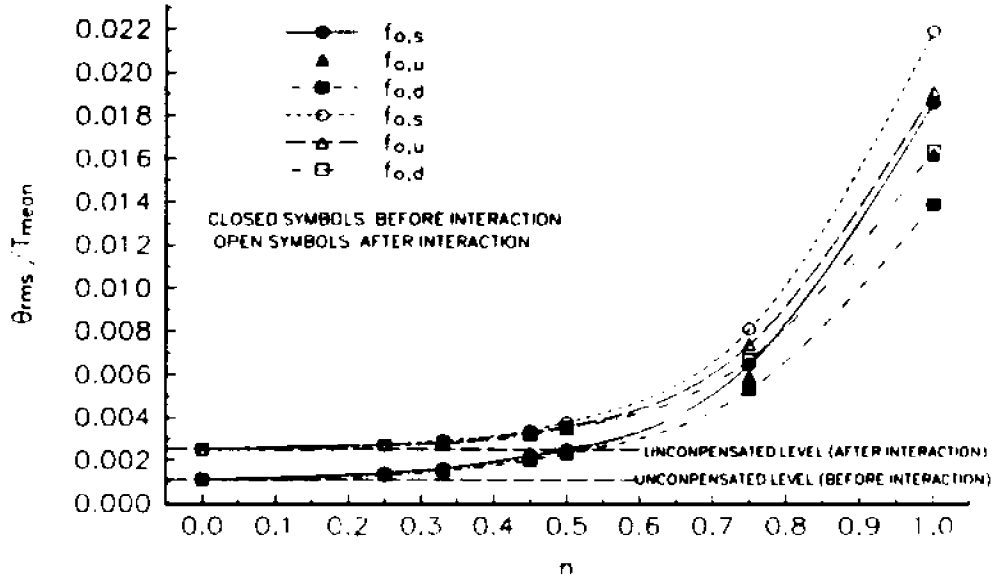

Figure B7: Compensation effect on θ_{rms}

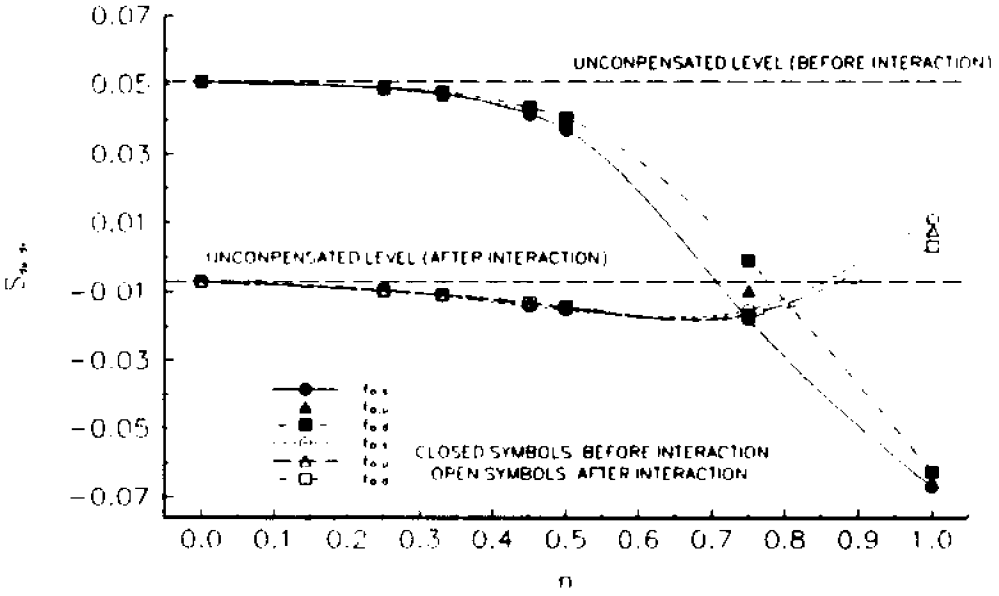

Figure B8: Compensation effect on $S_{\partial u/\partial x}$

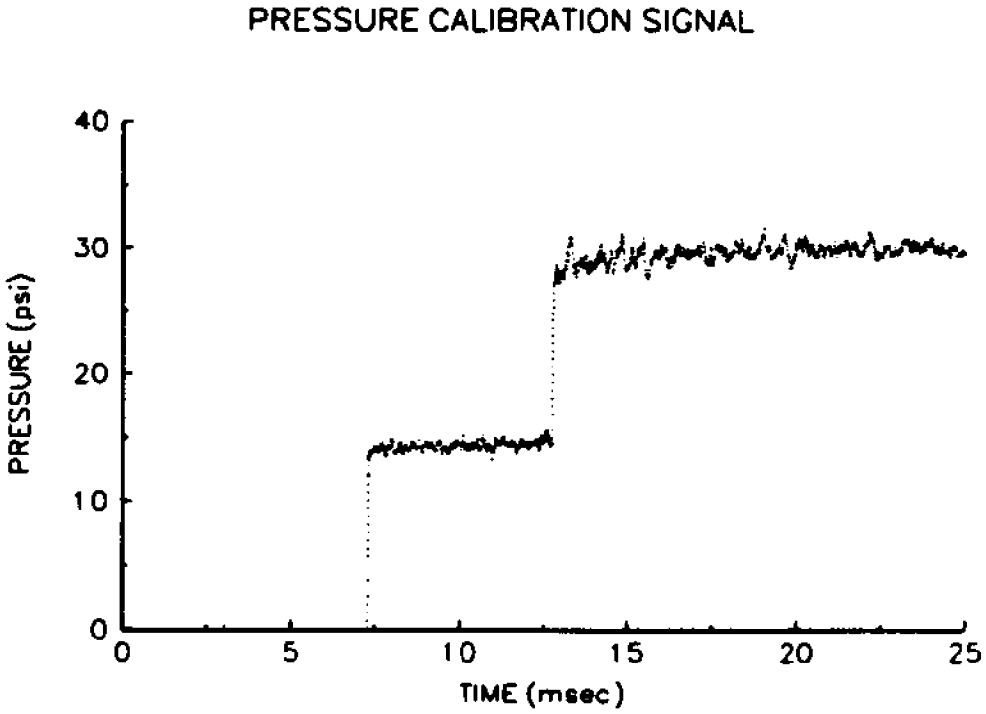

Figure B9: Pressure calibration signal

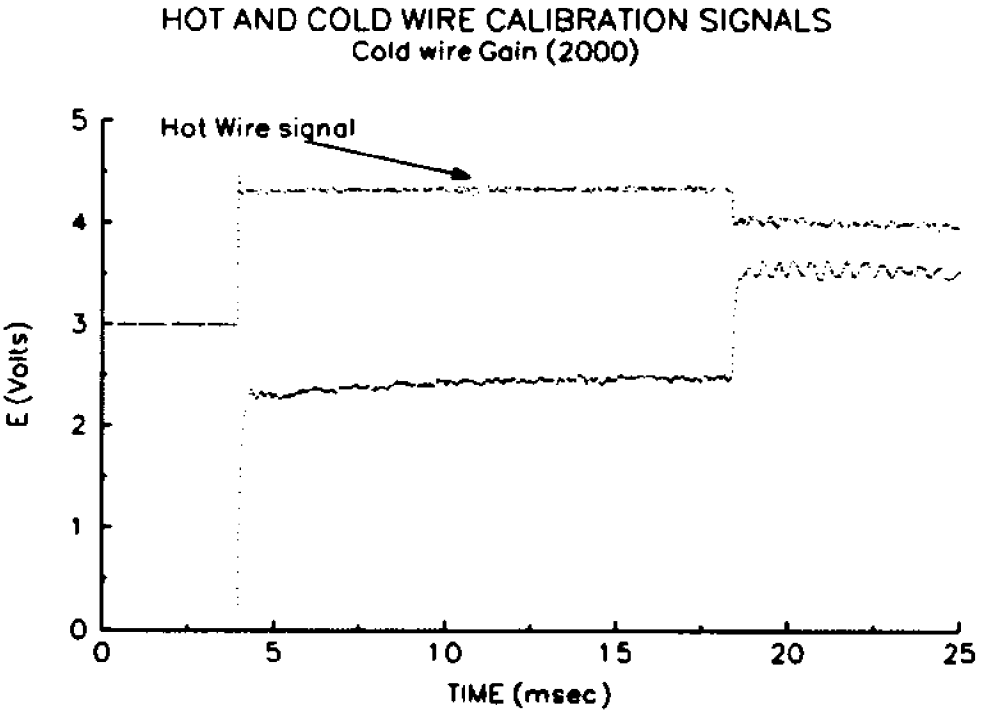

Figure B10: Hot and Cold Wire calibration signals

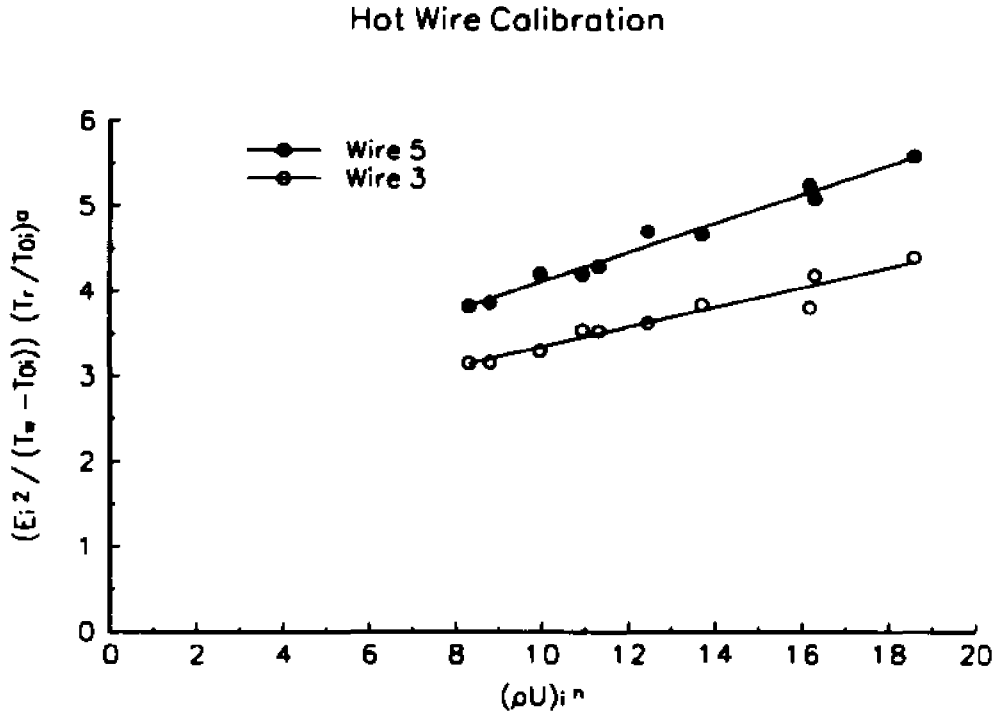

Figure B11: Typical Hot Wire calibration in shock tube flows

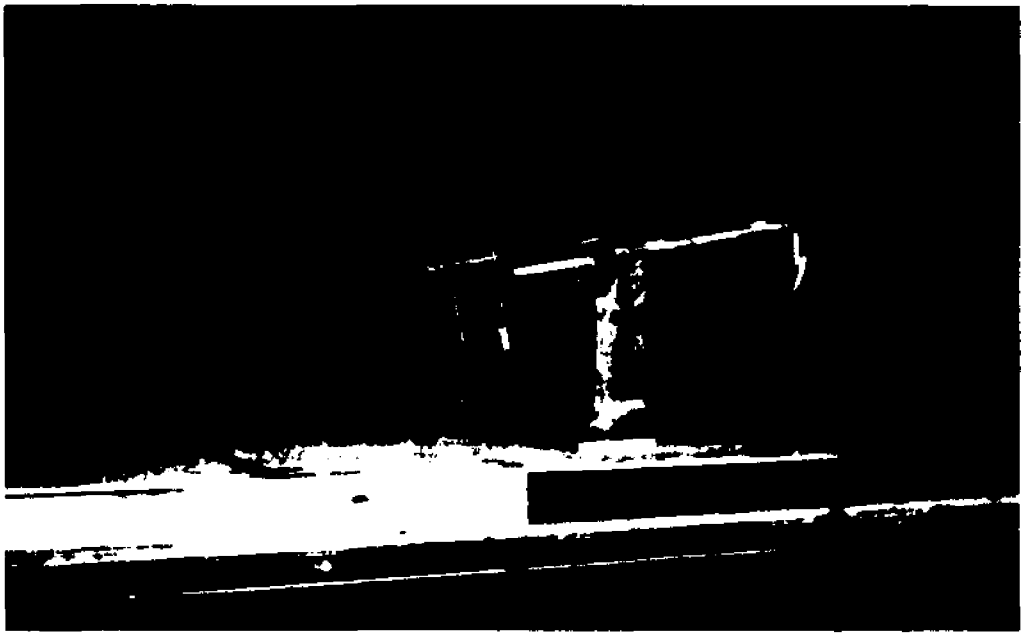

Figure B12: Photograph of calibration fixture in the wind tunnel with 6 X-wire probes installed for pitch calibration.

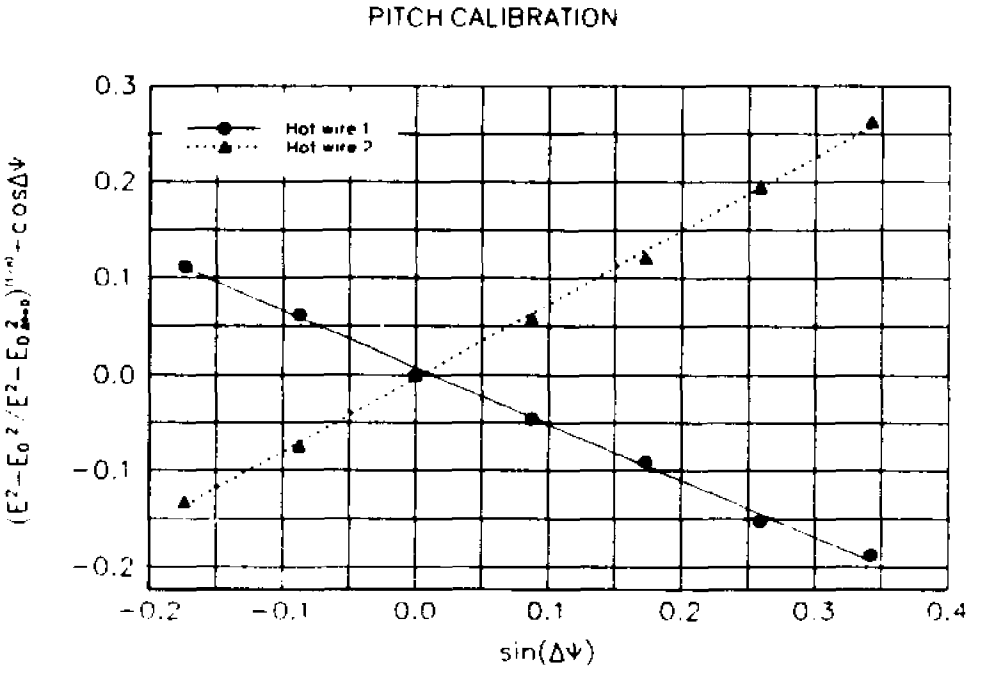

Figure B13: Pitch calibration of a three wire probe.

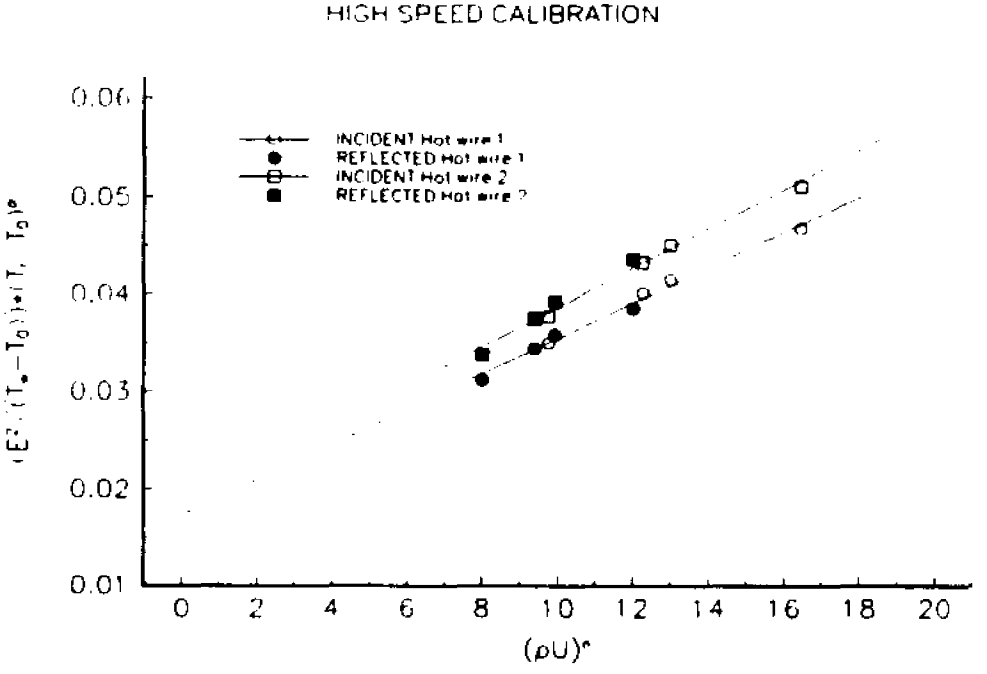

Figure B14: Velocity calibration of a three wire probe in the shock tube.

APPENDIX C

PROBE DESIGNS AND CONSTRUCTION

C1. RAKE ASSEMBLY AND PROBES

The rake was made out of stainless steel ASTM A269-T304L 5/16" tube with a 0.065" thick wall so the impact of the shock wave would not break it or bend it. Several materials and tube sizes were tested in the shock tube to determine the optimum size and material for the rake assembly. The materials that were tested were brass tubing, copper tubing and stainless steel tubing of various diameters and wall thickness. Initially a brass tubing was tested and the effects of the impact of the incident shock wave on the rake were devastating. A photograph of the above mentioned test, shown in figure C1, speaks for itself. Copper tubing was also tested with slightly better results. The above mentioned stainless steel tube was chosen since it had the best performance after testing different size tubes. The final design was also adapted because it can withstand the impact of the shock wave travelling at a Mach number of 4.

The prongs are made out of guitar stainless steel string 0.014" in diameter. Ceramics are made from Omegatite 350 by OMEGA Corp. model FRA-164116 and the wires used to connect the prongs with BNC receptacles were Teflon coated and 0.020" in diameter. Since all the wires pass through the rake's tube, these wires had to be used because they offer good electrical shielding and isolation, while the overall diameter of the wire is adequately small. Using this arrangement, the wires were protected by the impact of the shock wave and they

were able to exit the shock tube to be soldered to the BNC receptacles.

The four prongs of each probe were ground and two of them were opened up a small amount, while the other two were compressed a small amount. The above created a distance between two prongs of 0.8 mm and a distance of 1.5 to 1.8 mm between the other two prongs. The 0.8 mm prongs were used for velocity measurements and a 5 μm Platinum/Tungsten wire was fused on. Between the prongs separated 1.8 mm, a 2.5 μm Platinum/Tungsten wire was fused to be used for temperature measurements. Figure C2 shows a typical probe used on the rake assembly. A constant current circuit was externally connected on the 2.5 μm Platinum/Tungsten wire, so Constant Current Anemometry technique could have been applied as well as to facilitate the acquisition of data to be used later on as temperature measurements. The constant current circuit is shown in figure C3 typically uses a 1.5 V battery and a 5KΩ resistance resulting to a constant current through the circuit I of approximately 0.3 mA. The temperature wire was fed into EG&G pre-amps for amplification of the signal.

The stainless steel tube was machined accordingly to accept five probes at equally spaced distances. A figure of the rake assembly installed in the shock tube is given in chapter 6, figures 6.4a and 6.4b. The ceramic of each probe was enclosed in several brass tubing to add strength and taper the probe. It was then permanently glued on to the stainless steel tube. The minimum diameter of the probe was 1.8 mm and the maximum, at the connection with the stainless steel tube was 3 mm and its overall length 76.2 mm. A sketch of this probe is presented in figure C4.

C2. THREE WIRE PROBE ASSEMBLY AND PROBES

The stainless steel tube used for the three wire probes is the same as the one used for the rake assembly, the 5/16" OD with 0.065" thick walls stainless steel tube. Six assemblies were built using tubing of various lengths in order to position the assembly at different radial locations in the shock tube. Each tube is carrying one probe. The three wire probe carries 6 prongs (4 for hot wires (velocity measurements) and 2 for cold wires (temperature measurements)), 2 ceramics and the wiring as shown in figure C5. As in the rake design, the wiring is Teflon coated 0.020" in diameter and it passes through the stainless steel tubing. The two ceramics are made from Omegatite 350 by OMEGA Corp. models FRA-164116 and TRA-164116. One carries the cross wire prongs and the other the temperature prongs. The two ceramics are glued together to further enhance the rigidity of the probe. The temperature probes were opened up, as in the rake design, resulting a prong separation of 1.5 mm. Similarly to the rake probe, a Platinum/Tungsten 2.5 μm wire was fused on. External constant current circuit was also connected on each probe in order to apply the Constant Current Anemometry technique for temperature measurements.

The prongs to be used for the cross wires were cut and ground at about 45 degrees. The mutual angle produced by the two wires of the X-wire probe is about 90 degrees. The exact angle will be determined from the calibration procedure. Two photographs showing the three wire probe and its wires is shown in figure C6 and C7. The probe image was several times magnified in order to visualize the 5 μm and 2.5 μm Platinum/Tungsten wires. A ruler is offering a guide to size the probe. Each division on the ruler is 1 mm.

For each stainless steel tube a wedge was welded on to it to avoid any interference from the shock wave and the flow . Similar brass tubing was used to taper the probe and add strength. The probe was glued on to the stainless steel tubing.

A second set of three wire probes were also constructed by AUSPEX Corp. using the above design specifications. A photograph of the probe and its supporting probe is shown in figure C8.

C3. NINE WIRE PROBE

The 9-wire probes manufactured by AUSPEX Corp. consists of two major parts, the main support tube and the oval case which carries the 6 ceramics, prongs and hot/cold wires. A sketch of the nine wire probe and its dimensions is shown in figure C9.

The main support tube is a 3/8" with 1/16" thick walls, 12" long stainless steel and is design to withstand impacts from shock waves travelling up to M=4 when it is fully extended. At the end of the support tube an oval opening is machined so that the oval casing with the epoxied ceramics, prongs and hot wires can be permanently attached on the main support. A photograph of the nine wire probe and its supporting tube is shown in figure C10. The oval shape was chosen for the casing so that the frontal area of the probe is minimized. The oval casing is approximately 6 mm wide and 10 mm long. The prongs are stainless steel needles 0.018" OD and they are tapered at the end to minimize the aerodynamic load and interference on the hot wires. The oval case carries 6 ceramics which are all epoxied together. Three

ceramics are carrying the 12 prongs for the 6 hot wires and the other three carry 6 prongs for the 3 cold wires. The hot wires are 5 μm Platinum/Tungsten and the cold wires are 2.5 μm Platinum/Tungsten wires. Figure C11 presents a photograph of the 6 hot wires and the 3 cold wires. Also in this case the image of the nine wire probe was magnified to see the Platinum/Tungsten wires. External constant current circuit was connected on each probe so the Constant Current Anemometry technique can be applied for temperature measurements, shown in figure C2.

C4. PRESSURE TRANSDUCER FITTING

A special fitting was designed and built for the installation of each pressure transducer in the shock tube wall. The major concern was to built a leak proof assembly (fitting and pressure transducer) for static pressure up to 10 atm that could secure the pressure transducer in the fitting under these conditions and the impact exerted, by the passage of the shock wave, on the pressure transducer.

Brass was the material that was used for this fitting. Extensive machining was done to a 1/2" brass rod to look like the end result. Since the pressure tap on the shock tube has 1/4 NPT threads the rod was machined and threaded to 1/4 NPT. This was purposely done so that the fitting can be adjusted in a flush position with the inside wall of the shock tube. Two O-rings were used to seal the pressure transducer and a 5/32" brass tube was used to compress the O-ring on to the pressure transducer and therefore lock it in place. A set screw

is used to hold in place the brass tubing after compression of the O-rings. Figure C12 shows the brass fitting and its dimensions.

The fitting was tested, with the pressure transducer installed, with static pressure up to 8 atm and was found leak free. The 10 atm test was not performed since most of the transducers have a maximum static pressure limit of 7.8 atm. The sketch of a complete assembly can also be seen in figure 14 in Chapter 6. Ten pressure transducer fittings were built and tested.

C5. TOTAL PRESSURE PROBES

Mach Probes

To measure the time dependent total pressure, the pressure transducer must be installed in the freestream of the flowfield. Therefore a new probe was built incorporating some design from the three wire probe and some from the pressure fitting.

Namely a stainless steel tube was used to hold the probe at any radial position in the shock tube and a similar design of O-rings and compression tubing was used to secure the pressure transducer in the probe.

The stainless steel tube that was used for this assembly is the same used for the three wire probes (5/16 ' OD, 0.065" wall). At the end of the stainless steel tube a hole is drilled and tapped, since the probe which caries the pressure transducer was screwed on to the tube and locked in place with two nuts.

The probe is made out of brass and is tapered. The compression tubing that squeezes the two O-rings is U in shape. One end of it is used to compress the O-rings and the other end is entering the stainless steel tube from the back side. This is necessary because all wires coming out of the pressure transducer and the reference pressure needed for the operation of the pressure transducer are passing through the compression tube and entering the stainless steel tube where they can exit form the shock tube. This is needed since the impact of the shock wave will destroy the wiring and subsequently destroy the pressure transducer. One end of the compression tube was epoxied on to the stainless steel tube and the other end was held on the probe with a set screw. The assembly was tested for any leaks with a static pressure field up to 6 atm.

The dimensions and a sketch of the brass pressure transducer fitting and the Mach probe are shown in figures C13 and C14 respectively. Three of these probes were constructed with various lengths stainless steel tubes.

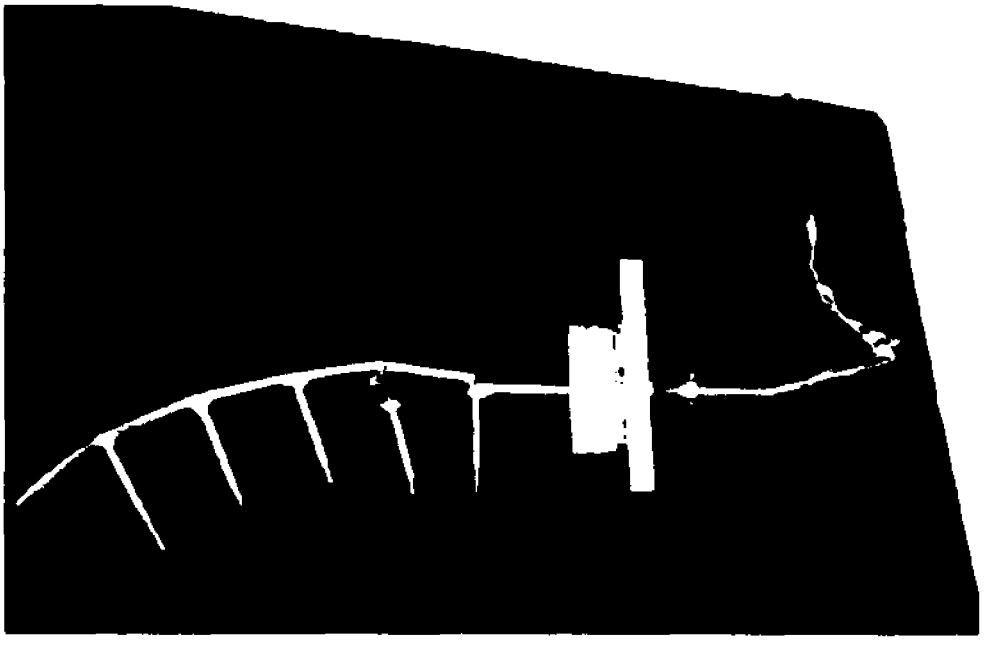

Figure C1: Photograph of an initial test performed for a hot wire rake

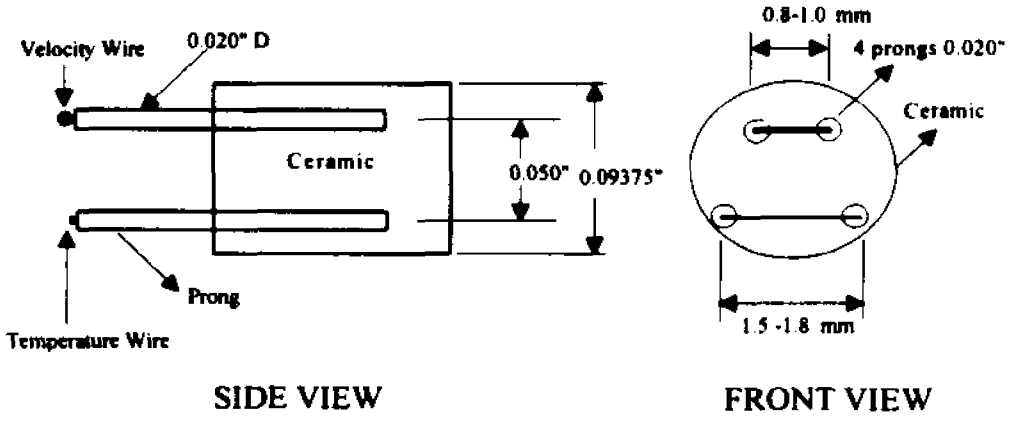

Figure C2: Front and side views of a typical rake probe (not to scale).

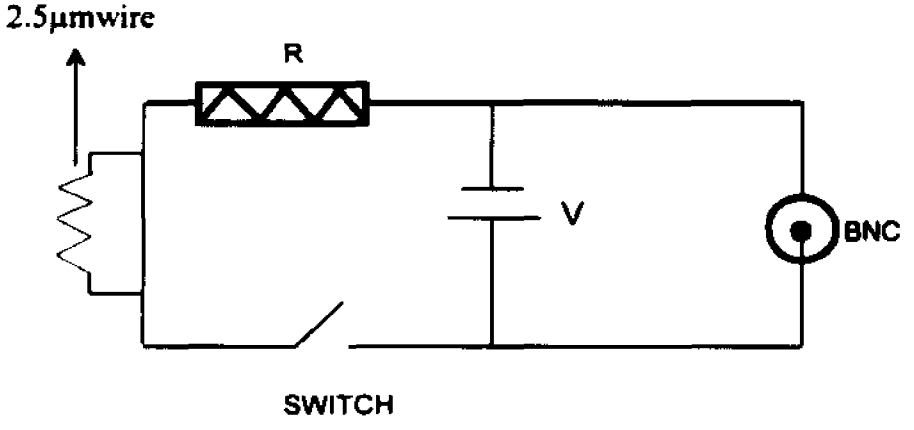

Figure C3: Constant current circuit used for all temperature wires.

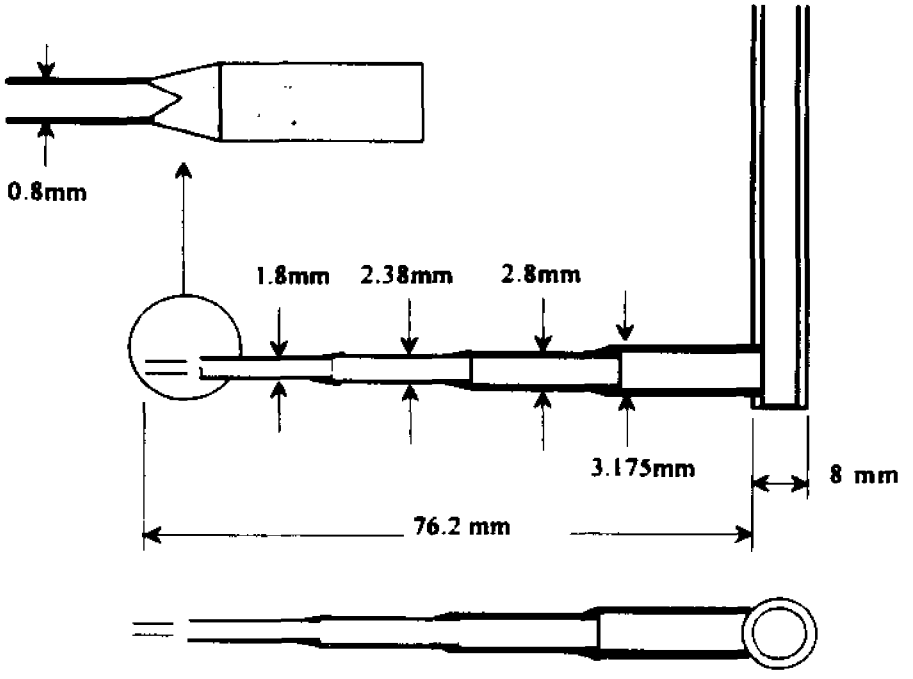

Figure C4: Hot wire rake probe (not to scale).

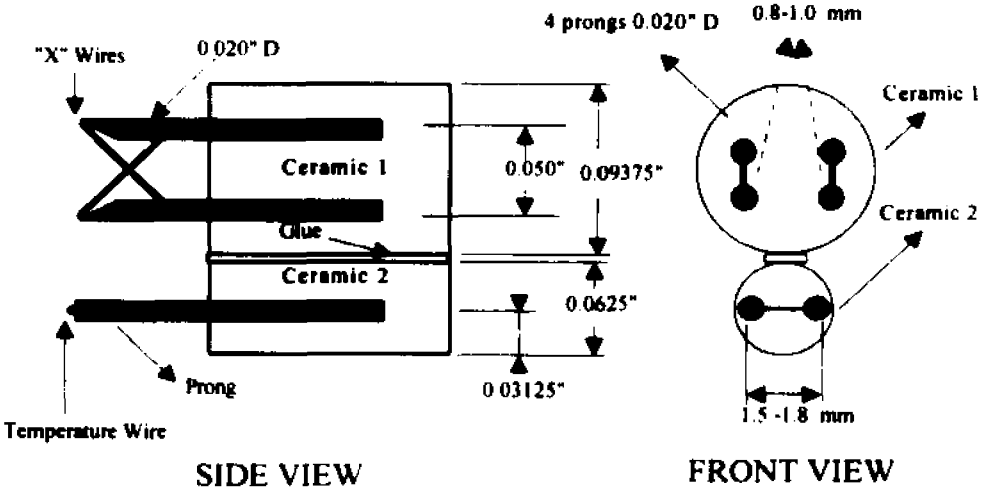

Figure C5: Side and front view of a typical three wire probe used for longitudinal and lateral velocity measurements. (Drawing shown not to scale)

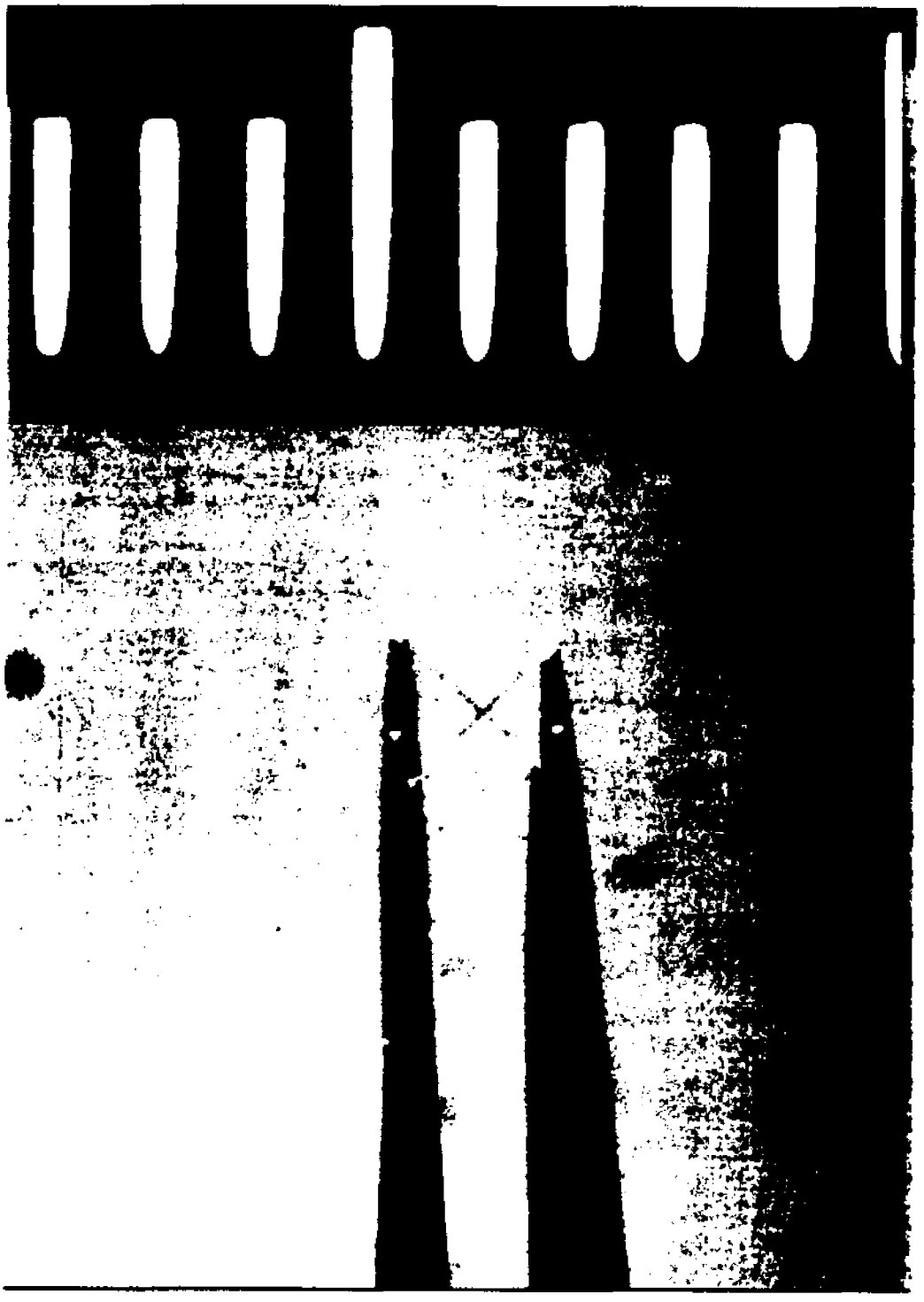

Figure C6 : Photograph of a three wire probe X wires are 5μm and cold wire is 2.5 μm

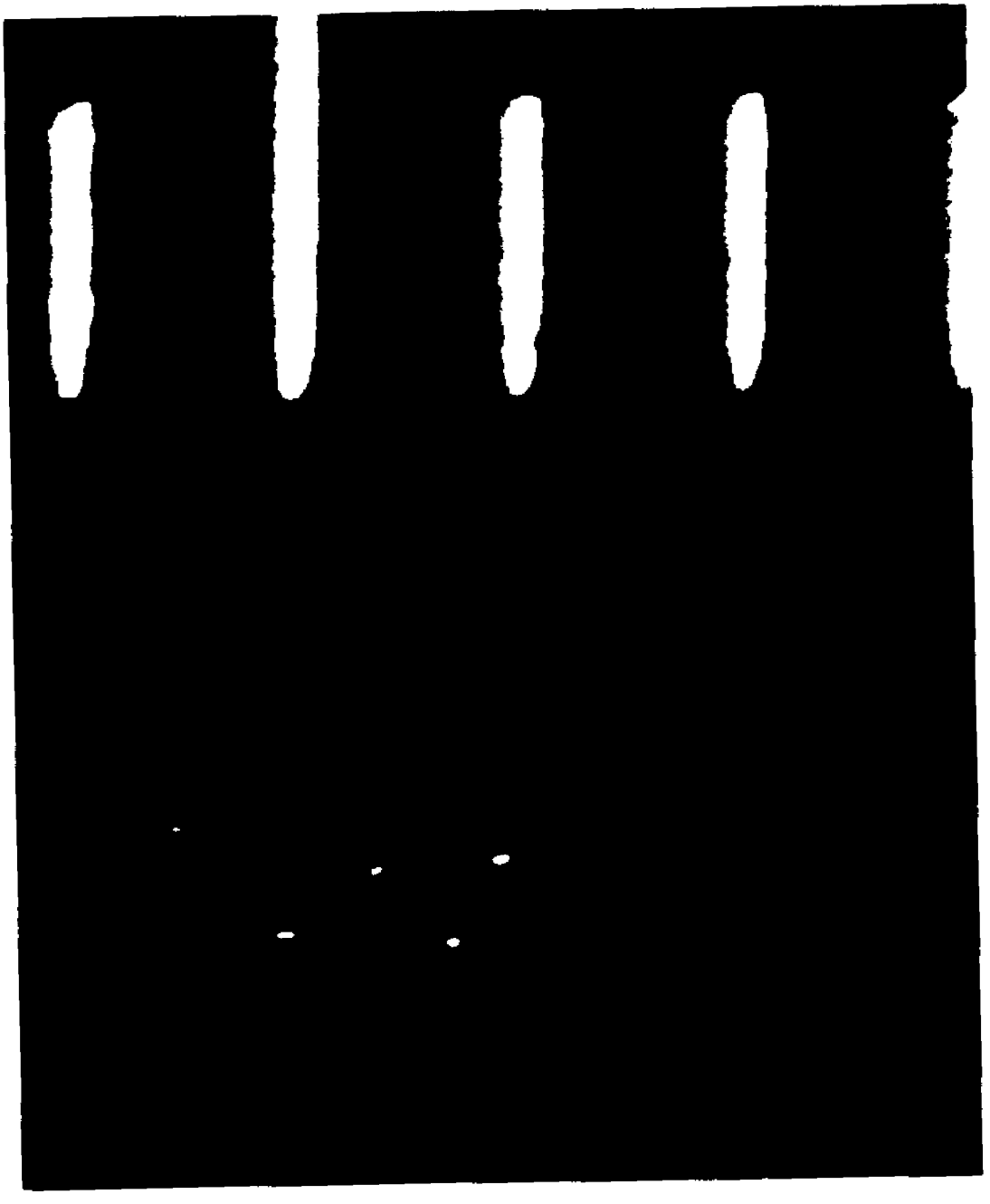

Figure C7 : Photograph of a three wire probe X wires are 5μm and cold wire is 2.5μm

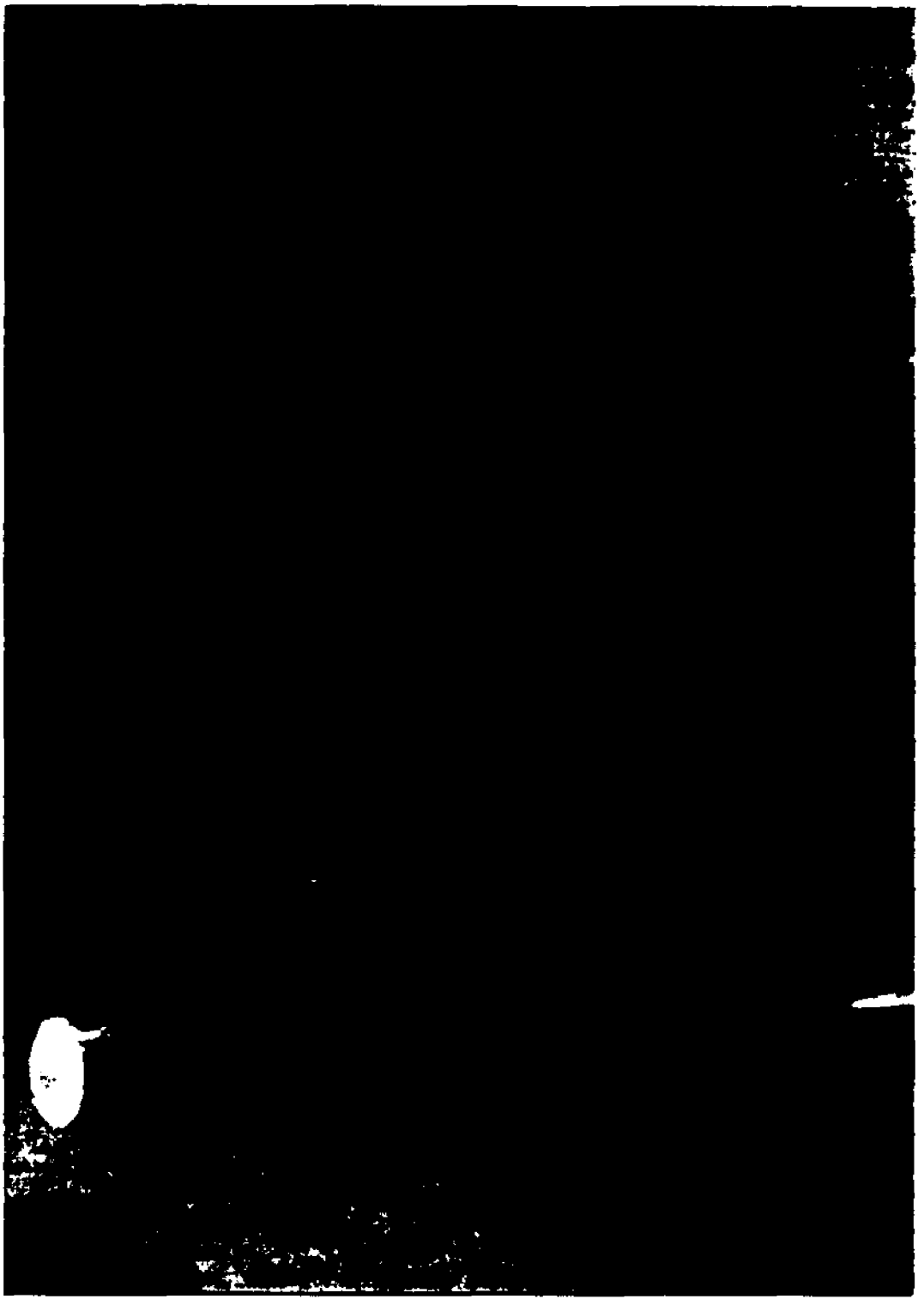

Figure C8: Photograph of a three wire probe and its supporting probe.

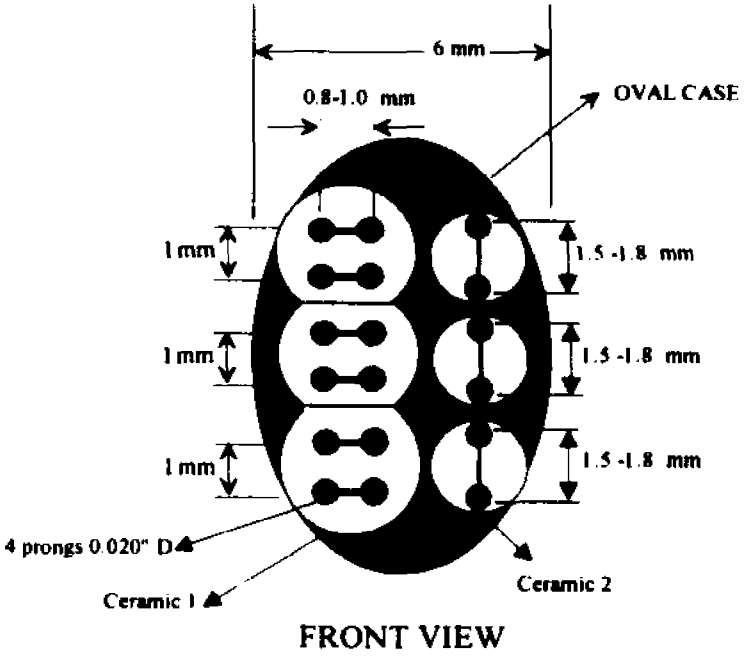

Figure C9: Front view of the 9 wire probe used for correlation measurements. (Drawing shown not to scale)

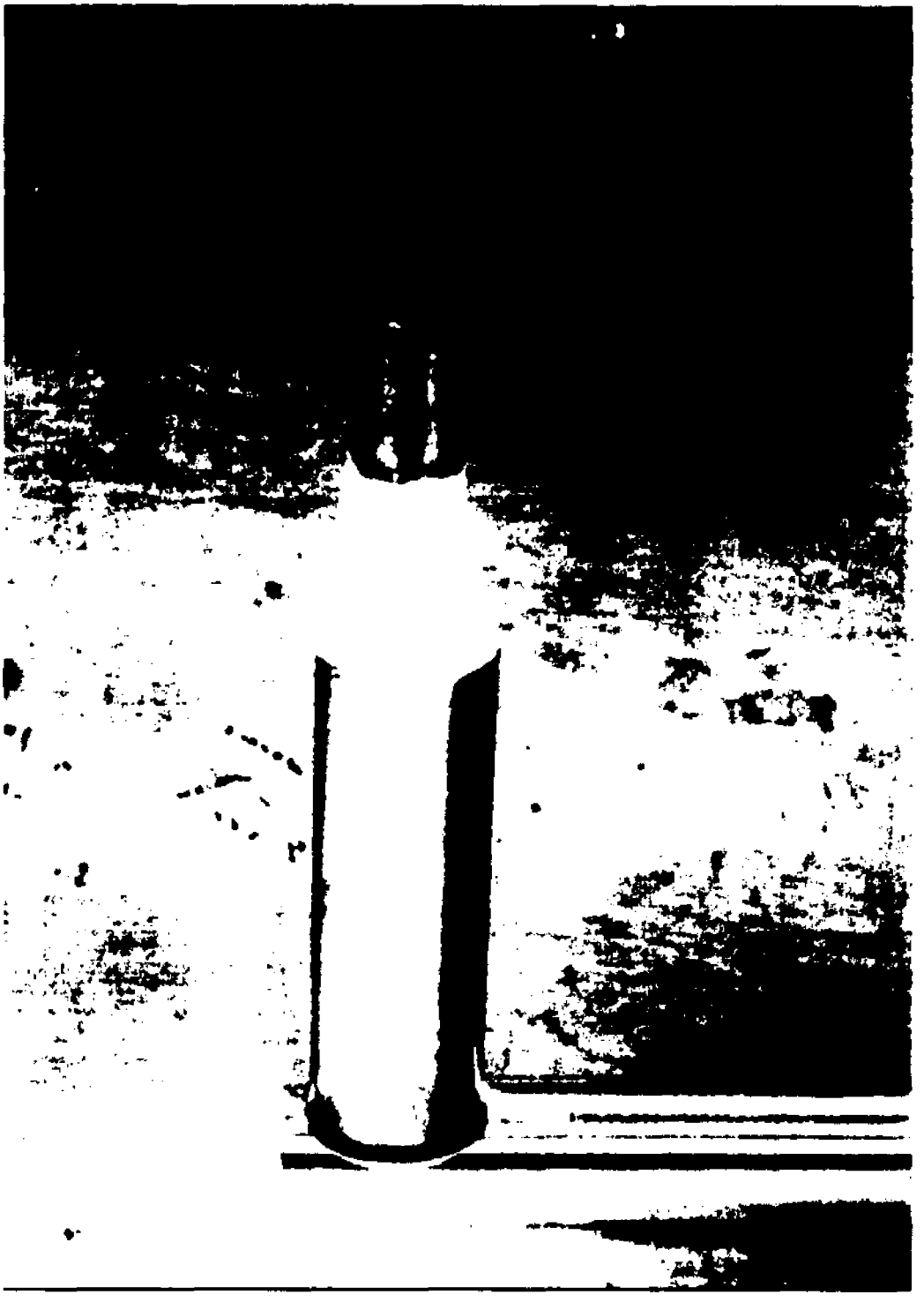

Figure C10: Photograph of the nine wire probe and its supporting probe.

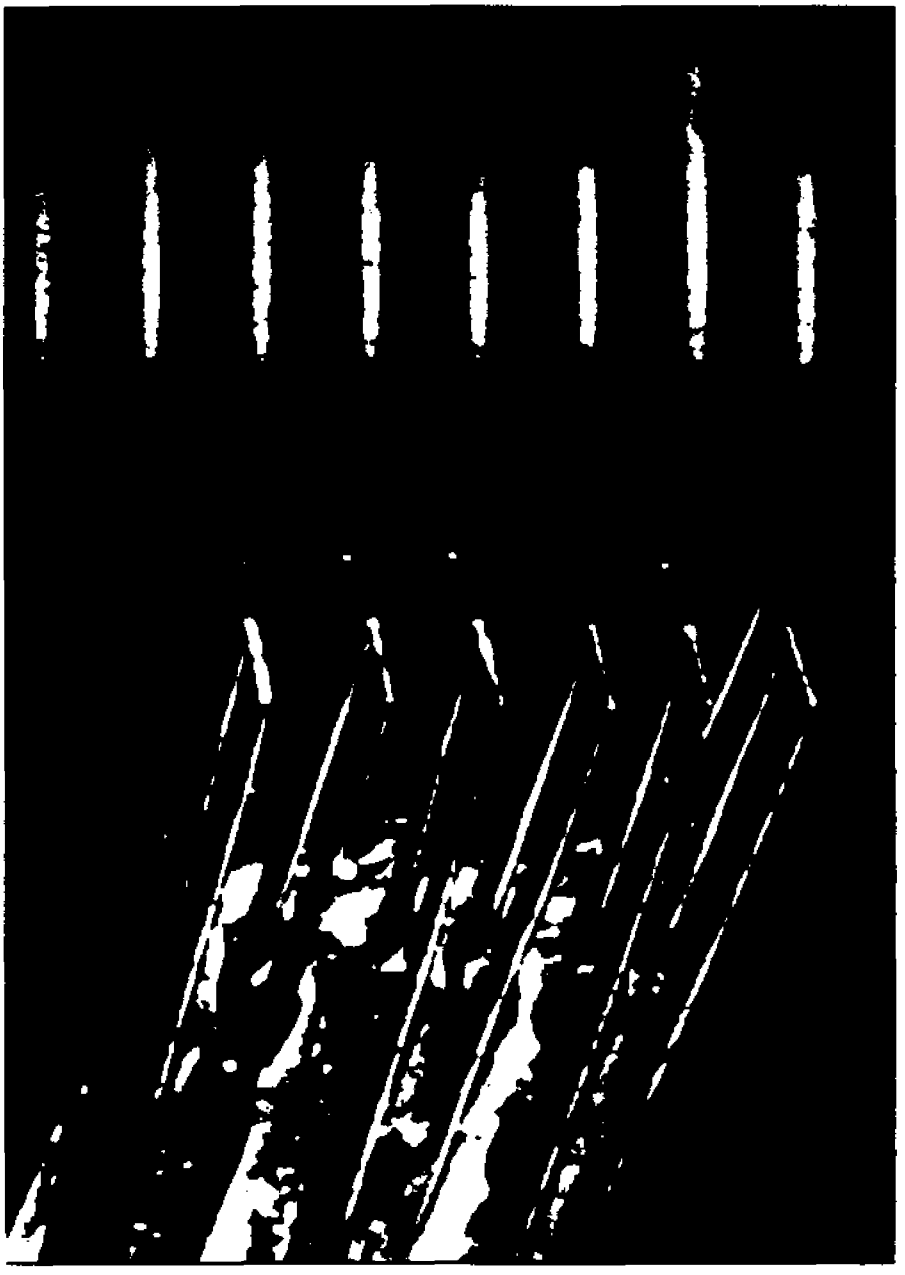

Figure C11: Photograph of the nine wire probe with 6 hot wires and 3 cold wires

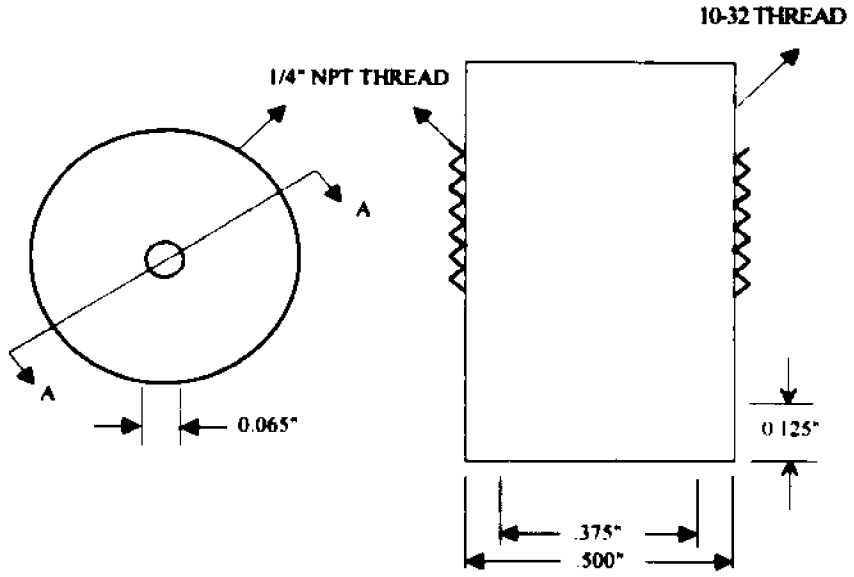

Figure C12: Sketch of the brass pressure transducer fitting (not to scale).

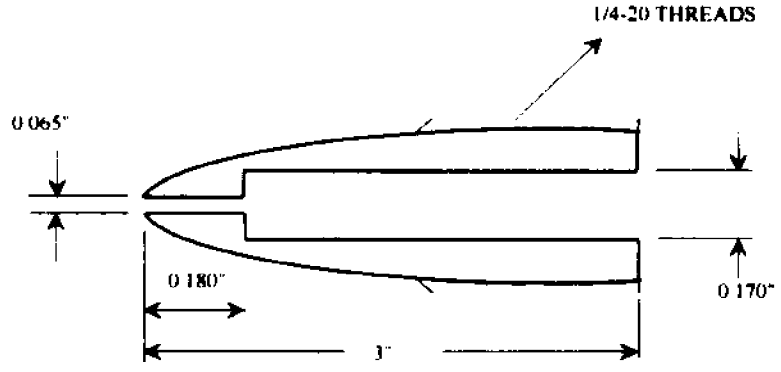

Figure C13: Sketch of the brass pressure transducer fitting used for the Mach probes (not to scale).

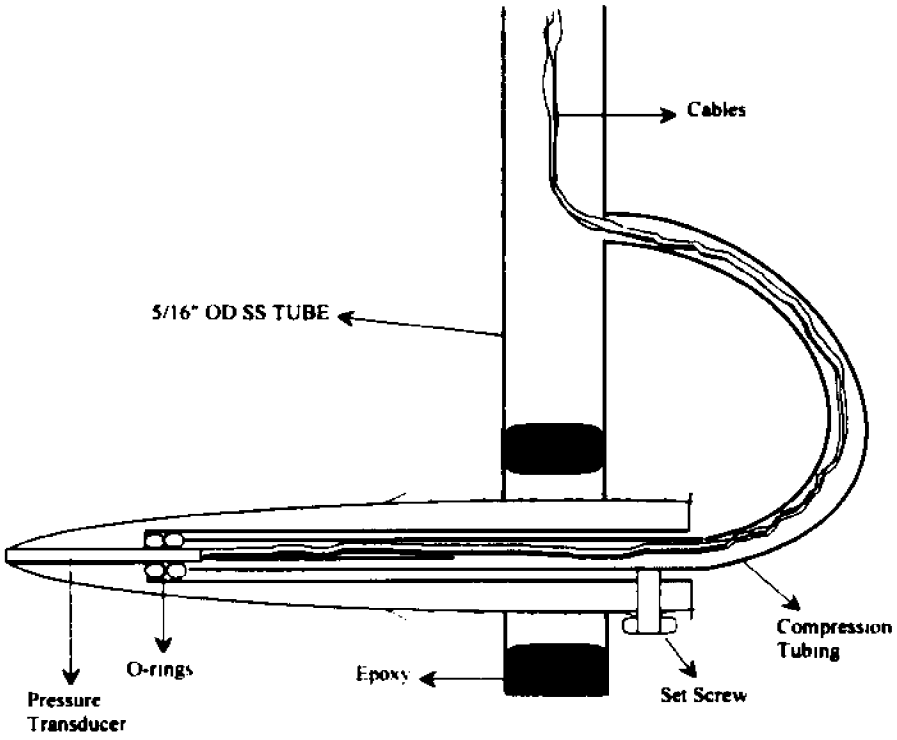

Figure C14: Sketch of a Mach probe with the pressure transducer installed
(Drawing not to scale)

APPENDIX D

RAYLEIGH SCATTERING

INTRODUCTION

Laser Anemometry is based on the scattering of light from particles. The introduction of suitable seed material into the flow is often difficult or simply not feasible. For example, LDV systems and hot wire anemometers provide single point information in a time averaged sense. Also the size of the probe volume must be increased so as not to exceed the frequency response of the photo detectors. The combination of these factors have led researchers working with high speed flow to examine the flows using the molecular scattering approach. The scattering of electromagnetic radiation may occur with or without damages in the frequency. The simplest of the scattering techniques is based on Rayleigh scattering. When there is no change in the frequency, the phenomenon is called Rayleigh scattering. Time histories of the fluctuating quantities permit the study of the instantaneous structure. New optical techniques allow instantaneous two dimensional density cross sections using Rayleigh scattering out high speed flows.

NOMENCLATURE

a = most probable speed

c = speed of light

c_s = speed of sound

G_R = total number of Rayleigh counts

h = Planck's constant

k = Boltzmann's constant

K = scattering wave

L_{sc}= length of the scattering volume along the probe

m = molecular mass

M = Mach number

MW = molecular weight

n = number density

N = number of molecules in the probe volume

N_A = Avogadro's number

P_L = power of the laser

P = pressure

R = universal gas constant

T = temperature

V = volume of the probe

γ = specific heat ratio

Γ_R = photon arrival rate

δ = density fluctuation

ε = overall efficiency

θ_s = scattering angle

λ = wavelength

ρ = density

σ = total cross section for light scattering by a molecule

χ = angle between incident electric field vector and the wave vector

Ω = solid angle

$\frac{d\sigma}{d\Omega}$ = scattering cross section

THEORY

Density changes across a shock wave can be measured by the scattering of photons excited by a laser beam. The amount of the emitted scattered photons depends on the number of molecules existing in the probe volume. Therefore the scattered volume is defined as $V_{sc} = N\, V_{mol}$ where N is the number of molecules in the probe volume.

The number of molecules existing in the probe depends on the molecular mass of the gas. Avogadro's number as well as the molecular weight of the gas. So the number of molecules in the probe can be expressed as follows:

$$m = \frac{MW}{N_A} N \quad \rightarrow \quad N = \frac{mN_A}{MW}$$

where N_A=6.022045x10^{23} molecules/grmoles.

For a perfect gas the equation of state for N molecules will give: $\frac{1}{V} = \frac{P}{N\frac{R}{N_A}T} \rightarrow \frac{1}{V} = \frac{P}{NkT}$, where $k = 1.38\text{x}10^{-23}\frac{J}{K}$, and $R = 8.314\frac{J}{Kmol}$. For N=1 the above

equation defines the number density (n) for a perfect gas. A similar expression can be obtained for the number density of a dilute gas.

For dilute gases the number density is related with the kinetic theory by Hirchfelder et al. (1954) as:

$$\frac{3}{2}kT=\frac{1}{n}\sum_j n_j\left(\frac{1}{2}m_j\bar{V}_j^2\right)(1)$$

$$P=\sum_j P_j=\sum_j n_j m_j\bar{V}_j^2 \qquad (2)$$

$$(1)\text{ and }(2)\rightarrow n=\frac{1}{3}\frac{P}{kT}$$

The mass average velocity and the overall density of the gas at a point are defined as:

$$V(r,t)=\frac{1}{\rho}\sum_j n_j m_j\bar{V}_j$$

$$\rho(r,t)=\sum_j n_j m_j$$

The relative fluctuation of density in a gas is given by Hirchfelder et al. (1954) as:

$$\delta=\frac{1}{N}\frac{kT}{\left(\frac{\partial P}{\partial n}\right)_T}$$

For a perfect gas the above relation becomes: $\delta=1/N$. This shows that, if the region is sufficiently small the number of molecules within the region fluctuates. This is to be expected if the region is of molecular dimensions. If the region is large enough the fluctuation of density from the average is small. This instantaneous inhomogeneity leads to macroscopically observable phenomena such as the scattering of light.

The total cross section (σ) for light scattering by a molecule is: $\sigma=\frac{512\pi^7\alpha^2}{3\lambda^4}$ in cm^2.

α is the polarizability of a molecule and is of the order 10^{-23} cm^3.

The detected photon arrival rate (Γ_e) by the CCD camera is defined by Seaholtz

(1991) as: $\Gamma_R = \frac{\epsilon P_o n L_e \lambda \Omega}{hc} \frac{d\sigma}{d\Omega} \sin^2\chi$. The experiment is assumed to have a minimum overall efficiency of 1% and the length of the scattering volume along the probe is assumed to be 1.5 cm. The YAG laser beam has energy of 30 mJ at a wavelength of 266 nm. The pulse duration of the laser beam is 5-6 nsec so the cross-sectional image is frozen in time. With the above information as well as χ=90°, average pressure P=50 psi, solid angle Ω = 2.4485×10^{-3} sr, c=299792458 m/sec, $\frac{d\sigma}{d\Omega} \approx 10^{-31}$ m^2/sr, h = 6.26176×10^{-34} J sec, and $n=P/3kT=1.33 \times 10^{25}$ m^{-3} the detected photon arrival rate is approximately $\Gamma_R = 4 \times 10^{10}$ photons/sec.

The total number of Rayleigh counts is defined as: $G_R = \Gamma_R \Delta t$ photons. Therefore for Δt=5 nsec G_R=200 photons.

The sensitivity of the CCD camera has to be determined by the number of scattered photons. Since most of the manufacturers of CCD cameras report the sensitivity of the cameras in units of lux photons have to be converted in this unit using the following conversion (1lux=10^{11} photons/mm^2/sec). Thus for 200 scattered photons, pulse duration of 5 nsec and an probe scattering area of 100 mm^2 the sensitivity of the CCD camera should be 0.004 lux. This can be considered as very low level of scattered light and possibly seeding of the flow is necessary.

The speed of sound (c_s) is given by: $c_s = \sqrt{\frac{\gamma kT}{m}}$ and the most probable speed (a)

is: $a=\sqrt{\frac{2kT}{m}}$.

Assuming that the average temperature T is about 500° K the speed of sound is equal to 453.6 m/sec and the most probable speed is 544.8 m/sec. Therefore the Mach number (M) of the flow is equal to 1.2 much lower than the real flow Mach number for this condition (for T=500 °K, M=0.7).

The scattering wave number (K) is given as: $K=\frac{4\pi}{\lambda}\sin(\frac{\theta_s}{2})$ for scattering angle $\theta_s=90°$ then $K=3.471\times10^{7}\ m^{-1}$.

APPENDIX E

DATA REDUCTION

E1. STATISTICAL ANALYSIS

Several statistical values of the useful data can be computed such as the mean field, the various rms values of the flowfield, mean time derivatives, mean time rms derivatives, mean skewness and flatness factors of the flowfield as well as their corresponding mean time derivatives.

The relations that follow are well known and established but for the completeness of this work are offered again here.

Mean value: $\bar{x} = \frac{1}{N}\sum_{i=1}^{N} x_i$

Variance of x: $VAR(x) = \frac{1}{N}\sum_{i=1}^{N} (x_i - \bar{x})^2$

R.M.S. value of x: $x_{rms} = \sqrt{VAR(x)}$

Skewness of x: $x_{skew} = \frac{\frac{1}{N}\sum_{i=1}^{N} (x_i - \bar{x})^3}{(VAR(x))^3}$

Flatness of x: $x_{flat} = \frac{\frac{1}{N}\sum_{i=1}^{N} (x_i - \bar{x})^4}{(VAR(x))^4}$

All the time derivatives were calculated as the difference between two consecutive data points divided by the time interval between those two points i.e.

$$\frac{dx}{dt} = \frac{x_{i+1} - x_i}{\Delta t} = y_i$$

Then all the previous mean expressions will be recalculated with y_i (time derivative) as input instead of x.

The cross correlation between the time dependent signal and the respective time derivative is also calculated as:

$$C_{xy} = \frac{\frac{1}{N}\sum_{i=1}^{N} x_i y_i - \bar{x}\,\bar{y}}{x_{rms} y_{rms}}$$

Applying the previous expressions on the acquired fluctuating fields the corresponding mean fields can be calculated. When the fluctuating fields are non-dimensionalized by the corresponding mean field before and after the interaction of the flow with the shock wave the amplification/attenuation ratios can be defined for pressure fluctuations (G_P), longitudinal velocity fluctuations (G_u), lateral velocity fluctuations (G_v), and temperature fluctuations (G_T) as:

$$G_P = \frac{\overline{P_d}}{\overline{P_u}}, \quad G_u = \frac{\overline{u_d}}{\overline{u_u}}, \quad G_v = \frac{\overline{v_d}}{\overline{u_u}}, \quad G_T = \frac{\overline{T_d}}{\overline{T_u}}$$

$$\frac{\overline{P_d - P_u}}{\overline{P_d - P_u}} \qquad \frac{\overline{u_u}}{\overline{u_u}} \qquad \frac{\overline{v_u}}{\overline{u_u}} \qquad \frac{\overline{T_u}}{\overline{T_u}}$$

In the above equation the symbols with the overbar signifies the mean field and the subscript denotes the region before, u, or after, d, the interaction.

Turbulence levels varied throughout the experiments due to the different mesh sizes

that were used as well as the different driver strengths were tested (rupturing pressure) producing different flow velocities.

CONDITIONS FOR ISOTROPY

Usually the condition for isotropy is defined as the invariance of the statistically averaged properties of turbulence under rotation of the coordinate system and under reflection with respect to the coordinate planes. The anisotropy tensor b_{ij} and the skewness of the velocity fluctuations is an indication of the flow isotropy. The requirement for isotropic flow is that the skewness of the velocity fluctuations and the anisotropy tensor has a zero value or a value close to zero. Occasionally in certain cases where energy is transferred from bigger to smaller eddies it is concluded that the fine structure of a non isotropic turbulent flow is almost isotropic or locally isotropic. In grid generated turbulence the position where the flow is locally isotropic is the position in the flow where the skewness of the velocity derivative fluctuations becomes constant. The value of the skewness of the velocity derivative depends on the turbulent Reynolds number, $Re_\lambda = u\lambda/\nu$.

The anisotropy tensor b_{ij} is defined as: $b_{ij} = \frac{\overline{u_i u_j}}{\overline{u_l u_l}} - \frac{1}{3}\delta_{ij}$ where u is velocity fluctuations

and δ is the Kronecker delta.

The flatness factor in grid generated turbulence is increased with increasing Re #. The flatness factor may be considered as a measure of the degree of intermittency, if intermittency is shown in another way to occur in the flow.

POWER LAWS

The turbulent kinetic energy of a flow is given as: $\overline{q^2} = \frac{1}{2}\left(\overline{u^2}+\overline{v^2}+\overline{w^2}\right)$. When isotropic turbulence is considered then $\overline{q^2} = \frac{3}{2}\overline{u^2}$.

Appropriate modelling and analysis of the mesh size (M) effects on the interaction and turbulence dissipation with the downstream distance should be considered. Previous results suggest that the position where the flow becomes isotropic is proportional to the Reynolds number based on the mesh size (Re_M) and dependent on the mesh size of the grids. The grid characteristics consist of the geometry of the grid and its associated drag when it is introduced into the flow. Since turbulence is created when the fluid passes through the grid the following relation was proposed by Batchelor and Townsend (1949) based upon the " linear" decay law defined as:

$$\frac{\overline{U^2}}{\overline{u^2}} = \frac{c}{C_D}\left[\frac{x}{M} - \left(\frac{x}{M}\right)_0\right]$$

where $\left(\frac{x}{M}\right)_0$ is the virtual origin. C_D is the coefficient of drag for a specific grid $C_D = \frac{\left(\frac{d}{M}\right)\left(2-\frac{d}{M}\right)}{\left(1-\frac{d}{M}\right)^4}$, c = 106 and (M / d) is the mesh-bar width ratio. It is experimentally found that for a square mesh grid with mesh-bar of 5-6 the value of $\frac{c}{C_D} \approx 77-135$.

Three characteristic regions can be found in the flow behind a grid. First is the

developing region close to the grid where rod wakes are merging and production of turbulent kinetic energy takes place. This region is followed by one where the flow is nearly homogeneous and isotropic but where appreciable energy transfer from one wave number to another occurs. This region is best described by the power law decay of velocity fluctuations as:

$$\frac{\overline{u^2}}{\overline{U^2}} = A\left[\frac{x}{M} - \left(\frac{x}{M}\right)_0\right]^n \qquad (1)$$

The virtual origin $\left(\frac{x}{M}\right)_0$, that is mentioned above, is used to account for the fact that the effective location where the turbulent velocity fluctuations that appear in the flow may not coincide with the location of the grid.

The third region or final region of decay is the farthest downstream of the grid and is dominated by strong viscous effects acting directly on the large energy containing eddies.

Compressible homogeneous and isotropic turbulence has not been yet set-up experimentally and decay laws for this case have yet to be established. The turbulent or fluctuation Mach number $M_t = \frac{q}{\bar{c}}$ seems to be the most appropriate parameter describing compressible turbulence. By extrapolating the validity of the previous law into compressible flows one can obtain the power law decay

$$M_t^2 = B\left[\frac{x}{M} - \left(\frac{x}{M}\right)_0\right]^n \qquad (2)$$

where $B = \frac{3A}{\bar{c}^2}$.

TRANSPORT EQUATION OF THE TURBULENT KINETIC ENERGY

The turbulent kinetic energy transport equation is (Lee et al. 1993)

$$\bar{\rho}\tilde{u}_k\frac{\partial(q^2/2)}{\partial x_k}+\bar{\rho}R_{ik}\frac{\partial\tilde{u}_i}{\partial x_k}+\overline{u_i''\frac{\partial\bar{p}}{\partial x_i}}+\overline{u_i''\frac{\partial p'}{\partial x_i}}+\frac{\partial(\overline{\rho u_i'' u_i'' u_k''/2})}{\partial x_k}-\overline{u_i''\frac{\partial\tau_{ik}}{\partial x_k}}=0$$

Where R_{ij} is the Reynolds stress tensor defined as: $R_{ij}=\overline{\rho u_i'' u_j''}/\bar{\rho}$ where $\tilde{u}_k$ is the mass-weighted average and u''_k is the fluctuation from $\tilde{u}_k$ according to Favre (1965).

In any part of the flow with the exception of the thin shock region, production by the mean strain is zero as well as work by mean pressure. Work done by pressure fluctuations shortly downstream of the shock and turbulent transport have been found by Lee et al. (1993) to be very small. Therefore for the present case

$$\bar{\rho}\tilde{u}_k\frac{\partial q^2/2}{\partial x_k}=\overline{u_i''\frac{\partial\tau_{ik}}{\partial x_k}}$$

$$-\tilde{u}_k\frac{\partial q^2/2}{\partial x_k}=-\frac{1}{\bar{\rho}}\overline{u_i''\frac{\partial\tau_{ik}}{\partial x_k}}=\epsilon \qquad (3)$$

Thus measurement of the convection of $q^2/2$ by the mean flow can provide a good estimate of the dissipative viscous term ϵ and its length scale L_ϵ through

$$\epsilon=\frac{\left(\frac{q^2}{2}\right)^{\frac{3}{2}}}{L_\epsilon} \qquad (4)$$

RELATIONS OF DECAYING ISOTROPIC TURBULENCE

From turbulent transport equation for decaying turbulence the dissipation rate can be calculated as:

$$-\overline{U}\frac{\partial \overline{q^2}}{\partial x} = \epsilon = \frac{(\overline{q^2})^{\frac{3}{2}}}{L_e} \qquad (5)$$

Once the calculation of the previous dissipation length scales is obtained then the dissipation rate ϵ as well as the associated micro scales (length, time, velocity) can be calculated. Using the non dimensionalized with the mesh size (M) downstream position the above equation can be transformed to:

$$-\frac{\epsilon M}{\overline{U}^3} = \frac{3}{2}\frac{\partial(\overline{u^2}/\overline{U}^2)}{\partial(x/M)} = \left(\frac{3}{2}\right)^{\frac{3}{2}}\frac{(\overline{u^2})^{\frac{3}{2}}}{L_e}\left[\frac{M}{\overline{U}^3}\right] \qquad (6)$$

From eq. (6) the decay rate can be calculated using the coefficients of the power law of eq. (1). Substitution of eq. (1) in eq. (6) yields:

$$\epsilon = \frac{3}{2}nA\left[\frac{x}{M} - \left(\frac{x}{M}\right)_0\right]^{(-n-1)}\left[\frac{\overline{U}^3}{M}\right] \qquad (7)$$

where A is the decay coefficient, $(x/M)_0$ is the virtual origin, n is the decay exponent, U is the mean flow velocity and M the mesh size.

The non dimensional dissipation length scale (L_e/M) can also be expressed as a function of the power law coefficients when eq. (1) and eq. (7) are used with eq. (6). The following expression can be obtained:

$$\frac{L_e}{M} = \sqrt{\frac{3A}{2n^2}\left[\frac{x}{M} - \left(\frac{x}{M}\right)_0\right]^{(-n+2)}}$$

When the turbulent decaying flowfield is compressed from the shock wave the longitudinal mean flow velocity of the compressed flowfield is substantially reduced. Consequently the non dimensional decay rate for the compressed flowfield has to be reevaluated using appropriate mean flow scaling. Equation (5) becomes:

$$-\frac{\epsilon M}{\overline{U_u}^3} = \frac{3}{2}\frac{\overline{U_d}}{\overline{U_u}}\frac{\partial(\overline{u^2}/\overline{U_u}^2)}{\partial(x/M)} = \left(\frac{3}{2}\right)^{\frac{3}{2}}\frac{(\overline{u^2})^{\frac{3}{2}}}{L_e}\left[\frac{M}{\overline{U_u}^3}\right] \qquad (8)$$

where subscript u refers to upstream conditions and subscript d refers to downstream conditions.

Similarly, with the induced flowfield, the ϵ and L_e/M can be expressed as functions of the power law coefficients and the associated mean flow velocities. Substitution of eq. (1) into eq. (8) yields:

$$\epsilon = \frac{3}{2}nA\left[\frac{x}{M} - \left(\frac{x}{M}\right)_0\right]^{(-n-1)}\left[\frac{\overline{U_u^2 U_d}}{M}\right]$$

and $\frac{L_e}{M} = \sqrt{\frac{3A}{2n^2}\left[\frac{x}{M} - \left(\frac{x}{M}\right)_0\right]^{(-n+2)}}\left[\frac{\overline{U_u}}{\overline{U_d}}\right]$ where A is the decay coefficient, $(x/M)_0$ is the virtual origin, n is the decay exponent obtained from analysis of the compressed flowfield, U_u is the mean flow velocity before interaction, U_d is the mean flow velocity after interaction and M the mesh size.

From the above analysis several length and time scales of turbulence, such as the

integral length scale of the flow and the dissipative length scale of decaying turbulence can be calculated. Complete analysis and alternate estimation of the different scales associated with the interaction and their physical relation on the decay of isotropic turbulence is given in the next section.

E2. FREQUENCY ANALYSIS

Transformation of the fluctuating time field (pressure, velocity, temperature) to the corresponding frequency field is obtained by the use of Fast Fourier Transform technique (FFT method). Routines were already written in the FORTRAN language to evaluate the following Fourier integral for discrete data points:

$$F_x(f) = \int_{-\infty}^{\infty} x(t) e^{-i\omega t} dt$$

The Fourier series that convert the time space to frequency space is given as:

$$F_x(f) = \sum_{j=0}^{N-1} e^{\frac{2\pi jt}{N}} x_j(t)$$

where $F_x(f)$ is the fluctuating field expressed in frequency.

When the information of the turbulent field is transformed from time domain to frequency domain the power spectral density, auto-correlation, cross-correlation, wavenumber spectrum as well as the wavenumbers of the fluctuating flowfield can be calculated as follows:

$$S_{xx} = \frac{|F_x(f)|^2}{T}$$

$$R_{xx}(\tau) = \frac{\overline{x(t) \cdot x(t-\tau)}}{\overline{x^2}}$$

$$C_{xy} = \frac{\overline{x(t) \cdot y(t)}}{\overline{x}\,\overline{y}}$$

$$k = \frac{2\pi f}{\overline{U}}$$

In the above expressions T is the period of the flow field, τ is the delay time introduced to calculate auto-correlation of a signal and $\overline{U}$ is the longitudinal mean flow field velocity obtained by 1-D inviscid analysis or measured from hot wires when available. A mismatch in wavenumbers arises when one tries to compare a fluctuating property for the same wavenumbers before and after the interaction. Mass flux before the interaction is larger than the mass flux after the interaction since the end wall is porous and part of the flow exits the shock tube. This also means that the mean longitudinal velocity of the flow after the interaction is also less than the mean longitudinal velocity before the interaction. Calculating the corresponding wavenumbers of the flowfield before and after the interaction we have:

$$k_a = \frac{2\pi f_a}{\overline{U_a}}, \qquad k_b = \frac{2\pi f_b}{\overline{U_b}}$$

where subscript (a) stands for values after interaction and subscript (b) for values before interaction.

It is unlikely that k_b and k_a will match for further analysis. Thus, a linear interpolating scheme was implemented in order to produce the matching wavenumbers as follows:

$\Delta k_a = k_a(i+1) - k_a(i)$ and $\Delta k_b = k_b(i+1) - k_b(i)$ where $\Delta k_a > \Delta k_b$ since the range of the

wavenumbers increases after some mass exits the shock tube. Consequently the longitudinal mean flow velocity decreases after the reflection of the shock wave on the porous end wall. Therefore for the same frequency interval the difference between two successive wavenumbers will be different before and after interaction and the difference will always be greater for Δk_a, since $\overline{U_a} < \overline{U_b}$.

The interpolated wavenumber and the associated amplitude of any fluctuating property of the flowfield at a specific wavenumber is calculated using the following expressions:

$$k_a(i+\Delta w) = \frac{k_b(i+n\Delta k_b)-k_a(i)}{\Delta k_a} + k_a(i)$$

where Δw is the deviation of the new value from the original ($k_a(i)$) and n is the number of intervals to be created in the range Δk_a

The associated amplitude of the fluctuating property of the flowfield at the interpolated wavenumber is obtained by:

$$x_a(i+\Delta w) = \left[\frac{k_b(i+n\Delta k_b)-k_a(i)}{\Delta k_a}\right] [x_a(i+1)-x_a(i)] + x_a(i)$$

The above process is shown on figure E1 and is repeated for the whole range of the wavenumbers for the flowfield after its interaction with the reflected shock wave, up to the maximum resolved wavenumber for the flowfield before its interaction with the reflected shock wave.

The matching of the wavenumbers allows the calculations of the amplification or attenuation ratio of the wave number spectrum ($G_{Sxx(k)}$) can be defined as:

$$G_{S_{xx}(k)} = \frac{S_{xx}(k)_a}{S_{xx}(k)_b}$$

If there exists an amplification of the of the wave number spectrum before and after the interaction then $G_{Sxx(k)} > 1$. No amplification exists when $G_{Sxx(k)} = 1$ and attenuation of the of the wave number spectrum is found if $G_{Sxx(k)} < 1$. Calculation of the flow wavenumbers and the wave number spectrum provide a good indication of the length scale structures associated with the flow.

CHARACTERISTIC SCALES OF TURBULENCE

As turbulence grows to its full development the larger eddies will produce through inertial interaction smaller eddies and therefore transferring energy to them. In the fully turbulent flow the small eddies will have the maximum kinetic energy. Therefore two separate scales will be needed to describe accurately the dissipation of turbulence.

One of them will be the integral length scale or macro scale which it will be approximately equal to the average size of the largest size eddies. The integral length scale, often used as l or $\mathfrak{L}$ for isotropic turbulence, is an important characteristic of the structure of turbulence. The integral length scale in effect measures the correlation distance between the velocities at two points of the flowfield.

The second length scale needed is associated with the smallest size eddies. This length scale is often called microscale or Taylor's microscale (λ) and is defined by the curvature of the autocorrelation coefficient. Depending on whether it is used for a measure of the size of the eddies or the eddy size responsible for dissipation (λ) can be referred to as

a microscale or a dissipation scale respectively. When (λ) is used as a microscale then it measures the rate of local change of velocity. In the literature the microscale (λ) usually can be expressed as a temporal or as a spatial variation of the autocorrelation coefficient. Then it becomes a little confusing separating the two. Here the microscale (λ) expressed as a temporal variation of the autocorrelation coefficient will be called as dissipation time scale or time microscale τ and is a measure of the most rapid changes that occur in the fluctuations of the velocity field. The time microscale τ is defined as:

$$\overline{\left(\frac{du}{dt}\right)^2} = \frac{\overline{2u^2}}{\tau^2}$$

The Taylor's microscale and the dissipation time scale are connected by: $\lambda = U \cdot \tau$.
Definition of even smaller scales associated with the viscous effects of the turbulent flow are often called inner scales or Kolmogorov's scales. As it is expected the inner scales are much smaller than the integral scales.

The integral time scale ($\mathfrak{L}_t$) of the interaction can be obtained, as mentioned earlier, with the use of auto correlation and can be considered as the measure of the turbulent behavior of the velocity field. It can be calculated as follows:

$$\mathfrak{L}_t = \int_0^{\infty} R_{uu}(\tau)d\tau$$

The integral length scale ($\mathfrak{L}$) is related to the integral time scale as: $\mathfrak{L} = \mathfrak{L}_t U$.
It is obvious that all of the above relations have to be considered for two different cases (before and after interaction) in order to have any meaningful results about the processes involved with the interaction of a normal shock wave with turbulent flows.

An alternate way to look at mechanisms involved in the interaction of the turbulent flow with the shock wave is by defining the amplification ratio of integral time scales ($G_{\mathcal{L}_t}$) and integral length scales ($G_{\mathcal{L}}$).

$$G_{\mathcal{L}_t} = \frac{(\mathcal{L}_t)_a}{(\mathcal{L}_t)_b}, \qquad G_{\mathcal{L}} = \frac{(\mathcal{L})_a}{(\mathcal{L})_b}$$

Both of the above definitions and consequent calculations, i.e. amplification of the wavenumber spectrum and amplification of the integral length scales, are expected to provide similar results, since low wavenumbers are associated with large length scales and high wavenumbers with small length scales.

At maximum kinetic energy, a wavenumber (k_e) is associated with. Then around it a range can be defined as the range of the energy containing eddies. Similarly the range that the eddies provide the main dissipation is associated at a range around a wavenumber ($k_d \approx 1/\eta$). As the size of the eddies decrease the viscous effects are contributing more and more into the dissipation of energy. Therefore at sufficiently high Reynolds numbers the energy that is dissipated by the large eddies can be neglected. This led Kolmogorov to make the hypothesis that at high wavenumbers turbulence can be determined by ϵ and ν. He called this state of turbulence as "universal" because it is not dependent on the external conditions. Several viscous scales or "inner" scales attempting to describe the structures involved in the turbulent flowfield, were introduced by Kolmogorov and are scaling length (η), time (τ), and velocity (u). The respective viscous scales are defined as follows:

$$\eta = \left(\frac{\nu^3}{\epsilon}\right)^{\frac{1}{4}} \qquad \tau = \left(\frac{\nu}{\epsilon}\right)^{\frac{1}{2}} \qquad u = (\nu\epsilon)^{\frac{1}{4}}$$

The above "inner" scales can be calculated for any flow if the dissipation rate (ϵ) is known. The dissipation rate can be calculated as: $\epsilon = \frac{u^3}{l}$ where l is the integral length scale of the same order as the calculated integral scale $\mathcal{L}$ since in turbulent flows the largest eddies tend to have size comparable to the width of the flow. Thus in the following discussion, l is treated as been equal to $\mathcal{L}$. When isotropic turbulence is considered then

$$\epsilon = 15\nu\overline{\left(\frac{\partial u}{\partial x}\right)^2} = 15\nu\frac{u^2}{\lambda^2}$$

where λ is Taylor's micro scale << l. The ratio of $\frac{\lambda}{l}$ is given as:

$$\frac{\lambda}{l} = \left(\frac{15}{A}\right)^{\frac{1}{2}} Re_l^{-\frac{1}{2}} = \frac{15}{A} Re_\lambda^{-1}$$

where A = 1. A similar expression can be obtained for the $\frac{\lambda}{\eta}$ ratio as:

$$\frac{\lambda}{\eta} = \left(\frac{225}{A}\right)^{\frac{1}{4}} Re_l^{\frac{1}{4}} = 15^{\frac{1}{4}} Re_\lambda^{\frac{1}{2}}$$

An alternate calculation of the velocity micro scale (λ_u) is offered by Groth and Johansson (1988) and it can be calculated from the rms values of the velocity field and its respective time derivative.

$$\lambda_u = \sqrt{2}\frac{\bar{U}\, u_{rms}}{\left(\frac{\partial u}{\partial t}\right)_{rms}}$$

Another approach to calculate the dissipation rate is by the calculation of the time depended wavenumber $k_d(t)$ as: $k_d(t) = \left(\frac{\epsilon(t)}{\nu^3}\right)^{\frac{1}{4}}$ which provides us only with an estimation for $\epsilon(t)$.

Many theoretical energy spectral models appear in the literature and the dissipation

rate ϵ must be known. Two of the most common models, Kolmogorov's and Pao's, are given here respectively.

$$E(k) = A\,\epsilon^{\frac{1}{2}}\,k^{-\frac{5}{3}}, \qquad E(k,t) = A\,\epsilon^{\frac{1}{2}}\,k^{-\frac{5}{3}}\,e^{\left[-\frac{3}{2B}\frac{\nu}{\epsilon^{\frac{1}{2}}}k^{\frac{4}{3}}\right]}$$

An alternate estimation of the time dependent dissipation rate valid for high wavenumbers and high Reynolds number flowfields according to Hinze (1975) can be calculated directly from the time derivative of the velocity rms as follows:

$$\epsilon(t) = -\frac{3}{2}\frac{du'^2}{dt} = 2\nu\int_0^{\infty} k^2\,E(k,t)\,dk$$

The definition can be applied to the equilibrium range of turbulence where practically the total dissipation is equal to the energy associated in this range. In this range turbulence is independent of external conditions. Any change in the characteristic scales of turbulence is a result of ϵ and ν only.

Temperature measurements were obtained at various locations simultaneously with the velocity measurements. An appropriate temperature micro scale with respect to the temperature fluctuating field (θ) and the average value of its spatial derivative can be defined as:

$$\lambda_\theta^2 = 2\overline{\theta}\left(\frac{\partial\theta}{\partial x_1}\right)^2$$

Experimental data will be checked against the theoretical estimates proposed by Corrsin (1951) :

$$\xi = \frac{\lambda_\theta}{\lambda_g} = \left(\frac{2}{Pr}\right)^{\frac{1}{2}} \approx 1.6$$

where Pr is the Prandtl number and λ_g is the velocity micro scale computed from the velocity decay law as proposed by Hinze (1975) and Budwig, Tavoularis and Corrsin (1985) as:

$$\lambda_g^2 = \frac{10\nu(x-x_0)}{\overline{U}\,\eta}$$

Temperature decay maybe following a velocity decay like rule as proposed by Sirivat and Warhaft (1983) as:

$$\frac{\overline{\theta^2}}{\left(M\frac{d\overline{T}}{dx}\right)^2} = \delta^2\left(\frac{x-x_0}{M}\right)^{2-n}$$

with T being the mean flow temperature and δ being calculated by ρ, ξ and the velocity decay constants.

A simpler decay law is also proposed by Warhaft and Lumley (1978) like $\frac{\overline{\theta^2}}{\overline{T}^2} = B\left(\frac{x-x_0}{M}\right)^m$.

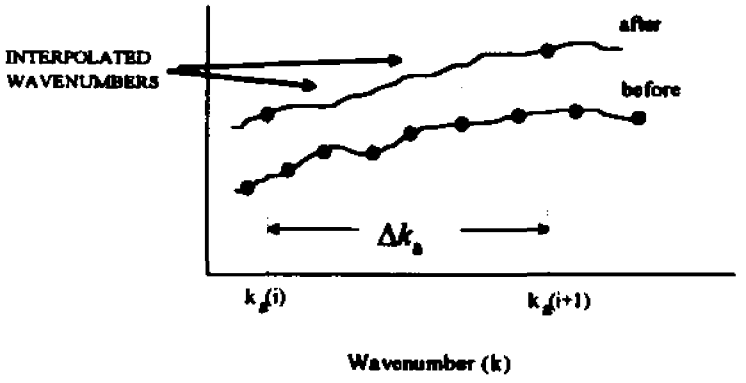

Figure E1: Graphical representation of the interpolation of the wavenumbers resolved during the flowfield after the interaction with the reflected shock wave.

APPENDIX F

SENSITIVITY ANALYSIS AND ERROR ESTIMATES

The most critical measurements relevant to this work were the time dependent measurements of the velocity and pressure fluctuations as well as measurements of all mean fields. The variance of velocity fluctuations and the kinetic energy fluctuations were found to be within 10% while pressure fluctuations in the free stream within 5%. The mean velocity and temperature were uniform within 5% and the mean Mach number within 3%.

The sensitivity of the power law coefficients (A, $(x/M)_0$, n) to changes of the fluctuations of kinetic energy was found by modifying the values of the fluctuations of kinetic energy within the limit of their uncertainties. This is necessary since the dissipation rate of kinetic energy (ϵ), the dissipative length scale (L_ϵ) and the Taylor's microscale (λ) were computed from the power law $\frac{3\overline{u^2}}{2\overline{U^2}} = A\left[\frac{x}{M} - \left(\frac{x}{M}\right)_0\right]^n$. The fluctuations of kinetic energy, obtained from experiments, were allowed to vary between ±10% of their values and the modified coefficients of the power law were compared with the ones used in the present work. The changes in ϵ, L_ϵ, and λ were investigated similarly.

When the fluctuations of kinetic energy were allowed to change consistently for all measurements, then the effect was only felt in A and ϵ which changed by the same amount while the dissipative length scale (L_ϵ) changed by approximately half as much and the Taylor's microscale (λ) by much less. For example if the fluctuations of kinetic energy were consistently increased by 10% then A and ϵ are increased by 10% and L_ϵ is increased by

approximately 5% and λ increases from 3% to less than 1% depending on x/M. For larger sizes of λ (greater x/M) the least deviation from the reported values was found. The opposite trend was found when the fluctuations of kinetic energy were consistently decreased by 10%.

The fluctuations of kinetic energy were also allowed to vary in an alternating fashion. Thus every other measurement was allowed to increase or decrease by 10%, i.e. the first measurement was increased by 10%, the second was decreased by 10%, the third was increased by 10% and so on. The effect of such exploits of the data were felt, as expected, on all coefficients of the power law. For the above case A was decreased by 20% the position of the virtual origin was increased by 15% and the power exponent decreased by 26%. As a result of all these variations of the power law coefficients the dissipation rate of kinetic energy decreased by 17%, the dissipative length scale increased between 6.7% and 20% and the Taylor's microscale increased from 4% to 10% depending on x/M. The opposite trend was found to be true for all power law coefficients and flowfield parameters when the first measurement was decreased by 10%, the second increased etc.

Two extreme and rather unrealistic cases were also tried. In the first case half of the measured values were increased by 10% and the other half were decreased by 10%. The effects on the decay coefficients were devastating. The decay coefficient A was increased 2.5 times while the decay exponent was increased by 140%. The position of the virtual origin was decreased by 75%. Even with such tremendous changes in the coefficients of the power law the dissipation rate of kinetic energy decreased by 25%, the dissipative length scale decreased by 50% and the Taylor's microscale decreased 30%. In the second case the opposite trend was applied in the measured values. Namely the first half of the measured values were

decreased by 10% and the other half were increased by 10%. The decay coefficient A was decreased by 50% and the decay exponent was decreased by 75% while the position of the virtual origin was increased by 20%. The dissipation rate of kinetic energy decreased by 73%, the dissipative length scale remained practically unchanged (2.6% change) and the Taylor's microscale was twice increased.

The last two cases, even though unrealistic, were performed in order to show the effects of the power law coefficients on the relevant parameters for this work (i.e. ϵ, L_e and λ).

All data were acquired simultaneously at multiple locations in the flowfield and thus the error associated with the measurements of velocity fluctuations is expected to be consistent for all measured locations. Therefore the first case, where consistent uncertainty was applied to the measured kinetic energy fluctuations, will provide the most probable estimate of the error in the computation of ϵ, L_e and λ. That is a maximum error of 10% in ϵ, 5% in L_e and 3% in λ can be assumed.

In addition to the above tests, several tests were performed by varying the coefficients of the power law individually. The deviation of q^2, ϵ, L_e and λ obtained from experimental data when the power law coefficient were varied can be found. Therefore presenting the sensitivity of the flow parameters on the coefficients of the power law. Figure F1 presents the effect of the decay coefficient on the above mentioned flow parameters. In this case the virtual origin $(x/M)_0$, and the decay exponent were kept constant. It can be seen that the fluctuations of kinetic energy and the dissipative length scale react linearly to the variation of A. For a ±20% variation in A, q^2 and L_e vary up to ±10%. Similar behavior is presented for

ϵ where for ±20% variation in A there exists the same variation in ϵ. The Taylor's microscale is insensitive to the variation of A. The effect of the variation in the location of the virtual origin is shown in figure F2. It can be seen that there exists a minimal effect on the fluctuations of kinetic energy while for ±10% variation in the location of the virtual origin none of the flow parameters is affected more than ±10%. Of interest is also the inversely proportional trend of the variation of L_e and λ on $\Delta(x/M)_0$. Again here the variation of ϵ is proportional to the variation applied (i.e. $\Delta(x/M)_0$). The effect of the variation of the decay exponent (n) on the flow parameters was performed for up ±20% of its original value. The results of this test can be found on figure F3. The first observation from this figure is that q^2 and ϵ were not affected more than ±7%. The second observation is that L_e and λ were non linearly affected by the variation of n with L_e being affected the most especially when n was decreased. Also the effect of the variation of n on L_e and λ presents an inversely proportional trend.

From all of the above figures it can be concluded that individual variation of the decay coefficients up to ±10% produced, for most of the cases, variation in the flow parameters less or at least equal to 10%. The question that remains unanswered is what is the combined effect of the decay coefficients on the flow parameters. That is, what is the effect when all three coefficient are allowed to vary? Because of the multiple combinations in the variation of the decay coefficient only a few will be presented to illustrate the combined effect.

Several cases with different combinations for the variation of the decay coefficients were tested and are presented in figures F4 to F8. It is interesting to investigate if the total error will compound or if it will possibly be additive. In the first case regardless of the

variation of the decay coefficients the error will keep adding and therefore it will never cancel out. If the second case holds then it is possible to cancel the total error in one or more flow parameters. Indeed if we will investigate the total error introduced by the variation of the individual power law coefficients (shown in figures F1 to F3) then it can be verified for the different cases presented in figures F4 to F8 that the average total error in q^2 and ϵ appears to be approximately additive and not compound. The same does not hold for L_e and λ.

Nevertheless figure F8 shows that even if each of the power law coefficients are under-estimated by 10% the total error propagated in q^2 is minimal, while the dissipative length scale and the Taylor's microscale will be underestimated by 13% and 7% respectively. Overestimation of the dissipation rate of kinetic energy will occur in the order of 20%.

From all of the above presented cases it can be concluded that the flow parameters remain within reasonable limits of deviation even when the power law coefficients were allowed to vary in an arbitrary manner.

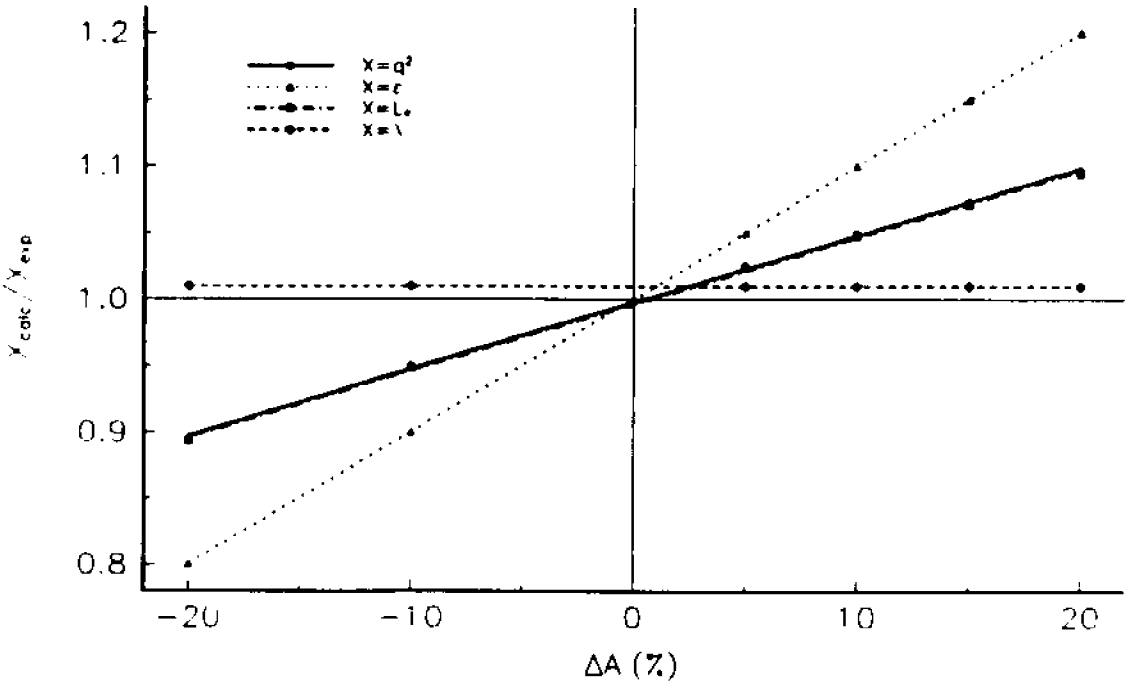

Figure F1: Effects of variation of A on several flow parameters.

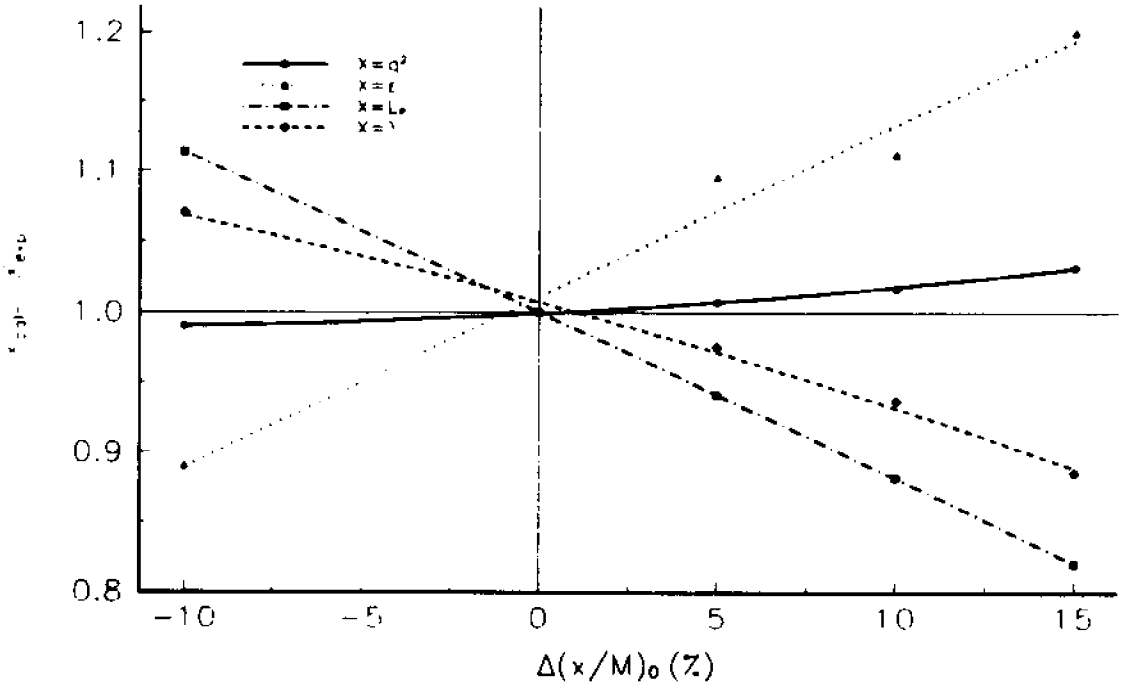

Figure F2: Effects of variation of $(x/M)_0$ on several flow parameters.

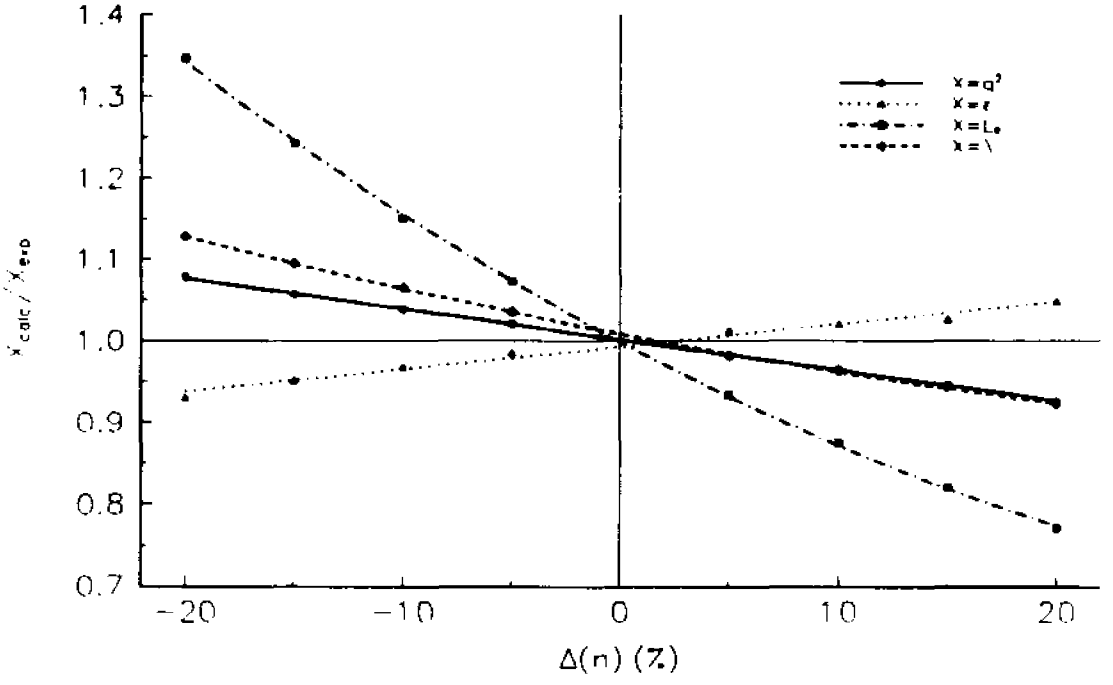

Figure F3: Effects of variation of n on several flow parameters.
$\Delta A = 20\%$, $\Delta(x/M)_0 = 15\%$, $\Delta n = -5\%$

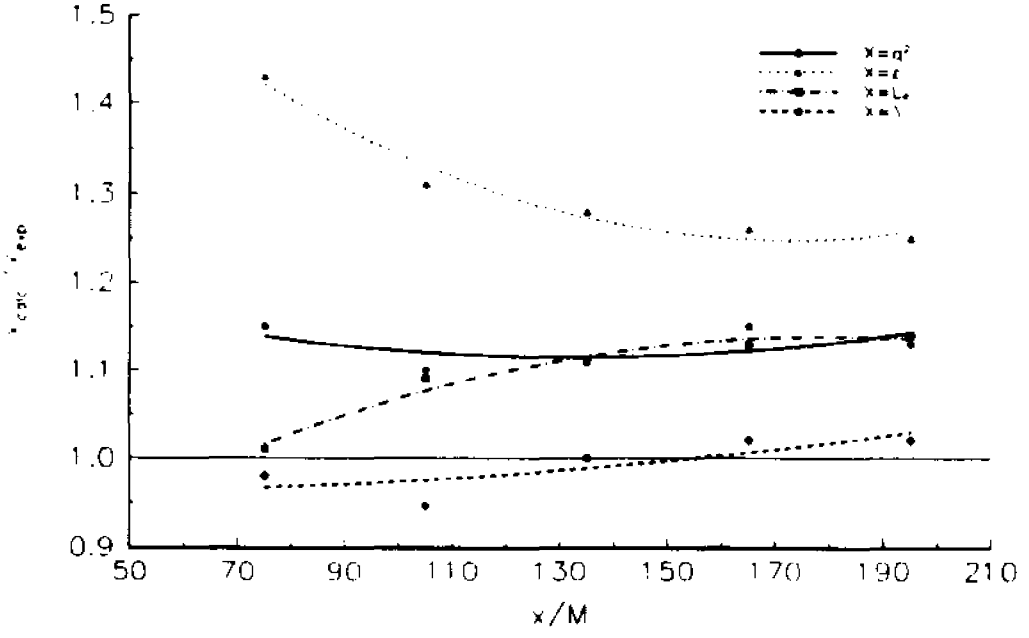

Figure F4: Effects for ΔA=20%, $\Delta x/M_0$=15%, Δn=-5% variation on several flow parameters.

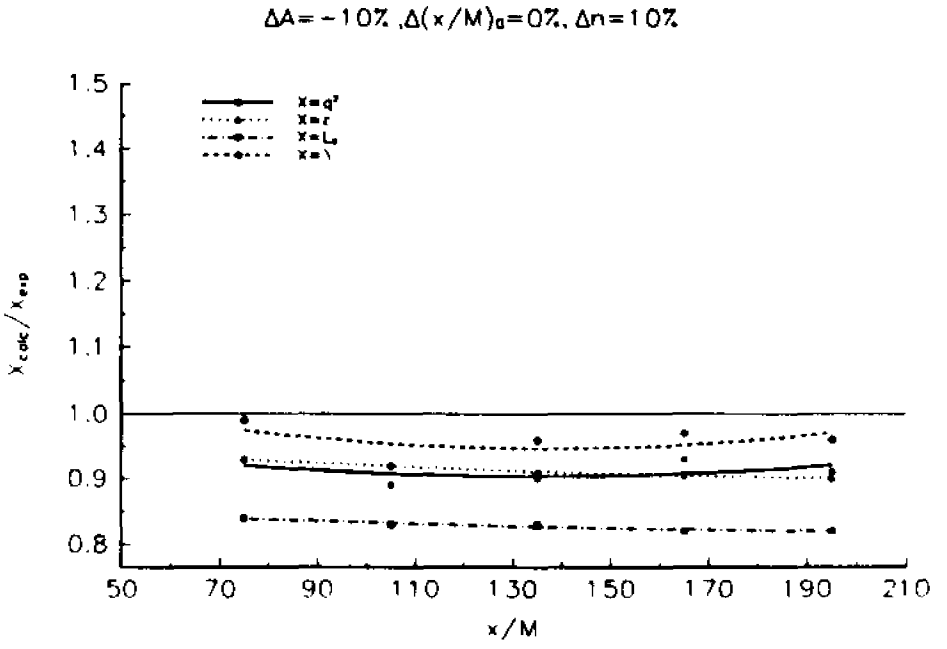

Figure F5: Effects for ΔA=-10%, $\Delta x/M_0$=0%, Δn=-10% variation on several flow parameters.

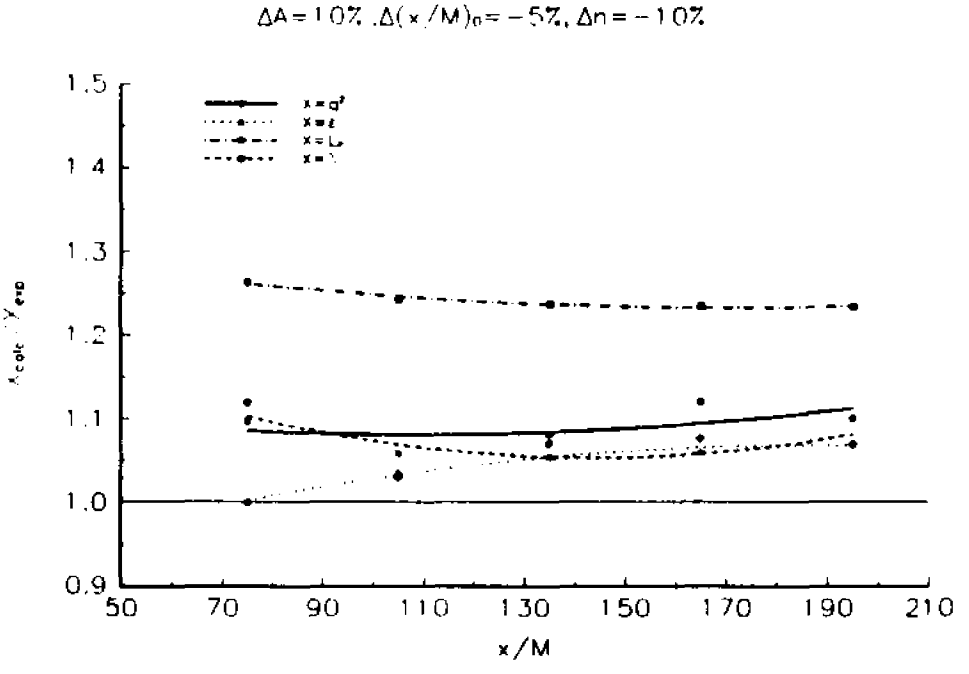

Figure F6: Effects for ΔA=10%, $\Delta x/M_0$=-5%, Δn=-10% variation on several flow parameters.

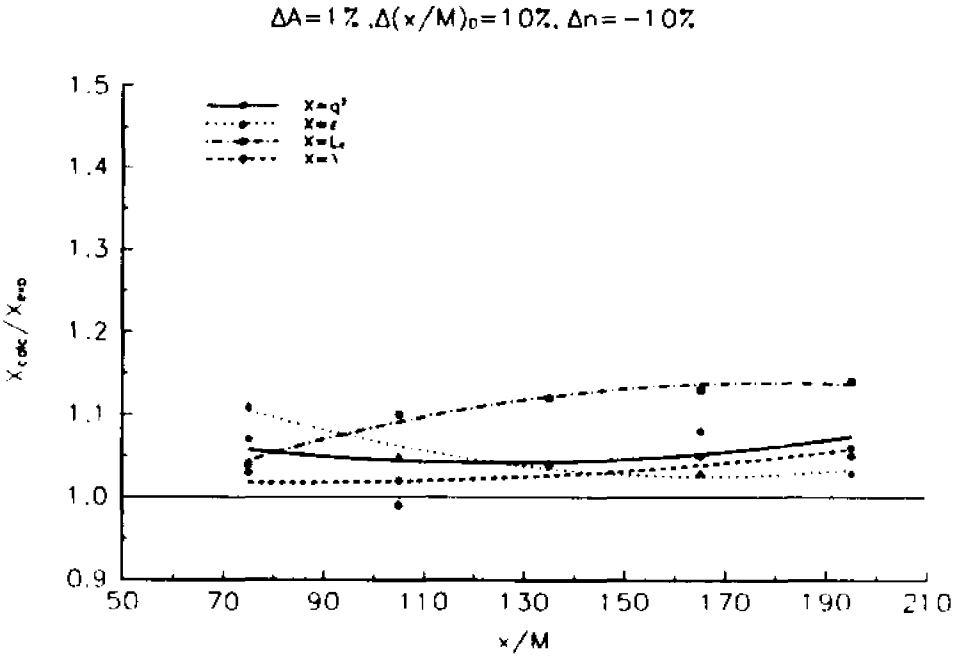

Figure F7: Effects for ΔA=1%, $\Delta x/M_0$=10%, Δn=-10% variation on several flow parameters.

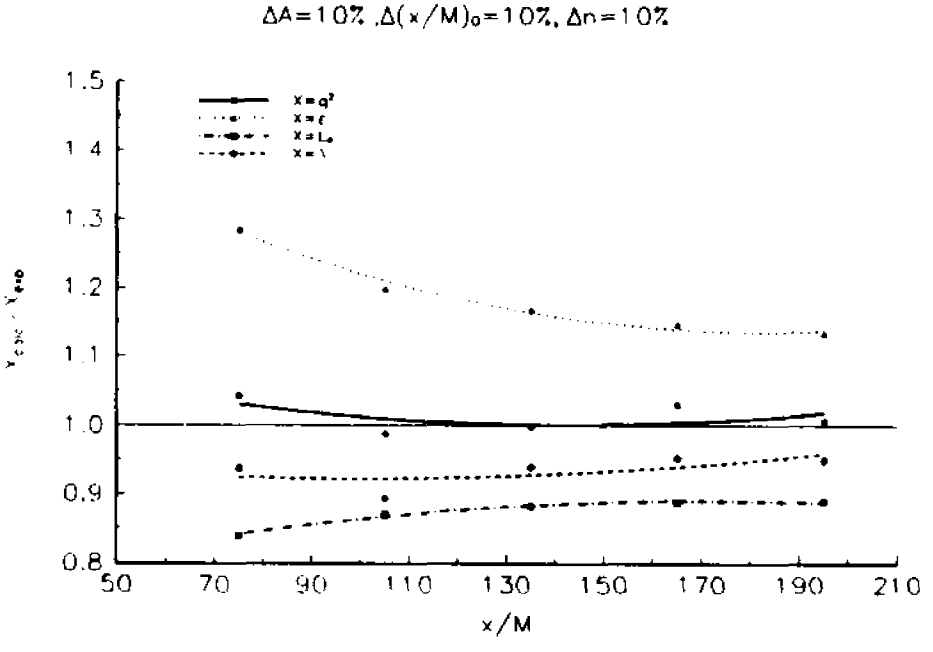

Figure F8: Effects for ΔA=10%, $\Delta x/M_0$=10%, Δn=10% variation on several flow parameters.

APPENDIX G

CALCULATION OF THE SKEWNESS OF THE VELOCITY DERIVATIVE

The skewness of thevelocity derivative, $S_{\partial u/\partial x}$, is a useful quantity which along with S_u qualifies the flow as isotropic. The flowfield was sampled at 333 kHz at every measuring location. Because of this high sampling rate, initial estimates of $S_{\partial u/\partial x}$ were found to be very low and below 0.1 for all investigated flowfields. Since $S_{\partial u/\partial x}$ represents the average rate of production of mean square vorticity by vortex stretching, a low value will either indicate absence of energy transfer, noise or oversampling. The first two reasons can be eliminated since turbulence intensities in the flowfield can reach values of 5% to 10% and signal to noise ratio of the sampled signals were of the order of 40:1 or better.

In orrder to investigate the effects of sampling rate on $S_{\partial u/\partial x}$ adjustable sampling was performed by skipping data points for calculations. The statistics of the velocity derivatives were recalculated for various effective sampling rates. Furthermore the time interval between measurements (Δt) was converted to space interval (Δx) by multiplying with the mean flow velocity $\overline{U}$. The space interval was non dimensionalized by the appropriateTaylor's microscale (λ) of each flowfield. The value of $S_{\partial u/\partial x}$ that was adpted was that where $\Delta x \approx \lambda$, since λ seems to be the appropriate scale characterizing this flowfield. Figure G1 presents the $S_{\partial u/\partial x}$ for various $\Delta x/\lambda$ values (i.e. various sampling rates). From this figure we can observe that there exists a large drop-off of the value of $S_{\partial u/\partial x}$ when the signal is oversampled.

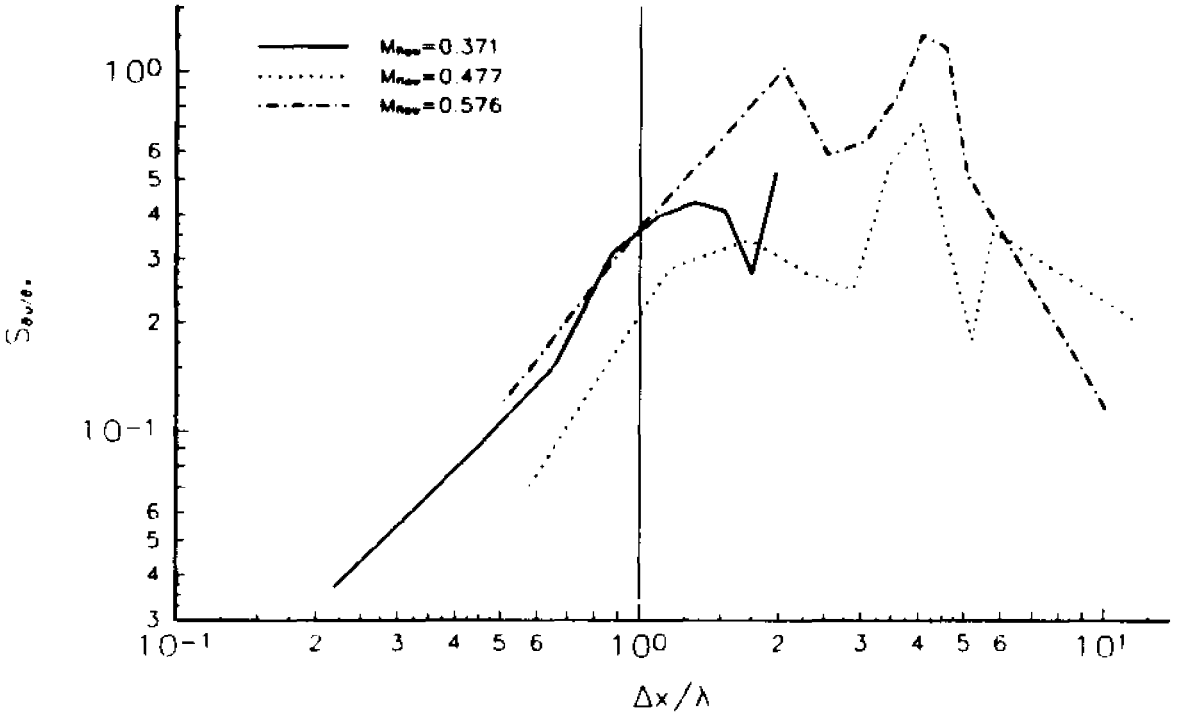

Figure G1: $S_{\partial u/\partial x}$ for several $\Delta x/\lambda$ values (various sampling rates).

REFERENCES

Agui, J., 1995, Private communication, Aerodynamics Laboratory, CCNY.

Alpher, R. A. and White, D. R., 1958, "Flow in Shock Tubes with Area Change at the Diaphragm Section," J. Fluid Mech., vol. 3, 457.

Anderson, D.J., 1982, "Modern Compressible Flow," McGraw-Hill, New York.

Andreopoulos, J. and Muck, K. C., 1987, "Some New Aspects of the Shock-Wave Boundary Layer Interaction in Compression Ramp Corner", J. Fluid Mech., vol.180, 405.

Antonia, R. A., Browne, L. W. B., and Chambers, A. J., 1981, " Determination of Time Constants of Cold Wires", Rev. Sci. Instrum., vol. 52 (9), pp. 1382.

Ardonceau, P. L., 1984, "The Structure of Turbulence in a Supersonic Shock-Wave/Boundary Layer Interaction", AIAA J., vol.22 (9), 1254.

Anyiwo, J. C. and Bushnell, D. M., 1982, "Turbulence Amplification in Shock-Wave Boundary Layer Interaction", AIAA J., vol.20, 893.

Barre, S., Dupont, P., Arzoumanian, E., Dussauge, J. P., and Debieve, J. F., 1993, "Some Recent Developments in Constant Current Hot-Wire Anemometry of Turbulent Supersonic Flows", ASME FED Vol. 167, p. 199-208, Symposium on Thermal Anemometry, Editors: Stock, D. E., Sherif, S. A., Smits, A. J., and Davidson, J.

Batchelor, G. K., and Townsend, A. A., 1949, " The Nature of Turbulent Motion at High Wave Numbers," Proc. Roy. Soc. A, 199, 238.

Bennett J. C. and Corrsin S., 1978, "Small Reynolds Number Nearly Isotropic Turbulence in a Straight Duct and Contraction," Phys. Fluids, 21 (12), 2129.

Betchov, R. and Lorenzen, C., 1974, "Phase Relations in Isotropic Turbulence," Phys. Fluids, 17 (8), 1503.

Beiser, A., 1981, "Concepts of Modern Physics," Mc Graw-Hill, New York.

Bradshaw, P., 1971, "An Introduction to Turbulence and its Measurements", Pergamon Press, New York.

Briassulis, G., and Andreopoulos, J., 1994, "Unsteady Pressure Field in Shock Wave Interaction with Grid Generated Turbulence in a Shock Tube," AIAA Paper No 94-2277.

Briassulis, G., and Andreopoulos, J., 1996, "High Resolution Measurements of Isotropic Turbulence Interacting with Shock Waves," AIAA Paper No 96-0042.

Briassulis, G., and Andreopoulos, J., 1996, "Compressibility Effects in Grid Generated Turbulence," AIAA Paper No 96-2055.

Briassulis, G., Agui, J., Andreopoulos, J. and Watkins, B. C., 1996, "The New Shock Tube Research Facility at CCNY for High Speed Turbulence Research," AIAA Paper No 96-0849.

Briassulis, G., Honkan, A., Andreopoulos, J. and Watkins, B. C., 1995, "Applications of Hot-Wire Anemometry in Shock Tube Flows," Exp. in Fluids, vol 19, 29.

Brown, J. L., Kussoy, M. I. and Coakley, T. J., 1985, "Turbulent Properties of Axisymetric Shockwave/Boundary Layer Interaction Flows," IUTAM Symposium, France.

Bird, G. A., 1959, "The Effect of Wall Shape on the Degree of Reinforcement of a Shock Wave Moving into a Convergent Channel," J. Fluid Mech., vol. 5, 60.

Buckingham, A. C., 1990, "Interactive Shock Structure Response to Turbulence," AIAA Paper No 90 - 1642.

Budwig, R., Tavoularis S., and Corrsin S., 1985, "Temperature Fluctuations and Heat Flux in Grid Generated Isotropic Turbulence with Streamwise and Transverse Mean-Temperature Gradients," J. Fluid Mech., vol. 153, 441.

Budwig, R., Zwart, P., J., Nguyen, V., and Tavoularis, S., "Grid Generated Turbulence in Compressible Streams," 2nd Symp. on Transitional and Turbulent Compressible Flows, Aug. 1995.

Charatis, G., Doherty, L. R., and Wilkerson, T. D. 1957, "C_2 and CN Emission in the Shock Tube," J. Chem. Phys., 27, 1415.

Chisnell, R. F., 1957, "The Motion of a Shock Wave in a Channel, with Applications to Cylindrical and Spherical Shock Waves," J. Fluid Mech., vol. 2, 286.

Chu, B. T. and Kovasznay, L. S. G., 1957,"Non-linear Interactions in a Viscous Heat-Conducting Compressible Flow," J. Fluid Mech., vol.3, 494.

Coleman, G. N. and Mansour, N. N., 1991, "Simulation and Modeling of Homogeneous Compressible Turbulence Under Isotropic Mean Compression," Eighth Symposium on Turbulence Shear Flows, Munich.

Corrsin, S., 1951, "The decay of isotropic temperature fluctuations in an isotropic turbulence," J. Aero. Sci., vol. 18, 417.

Deckker, B. E. L. and Weekes, M. E., 1976," The Unsteady Boundary Layer in a Shock Tube," Proc. Instn. Mech. Engrs. vol. 190, 287.

Debieve, J. F. and Lacharme, J. P., 1985, "A Shock Wave Free Turbulence Interactions", IUTAM Conference, Paris.

Dosanjh, D. S. and Weeks, T. M., 1964, "Interaction of a Starting Vortex as well as Karman Vortex Streets with Travelling Shock Wave", AIAA Paper No. 64-425.

Erbeck, R. and Merzkirch, W., 1988, "Speckle Photographic Measurement of Turbulence in an Airstream With Fluctuating Temperature," Exp. Fluids 8, 89.

Favre, A., 1965, "Équations des Gaz Turbulents Compressibles I," J. Méc., vol 4, 361.

Frenkiel, F., N., and Klebanoff, P., H., 1971, "Statistical Properties of Velocity Derivatives in Turbulent Field," J. Fluid Mech., vol. 48, 183.

Frenkiel, F., N., Klebanoff, P., H., and Huang, T., T., 1979, "Grid Turbulence in Air and Water," Phys. Fluids, 22 (9), 1606.

Gibson, C. H., Stegen, G. R., and Williams, R. B., 1970, "Statistics of the Fine Structure of Turbulent Velocity and Temperature Fields Measured at High Reynolds Number," J. Fluid Mech., vol. 41, 153.

Glass, I. I., 1958, U.T.I.A. Review No. 12.

Goldsworthy, F. A., 1959, "The Structure of a Contact Region, with Application to the Reflection of a Shock from a Heat-Conducting Wall," J. Fluid Mech., vol. 5, 164.

Groth, J., and Johansson, A. V., 1988, "Turbulence Reduction by Screens", J. Fluid Mech., vol. 197, 139.

Gutmark, E., J., Schadow, K., C., and Yu, K., H., 1995, "Mixing Enhancement in Supersonic Free Shear Flows," Annu. Rev. Fluid Mech., vol. 27, 375.

Hall, J. G., 1958, U.T.I.A. Review No. 12, part II.

Hancock, P. E. and Bradshaw P., 1983, "The Effect of Free-Stream Turbulence on Turbulent Boundary Layers," J. Fluid Eng., vol. 105, 284.

Hartung, L. C. and Duffy, R. E., 1986, "Effects of Pressure on Turbulence in Shock-Induced Flows", AIAA Paper No 86-0127.

Hayakawa, K., Smits, A. J., and Bogdonoff, S. M., 1984, "Turbulence Measurements in a Compressible Reattaching Shear Layer," AIAA Journal, vol. 22, 889.

Hertzberg, A. and Kantrowitz, A., 1950, "Studies with an Aerodynamically Instrumented Shock Tube," J. Applied Physics, vol.21, 874.

Hinze, J. O., 1975, "Turbulence," 2nd. edn., McGraw-Hill, New York.

Hirchfelder, J. O., Curtiss, C. F., and Bird, R. B., 1954, "Molecular Theory of Gases and Liquids," John Wiley & Sons, New York, pp. 101, 714-721, 893.

Honkan, A. and Andreopoulos, J., 1990, "Experiments in a Shock Wave / Homogeneous Turbulence Interaction", 21st Fluid Dynamics, Plasmadynamics and Lasers Conference, AIAA paper #90-1647.

Honkan, A. and Andreopoulos, J., 1992, "Rapid Compression of Grid-Generated Turbulence by a Moving Shock Wave", Phys. Fluids A, 4 (11).

Honkan, A. Watkins C. B. and Andreopoulos, J., 1994, "Experimental Study of Interactions of Shock Wave with Free Stream Turbulence" , J. Fluids Eng., vol. 116, 763.

Horstman, C. C., Settles, G. S., Williams, D. R., and Bogdonoff, S. M., 1982, "A Reattaching Free Shear Layer in Compressible Turbulent Flow," AIAA Journal, vol. 20, 79.

Jacquin, L., Blin, E., and Geffroy,P., 1991, "Experiments on Free Turbulence/Shock Wave Interaction," Eighth Symposium on Turbulence Shear Flows, Munich.

Keller, J. and Merzkirch, W., 1990, "Interaction of a Normal Shock with a Compressible Turbulent Flow", Exp. Fluids 8, 241.

Kistler, A., L., and Vrebalovich, T., 1966, "Grid Turbulence at large Reynolds numbers," J. Fluid Mech., vol. 26, 37.

Kovasznay L. S. G., 1950, "The Hot-Wire Anemometer in Supersonic Flows", J. of the Aeronautical Sciences, 17, 565-573.

Kuo, A. Y., and Corrsin, S., 1971, "Experiments on Internal Intermittency and Fine Structure Distribution Functions in Fully Turbulent Flows," J. Fluid Mech., vol. 50, 285.

Kuntz, T. W., Amatucci, V. A. and Addy A. L., 1987, "Turbulent Boundary Layer Properties Downstream of the Shockwave/Boundary Layer Interaction," AIAA Journal, vol. 25, 668.

Kussoy, M. I., Brown, J. D., Brown, J. L., Lockman, W. K. and Horstman, C. C., 1987, "Fluctuations and Massive Separation in Three Dimensional Shock Wave/Boundary Layer Interactions," ASME Fluids Engineering Conference, Washington D.C.

Lacey, J. and Long, D., 1990, "A Wave Diagram Computational Method With Application to a Free Piston Shock Tube," AIAA Paper No 90 - 1378.

Lapworth, K. C., 1959, "An Experimental Investigation of the Stability of Plane Shock Waves," J. Fluid Mech., vol. 6, 469.

LaRue, J. C., and Libby, P. A., 1978, "Temperature Fluctuations in the Plane Turbulent Wake", Phys. of Fluids 17,1956-1967.

Lee, L. and Lele, S. K. and Moin, P., 1991, "Direct Numerical Simulation and Analysis of Shock Turbulence Interaction", AIAA Paper No 91-0523.

Lee, L., Lele, S. K. and Moin, P., 1993, "Direct Numerical Simulation of Isotropic Turbulence Interacting with a Weak Shock Wave", J. Fluid Mech., vol. 251, 533.

Lee, L. and Lele, S. K. and Moin, P., 1994, "Interaction of Isotropic Turbulence with a Strong Shock Wave," AIAA Paper No 94-0311.

Mills, R. R., Kistler, A., L., O'Brien, V., and Corrsin, S., 1958, "Turbulence and Temperature Fluctuations Behind a Heated Grid," N.A.C.A. Tech. Note No. 4288.

Mohamed, S. M., and LaRue, C. J., 1990, "The Decay Power Law in Grid Generated Turbulence," J. Fluid Mech., vol. 219, 195.

Morkovin M.V., 1956, "Fluctuations and Hot-Wire Anemometry in Compressible Flows", AGARDograph 24.

Morkovin M.V., 1960, "Note on Assessment of Flow Disturbances at a Blunt Body traveling at Supersonic Speeds Owing to Flow Disturbances in Free Stream " J. Applied Mechanics, vol. 27, 223-229.

McKenzie, J. F., and Westphal, K. O., 1968, "Interaction of Linear Waves with Oblique Shock Waves," Phys. Fluids, vol. 11 (11), 2350.

Payne, R. B., 1957, "A Numerical Method for a Converging Cylindrical Shock," J. Fluid Mech., vol. 2, 185.

Resler, E. L., Lin, S., Kantrowitz, A., 1952, "The Production of High Temperature Gases in Shock Tubes", J. of Applied Physics, vol. 23 (12), 1390.

Ribner, H. S. 1955. "Convection of a Pattern of Vorticity Through a Shock Wave," NACA Rapt. 1233.

Ribner, H. S., 1986, "Spectra of Noise and Amplified Turbulence Emanating from Shock-Turbulence Interaction," AIAA Journal, vol. 25, 436.

Roshko, A., 1960, "On Flow Duration in Low-Pressure Shock Tubes," Phys. Fluids, vol.3 (6), 835.

Rotman, D. 1991, "Shock Wave Effects on a Turbulent Flow" Phys. Fluids A, vol.3 (7), 1792.

Saad, A. M, 1985, "Compressible Flow," Prentice-Hall, New Jersey.

Samimy, M., Petrie, H. L., and Addy, A. L., 1986, "A Study of Compressible Turbulent Reattaching Free Shear Layers," AIAA Journal, vol. 24, 261.

Seaholtz, R. G., 1991, "High-speed laser anemometry based on spectrally resolved Rayleigh scattering," Laser Anemometry-Volume 2, ASME, pp.465.

Settles, G. S., Fitzpatrick, T. J., and Bogdonoff, S. M., 1979, "Detailed Study of Attached and Separated Compression Corner Flowfields in High Reynolds Number Supersonic Flow," AIAA Journal, vol. 17, 579.

Settles, G. S., Williams, D. R., Baca, B. K., and Bogdonoff, S. M., 1982, "Reattachment of a Compressible Turbulent Free Shear Layer," AIAA Journal, vol. 20, 60.

Sirivat, A., and Warhaft, Z., 1983, "The effect of a passive cross-stream temperature gradient on the evolution of temperature variance and heat flux in grid turbulence," J. Fluid Mech., vol. 128, 323.

Smith, D. R., Poggie, J., and Smits, A. J., 1990, "Application of Rayleigh scattering to supersonic turbulent flows," Int. Symp. on Applications of Laser-Doppler Anemometry to Fluid Mechanics, Lisbon, Portugal.

Smits A. J., and Muck K. C., 1987, "Experimental Study of Three Shock Wave/Boundary layer Interactions," J. Fluid Mech., vol. 182, pp. 291.

Smits, A. J., Muck, K. C., and Hayakawa, K., 1983, "Constant Temperature Anemometer Practice in Supersonic Flows. Part 1. The Normal Wire" Exp. Fluids, vol. 2, 23.

Spina, E., F., Smits, A., J., and Robinson, S., K., 1994, "The Physics of Supersonic Turbulent Boundary Layers," Annu. Rev. Fluid Mech., vol. 26, 287.

Stainback, P. C., and Nagabushana, K. A., 1993, "Review of Hot-Wire Anemometry Techniques and the Range of Their Applicability", ASME FED Vol. 167, p. 93-134, Symposium on Thermal Anemometry, Editors: Stock, D. E., Sherif, S. A., Smits, A. J., and Davidson, J.

Stewart, R. W., and Townsend, A. A., 1951, "Similarity and Self Preservation in Isotropic Turbulence," Proc. Roy. Soc. A, 243, 359.

Tan-Atichat, J., Nagib, H., M., and Loehrke, R., I., 1982, "Interaction of Free-Stream Turbulence with Screens and Grids: A Balance between Turbulence Scales," J. Fluid Mech., vol. 114, 501.

Tavoularis S., and Corrsin S., 1981, "Experiments in nearly Homogeneous Turbulent Shear Flow with a Uniform Mean Temperature Gradient. Part 1," J. Fluid Mech., vol. 104, 311.

Tavoularis S., and Corrsin S., 1981, "Experiments in nearly Homogeneous Turbulent Shear Flow with a Uniform Mean Temperature Gradient. Part 2. The Fine Structure," J. Fluid Mech., vol. 104, 349.

Tavoularis S., Bennett J. C. and Corrsin S., 1978, "Velocity derivative skewness in small Reynolds number, nearly isotropic turbulence," J. Fluid Mech., vol. 88, 63.

Taylor, G. I., 1938, "Production and Dissipation of Vorticity in a Turbulent Fluid," Proc. Roy. Soc. A, 164, 15.

Tsinober, A., Kit, E., and Dracos, T., 1992, "Experimental Investigation of the Field of Velocity Gradients in Turbulent Flows," J. Fluid Mech., vol. 242, 169.

Trolier J. W. and Duffy, R. E., 1985, "Turbulent Measurements in Shock-Induced Flows," AIAA J., vol. 23(8), 1172.

Viecelli, J. A., 1989, "Implosion and Shock Compression of Two-Dimensional Eddy Structures," Phys. Fluids A, Vol. 1, (4), 753.

Walker, J. D. A. and Dennis, S. C. R., 1972, "The Boundary Layer in a Shock Tube," J. Fluid Mech., vol. 56, 19.

Warhaft, Z., and Lumley, J. L., 1978, "An Experimental Study of the Decay of Temperature Fluctuations in Grid-Generated Turbulence," J. Fluid Mech., vol. 88, 659.

Weir, A. D., Wood, D. H. and Bradshaw, P., 1981, "Interacting Turbulent Shear Layers in a Plane Jet", J. Fluid Mech, vol. 107, 237.

White, D. R., 1958, "Influence of Diaphragm Opening Time on Shock-Tube Flows," J. Fluid Mech., vol. 4, 585.

Whitham, G. B., 1956, "On the Propagation of Weak Shock Waves," J. Fluid Mech., vol. 1, 290.

Whitham, G. B., 1957, "A New Approach to Problems of Shock Dynamics. Part I Two-Dimensional Problems," J. Fluid Mech., vol. 2, 145.

Whitham, G. B., 1958, "On the Propagation of Shock Waves Through Regions of Non-Uniform Area of the Flow," J. Fluid Mech., vol. 4, 337.

Wyngaard, J. C., 1968, " Measurements of Small Scale Turbulence Structure with Hot-Wires", J. Phys. E: Sci. Instr., vol 1, pp. 1105.

Wyngaard, J. C., 1971, "The Effect of Velocity Sensitivity on Temperature Derivative Statistics in Isotropic Turbulence," J. Fluid Mech., vol. 48, 763.

Zwart, P., Budwig, R., and Tavoularis, S., 1996, "Grid Turbulence in Compressible Flow," private communication.